Universidad de Oviedo

Programa de Física de la Materia Condensada

GRAFENOS PROCESABLES EN FASE LÍQUIDA CON CARACTERÍSTICAS OPTIMIZADAS MEDIANTE EL CONTROL MICROSCÓPICO DE SU ESTRUCTURA

TESIS DOCTORAL

RUBÉN ROZADA RODRÍGUEZ

JULIO 2014

Agradecimientos

Quiero expresar mi más sincero agradecimiento a mis directores de tesis Juan Ignacio Paredes Nachón, Silvia María Villar Rodil y Juan Manuel Díez Tascón, así como a los doctores Fabián Suarez García y Amelia Martínez Alonso, por la confianza depositada en mí para la realización de esta tesis doctoral en su grupo de investigación. Quiero agradecer especialmente a mis directores de tesis su constante apoyo y asesoramiento a lo largo de estos años.

Al doctor Jesús Ángel Blanco Rodríguez por aceptar ser el tutor de esta tesis.

Al Ministerio de Educación por la concesión de una beca predoctoral del programa de Formación del Profesorado Universitario.

Al Consejo Superior de Investigaciones Científicas y al Instituto Nacional del Carbón por brindarme los medios necesarios para el desarrollo de esta tesis.

Al personal laboral del Instituto, y muy especialmente a Luis, Diego y Aníbal.

A los doctores Pablo Solís Fernández y Laura Guardia, que siempre han estado dispuestos a ayudarme y me han enseñado muchas cosas. También al resto de mis compañeros de laboratorio y/o de despacho que se han portado fenomenalmente conmigo: Tomás, Miguel, Katia, Marina, Susi, Marley, Bea, Marlén, Nacho, Chema, Roberto y Pocho.

A mis compañeros habituales en el comedor: Ángela, Victor, Borja, Nuria, Alicia, Carolina y Juana Mari. Echaré de menos comer con vosotros.

A mis amigos de toda la vida: Marina, Victor, Nuria, Irene, Unai, Alberto y miembros de la P.E. Me considero afortunado de tener amigos como vosotros.

A mis abuelos, a mis padres, a mi hermano y a Isa. Os quiero por encima de todo. No me faltéis nunca.

Resumen

El objetivo principal de la presente tesis doctoral consiste en desarrollar estrategias que permitan mejorar las características de grafeno producido en fase líquida mediante la ruta del óxido de grafito, de modo que se pueda compatibilizar la relativa simplicidad y alto rendimiento de dicha ruta con la perfección estructural de las láminas de grafeno generadas mediante otros métodos. El desarrollo de dichas estrategias se ha apoyado en el estudio detallado de las láminas mediante diferentes técnicas de caracterización que también han permitido evaluar su efectividad.

Se estudió el proceso de reducción del óxido de grafito exfoliado (óxido de grafeno) mediante reactivos químicos o radiación ultravioleta. El exámen del óxido de grafeno reducido mediante distintos agentes, que permiten distintos grados de reducción, indica que este proceso elimina primordialmente los grupos funcionales oxígenados más lábiles, situados en el plano basal. Además, las imágenes por microscopía de efecto túnel a escala atómica muestran que las láminas reducidas desarrollan dominios ordenados, cuyo tamaño depende del grado de reducción, en convivencia con regiones todavía oxidadas. Por otra parte, es posible conseguir un alto grado de reducción de las dispersiones coloidales de óxido de grafeno mediante irradiación con luz ultravioleta sin necesidad de fotocatalizadores o reactivos químicos. Además, es posible aprovechar el ambiente reactivo que se genera en las láminas para degradar un contaminante como la rodamina B o para la preparación de materiales híbridos "grafeno-nanopartícula de oro" que pueden ser usados como substratos para espectroscopía Raman amplificada por superficie y como catalizadores.

También se estudió el curado de las láminas de óxido de grafeno reducido químicamente mediante tratamientos térmicos a alta temperatura. La eliminación completa de los grupos funcionales en el óxido de grafeno se logra a temperaturas moderadamente elevadas (1500 °C). El curado estructural definitivo de las láminas requiere la eliminación de las vacantes generadas durante la sustracción de los grupos funcionales. Este proceso está gobernado por la migración de vacantes hacia los bordes de las láminas, que conducirá al curado de éstas siempre que el tamaño de las vacantes y/o su densidad no sean demasiado grandes. Esta condición se satisface en el óxido de grafeno reducido químicamente pero no en el óxido de grafeno sin reducir. La eliminación definitiva de las vacantes atómicas requiere la utilización de temperaturas en torno a 1800-1950 °C si las láminas están depositadas sobre un substrato inerte, como las terrazas prístinas del grafito. Si las láminas se encuentran sobre un substrato reactivo, tal como cuando se encuentran ensambladas formando un filme, las interacciones interlaminares (enlaces covalentes entre átomos de carbono insaturados en bordes de vacantes) entorpecen la migración de las vacantes hacia los bordes de las láminas y el curado definitivo requiere temperaturas aún más altas, en torno a 2400 °C.

Por último, se estudió la influencia de las vacantes atómicas sobre las propiedades eléctricas del grafeno. Para ello se recurrió a grafeno de mayor calidad estructural, producido mediante depósito químico en fase vapor. Mediante plasma de oxígeno generado por microondas se consiguieron densidades de vacantes en el rango de 10^3-10^5 μm^{-2} variando la intensidad del plasma y el tiempo de exposición. La introducción de vacantes produjo un exceso neto de portadores de carga positiva (dopaje tipo p) y un descenso de la movilidad de los portadores de carga, que se atribuye a la dispersión de dichos portadores por las vacantes.

Abstract

The main aim of the present doctoral thesis is to develop strategies that enable improving the quality of graphenes produced in the liquid phase by the so called "graphite oxide route", so as to combine the simplicity and high performance of this route with the quality of the sheets produced by other methods. The development of these strategies relies on the detailed examination of the sheets by different characterization techniques that have also allowed to assess their effectivity.

The reduction of exfoliated graphite oxide (graphene oxide) by means of chemical agents or ultraviolet light has been studied. The examination of graphene oxide reduced by different agents, which enables to attain various reduction degrees, indicates that this process mainly eliminates the most labile oxygen groups, located in basal plane positions. Besides, scanning tunneling microscopy images reveal that the reduced sheets develop ordered domains, the size of which depends on the reduction degree attained, coexisting with still oxidized regions. On the other hand, it is possible to achieve a high degree of reduction for colloidal suspensions of graphene oxide using ultraviolet radiation in the absence of chemical reactants or photocatalysts. In addition, it is also possible to benefit from the reactive environment that is generated in the proximity of the sheets to induce the degradation of a pollutant such as rhodamine B or to synthesise "graphene-gold nanoparticle" hybrids that can be used as substrates for surface enhanced Raman spectroscopy or as catalysts.

The healing of chemically reduced graphene oxide sheets by means of high temperature annealing has also been studied. The complete elimination of the oxygen functional groups present in graphene oxide is accomplished at moderately high temperatures (1500 °C). The full structural healing of the sheets requires the elimination of the vacancies generated during the decomposition of the functional groups. This process is governed by the migration of atomic vacancies towards the edge of the sheets, which leads to the reparation of the sheets as long as the vacancy size and/or their density do not become too large. This requirement is fulfilled in reduced graphene oxide but not in the unreduced sheets. The full elimination of the atomic vacancies necessitates temperatures around 1800-1950 °C when the sheets are deposited on an inert substrate, such as the terraces of pristine graphite. If the sheets are deposited on a reactive substrate (that is the case for sheets assembled into a film), the interlayer interactions between unsaturated carbon atoms located at the border of the vacancies hinder the migration of the latter towards the sheet edges and thus, the temperatures required for complete healing are higher (2400 °C).

Finally, the effect of the atomic vacancies on the electric properties of the graphene has been investigated. This study has been performed using graphene of high structural quality produced by chemical vapor deposition. By means of a microwave-generated oxygen plasma, the introduction of vacancy densities ranging from 10^3 to 10^5 μm^{-2} was

made possible by tuning the plasma intensity and the exposure time. The introduction of vacancies led to a net excess of positive charge carriers (p-type doping) and a decrease in the charge carrier mobility, which is attributed to the scattering of the carriers by the vacancies

Introducción 1

1. Introducción

1.1 El grafeno

El grafeno es un material bidimensional que consiste en una monocapa de átomos de carbono dispuestos en una red en panal de abeja. El grafeno constituye la unidad estructural básica de otras importantes formas alotrópicas del carbono como el grafito, los nanotubos de carbono o los fullerenos, tal y como muestra la Figura 1 [1]. De hecho, mucho tiempo antes de que fuese aislado por primera vez, este material ya había sido objeto de estudio por tratarse de un modelo teórico útil en el estudio de estas formas alotrópicas. En ese momento, diversas predicciones teóricas señalaban que las redes cristalinas de baja dimensionalidad, como el grafeno, serían inestables a cualquier temperatura finita. Esta inestabilidad se produciría como consecuencia de las fluctuaciones térmicas, que darían lugar a desplazamientos de los átomos comparables a las distancias interatómicas, imposibilitando la existencia de orden a largo alcance [2]. Además, algunos trabajos experimentales con láminas delgadas, en los que se observaba que la estabilidad de dichas láminas disminuía al reducir su espesor, parecían respaldar este supuesto [3]. Sin embargo, estas hipótesis se vieron invalidadas en el año 2004, cuando los físicos Geim y Novoselov lograron el aislamiento de copos muy finos de grafito y, finalmente, de grafeno monocapa [4, 5].

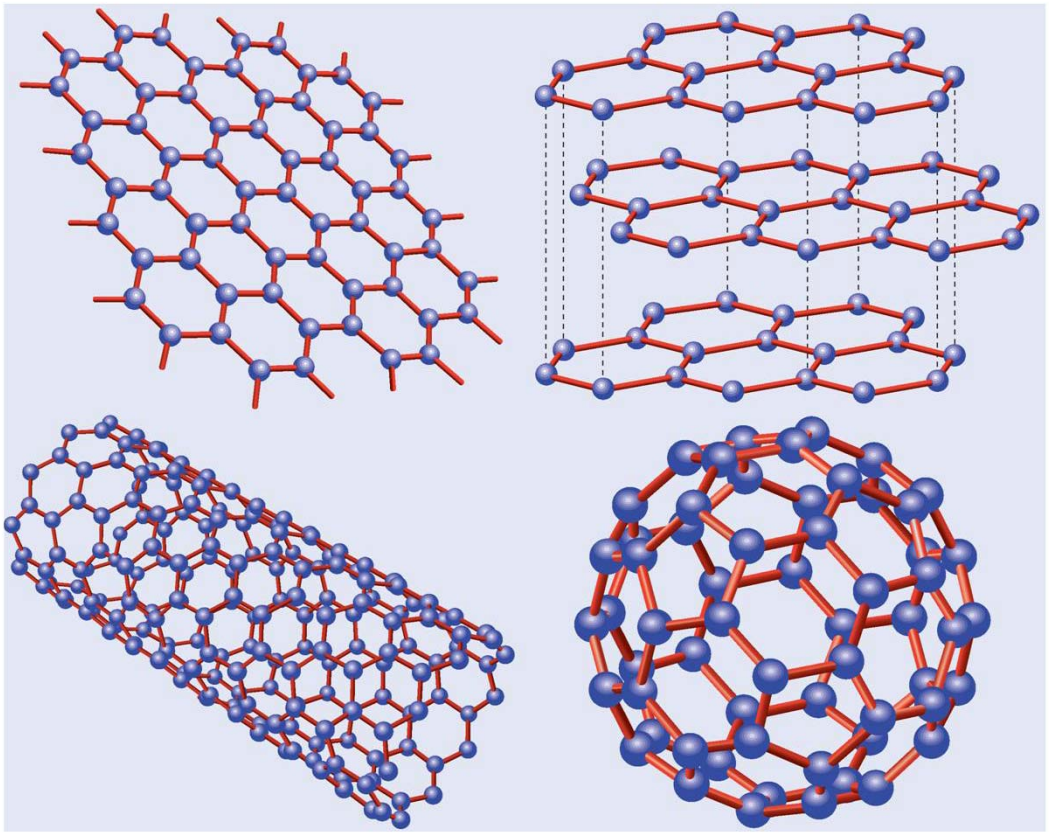

Figura 1. Formas alotrópicas del carbono basadas en grafeno. Reproducido de [6].

En determinados contextos, la palabra grafeno también puede adoptar un significado más amplio, llegando a englobar grafito de unas pocas capas (<10). Sin embargo, en ese caso suele especificarse si se trata de grafeno monocapa, bicapa o multicapa debido a la fuerte dependencia de las propiedades del grafeno con el número de capas.

1.2 Estructura del grafeno

El origen de la estructura en panal de abeja del grafeno se encuentra en la hibridación sp^2 de los orbitales átomicos del carbono, según la cual, los orbitales $2p_x$ y $2p_y$ se combinan con el orbital 2s para formar tres orbitales híbridos mientras que el orbital $2p_z$ permanece sin cambio. En virtud de dicha hibridación, los tres orbitales híbridos en disposición trigonal en el plano solapan frontalmente con los orbitales de los primeros vecinos formando fuertes enlaces covalentes tipo σ, mientras que el orbital $2p_z$, que es perpendicular al plano, solapa lateralmente formando enlaces tipo π.

1.3 Propiedades y aplicaciones del grafeno

Las excelentes propiedades del grafeno también son una consecuencia directa de la hibridación sp^2 de los átomos de carbono. Por ejemplo, el grafeno debe su escasa reactividad o su elevada resistencia mecánica a sus fuertes enlaces σ en el plano, en los que los electrones están localizados entre los núcleos de los átomos enlazados. De forma análoga, sus propiedades opto-electrónicas derivan de la deslocalización de los electrones de los orbitales $2p_z$.

1.3.1 Propiedades eléctricas

La estructura electrónica del grafeno se puede describir mediante un modelo de enlace fuerrte en el que los estados electrónicos se representan mediante una combinación lineal de orbitales atómicos $2p_z$. Según este modelo, la relación de dispersión de la energía de las bandas de valencia, π, y de conducción, π*, se puede expresar mediante la expresión [7]:

$$E(k_x, k_y) = \pm\gamma\sqrt{1 + 4cos\left(\frac{\sqrt{3}k_x a}{2}\right)cos\left(\frac{k_y a}{2}\right) + 4cos^2\left(\frac{k_y a}{2}\right)} \qquad (1)$$

donde γ es la energía de solapamiento entre primeros vecinos (γ~2.7eV), a es el parámetro de red del grafeno (a=0.246 nm) y k_x, k_y son las componentes del vector de onda. De acuerdo con la ecuación (1), las bandas de valencia y conducción en el grafeno son simétricas y llegan a tocarse en los seis puntos K de la zona de Brillouin, también denominados puntos de Dirac o de neutralidad de carga (Figura 2). En el estado fundamental el nivel de Fermi pasa por los puntos de Dirac, lo que significa que la banda de valencia está totalmente ocupada y los electrones de mayor energía ocupan estados en torno a dichos puntos. Puesto que la estructura electrónica difiere de la de un metal, en la que el nivel de Fermi se encuentra en la banda de conducción, o la de un semicon-

ductor, en la que el nivel de Fermi se sitúa en el gap de banda que separa la banda de valencia y la banda de conducción, se considera que el grafeno es un semi-metal con solapamiento de banda cero o un semiconductor de gap de banda cero. La relación de dispersión en las proximidades de los puntos de Dirac (±0.6 eV) es lineal, lo que implica que los portadores de carga en ese rango de energías se mueven con la misma velocidad, denominada velocidad de Fermi, $v_F=10^6$ m/s. La simetría de la red impide la retrodispersión de los electrones, lo que le confiere una extraordinaria conductividad eléctrica, llegándose a medir movilidades electrónicas superiores a 2×10^5 cm^2 V^{-1} s^{-1} en grafeno monocapa suspendido [8].

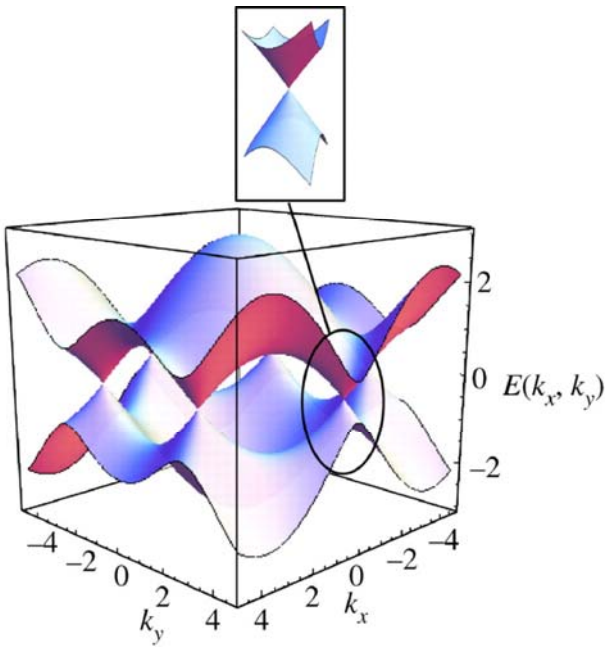

Figura 2. Representación 3D de la relación de dispersión en la primera zona de Brillouin resaltando la forma cónica y simétrica de dicha dispersión en los puntos K de dicha zona. Reproducido de [9].

En el grafeno, la densidad de portadores de carga puede ser controlada mediante la introducción de determinados defectos o impurezas (dopaje) o a través de la aplicación de un campo eléctrico externo (efecto de campo). En grafeno sin dopar, la resistividad alcanza su máximo valor cuando el nivel de Fermi cruza el punto de Dirac, es decir, en ausencia de campo eléctrico aplicado. Sin embargo, debido al dopaje inducido por el substrato o por adsorbatos presentes en la superficie del grafeno, el punto de neutralidad de carga siempre se encuentra desplazado un cierto voltaje de puerta. La posibilidad de modular las propiedades eléctricas del grafeno mediante la aplicación de un campo eléctrico resulta interesante para el desarrollo de determinadas aplicaciones electrónicas basadas en grafeno, como dispositivos de radiofrecuencia [10]. Sin embargo, la ausencia de gap de banda limita su implementación en dispositivos de tipo lógico, ya que la modulación no consigue producir estados de apagado bien definidos, es decir, no tiene la capacidad para hacer que la densidad de corriente que fluye a través del grafeno difiera en varios órdenes de magnitud. Hasta el momento, varias estrate-

gias basadas en el dopaje químico [11], la interacción con sustratos [12], la aplicación de campos eléctricos y magnéticos [13], el uso de bicapas [14, 15] o el confinamiento lateral de los portadores en nanocintas de grafeno [16, 17] han permitido modificar la estructura electrónica e incluso inducir un gap de banda en el grafeno.

1.3.2 Propiedades ópticas

La transmitancia en el grafeno monocapa suspendido dentro del rango del visible es independiente de la longitud de onda, pudiendo expresarse como [18]:

$$T = 1 - \pi\alpha = 0.977 \qquad (2)$$

donde α es la constante de estructura fina. Por lo tanto, el grafeno monocapa es un material casi transparente. La opacidad (1-T=2.3 %) aumenta linealmente con el número de capas. Además, su reflectancia es despreciable (<0.1%).

Debido a su transparencia y a su baja resistividad, el grafeno constituye un candidato ideal para sustituir al óxido mixto de indio y estaño (ITO) en la fabricación de electrodos transparentes para dispositivos electrónicos como pantallas [19, 20], LEDs orgánicos [21] o células fotovoltaicas [22]. Además, a diferencia del ITO, el grafeno es un material flexible, por lo que facilitaría el desarrollo de dispositivos electrónicos plegables [23].

1.3.3 Propiedades mecánicas

Las propiedades mecánicas de láminas de grafeno prístino han podido ser determinadas mediante experimentos de nanoindentación en un microscopio de fuerza atómica, presentando un módulo de Young de ~1.0 TPa y una resistencia a la tracción superior a ~100 GPa [24]. De acuerdo con estos valores, el grafeno constituye el material de mayor resistencia mecánica a la tracción conocido.

Debido a sus extraordinarias propiedades mecánicas, se ha propuesto el uso de grafeno como material de refuerzo en compuestos polímero-grafeno. El grafeno podría superar a los nanotubos de carbono en esta función, ya que su gran área superficial permite maximizar el contacto con la matriz polimérica. Sin embargo, para aprovechar esta característica debe conseguirse una dispersión homogénea de las láminas dentro de la matriz, lo cual resulta difícil debido a la baja dispersabilidad de las láminas de grafeno prístino. No obstante, estudios recientes han observado que la introducción de defectos por debajo de un cierto rango tiene efectos limitados en parámetros como el módulo de Young o la resistencia mecánica [25]. Esto tiene importantes implicaciones en el diseño de materiales compuestos, ya que indica que la formación de enlaces covalentes entre el grafeno y la matriz no limitaría su capacidad como material de refuerzo. Además, abre la puerta al uso de materiales como el óxido de grafeno reducido que, puesto que puede dispersarse en determinados disolventes, facilitaría la labor de dispersar las láminas dentro de la matriz de forma homogénea.

1.3.4 Propiedades térmicas

La conductividad térmica a temperatura ambiente de grafeno monocapa suspendido se sitúa en torno a $\kappa \sim 5000$ W m^{-1} K^{-1}. Por lo tanto, el grafeno es el mejor conductor térmico que existe, superando a otras formas de carbono basadas en la hibridación sp^2 como los nanotubos de carbono ($\kappa \sim 3500$ W m^{-1} K^{-1}) o el grafito, cuya conductividad térmica longitudinal es $\kappa \sim 1910$ W m^{-1} K^{-1} [26]. En estos materiales, los fuertes enlaces covalentes en el plano permiten la propagación eficiente de los fonones. Además, la conductividad térmica del grafeno duplica la del siguiente mejor conductor, el diamante ($\kappa \sim 1200$-2000 W m^{-1} K^{-1}). Sin embargo, la conductividad térmica del grafeno se reduce a $\kappa \sim 600$ W m^{-1} K^{-1} cuando éste se encuentra soportado sobre un substrato como el dióxido de silicio [27]. A pesar de ello, este valor continua siendo mayor que el del cobre (en un factor 2) o el del silicio (en un factor 50), que son los materiales usados en la electrónica actual [28]. Por lo tanto, el grafeno constituye un material muy atractivo para ser usado como elemento de disipación de calor en dispositivos electrónicos, puesto que la miniaturización de este tipo de dispositivos ha hecho necesario que dicha disipación se realice de modo eficiente.

1.3.4 Propiedades químicas

El grafeno es un material químicamente anisótropo, ya que su reactividad en el plano basal es muy baja (excepto para reacciones de oxidación), mientras que sus bordes son altamente reactivos debido a la presencia de insaturaciones. El área superficial del grafeno es máxima debido a que su espesor es de tan solo un átomo, siendo su valor teórico de ~ 2600 m^2 g^{-1}. Esta propiedad, junto con su elevada conductividad eléctrica, convierte al grafeno en un buen candidato para remplazar al grafito en la fabricación de ánodos de ion-litio [29]. Además, le confiere un enorme potencial en el desarrollo de sensores de gran sensibilidad [30] o como soporte de catalizadores [31].

Por otra parte, se ha podido observar que el grafeno constituye una membrana impermeable a gases. Esto hace posible la separación de gases o líquidos a través de una barrera de un átomo de espesor [32]. Además, mediante la creación controlada de poros pueden fabricarse tamices moleculares [33, 34]. El mínimo espesor de dichos tamices maximizaría el flujo de las especies deseadas a través de la membrana, mientras que su robustez estaría asegurada en base a las excelentes propiedades mecánicas del grafeno.

1.3 Métodos de preparación

Los métodos de preparación de grafeno pueden clasificarse de acuerdo a las dos metodologías tradicionales para la obtención de materiales nanoestructurados: “top-down” o descendentes y “bottom-up” o ascendentes.

1.3.1 Métodos "top-down"

Las metodologías "top-down" se basan en la separación de las láminas de grafeno que forman un cierto material carbonoso "bulk" que tenga al grafeno como su unidad estructural básica. En los materiales grafíticos, las láminas de grafeno se encuentran apiladas y unidas mediante fuerzas de van der Waals. A pesar de que este tipo de interacción es mucho más débil que la asociada al enlace covalente en el plano de las láminas, no resulta sencillo separar dichas láminas de manera eficiente y sin que éstas se vean dañadas de uno u otro modo. Al conjunto de metodologías "top-down" pertenece el primer método empleado con éxito para aislar grafeno, conocido como exfoliación micromecánica, que consiste en la exfoliación repetida de una pieza de grafito mediante cinta adhesiva [4]. Los copos se transfieren a SiO_2/Si y son identificados por medio de un microscopio óptico aprovechando el cambio de índice de refracción entre el grafeno y dicho substrato. Debido a que el procesado es mínimo, este método permite obtener grafeno de alta calidad. No obstante, no es un método adecuado para la obtención de grafeno que pueda ser usado con fines prácticos debido a su bajo rendimiento, limitándose su uso a estudios de tipo fundamental sobre las propiedades del grafeno. Esto ha motivado el desarrollo y la optimización de otros métodos con un rendimiento mucho mayor que proporcionen grafeno con la mayor calidad posible. Los métodos "top-down" que han suscitado un mayor interés por su potencial para la producción de grafeno a gran escala son la exfoliación mecánica de grafito en disolventes adecuados y la exfoliación de óxido de grafito.

1.3.1.1 Exfoliación mecánica de grafito en disolventes

Este método consiste en la exfoliación de grafito en un cierto disolvente con capacidad para estabilizar las láminas de grafeno típicamente mediante el uso de ultrasonidos, o tal y como se ha propuesto más recientemente, mediante el uso de mezcladoras de cizalla [35]. El uso de mezcladores de cizalla resulta más adecuado para la escalabilidad del proceso, ya que supera la limitación que supone el uso de ultrasonidos en cuando a ritmo de producción se refiere. Este método posibilita la obtención de dispersiones coloidales estables de grafeno de alta calidad, aunque la concentración máxima dispersada y el rendimiento en grafeno monocapa son relativamente bajos (~0.01 mg mL^{-1} y 10-30%) [36]. Aunque la dispersabilidad puede mejorarse aumentando el tiempo de tratamiento de exfoliación, esto provoca una disminución del tamaño de lámina y un aumento de la concentración de defectos [37]. La eficiencia de exfoliación y estabilización coloidal depende en gran medida de la elección del disolvente, encontrándose los mejores resultados para disolventes con energía superficial y parámetros de solubilidad de Hansen semejantes a los del grafeno [38, 39]. La coincidencia de parámetros de solubilidad entre grafeno y disolvente permite minimizar el coste energético de exfoliar y dispersar el grafito. Lamentablemente, la mayor parte de los disolventes con estas características poseen un elevado punto de ebullición, dificultando su eliminación en el uso de estas dispersiones como recubrimientos o para el procesado de filmes. El agua

no es un disolvente apropiado para la obtención de grafeno por esta vía, ya que su energía superficial y parámetros de solubilidad difieren notablemente de los del grafeno. No obstante, la preparación de dispersiones acuosas coloidalmente estables es posible en presencia de estabilizantes adecuados, tales como surfactantes [40], biomoléculas [41] o polímeros [42].

1.3.1.2 Ruta del óxido de grafito

Entre los métodos "top-down" para la síntesis de grafeno destaca la denominada ruta del óxido de grafito, que aprovecha la mayor facilidad de separar entre sí las láminas de este compuesto en comparación con el grafito. Este método consta a grandes rasgos de tres etapas: (1) la oxidación del grafito para dar lugar a óxido de grafito, (2) la exfoliación del óxido de grafito en medio acuoso u orgánico para obtener dispersiones coloidales de óxido de grafeno (GO) y (3) la reducción del óxido de grafeno para obtener óxido de grafeno reducido (rGO) (Figura 3).

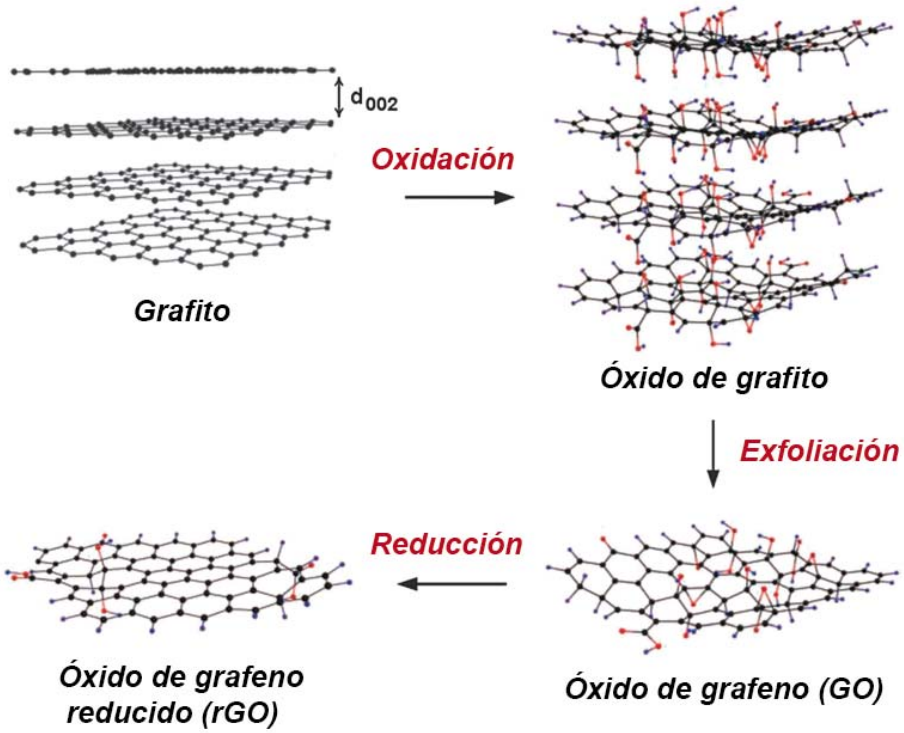

Figura 3: Ruta del óxido de grafito para la síntesis de grafeno. Reproducido de [43].

a) Oxidación del grafito

La oxidación del óxido de grafito se puede realizar mediante distintos métodos, siendo el método de Hummers el más extendido [44]. Consiste en un tratamiento en medio fuertemente ácido que introduce funcionalidades oxigenadas en la estructura carbonosa, cuya presencia debilita por un lado las fuerzas cohesivas entre láminas de grafeno vecinas y, por otro, introduce afinidad por ciertos disolventes. El modelo más aceptado para la estructura del óxido de grafito es el de Lerf-Klinowski [45, 46]. Dicho modelo

describe el óxido de grafito como un material no estequiométrico de estructura laminar formada por planos de átomos de carbono con grupos hidroxilo y epoxi decorando el plano basal y grupos carboxilo y carbonilo situados en los bordes de las láminas (Figura 4). No obstante, la utilización de distintos métodos de oxidación da lugar a variaciones en la composición del óxido de grafito [47, 48], lo que ha propiciado la investigación de métodos alternativos que permitan obtener óxido de grafeno con características mejoradas [49, 50]. También se ha estudiado el desarrollo de procesos de oxidación alternativos, capaces de minimizar el impacto ambiental del método de Hummers [51].

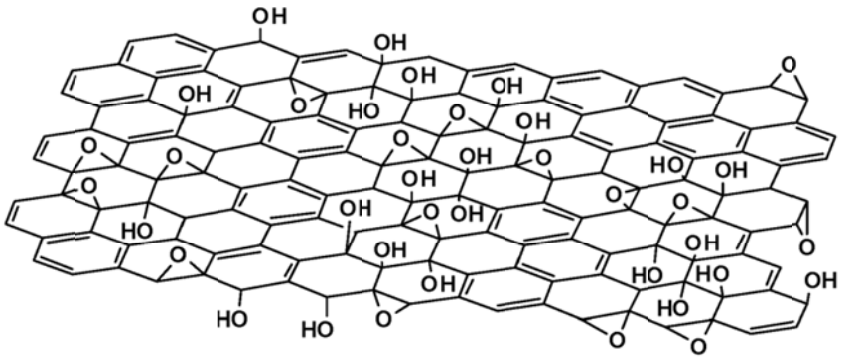

Figura 4. Representación de la estructura de las láminas de óxido de grafeno según el modelo de Lerf-Klinowski. Reproducido de [52].

b) Exfoliación del óxido de grafito en medio líquido

Los grupos oxigenados que decoran las láminas de GO les confieren carácter polar e hidrófilo. El aumento de la distancia interlaminar, debido a la presencia de dichos grupos, debilita la fuerza de van der Waals que mantiene unidas las láminas, facilitando su exfoliación en medio acuoso o en disolventes orgánicos polares mediante uso de ultrasonidos o mediante una agitación prolongada. De esta manera, se pueden obtener dispersiones coloidales estables de óxido de grafeno monocapa en medio acuoso y orgánico con concentraciones de hasta ~10-20 mg mL^{-1}. Dicha estabilidad surge de la repulsión electrostática entre los grupos funcionales (desprotonados) presentes en dichas láminas [53].

c) Reducción del óxido de grafeno

Las propiedades del óxido de grafeno difieren enormemente respecto a las que caracterizan al grafeno prístino. Esto se debe principalmente al gran número de grupos funcionales y defectos presentes en el óxido de grafeno. La conductividad eléctrica, por ejemplo, se ve seriamente afectada por la alteración que dichos grupos producen en la hibridación sp^2 de las láminas, convirtiendo al óxido de grafeno en un material eléctricamente aislante. No obstante, mediante un proceso de reducción, es posible eliminar gran parte de estos grupos funcionales y restaurar significativamente la conductividad

eléctrica [54]. Las láminas de óxido de grafeno reducido siguen siendo coloidalmente estables bajo determinadas condiciones, por ejemplo en medio acuoso básico en ausencia de concentraciones significativas de electrolitos.

El agente reductor más utilizado para la reducción del óxido de grafeno es la hidracina (H_2N-NH_2) [55, 56], obteniéndose dispersiones de óxido de grafeno reducido coloidalmente estables a concentraciones por debajo de 1 mg mL^{-1}. La alta toxicidad de este reactivo ha motivado la búsqueda agentes reductores alternativos, como la vitamina C, que no siendo nocivos para la salud, resultan tan efectivos como la hidracina en términos de desoxigenación y recuperación de la conductividad de las láminas [57, 58]. Del mismo modo, ha propiciado el desarrollo de estrategias alternativas que permitan llevar a cabo la reducción del óxido de grafeno en ausencia de agentes reductores. Un buen ejemplo de esta vía de acción lo constituye la exfoliación y reducción del óxido de grafito de forma simultánea mediante un calentamiento rápido hasta temperaturas de ~1000 °C. En este método ampliamente utilizado en la producción comercial de grafeno, la exfoliación se produce por la acumulación en el espacio interlaminar de gases generados en la descomposición térmica de los grupos funcionales presentes en las láminas [59]. Del mismo modo, se conocen varios métodos de reducción que no requieren el uso de reactivos reductores. Los que han suscitado un mayor interés son la reducción solvotérmica, la reducción electroquímica y la reducción fotoinducida.

La reducción solvotérmica aprovecha el hecho de que la descomposición de gran parte de los grupos funcionales oxigenados presentes en el óxido de grafeno tiene lugar a temperaturas relativamente bajas (150-250 °C) [60]. Este método puede aplicarse a dispersiones acuosas (reducción hidrotérmica) [61] o dispersiones en disolventes orgánicos [62] y, puesto que las temperaturas necesarias para la reducción son en muchos casos superiores a la temperatura de ebullición del disolvente a presión atmosférica, resulta necesario trabajar con autoclaves a altas presiones.

La reducción electroquímica se basa en la captación de electrones por parte de las láminas de óxido de grafeno en el cátodo de una celda electroquímica [63]. El proceso de reducción se efectúa a temperatura ambiente y permite la obtención de un filme de óxido de grafeno reducido electroquímicamente (ERGO) a partir de una dispersión de GO. Dicho proceso puede realizarse mediante un solo paso, en el que la reducción de las láminas de GO y su deposición sobre un substrato que actúa como electrodo ocurren de forma simultánea. En este caso, la disminución de la estabilidad coloidal de la dispersión de láminas de ERGO debido a la pérdida de funcionalidades oxigenadas provoca que dichas láminas se adhieran a la superficie del electrodo. Por otra parte, la reducción electroquímica también se puede realizar en dos etapas, depositando primero el GO sobre un substrato para generar un filme que se utiliza posteriormente como cátodo de la celda electroquímica, consiguiéndose así su reducción [64].

La reducción fotoinducida se realiza normalmente en presencia de fotocatalizadores y tiene la capacidad de reducir láminas de óxido de grafeno mientras éstas se encuentran en dispersión coloidal. Los fotocatalizadores son generalmente nanopartículas de semiconductores como dióxido de titanio [65], óxido de zinc [65] o vanadato de bismuto [66]. En estas partículas, la absorción de radiación UV, cuya energía es mayor que el gap del semiconductor, da lugar a la excitación de electrones desde la banda de valencia a la banda de conducción, con la consiguiente generación de huecos. El consumo de huecos por parte de una especie aceptora de huecos como el etanol crea un exceso de electrones en las nanopartículas, permitiendo que estos sean transferidos a las láminas de óxido de grafeno y usados para su reducción. A pesar de que en los trabajos citados anteriormente, la reducción del óxido de grafeno en ausencia de fotocatalizador no resulta significativa [65], existe un ejemplo en la literatura en el que se consigue reducir óxido de grafeno únicamente con luz ultravioleta. No obstante, el proceso no está optimizado y se requieren tiempos de exposición largos para alcanzar grados de reducción muy limitados [67], por lo cual resultaría interesante establecer las condiciones óptimas para este proceso.

Ninguno de los métodos mencionados anteriormente permite eliminar completamente las funcionalidades oxigenadas introducidas en la etapa de oxidación. Por ello, resultaría interesante averiguar qué condiciones son necesarias para eliminar completamente las funcionalidades oxigenadas y defectos estructurales en el grafeno. Tal como sugieren varios trabajos recientes [68, 69], esto podría ser posible a través de tratamientos de grafitización, que son tratamientos térmicos a muy alta temperatura (entre 2200 °C y 3000 °C) realizados en atmósfera inerte capaces de transformar un material carbonoso no grafítico en un material grafítico. Estos cambios estructurales van acompañados del aumento de las conductividades eléctrica y térmica así como de la mejora de diversas propiedades del material.

1.3.2 Métodos "bottom-up"

En las metodologías "bottom-up" el grafeno se obtiene a partir de la descomposición de un precursor orgánico, generalmente a alta temperatura. Las principales vías de producción de grafeno dentro de esta categoría son el crecimiento epitaxial en carburo de silicio y el depósito químico en fase vapor (CVD) de hidrocarburos sobre metales de transición.

1.3.2.1 Crecimiento epitaxial en carburo de silicio

Este método se basa en el calentamiento del carburo de silicio a temperaturas entre 1100 y 1600 °C, lo cual provoca la sublimación del silicio (que es favorable frente a la del carbono) y el reordenamiento de los átomos de carbono que permanecen en la muestra (Figura 5) [70]. El crecimiento se puede realizar en ultra-alto vacío. No obstante, la utilización de una atmósfera de argón [71] o una pequeña cantidad de disilano (Si_2H_6) [72] permite reducir el ritmo de sublimación del silicio y elevar la temperatura

de síntesis varios centenares de grados para obtener grafeno de mayor calidad. Las estructuras más comúnmente utilizadas son los politipos hexagonales 4H o 6H, aunque también puede emplearse la fase cúbica 3C. Además, el grafeno forma estructuras conmensuradas tanto en la cara rica en silicio SiC(0001) como en la cara rica en carbono SiC(000$\bar{1}$), presentando el crecimiento en una u otra cara distintas características [73].

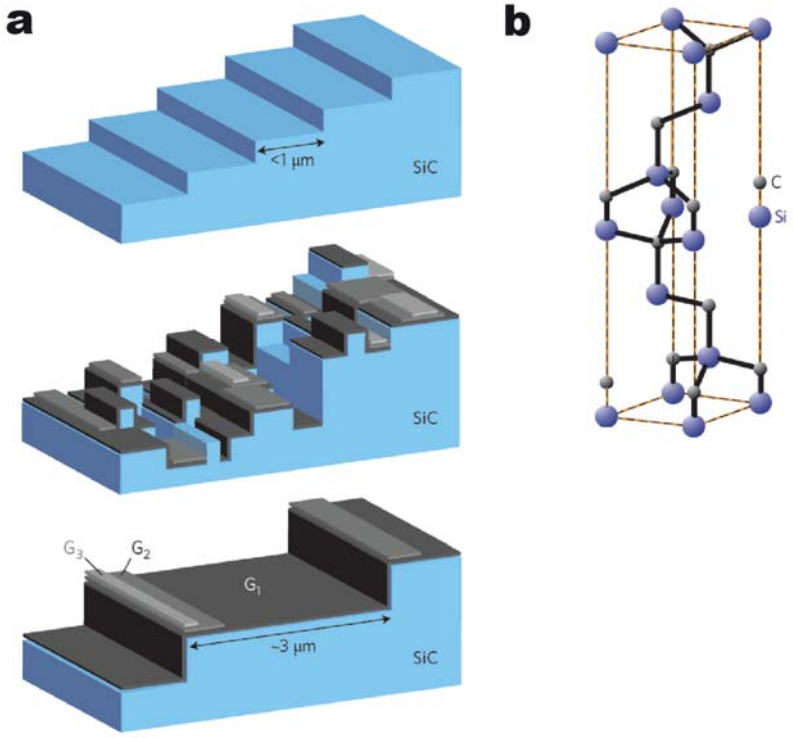

Figura 5. (a) Evolución de la superficie durante el calentamiento de la cara rica en Si del SiC. (b) celda unidad del 6H-SiC. Reproducido de [70].

Las posibles aplicaciones del grafeno producido por este método están principalmente relacionadas con el desarrollo de dispositivos electrónicos debido a que descansa sobre un substrato tecnológicamente relevante y su transferencia a otro substrato no resulta imprescindible. Sin embargo, las obleas de carburo de silicio hexagonal tienen un elevado coste, lo cual representa un obstáculo para su implantación comercial [23].

1.3.2.2 Depósito químico en fase vapor sobre metales de transición

El grafeno producido a través de este método proviene de la descomposición de gases ricos en carbono (generalmente metano) sobre una superficie metálica catalítica y la recombinación de este elemento sobre dicha superficie. El crecimiento de grafeno en un cierto metal puede ser un proceso catalizado por la superficie o resultar de la segregación de átomos de carbono disueltos en el metal al enfriar el sistema, a causa de la disminución de la solubilidad del carbono en dicho metal al bajar la temperatura.

El crecimiento de grafeno sobre cobre es un proceso catalizado por la superficie [74]. Una ventaja de este tipo de procesos es que el crecimiento se detiene una vez que toda

la superficie ha sido recubierta, lo que facilita la obtención de grafeno monocapa siempre que se realice bajo determinadas condiciones. De lo contrario, se observa la aparición de parches de grafeno multicapa. El crecimiento de grafeno sobre níquel tiene lugar a través del mecanismo de segregación [75], lo que dificulta la obtención de grafeno monocapa.

El crecimiento de grafeno sobre cobre se produce de forma continua sobre las fronteras de grano del metal, permitiendo crecer láminas de grafeno de grandes dimensiones sobre filmes policristalinos de este material [19]. No obstante, las fronteras de grano suelen inducir defectos en las láminas de grafeno como, por ejemplo, regiones de grafeno multicapa, que degradan significativamente sus propiedades. Por lo tanto, el tipo de substrato utilizado resulta decisivo a la hora de obtener grafeno de gran calidad [76].

El grafeno producido por este método se puede utilizar en el desarrollo de dispositivos electrónicos. Sin embargo, esto exige transferir el grafeno a substratos tecnológicamente relevantes, lo cual se consigue recubriendo el grafeno con un cierto polímero, atacando el metal y disolviendo el polímero tras situar el grafeno sobre el nuevo substrato. Mediante este método se consigue transferir el grafeno a un substrato eléctricamente aislante (por ejemplo, SiO_2/Si) sin que su calidad estructural se vea dañada de forma significativa.

1.4 Modificación de grafenos

En el grafeno, al igual que en los semiconductores convencionales, la introducción de bajas concentraciones de determinados defectos tiene la capacidad de modificar considerablemente sus propiedades. Como se ha mencionado anteriormente, la introducción de defectos o impurezas en el grafeno permite modular propiedades electrónicas como la densidad de portadores de carga. También resulta intuitivo pensar que la introducción de defectos que impliquen la presencia de enlaces insaturados debe aumentar la reactividad del grafeno [77]. Por lo tanto, la ingeniería de defectos en grafeno podría permitir en un futuro obtener la funcionalidad deseada en diferentes tipos de aplicaciones basadas en este material. Sin embargo, la creación de defectos en el grafeno se ve en gran medida obstaculizada por la escasa reactividad de este material, siendo ésta especialmente baja en el plano basal. La forma más común de sortear dicho obstáculo consiste en aprovechar su menor resistencia química frente a elementos del grupo VI de la tabla periódica, como el oxígeno [78]. La oxidación presenta ciertas ventajas respecto a otros métodos basados en el bombardeo de electrones [79] o iones [80, 81], como son la disponibilidad del oxígeno o la posibilidad de acceder a la muestra desde múltiples direcciones durante el tratamiento. De este modo, la oxidación constituye uno de los métodos más efectivos de modificación superficial de grafenos. Dicha oxidación puede tener lugar en presencia de oxígeno molecular a alta temperatura [82, 83], en tratamientos con ozono generado mediante radiación ultravioleta [84] así como

en diferentes tipos de plasma (microondas [85], radiofrecuencia [34, 86] o acoplamiento inductivo [87, 88]).

1.4.1 Oxidación mediante plasma de oxígeno

La oxidación de grafeno mediante plasma de oxígeno es un método muy atractivo desde el punto de vista tecnológico, ya que puede ser integrado en los esquemas de producción en masa actuales, requiere tiempos de exposición muy cortos debido a la gran reactividad este tipo de materiales frente al oxígeno atómico y además, la intensidad del tratamiento puede ser controlada mediante la elección adecuada de los parámetros de operación. Dicha capacidad para controlar la densidad de defectos ha sido puesta de manifiesto previamente en el tratamiento de otros materiales de tipo grafítico [89].

El plasma de oxígeno generado por microondas resulta más adecuado para realizar ataques de tipo químico que otros plasmas de menor frecuencia (plasmas de radiofrecuencias) debido a que la alta frecuencia de la radiación empleada (2.45 GHz) impide el ataque por bombardeo de iones de la superficie y a que la cantidad de especies reactivas que se generan es mayor. Las distintas especies reactivas que componen este tipo de plasma (principalmente oxígeno atómico e iones de oxígeno molecular) reaccionan químicamente con los átomos de carbono situados en el plano basal o en bordes del material grafítico. Estas reacciones dan lugar a la eliminación de átomos de carbono en forma de CO y CO_2 con la consiguiente generación de vacantes atómicas o agujeros dependiendo de la duración e intensidad del tratamiento [85]. Además de la generación de este tipo de defectos intrínsecos, también se espera la introducción de ciertas funcionalidades oxigenadas que pueden fijarse a los bordes de dichas vacantes.

1.5 Referencias

[1]Allen MJ, Tung VC, Kaner RB. Honeycomb carbon: a review of graphene. Chem Rev 2010;110(1):132-45.
[2]Mermin ND. Crystalline order in two dimensions. Phys Rev 1968;176(1):250-4.
[3]Venables JA, Spiller GDT, Hanbucken M. Nucleation and growth of thin films. Rep Prog Phys 1984;47(4):399.
[4]Novoselov KS, Geim AK, Morozov SV, Jiang D, Zhang Y, Dubonos SV, et al. Electric field effect in atomically thin carbon films. Science 2004;306(5696):666-9.
[5]Novoselov KS, Geim AK, Morozov SV, Jiang D, Katsnelson MI, Grigorieva IV, et al. Two-dimensional gas of massless Dirac fermions in graphene. Nature 2005;438(7065):197-200.
[6]Castro Neto AH, Guinea F, Peres NMR, Novoselov KS, Geim AK. The electronic properties of graphene. Rev Mod Phys 2009;81(1):109-62.
[7]Wong H-SP, Akinwande D. Carbon nanotube and graphene device physics. Cambridge University Press; 2011.
[8]Bolotin KI, Sikes KJ, Jiang Z, Klima M, Fudenberg G, Hone J, et al. Ultrahigh electron mobility in suspended graphene. Solid State Commun 2008;146(9–10):351-5.

[9]Vishveshwara S. A glimpse of quantum phenomena in optical lattices. Philos Trans A Math Phys Eng Sci 2012;370(1969):2916-29.
[10]Schwierz F. Graphene transistors. Nat Nanotechnol 2010;5(7):487-96.
[11]Zhang H, Bekyarova E, Huang J-W, Zhao Z, Bao W, Wang F, et al. Aryl functionalization as a route to band gap engineering in single layer graphene devices. Nano Lett 2011;11(10):4047-51.
[12]Wang QH, Jin Z, Kim KK, Hilmer AJ, Paulus GL, Shih C-J, et al. Understanding and controlling the substrate effect on graphene electron-transfer chemistry via reactivity imprint lithography. Nat Chem 2012;4(9):724-32.
[13]Das A, Pisana S, Chakraborty B, Piscanec S, Saha SK, Waghmare UV, et al. Monitoring dopants by Raman scattering in an electrochemically top-gated graphene transistor. Nat Nanotechnol 2008;3(4):210-5.
[14]Zhang Y, Tang TT, Girit C, Hao Z, Martin MC, Zettl A, et al. Direct observation of a widely tunable bandgap in bilayer graphene. Nature 2009;459(7248):820-3.
[15]Ohta T, Bostwick A, Seyller T, Horn K, Rotenberg E. Controlling the electronic structure of bilayer graphene. Science 2006;313(5789):951-4.
[16]Solis-Fernandez P, Yoshida K, Ogawa Y, Tsuji M, Ago H. Dense arrays of highly aligned graphene nanoribbons produced by substrate-controlled metal-assisted etching of graphene. Adv Mater 2013;25(45):6562-8.
[17]Han MY, Ozyilmaz B, Zhang Y, Kim P. Energy band-gap engineering of graphene nanoribbons. Phys Rev Lett 2007;98(20):206805.
[18]Nair RR, Blake P, Grigorenko AN, Novoselov KS, Booth TJ, Stauber T, et al. Fine structure constant defines visual transparency of graphene. Science 2008;320(5881):1308.
[19]Bae S, Kim H, Lee Y, Xu X, Park JS, Zheng Y, et al. Roll-to-roll production of 30-inch graphene films for transparent electrodes. Nat Nanotechnol 2010;5(8):574-8.
[20]Blake P, Brimicombe PD, Nair RR, Booth TJ, Jiang D, Schedin F, et al. Graphene-based liquid crystal device. Nano Lett 2008;8(6):1704-8.
[21]Matyba P, Yamaguchi H, Eda G, Chhowalla M, Edman L, Robinson ND. Graphene and mobile ions: the key to all-plastic, solution-processed light-emitting devices. ACS Nano 2010;4(2):637-42.
[22]Wang X, Zhi L, Mullen K. Transparent, conductive graphene electrodes for dye-sensitized solar cells. Nano Lett 2008;8(1):323-7.
[23]Edwards RS, Coleman KS. Graphene synthesis: relationship to applications. Nanoscale 2013;5(1):38-51.
[24]Lee C, Wei X, Kysar JW, Hone J. Measurement of the elastic properties and intrinsic strength of monolayer graphene. Science 2008;321(5887):385-8.
[25]Zandiatashbar A, Lee GH, An SJ, Lee S, Mathew N, Terrones M, et al. Effect of defects on the intrinsic strength and stiffness of graphene. Nat Commun 2014;5:3186.
[26]Balandin AA, Ghosh S, Bao W, Calizo I, Teweldebrhan D, Miao F, et al. Superior thermal conductivity of single-layer graphene. Nano Lett 2008;8(3):902-7.
[27]Seol JH, Jo I, Moore AL, Lindsay L, Aitken ZH, Pettes MT, et al. Two-dimensional phonon transport in supported graphene. Science 2010;328(5975):213-6.
[28]Huang X, Qi X, Boey F, Zhang H. Graphene-based composites. Chem Soc Rev 2012;41(2):666-86.

[29]Yoo E, Kim J, Hosono E, Zhou H-s, Kudo T, Honma I. Large reversible Li storage of graphene nanosheet families for use in rechargeable lithium ion batteries. Nano Lett 2008;8(8):2277-82.
[30]Schedin F, Geim AK, Morozov SV, Hill EW, Blake P, Katsnelson MI, et al. Detection of individual gas molecules adsorbed on graphene. Nat Mater 2007;6(9):652-5.
[31]Machado BF, Serp P. Graphene-based materials for catalysis. Catal Sci Technol 2012;2(1):54-75.
[32]Bunch JS, Verbridge SS, Alden JS, van der Zande AM, Parpia JM, Craighead HG, et al. Impermeable atomic membranes from graphene sheets. Nano Lett 2008;8(8):2458-62.
[33]Koenig SP, Wang L, Pellegrino J, Bunch JS. Selective molecular sieving through porous graphene. Nat Nanotechnol 2012;7(11):728-32.
[34]Xie G, Yang R, Chen P, Zhang J, Tian X, Wu S, et al. A general route towards defect and pore engineering in graphene. Small 2014;10(11):2280-4.
[35]Paton KR, Varrla E, Backes C, Smith RJ, Khan U, O'Neill A, et al. Scalable production of large quantities of defect-free few-layer graphene by shear exfoliation in liquids. Nat Mater 2014;13(6):624-30.
[36]Coleman JN. Liquid-phase exfoliation of nanotubes and graphene. Adv Funct Mater 2009;19(23):3680-95.
[37]Khan U, O'Neill A, Lotya M, De S, Coleman JN. High-concentration solvent exfoliation of graphene. Small 2010;6(7):864-71.
[38]Hernandez Y, Nicolosi V, Lotya M, Blighe FM, Sun Z, De S, et al. High-yield production of graphene by liquid-phase exfoliation of graphite. Nat Nanotechnol 2008;3(9):563-8.
[39]Hernandez Y, Lotya M, Rickard D, Bergin SD, Coleman JN. Measurement of multicomponent solubility parameters for graphene facilitates solvent discovery. Langmuir 2010;26(5):3208-13.
[40]Guardia L, Fernández-Merino MJ, Paredes JI, Solís-Fernández P, Villar-Rodil S, Martínez-Alonso A, et al. High-throughput production of pristine graphene in an aqueous dispersion assisted by non-ionic surfactants. Carbon 2011;49(5):1653-62.
[41]Laaksonen P, Kainlauri M, Laaksonen T, Shchepetov A, Jiang H, Ahopelto J, et al. Interfacial engineering by proteins: exfoliation and functionalization of graphene by hydrophobins. Angew Chem Int Ed 2010;49(29):4946-9.
[42]Bourlinos AB, Georgakilas V, Zboril R, Steriotis TA, Stubos AK, Trapalis C. Aqueous-phase exfoliation of graphite in the presence of polyvinylpyrrolidone for the production of water-soluble graphenes. Solid State Commun 2009;149(47-48):2172-6.
[43]Bai H, Li C, Shi G. Functional composite materials based on chemically converted graphene. Adv Mater 2011;23(9):1089-115.
[44]Hummers WS, Offeman RE. Preparation of graphitic oxide. J Am Chem Soc 1958;80(6):1339.
[45]Lerf A, He H, Forster M, Klinowski J. Structure of Graphite Oxide Revisited. J Phys Chem B 1998;102(23):4477-82.
[46]He H, Klinowski J, Forster M, Lerf A. A new structural model for graphite oxide. Chem Phys Lett 1998;287(1-2):53-6.
[47]Petit C, Seredych M, Bandosz TJ. Revisiting the chemistry of graphite oxides and its effect on ammonia adsorption. J Mater Chem 2009;19(48):9176.

[48]Poh HL, Sanek F, Ambrosi A, Zhao G, Sofer Z, Pumera M. Graphenes prepared by Staudenmaier, Hofmann and Hummers methods with consequent thermal exfoliation exhibit very different electrochemical properties. Nanoscale 2012;4(11):3515-22.
[49]Marcano DC, Kosynkin DV, Berlin JM, Sinitskii A, Sun Z, Slesarev A, et al. Improved synthesis of graphene oxide. ACS Nano 2010;4(8):4806-14.
[50]Xu Y, Sheng K, Li C, Shi G. Highly conductive chemically converted graphene prepared from mildly oxidized graphene oxide. J Mater Chem 2011;21(20):7376-80.
[51]Chen J, Yao B, Li C, Shi G. An improved Hummers method for eco-friendly synthesis of graphene oxide. Carbon 2013;64(0):225-9.
[52]Dreyer DR, Park S, Bielawski CW, Ruoff RS. The chemistry of graphene oxide. Chem Soc Rev 2010;39(1):228-40.
[53]Li D, Muller MB, Gilje S, Kaner RB, Wallace GG. Processable aqueous dispersions of graphene nanosheets. Nat Nanotechnol 2008;3(2):101-5.
[54]Gomez-Navarro C, Weitz RT, Bittner AM, Scolari M, Mews A, Burghard M, et al. Electronic transport properties of individual chemically reduced graphene oxide sheets. Nano Lett 2007;7(11):3499-503.
[55]Stankovich S, Dikin DA, Piner RD, Kohlhaas KA, Kleinhammes A, Jia Y, et al. Synthesis of graphene-based nanosheets via chemical reduction of exfoliated graphite oxide. Carbon 2007;45(7):1558-65.
[56]Tung VC, Allen MJ, Yang Y, Kaner RB. High-throughput solution processing of large-scale graphene. Nat Nanotechnol 2009;4(1):25-9.
[57]Fernández-Merino MJ, Guardia L, Paredes JI, Villar-Rodil S, Solís-Fernández P, Martínez-Alonso A, et al. Vitamin C is an ideal substitute for hydrazine in the reduction of graphene oxide suspensions. J Phys Chem C 2010;114(14):6426-32.
[58]Zhang J, Yang H, Shen G, Cheng P, Zhang J, Guo S. Reduction of graphene oxide via L-ascorbic acid. Chem Commun 2010;46(7):1112-4.
[59]McAllister MJ, Li J-L, Adamson DH, Schniepp HC, Abdala AA, Liu J, et al. Single sheet functionalized graphene by oxidation and thermal expansion of graphite. Chem Mater 2007;19(18):4396-404.
[60]Mattevi C, Eda G, Agnoli S, Miller S, Mkhoyan KA, Celik O, et al. Evolution of electrical, chemical, and structural properties of transparent and conducting chemically derived graphene thin films. Adv Funct Mater 2009;19(16):2577-83.
[61]Zhou Y, Bao Q, Tang LAL, Zhong Y, Loh KP. Hydrothermal dehydration for the "green" reduction of exfoliated graphene oxide to graphene and demonstration of tunable optical limiting properties. Chem Mater 2009;21(13):2950-6.
[62]Zhou D, Cheng Q-Y, Han B-H. Solvothermal synthesis of homogeneous graphene dispersion with high concentration. Carbon 2011;49(12):3920-7.
[63]Chen L, Tang Y, Wang K, Liu C, Luo S. Direct electrodeposition of reduced graphene oxide on glassy carbon electrode and its electrochemical application. Electrochem Commun 2011;13(2):133-7.
[64]Toh SY, Loh KS, Kamarudin SK, Daud WRW. Graphene production via electrochemical reduction of graphene oxide: synthesis and characterisation. Chem Eng J 2014;251(0):422-34.
[65]Williams G, Seger B, Kamat PV. TiO_2-graphene nanocomposites. UV-assisted photocatalytic reduction of graphene oxide. ACS Nano 2008;2(7):1487-91.

[66]Ng YH, Iwase A, Kudo A, Amal R. Reducing graphene oxide on a visible-light $BiVO_4$ photocatalyst for an enhanced photoelectrochemical water splitting. J Phys Chem Lett 2010;1(17):2607-12.
[67]Ding YH, Zhang P, Zhuo Q, Ren HM, Yang ZM, Jiang Y. A green approach to the synthesis of reduced graphene oxide nanosheets under UV irradiation. Nanotechnology 2011;22(21):215601.
[68]Long D, Li W, Qiao W, Miyawaki J, Yoon SH, Mochida I, et al. Graphitization behaviour of chemically derived graphene sheets. Nanoscale 2011;3(9):3652-6.
[69]Ghosh T, Biswas C, Oh J, Arabale G, Hwang T, Luong ND, et al. Solution-processed graphite membrane from reassembled graphene oxide. Chem Mater 2012;24(3):594-9.
[70]Sutter P. Epitaxial graphene: how silicon leaves the scene. Nat Mater 2009;8(3):171-2.
[71]Emtsev KV, Bostwick A, Horn K, Jobst J, Kellogg GL, Ley L, et al. Towards wafer-size graphene layers by atmospheric pressure graphitization of silicon carbide. Nat Mater 2009;8(3):203-7.
[72]Tromp RM, Hannon JB. Thermodynamics and kinetics of graphene growth on SiC(0001). Phys Rev Lett 2009;102(10):106104.
[73]Srivastava N, He G, Mende PC, Feenstra RM, Sun Y. Graphene formed on SiC under various environments: Comparison of Si-face and C-face. J Phys D: Appl Phys 2012;45(15):154001.
[74]Li X, Cai W, An J, Kim S, Nah J, Yang D, et al. Large-area synthesis of high-quality and uniform graphene films on copper foils. Science 2009;324(5932):1312-4.
[75]Reina A, Jia X, Ho J, Nezich D, Son H, Bulovic V, et al. Large area, few-layer graphene films on arbitrary substrates by chemical vapor deposition. Nano Lett 2009;9(1):30-5.
[76]Zhao L, Rim KT, Zhou H, He R, Heinz TF, Pinczuk A, et al. Influence of copper crystal surface on the CVD growth of large area monolayer graphene. Solid State Commun 2011;151(7):509-13.
[77]Banhart F, Kotakoski J, Krasheninnikov AV. Structural defects in graphene. ACS Nano 2011;5(1):26-41.
[78]Pierson HO. Handbook of carbon, graphite, diamonds and fullerenes: processing, properties and applications. Noyes Publications; 1994.
[79]Robertson AW, Allen CS, Wu YA, He K, Olivier J, Neethling J, et al. Spatial control of defect creation in graphene at the nanoscale. Nat Commun 2012;3:1144.
[80]Nakaharai S, Iijima T, Ogawa S, Suzuki S, Li SL, Tsukagoshi K, et al. Conduction tuning of graphene based on defect-induced localization. ACS Nano 2013;7(7):5694-700.
[81]Kim J-H, Hwang JH, Suh J, Tongay S, Kwon S, Hwang CC, et al. Work function engineering of single layer graphene by irradiation-induced defects. Appl Phys Lett 2013;103(17):171604.
[82]Yamada Y, Murota K, Fujita R, Kim J, Watanabe A, Nakamura M, et al. Subnanometer vacancy defects introduced on graphene by oxygen gas. J Am Chem Soc 2014;136(6):2232-5.
[83]Takahashi T, Sugawara K, Noguchi E, Sato T, Takahashi T. Band-gap tuning of monolayer graphene by oxygen adsorption. Carbon 2014;73:141-5.
[84]Yang D-P, Wang X, Guo X, Zhi X, Wang K, Li C, et al. UV/O_3 generated graphene nanomesh: formation mechanism, properties, and FET studies. J Phys Chem C 2014;118(1):725-31.

[85]Paredes JI, Martínez-Alonso A, Tascón JMD. Early Stages of Plasma Oxidation of Graphite: Nanoscale Physicochemical Changes As Detected by Scanning Probe Microscopies. Langmuir 2002;18(11):4314-23.
[86]Nourbakhsh A, Cantoro M, Vosch T, Pourtois G, Clemente F, van der Veen MH, et al. Bandgap opening in oxygen plasma-treated graphene. Nanotechnology 2010;21(43):435203.
[87]Felten A, Eckmann A, Pireaux JJ, Krupke R, Casiraghi C. Controlled modification of mono- and bilayer graphene in O_2, H_2 and CF_4 plasmas. Nanotechnology 2013;24(35):355705.
[88]Dong Chul K, Dae-Young J, Hyun-Jong C, YunSung W, Jai Kwang S, Sunae S. The structural and electrical evolution of graphene by oxygen plasma-induced disorder. Nanotechnology 2009;20(37):375703.
[89]Paredes JI, Solís-Fernández P, Martínez-Alonso A, Tascón JMD. Atomic vacancy engineering of graphitic surfaces: controlling the generation and harnessing the migration of the single vacancy. J Phys Chem C 2009;113(23):10249-55.

Objetivos y planteamiento de la memoria 2

2. Objetivos y planteamiento de la memoria

2.1 Objetivos

El grafeno constituye un material con un gran potencial para múltiples aplicaciones debido a sus excepcionales propiedades físicas. No obstante, el desarrollo de muchas de estas aplicaciones dependerá de la disponibilidad de métodos de producción del material en grandes cantidades y a bajo coste.

Los métodos basados en la exfoliación de grafito u óxido de grafito en fase líquida para dar lugar a suspensiones coloidales de grafeno cumplen estos requisitos. En particular, la obtención de grafeno a través de la ruta del óxido de grafito resulta especialmente atractiva debido a que permite obtener láminas monocapa con un alto rendimiento. Sin embargo, a pesar de que el óxido de grafito exfoliado (óxido de grafeno) se somete a un proceso de reducción química que consigue eliminar muchos de los grupos funcionales introducidos durante la oxidación y recuperar parcialmente la conjugación electrónica, el material preparado por esta vía contiene aún muchos defectos que deterioran sus propiedades y limitan su uso en muchas aplicaciones.

Así, en la presente tesis doctoral se plantea como objetivo general el desarrollo de estrategias que permitan mejorar la calidad del grafeno producido en fase líquida mediante la ruta del óxido de grafito.

Los objetivos específicos que se plantean son los siguientes:

- Estudiar de forma detallada el proceso de reducción química y explorar estrategias alternativas de reducción.
- Estudiar el curado completo de los defectos generados en la estructura del óxido de grafeno durante la oxidación.
- Estudiar la influencia de determinados defectos en las propiedades físicas del grafeno.

2.2 Organización de la memoria

En el capítulo 1 se realiza una introducción al grafeno y sus propiedades y se describe el estado del arte en cuanto a métodos de producción se refiere, haciendo especial hincapié en la ruta del óxido de grafeno. También se describe la modificación de grafeno mediante plasma de oxígeno en relación a otros métodos de modificación. El capítulo 2 (este capítulo) está dedicado a formular los objetivos y presentar la organización de la memoria. En el capítulo 3 se describen los principales materiales empleados en la realización del presente trabajo, así como los distintos métodos de preparación, de modificación o de cálculo, mientras que en el capítulo 4 se describen las principales técnicas de caracterización de materiales empleadas.

En el capítulo 5 se presentan los resultados obtenidos en la presente tesis doctoral y el análisis y discusión de los mismos. Estos resultados se recogen en un compendio de artículos, publicados o enviados a revistas científicas del área de ciencia de los materiales. Los índices de calidad de las revistas, así como el puesto que ocupan dichas revistas en relación al número total de revistas del área correspondiente, se recogen en la tabla 1.

Revista	Índice de Impacto	Puesto/ nº total de revistas	Area
Journal of Alloys and Compounds	2.390	49/241	Materials Science, Multidisciplinary.
Carbon	5.868	23/241	Materials Science, Multidisciplinary.
Nano Research	7.392	17/241	Materials Science, Multidisciplinary.

Tabla 1. Índices de calidad (2012) de las revistas en las que se han publicado los artículos elaborados en la pretente tesis doctoral. Fuente: Journal Citation Reports (2012).

El capítulo 5 se estructura en tres bloques, que corresponden a los tres objetivos específicos planteados anteriormente. Cada bloque va precedido de un resumen en el que se amplía la descripción de los objetivos y se exponen los principales resultados de los artículos contenidos en dichos bloques. En el capítulo 6 se presentan las conclusiones generales de la tesis doctoral. Por último, se incluye un anexo en el que se recogen una serie de publicaciones complementarias generadas durante la elaboración de la tesis doctoral, así como las contribuciones a congresos.

Materiales y métodos 3

3. Métodos de preparación de materiales

3.1 Preparación de óxido de grafeno (GO)

La preparación de óxido de grafito se llevó a cabo en fase líquida mediante el método de Hummers [1]. Dicho método consiste en la oxidación de grafito en medio fuertemente ácido con $KMnO_4$ y $NaNO_3$. El grafito de partida fue grafito natural en polvo (Fluka 50870), y por cada gramo de grafito se utilizaron 23 mL de H_2SO_4, 3 g de $KMnO_4$ y 0.75 g de $NaNO_3$. Tras ser sometido a un proceso de purificación, el óxido de grafito obtenido fue dispersado en agua milli-Q mediante ultrasonidos. El material exfoliado se separó del no exfoliado centrifugando dicha dispersión en una centrifuga Eppendorf 5424 durante 10 min a una fuerza centrífuga de 20000 g. El 75% del volumen del sobrenadante resultante constituye una suspensión coloidal estable de láminas de GO.

3.2 Reducción química de GO

Este proceso puede realizarse en medio acuoso básico (pH~10) partiendo de 20 mL de suspensión de óxido de grafeno (0.1 mg mL^{-1}) con 40 μL de NH_3 (25%) y añadiendo un agente reductor, como la hidrazina (0.05 μL N_2H_4 por mL de disolución) [2].

3.3 Grafitización de papeles y monocapas de GO reducido

Los tratamientos de grafitización se realizaron en un horno eléctrico trifásico Xerion dotado de un programador de temperatura Eurotherm 2704. El horno emplea una resistencia de grafito de sección cilíndrica. La muestra se introduce en un crisol de grafito, que se introduce a su vez en la cámara interna del horno, también hecha de grafito. La cámara interna está rodeada por fieltro de grafito que actúa como aislante térmico. Todo el sistema se encuentra refrigerado por medio de camisas de agua alimentadas por un sistema de refrigeración externo Rittal. Un termopar Ni/Cr tipo K situado en la zona central de la cámara interna controla la temperatura hasta 950 °C. A partir de este punto, el termopar se retira automáticamente de la cámara y la medición de temperatura se realiza por medio de un pirómetro óptico Keller modelo PZ30.

En nuestro caso los tratamientos de grafitización se realizaron bajo flujo de argón (~2 L min^{-1}) utilizando rampas de calentamiento de 50 °C min^{-1} (20-700 °C), 100 °C min^{-1} (700-1000 °C), 25 °C min^{-1} (1000-2000 °C), 10 °C min^{-1} (2000-2700 °C) y tiempos de residencia de 1 h a la máxima temperatura. Los materiales tratados fueron papeles (filmes delgados) de óxido de grafeno reducido preparados por filtración a vacío de dispersiones de óxido de grafeno reducido, así como láminas de óxido de grafeno con distintos grados de reducción depositadas sobre HOPG a partir de dispersiones diluídas.

3.4 Fotorreducción de láminas de GO mediante radiación ultravioleta (UV)

La reducción de láminas de GO puede lograrse mediante el simple uso de radiación UV. El dispositivo experimental consta de un matraz de tres bocas que contiene la dis-

persión de óxido de grafeno (10 mL, 0.1 mg mL^{-1}). Una de las bocas se usa para insertar la guía de ondas que libera la radiación UV mientras que las otras dos sirven para introducir un flujo de argón en la disolución y para controlar la temperatura (Figura 6). El flujo de argón (45 mL min^{-1}) agita la dispersión asegurando una exposición uniforme de las láminas a la radiación, y al mismo tiempo la desgasifica, evitando la reoxidación de las láminas por parte de moléculas de oxígeno disueltas en el medio. El tiempo de tratamiento varía entre 5 min y 24 h.

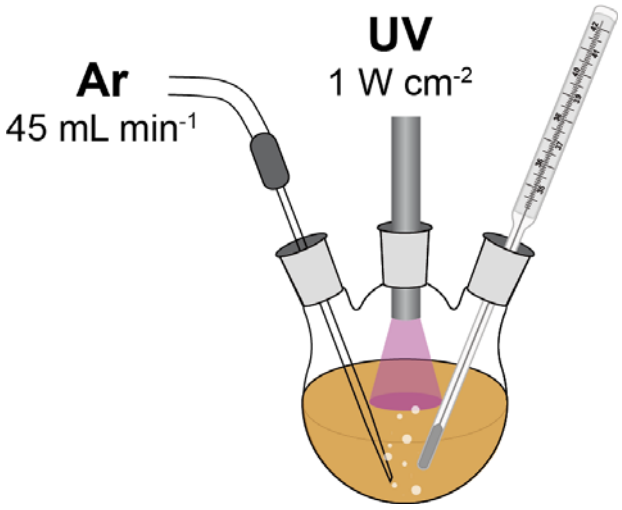

Figura 6. Dispositivo experimental para la reducción de óxido de grafeno y la generación de nanopartículas de oro en láminas de óxido de grafeno mediante radiación UV.

En este trabajo se empleó una lámpara de arco de mercurio BlueWave 50 (Dymax) que emite en un rango de longitudes de onda 280-450 nm con la siguiente distribución de intensidades: 15% (280-320 nm), 40% (320-390 nm) y 45% (390-450 nm). La radiación se libera desde el extremo de una guía de ondas de 5 mm de diámetro situada a una distancia de 15 mm de la superficie de la dispersión. La intensidad de la radiación a dicha distancia de la guía de ondas se determinó por medio de un sensor UVM-CP (UV-Consulting Peschl), siendo de 1.0-1.2 W cm^{-2} para todo el rango de longitudes de onda en que emite la lámpara.

3.5 Generación de nanopartículas de Au en GO asistida por radiación UV

La generación de nanopartículas de oro utiliza el mismo dispositivo experimental empleado en la fotorreducción de láminas de GO (Figura 6). En este caso, un precursor metálico (3 μm HAuCl) y una disolución de amoníaco [10 μl NH_3(25%)] se añaden a la suspensión de láminas de óxido de grafeno (10 mL, 0.1 mg mL^{-1}). El tiempo de tratamiento varía entre 30 min y 6 h. Para obtener disoluciones homogéneas se emplean de 4 a 10 ciclos de sedimentación (vía centrifugación a 20.000g, 30 min) y redispersión del material sedimentado en agua milli-Q.

3.6 Oxidación superficial mediante plasma de oxígeno

Los tratamientos de oxidación superficial se realizaron en un equipo 200-G (Technics Plasma). El plasma se produce mediante radiación de microondas de frecuencia 2.45 GHz. Los tratamientos se llevaron a cabo en condiciones de vacío (1.0 mbar) y utilizando O_2 de pureza 0.9990 % como gas precursor.

3.7 Simulaciones de dinámica molecular

Las simulaciones teóricas constituyen una herramienta muy útil en la interpretación de los estudios experimentales realizados mediante microscopías de proximidad. En este trabajo, los estudios sobre el curado de láminas de rGO depositadas sobre grafito se interpretaron con la ayuda de simulaciones de dinámica molecular. Debido a que estas simulaciones proporcionan información de fenómenos que ocurren bajo condiciones experimentales no accesibles in situ mediante las microscopías de proximidad, resultaron de gran utilidad para comprender los mecanismos que gobiernan este proceso.

Para reproducir la lámina de rGO depositada sobre el sustrato se utilizó un sistema formado por 5 planos grafíticos. Las simulaciones se realizaron usando condiciones de contorno periódicas en dichos planos (XY) y condiciones libres en la dirección perpendicular (Z). La supercelda contiene 12x16 celdas unidad rectangulares en el plano XY de tamaño $(\sqrt{3}r_0, 3r_0)$, donde r_0 es la longitud del enlace entre átomos de carbono, donde cada celda unidad contiene 4 átomos de carbono. Por lo tanto cada capa de grafeno prístino de la supercelda contiene 768 átomos de carbono.

La interacción entre los átomos de carbono se simula mediante un potencial empírico de muchos cuerpos que representa los enlaces covalentes mediante un potencial de corto alcance tipo Tersoff [3] e incluye un potencial de largo alcance para representar la interacción de van der Waals entre capas de grafito [4]. Las simulaciónes se llevaron a cabo a temperatura constante utilizando un termostato tipo Nose-Hoover. Las ecuaciones de movimiento se resolvieron utilizando un paso temporal de 0.5 fs.

3.6 Referencias

[1]Hummers WS, Offeman RE. Preparation of graphitic oxide. J Am Chem Soc 1958;80(6):1339.
[2]Li D, Muller MB, Gilje S, Kaner RB, Wallace GG. Processable aqueous dispersions of graphene nanosheets. Nat Nanotechnol 2008;3(2):101-5.
[3]Marcos PA, Alonso JA, Rubio A, López MJ. Simulating the thermal stability and phase changes of small carbon clusters and fullerenes. Eur Phys J D 1999;6(2):221-33.
[4]Nordlund K, Keinonen J, Mattila T. Formation of Ion Irradiation Induced Small-Scale Defects on Graphite Surfaces. Physical Review Letters 1996;77(4):699-702.

Técnicas de caracterización 4

4. Técnicas de caracterización

4.1 Microscopías de proximidad

(Scanning probe microscopy, SPM)

El término microscopías de proximidad aglutina a un conjunto de técnicas que hacen uso de sondas situadas típicamente de unos pocos nanómetros de la superficie del material a estudiar para rastrear diferentes tipos de interacción, permitiendo explorar diferentes propiedades de la superficie a nivel microscópico. Su funcionamiento consiste en realizar un barrido secuencial de la superficie registrando los cambios en la interacción sonda-muestra, que pueden relacionarse con la posición vertical de la sonda y ser convertidos generalmente en una imagen de la topografía de la superficie a escala nanométrica. Por ello, las SPM son poderosas herramientas de metrología superficial. No obstante, las SPM ofrecen una gran versatilidad y, a pesar de que su uso más común es la determinación de la topografía superficial de las muestras, también permiten el estudio de muchas otras propiedades superficiales.

Debido a que su funcionamiento es análogo, los diferentes tipos de microscopios de proximidad poseen una serie de elementos en común. Además del tipo de sonda concreto y un sistema de detección del tipo de interacción, incorporan un escáner, un sistema para realizar el acercamiento de la sonda a la superficie, una electrónica de retroalimentación, un método que permita aislar las vibraciones ambientales y un equipo informático para realizar la adquisición de los datos. El escáner es un dispositivo formado por un conjunto de elementos piezocerámicos dispuestos geométricamente de tal forma que, mediante la aplicación de un voltaje, se consigue el movimiento relativo de la sonda y la muestra en las tres direcciones espaciales. Puesto que el rango de acción del escáner en el eje vertical está limitado a unos 10 μm, y a que la interacción entre la sonda y la superficie sólo es medible cuando ambas están muy próximas, resulta imprescindible utilizar un sistema que permita acercar ambas hasta una distancia dentro de este rango de acción. Este proceso se realiza inicialmente de forma manual mediante tornillos de alta precisión, con el apoyo visual de un microscopio óptico acoplado al de proximidad. Posteriormente, el acercamiento continúa de forma automática, siendo el sistema de retroalimentación el encargado de mover uno de estos tornillos hasta alcanzar el valor de señal preestablecido con el que se desea realizar la medida. Por último, debido a la alta resolución que se logra con estos instrumentos, resulta necesario aislar el sistema de las vibraciones ambientales mediante el uso de plataformas adecuadas capaces de filtrar las altas frecuencias. Asimismo, el diseño del microscopio es rígido y compacto, lo que contribuye a eliminar las vibraciones de baja frecuencia.

Las primeras técnicas en surgir pertenecientes a esta familia fueron la microscopía de efecto túnel (scanning tunneling microscopy, STM), en 1982 [1], y la microscopía de fuerza atómica (atomic force microscopy, AFM), en 1986 [2]. Los microscopios comerciales actuales suelen incorporar ambas técnicas, realizándose el cambio de una a otra mediante el simple remplazo de la cabeza del microscopio, ya que es ahí donde se concentran los elementos específicos de cada técnica, como el tipo de sonda empleado o el sistema de detección de la interacción. En este trabajo se empleó un equipo Nanoscope IIIa Multimode (Veeco Instruments) con la capacidad para trabajar como STM o diferentes variantes de AFM.

4.1.1 Microscopía de efecto túnel

(Scanning tunneling microscopy, STM)

El STM fue la primera técnica capaz de generar imágenes en espacio real con resolución atómica de una superficie. Su funcionamiento se basa en el efecto túnel, un fenómeno de origen cuántico, en virtud del cual una partícula es capaz de atravesar una barrera de energía potencial superior a la energía cinética de dicha partícula. En este tipo de microscopía de proximidad, la sonda consiste en una punta metálica afilada compuesta generalmente de tungsteno o una aleación de Pt/Ir, y la corriente túnel que se genera es aprovechada directamente por el sistema de retroalimentación. La corriente túnel se genera al aplicar una diferencia de potencial entre la punta y la muestra, al mismo tiempo que se acercan ambos a distancias inferiores a 1 nm. En esa situación, se establece un flujo de electrones a través de la barrera de potencial que separa ambos electrodos. Puesto que la técnica requiere el establecimiento de una corriente entre la punta y la muestra, sólo puede emplearse en el estudio de materiales eléctricamente conductores. No obstante, también ha sido aplicada con éxito a materiales aislantes atómicamente delgados.

La densidad de corriente túnel J_t que fluye a través de una barrera de potencial en el régimen de voltajes pequeños (caso relevante para la microscopía de efecto túnel), viene dada por la expresión [3]:

$$J_t \approx \frac{e^2\kappa}{2\pi h} \cdot \frac{V}{d} \cdot e^{-2\kappa d} \qquad (3)$$

donde

$$\kappa = \sqrt{\frac{2m_e\Phi_{eff}}{\hbar^2}} \qquad (4)$$

V es el voltaje aplicado a los electrodos, d denota la distancia de separación entre los electrodos, mientras que Φ_{eff} representa la altura efectiva de la barrera obtenida a partir

de las funciones trabajo de la punta Φ_p y la muestra Φ_m según $\Phi_{eff} \approx (\Phi_p + \Phi_m)/2$. La dependencia exponencial de la corriente túnel con la distancia de separación entre los electrodos provoca que la mayor parte de la corriente túnel sea la que circule entre los átomos más próximos de la punta y la muestra. Este carácter extremadamente local de la microscopía de efecto túnel resulta en la elevada resolución de la técnica, tanto lateral (~0.1 nm) como vertical (~0.01 nm).

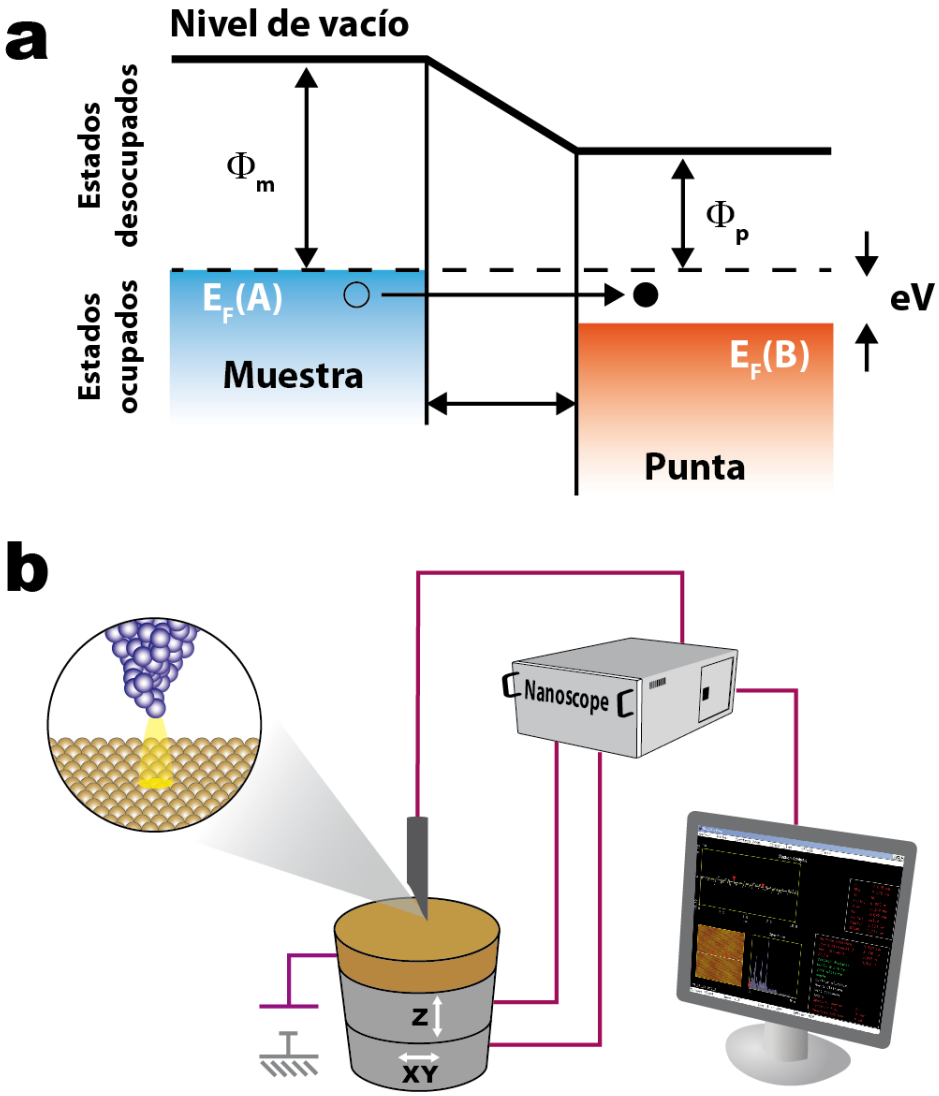

Figura 7. (a) Diagrama de transferencia electrónica en microscopía de efecto túnel. (b) Esquema de los diferentes elementos que componen un microscopio de efecto túnel.

Sin embargo, además de la mencionada dependencia de la corriente túnel con la distancia que separa los electrodos, la corriente túnel varía proporcionalmente con la densidad local de estados de la muestra cerca del nivel de Fermi, ya que sólo los electrones cerca del nivel de Fermi tienen energía suficiente para atravesar la barrera de potencial [4]. De este modo, las imágenes obtenidas constituyen una superposición de la topografía y de las propiedades electrónicas de la superficie. Por lo tanto, a pesar de la gran

ventaja que supone la elevada resolución lateral de la técnica, la interpretación de imágenes que resuelven rasgos atómicos (p. ej. vacantes atómicas, nitrógeno sustitucional) o de superficies con propiedades electrónicas heterogéneas (p. ej. patrones de Moiré), debe realizarse cautelosamente.

Otro factor que contribuye a entorpecer la interpretación de las imágenes de STM es el tamaño finito de las puntas, ya que no sólo implica una disminución del poder de resolución de la técnica sino que también da lugar a la aparición de artefactos. Uno de los más comunes es la aparición de "múltiples puntas", que se produce cuando el extremo de la punta consta de dos o más protuberancias que están a distancias similares de la superficie. Este alejamiento de la geometría ideal da lugar a la repetición artificial de rasgos presentes en la superficie, generando patrones regulares cuya identificación es posible en la mayor parte de los casos.

Las imágenes de STM mostradas en este trabajo fueron tomadas en condiciones ambientales, empleando puntas de Pt/Ir (80/20) (Bruker Corporation), trabajando en modo de corriente constante. Los parámetros túnel típicamente empleados fueron 200 pA - 500 pA/100 mV-1 V en imágenes a escala nanométrica, y 500 pA – 2 nA/ 10 mV – 100 mV en imágenes a escala atómica.

4.1.2 Microscopía de fuerza atómica

(Atomic force microscopy, AFM)

El microscopio de fuerza atómica se basa en la detección de la fuerza que se produce entre los átomos situados en el extremo de la sonda y los átomos o moléculas que constituyen la superficie de la muestra. El tipo de fuerzas que se detectan en AFM incluye fuerzas electrostáticas, fuerzas de van der Waals o fuerzas de fricción, entre otras. La dependencia con la distancia, *r*, de la fuerza que actúa entre átomos o moléculas neutros se puede describir adecuadamente mediante el potencial de Lennard-Jones:

$$V(r) = 4\epsilon\left[\left(\frac{\sigma}{r}\right)^{12} - \left(\frac{\sigma}{r}\right)^{6}\right] \qquad (5)$$

donde ϵ representa la altura del potencial y σ representa la distancia (finita) a la que el potencial es cero. Esta expresión contiene un primer término de carácter repulsivo, de corto alcance, debido al principio de exclusión de Pauli, y un segundo término de carácter atractivo, de largo alcance, debido a la fuerza de van der Waals. Puesto que este tipo de fuerzas están presentes en todo tipo de materiales, la microscopía de fuerza atómica puede ser aplicada también al estudio de materiales eléctricamente no conductores. No obstante, debido a que esta interacción decae más lentamente que la corriente túnel, la resolución obtenida (~1-2 nm) es generalmente menor que la que se obtiene por STM.

El sistema necesario para la detección de estas fuerzas añade cierta complejidad a este tipo de microscopía. En este caso, el sensor de fuerzas consiste en una lámina flexible denominada cantiléver, en cuyo extremo se ubica la punta. Los cambios inducidos en el cantiléver, a causa de las fuerzas que se generan entre la punta y la superficie de la muestra, son detectados por medio de un haz láser (en la variante más extendida) que, tras incidir sobre el cantiléver, es reflejado hacia un fotodetector segmentado que genera una señal eléctrica que puede ser procesada electrónicamente.

La microscopía de fuerza atómica distingue entre modos estáticos, en los que la fuerza de interacción se detecta simplemente monitorizando cambios en la flexión o torsión del cantiléver, y modos dinámicos de operación. Estos últimos permiten eludir en gran medida los efectos invasivos de los que adolecen los modos estáticos, que se originan como consecuencia de que la punta se encuentra en permanente contacto (interacción repulsiva) con la superficie. En los modos dinámicos se acopla un dispositivo piezoeléctrico al cantiléver, forzándole a oscilar a una determinada frecuencia, y la fuerza de interacción con la superficie se detecta a través de la modulación que ésta produce en la amplitud o la frecuencia de oscilación del cantiléver. La elección de una u otra característica de la oscilación del cantiléver para generar la señal de retroalimentación da lugar a los distintos modos dinámicos. El modo de modulación de amplitud (AM-AFM), también conocido como "tapping" o modo de contacto intermitente, utiliza la amplitud de oscilación del cantiléver para generar la señal de retroalimentación, mientras que el modo de modulación de frecuencia (FM-AFM), también conocido como modo de "no contacto", emplea la frecuencia de resonancia [5].

En el modo "tapping" se hace oscilar el cantiléver con una amplitud relativamente elevada (100-200 nm), aproximando la punta y la muestra hasta que su separación de equilibrio sea inferior a la amplitud de oscilación del cantiléver. En estas condiciones, se produce una disminución de dicha amplitud, debido al contacto de la punta con la superficie en el punto más bajo de su oscilación. La toma de imágenes topográficas se realiza mediante un barrido secuencial de la superficie, manteniendo constante la amplitud de oscilación y registrando los cambios en la posición vertical de la sonda. En su movimiento oscilatorio, la punta se ve sometida a fuerzas tanto atractivas como repulsivas. Sin embargo, la fuerza neta que actúa sobre la punta puede ajustarse, de modo que sea atractiva o repulsiva, modificando la amplitud de oscilación libre del cantiléver (a través del voltaje aplicado al dispositivo piezoeléctrico que produce la oscilación) y la distancia que separa el cantiléver en su conjunto de la superficie. De esta forma, reduciendo la amplitud de oscilación del cantiléver a la vez que mantenemos una separación cantiléver-muestra relativamente elevada, logramos trabajar en régimen atractivo, el cual resulta menos invasivo que el régimen repulsivo, ya que minimiza la fuerza de contacto entre la punta y la muestra.

Por último, además de la variación de la amplitud y la frecuencia de resonancia del cantiléver, la interacción entre la punta y la muestra produce una variación del ángulo de fase de la oscilación del cantiléver respecto a la fase de oscilación libre de éste. Este tipo de imágenes puede ser sensible a variaciones en la composición química de la superficie de la muestra, proporcionando un contraste que resulta muy útil en la identificación de diferentes materiales presentes en una misma muestra o incluso de heterogeneidades en la composición química en un mismo material [6].

Las imágenes de AFM mostradas en este trabajo fueron tomadas en modo "tapping" en condiciones ambientales, utilizando cantilévers de silicio de constante de fuerza ~40 Nm^{-1} y frecuencias de resonancia ~200-300 kHz (Bruker Corporation).

4.2 Microscopía electrónica

(Electron microscopy, EM)

La resolución se define en microscopía como la distancia entre dos objetos que pueden visualizarse de forma independiente. La resolución de los microscopios ópticos está limitada por difracción a la mitad de la longitud de onda de la luz visible más corta, siendo aproximadamente 200 nm. Para salvar dicha limitación, un microscopio electrónico utiliza en su lugar un haz de electrones, con longitudes de onda asociadas mucho menores. Cuando se hace incidir dicho haz sobre una muestra, se genera una amplia variedad de señales debido a su interacción con el sólido, que pueden ser usadas para la formación de la imagen. Esto da lugar a los diferentes tipos de microscopía electrónica, entre los que destacan la microscopía electrónica de transmisión (TEM) y la microscopía electrónica de barrido (SEM).

4.2.1 Microscopía electrónica de transmisión

(Transmission electron microscopy, TEM)

El TEM es un instrumento que proporciona imágenes de una muestra delgada (<200 nm) con una resolución lateral que alcanza los 0.2 nm [7]. Por otra parte, es capaz de proporcionar patrones de difracción de electrones que resultan útiles en el análisis de muestras cristalinas. En un microscopio TEM, la imagen se forma mediante lentes magnéticas que focalizan los electrones que atraviesan la muestra, tras haber sufrido procesos de dispersión elástica o inelástica. En imágenes de baja ampliación, el contraste de la imagen se debe a la absorción de electrones por el material debido a cambios en el grosor o en la composición de la muestra. Sin embargo, para la correcta interpretación de imágenes de alta resolución suele ser necesaria la ayuda de otras técnicas o de simulación de imágenes.

En este trabajo se empleó un TEM JEOL 2000 EX-II operado a 160 kV para obtener imágenes de láminas de grafeno decoradas con nanopartículas de oro. Para ello, varios microlitros de una suspensión acuosa de este material híbrido diluída en etanol fueron depositados sobre rejillas de cobre cubiertas por una capa delgada y continua de carbono.

4.2.2 Microscopía electrónica de barrido
(Scanning electron microscopy, SEM)

El SEM es un tipo de microscopio electrónico que proporciona imágenes de la morfología de una muestra independientemente de su grosor, ya que en este caso no se miden electrones transmitidos sino reflejados, con una resolución de ~1-50 nm. Debido a su amplia profundidad de campo, el SEM es comúnmente empleado como sustituto del microscopio óptico cuando la resolución de este último no resulta suficiente. En este caso, las señales que se utilizan para formar la imagen proceden de la detección de los electrones retrodispersados o de los electrones secundarios. Los electrones retrodispersados son una cierta fracción de los electrones del haz incidente que abandonan el material sin haber perdido parte de su energía en procesos de dispersión inelástica en su interior. Las imágenes obtenidas mediante la detección de electrones dispersados elásticamente son sensibles a la topografía de la muestra pero también a su composición, ya que átomos más pesados producen más electrones retrodispersados. Por su parte, los electrones secundarios se producen como consecuencia de procesos inelásticos de ionización producidos por el haz incidente. Debido a que su energía es menor de 50 eV, este tipo de electrones son rápidamente reabsorbidos por los átomos del material, de modo que sólo los procedentes de átomos más superficiales van a contribuir a formar la imagen. Por lo tanto, las imágenes obtenidas mediante la detección de electrones secundarios reflejan de modo más fiel la topografía superficial. La focalización de los electrones retrodispersados o de los electrones secundarios mediante lentes magnéticas es difícil debido a que el rango de energías de estos electrones es demasiado bajo. Por esta razón, la imagen se forma realizando un barrido con el haz de electrones localizado en un punto del material mientras se detecta la cantidad de electrones (retrodispersados o secundarios) que abandonan dicho punto [8].

4.2.3 Análisis por dispersión de energía de rayos X
(Energy-dispersive X-ray spectroscopy, EDX)

El EDX se basa en la detección de los rayos X que se generan debido a la irradiación de una muestra con un haz de electrones. Esta irradiación genera rayos X cuya energía depende de los elementos presentes en la muestra. Estos fotones se generan cuando el haz de electrones incidente arranca un electrón de alguna capa interna de un átomo generando un hueco, y otro electrón situado en un nivel de energía superior realiza

una transición para ocupar dicho hueco. Esta relajación del átomo viene acompañada de la emisión de un fotón de energía igual a la diferencia de energía entre dichos niveles, la cual es característica de cada especie atómica. Por lo tanto, mediante esta técnica es posible realizar el análisis químico de los diferentes elementos presentes en la muestra [7].

En este trabajo se empleó un SEM con emisión electrónica de campo Quanta FEG 650 (FEI Company) que incorpora un detector de rayos X para EDX. Las imágenes de SEM incluidas en esta tesis fueron obtenidas utilizando electrones secundarios (detector Everhart-Thornley).

4.3 Espectroscopía

3.3.1 Espectroscopía de absorción ultravioleta-visible

(Ultraviolet–visible spectroscopy, UV-vis)

La espectroscopía de absorción UV-vis es una técnica no destructiva de análisis que consiste en hacer incidir un haz de fotones de un rango que va típicamente del UV medio al infrarojo cercano sobre una muestra y detectar la radiación transmitida. Idealmente, la radiación que no se transmite es absorbida por la muestra debido a transiciones entre niveles electrónicos. La técnica se fundamenta en la cuantización de los niveles energéticos, es decir, en el hecho de que para que un determinado tipo de molécula absorba radiación electromagnética, y sus electrones promocionen desde orbitales moleculares en el estado fundamental (n,σ,π) a orbitales moleculares excitados (σ^*,π^*), la energía del fotón incidente debe coincidir con la separación de energía entre dichos estados. En una molécula, para cada estado electrónico existe un conjunto discreto de niveles de energía muy próximos entre sí debido a los diferentes estados vibracionales y rotacionales posibles [9]. Por lo tanto, los espectros obtenidos mediante esta técnica no se componen de picos estrechos, sino de bandas anchas centradas en torno a la longitud de onda de la transición electrónica. Además, la espectroscopía de absorción UV-vis se lleva a cabo normalmente en disoluciones de la muestra que se desea estudiar, por lo que la interacción no uniforme con las moléculas del disolvente (especialmente en el caso de disolventes polares, como el agua) tiene como resultado un ensanchamiento adicional [10]. Las moléculas del aire absorben radiación UV por debajo de 190 nm, por lo que sus bandas de absorción solapan con las de la muestra en este rango de longitudes de onda. Además, para muestras en disolución, las propias moléculas del disolvente absorben radiación por debajo de una longitud de onda determinada (190 nm en el caso del agua), ocultando cualquier absorción procedente del soluto. El rango de longitudes de onda accesible para espectrómetros operados en atmósfera de aire es de 190-1100 nm. La radiación electromagnética con este rango de longitudes de onda es capaz de provocar transiciones electrónicas entre orbitales mole-

culares HOMO (highest ocupied molecular orbital) y LUMO (lowest unoccupied molecular orbital) poco separados. En el caso de moléculas orgánicas, son accesibles las transiciones relacionadas con insaturaciones, es decir, las que implican orbitales de tipo π, como $\pi \rightarrow \pi^*$ y n $\rightarrow \pi^*$, donde n designa a orbitales no enlazantes relacionados con la presencia de heteroátomos en la molécula. Si existe conjugación, la separación en energía entre HOMO y LUMO disminuye y se produce un desplazamiento del máximo de absorción a mayor longitud de onda [11]. Además de la localización del máximo de absorción λ_{max}, la intensidad de éste proporciona información sobre la facilidad con la que se produce una transición electrónica concreta. Un conjunto de reglas de selección mecano-cuánticas establece qué tipo de transiciones ocurren con mayor ("permitidas") o menor probabilidad ("prohibidas"). Estas reglas de basan en consideraciones de simetría de los estados involucrados en dicha transición. Si la transición correspondiente a una longitud de onda ocurre fácilmente, la molécula absorberá intensamente radiación a esa longitud de onda. A través del denominado "coeficiente de extinción molar (ϵ)" se cuantifica la capacidad de absorción de la radiación de una sustancia a una longitud de onda determinada. Existe una relación entre la concentración en disolución de una sustancia que absorbe radiación, c, y la cantidad de radiación absorbida, que en determinadas condiciones viene dada por la ley de Lambert-Beer:

$$A = log\left(\frac{I_0}{I}\right) = -\log T = \epsilon l c \qquad (6)$$

donde I_0 e I son las intensidades de luz incidente y transmitida, T es la transmitancia medida directamente por el equipo, A es la absorbancia y l es el paso óptico o longitud del medio atravesada por la luz. Esta expresión permite cuantificar concentraciones de sustancias disueltas a partir de medidas de absorbancia.

La espectroscopía de absorción UV-vis resulta útil en el estudio de dispersiones de óxido de grafeno y óxido de grafeno reducido, ya que ambos son sistemas con un alto grado de aromaticidad y, por tanto, susceptibles de ser detectados y cuantificados mediante esta técnica. Cuantitativamente se ha utilizado para estimar la concentración de óxido de grafeno en dispersión coloidal, a partir de la obtención de rectas de calibrado de dispersiones con concentración conocida por haber sido pesado el soluto en seco. Cualitativamente, se usa para determinar el grado de reducción del óxido de grafeno [Figura 8(a)]. En el óxido de grafeno, el tipo de transiciones observables son la transición $\pi \rightarrow \pi^*$, que da lugar a una banda de absorción localizada a 231 nm, y la n $\rightarrow \pi^*$, que debido a que es una transición "prohibida" da lugar a una banda menos intensa, observándose como un hombro de la banda principal a 300 nm. A medida que aumenta la conjugación electrónica, por ejemplo, en procesos de reducción del óxido de grafeno, la banda $\pi \rightarrow \pi^*$ se desplaza hacia el rojo hasta situarse a 268 nm, lo que hace posible monitorizar el proceso de reducción.

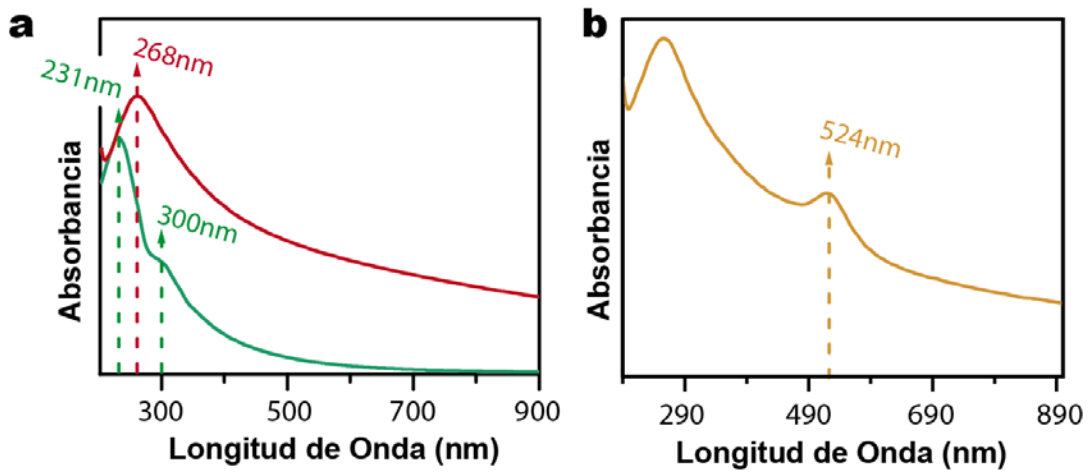

Figura 8. Espectro de absorción UV-vis para el óxido de grafeno (verde) y el óxido de grafeno reducido (rojo) (a) y para el material híbrido constituido por nanopartículas de oro crecidas sobre láminas de óxido de grafeno (b).

En materiales de baja dimensionalidad, como las nanopartículas metálicas, la radiación UV-vis también puede ser absorbida por el plasma de electrones deslocalizados cuando la frecuencia de dicha radiación coincide con la frecuencia natural de la oscilación de los electrones en torno a los núcleos. Dicho fenómeno se conoce como resonancia plasmónica superficial localizada (LSPR) y presenta la peculiaridad de que la frecuencia de resonancia varía dependiendo de la forma y el tamaño de las nanopartículas. En este trabajo la banda de absorción a 524 nm, característica de nanoestructuras de oro, permitió monitorizar la síntesis de materiales híbridos consistentes de láminas de óxido de grafeno reducido y nanopartículas de oro

Los espectros de absorción UV-vis fueron adquiridos mediante un espectrofotómetro dispersivo de doble haz Heλios α (Thermo Spectronic). Las fuentes de luz son dos: una lámpara de deuterio, que emite luz en el rango UV y otra de tungsteno, que emite luz en el rango visible e IR. La luz emitida por la fuente pasa primero a través de un monocromador de red de difracción, que descompone la luz en diferentes longitudes de onda que la componen. La luz se divide con un espejo curvado en dos haces de igual intensidad: un haz pasa a través de la muestra y el otro a través de la celda de referencia, que contiene el disolvente puro. Se enfoca cada haz en un detector que mide la relación de intensidades de los dos haces o transmitancia. La absorbancia se calcula como el logaritmo de dicha relación. Se utilizaron celdas de sílice fundida con paso óptico de 1 cm.

4.3.2 Espectroscopía infrarroja

(Fourier transform infrared spectroscopy, FTIR)

La espectroscopía infrarroja consiste en el estudio de la absorción, por parte de las moléculas que constituyen una muestra, de radiación electromagnética en el rango del infrarrojo. La radiación en este rango espectral tiene la energía adecuada para producir transiciones entre niveles vibracionales de la inmensa mayoría de especies moleculares, pero estas transiciones solo se producen si la energía de la radiación coincide con la diferencia de energía de los estados vibracionales [12]. Puesto que los estados vibracionales son característicos para cada especie molecular, la espectroscopía infrarroja es una técnica muy útil de caracterización de materiales.

Los movimientos de vibración de una especie molecular se pueden descomponer de acuerdo con sus modos normales de vibración, que son oscilaciones en fase de los átomos con una frecuencia característica. Cada modo de vibración posee una serie de niveles cuantizados de energía $E_v = h\omega(\upsilon + 1/2)$ donde υ es el número cuántico vibracional υ=0,1,2… (aproximación armónica, que considera el enlace químico como un muelle que une dos átomos). Para que se pueda producir una transición a un nivel vibracional excitado, la frecuencia de la radiación, ω, debe coincidir con la frecuencia característica de un modo de vibración de la molécula. Además, existe un conjunto de reglas de selección mecano-cuánticas qué establecen qué transiciones están permitidas. Una regla de selección global impone que para que la vibración molecular pueda absorber energía debe producir un cambio en el momento dipolar de la molécula [10]. Con la excepción de las moléculas homonucleares, todas las moléculas orgánicas e inorgánicas absorben radiación IR, lo cual ofrece la posibilidad de determinar un número extraordinariamente grande de sustancias. La frecuencia de la vibración es mayor cuanto mayor sea la fuerza del enlace (constante de fuerza del muelle) y menor sea la masa reducida de los átomos implicados (masa en el extremo del muelle). Por ello, los grupos funcionales con enlaces con alta polaridad donde las fuerzas de enlace son altas y los enlaces que implican átomos de hidrógeno, donde la masa reducida es pequeña, tienen frecuencias relativamente altas, desacopladas de las del resto de la sustancia. Así, los grupos funcionales absorben radiación infrarroja en un rango específico de números de onda independientemente de la estructura del resto de la molécula. De este modo, la correlación ente la posición de la banda y la estructura química se usa para identificar grupos funcionales específicos en una muestra.

Como la intensidad de las bandas de absorción asociadas a cada grupo funcional es proporcional al número de grupos presentes, la espectroscopía infrarroja permite estimar el grado de reducción del óxido de grafeno tras tratamientos de reducción.

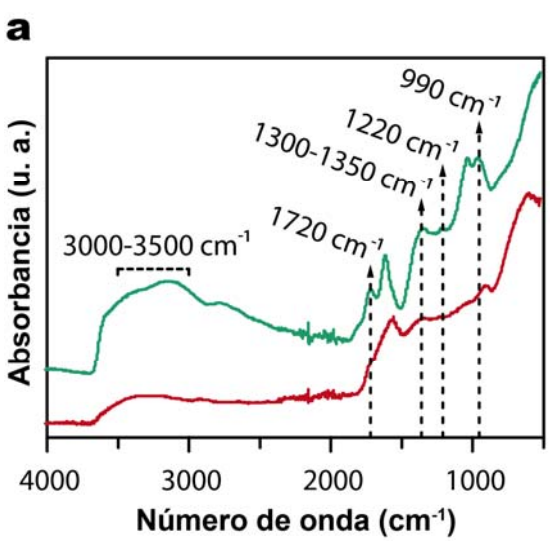

b

Banda (cm^{-1})	Vibración
3000-3500	Tensión O-H
1720	Tensión C=O
1300-1350	Tensión C-OH
1220	Respiración grupos epoxi
990	Vibración grupos epoxi, éter o peróxido

Figura 9. (a) Espectro infrarrojo de filmes de óxido de grafeno (verde) y óxido de grafeno reducido mediante radiación UV (rojo). (b) Vibraciones asociadas a las principales bandas del espectro infrarrojo en este tipo de materiales.

4.3.3 Espectroscopía infrarroja por reflexión total atenuada

(Attenuated total reflection - Fourier transform infrared spectroscopy ATR-FTIR)

Las bandas de absorción de un espectro infrarrojo se pueden obtener midiendo la intensidad de la radiación que se transmite a través de la muestra mientras se varía la longitud de onda de la radiación incidente. Sin embargo, esta metodología de transmisión no siempre es adecuada para el estudio de medios que absorben demasiada radiación o medios con una superficie rugosa que dispersa la radiación. La espectroscopía infrarroja de reflexión total atenuada proporciona una metodología alternativa a la de transmisión. Este método consiste en la colocación de un prisma de un material transparente al infrarrojo (diamante, silicio…) en contacto con la muestra. La radiación incidente penetra por un extremo del prisma y emerge por el lado opuesto tras sufrir varios fenómenos de reflexión interna. En el fenómeno de reflexión interna se produce una onda evanescente que penetra en la muestra una distancia ~0.5-2 μm y, debido a que el material absorbe parte de la radiación, la reflexión interna se atenúa [13]. En este modo de espectroscopía infrarroja la intensidad de las bandas depende del ángulo de incidencia del haz pero no depende de la cantidad de muestra depositada.

En este trabajo se empleó un espectrómetro Nicolet 8700 (Thermo Scientific) en el modo de reflexión total atenuada para medir los espectros de absorción de filmes de óxido de grafeno y óxido de grafeno reducido mediante radiación UV.

4.3.4 Espectroscopía Raman

(Raman spectroscopy)

En la espectroscopía Raman se irradia la muestra con un haz láser de una determinada longitud de onda. Dicha radiación polariza la nube de electrones que rodea el núcleo de los átomos o moléculas que constituyen la muestra de manera que éstos promocionan a "estados virtuales" de excitación cuya energía está determinada por la energía del haz incidente. Estos estados virtuales, que no son estados de excitación propios de las moléculas, son inestables por lo que se produce un rápido decaimiento que viene acompañado de la emisión de fotones. El proceso anterior puede tener lugar de forma elástica o inelástica. La mayor parte de la radiación incidente experimenta un proceso de dispersión elástica, o dispersión Rayleigh. En este caso, la distorsión de la nube electrónica no induce el movimiento del núcleo y, debido a la liviandad de los electrones, los fotones apenas pierden energía por lo que son dispersados con una frecuencia similar a la del haz incidente. No obstante, un pequeño número (un fotón de cada 10^6-10^8) es dispersado de forma inelástica, transfiriendo parte de su energía al núcleo, por lo que se produce una disminución de la frecuencia de la radiación dispersada [14]. En este proceso, denominado dispersión Stokes, las moléculas promocionan desde el estado de vibración fundamental a un estado virtual y finalmente decaen a un estado excitado de vibración [Figura 10 (a)]. La dispersión inelástica también puede dar lugar a un aumento de la frecuencia de la radiación dispersada si el núcleo transfiere energía al fotón. En este proceso, conocido como dispersión anti-Stokes, las moléculas promocionan desde un estado excitado de vibración a un estado virtual y finalmente decaen al estado de vibración fundamental. Ambos tipos de dispersión proporcionan información equivalente de los estados de vibración propios de las especies presentes en la muestra a través de la diferencia entre la energía del haz incidente y del haz dispersado inelásticamente. En condiciones normales de temperatura, la dispersión Stokes proporciona espectros de mayor intensidad ya que las moléculas se encuentran en su estado fundamental y las transiciones Stokes son más probables.

Sólo determinados estados de vibración son observables por espectroscopía Raman dada la existencia de ciertas reglas de selección impuestas por la mecánica cuántica. No obstante, una regla de selección básica dicta que las bandas intensas en Raman proceden de vibraciones que producen un cambio en la polarizabilidad de la molécula (que mide la deformabilidad del enlace debida a la acción de un campo eléctrico) [14]. Normalmente, las vibraciones simétricas, en las que la facilidad para distorsionar el enlace depende de la distancia que separa los núcleos, dan lugar a banda intensas en Raman.

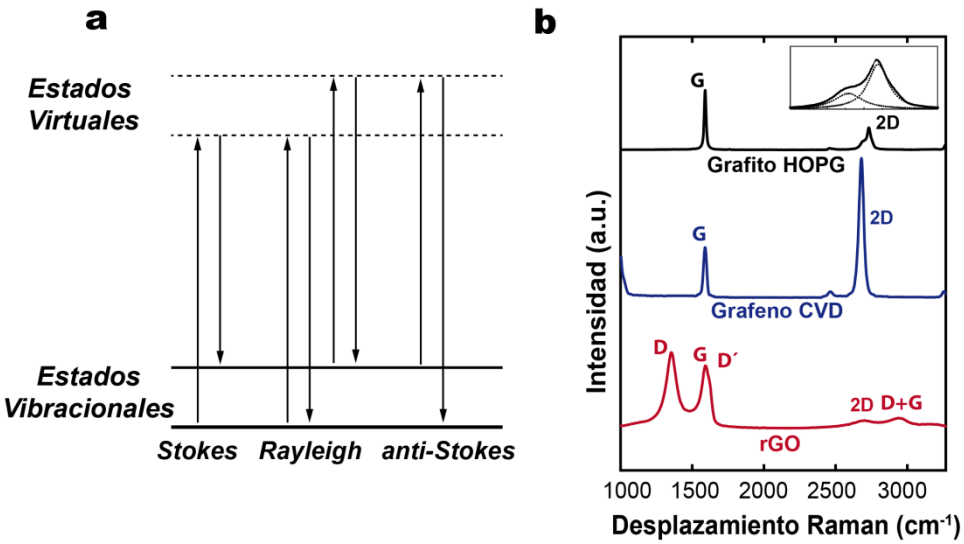

Figura 10. (a) Diagrama explicativo de los procesos de dispersión Rayleigh y Raman. (b) Espectros Raman del grafito HOPG, grafeno monocapa sobre SiO_2 y óxido de grafeno reducido (rGO).

Lo dicho hasta aquí se refiere a espectroscopía Raman molecular, pero la espectroscopía Raman puede también emplearse en el estudio de sólidos cristalinos, donde la radiación incidente induce vibraciones que se propagan por toda la red. En la Figura 10(b) se muestran los espectros Raman de grafito HOPG prístino, de grafeno monocapa crecido por CVD y transferido a SiO_2 y de óxido de grafeno reducido (filme). El espectro de primer orden en este tipo de materiales grafíticos está constituido por una serie de bandas características en el rango de 1000-2000 cm^{-1}, mientras que el espectro de segundo orden comprende un conjunto de bandas en el rango de 2300-3300 cm^{-1} [15]. En el grafito prístino el espectro de primer orden está constituido por una única banda localizada a ~1581 cm^{-1}, que recibe el nombre de banda G debido a su alta intensidad en grafito prístino. El espectro de segundo orden consta principalmente de una banda situada a ~2708 cm^{-1}, que se conoce como banda 2D. Esta banda es altamente asimétrica en el grafito prístino debido al apilamiento tipo Bernal o AB de las capas grafíticas del material. En grafeno monocapa prístino las bandas G y 2D también son las que proporcionan mayor intensidad. No obstante, la banda 2D es simétrica debido a la ausencia de apilamiento alguno y además la relación de intensidades de las bandas D y G está invertida respecto al grafito prístino. Dos bandas adicionales localizadas a ~1350 cm^{-1} y ~1620 cm^{-1} surgen en el espectro de primer orden del óxido de grafeno reducido. Dichas bandas reciben el nombre de D y D´ debido a su emergencia en materiales grafíticos con un cierto grado de desorden estructural. El cociente entre la intensidad integrada de las bandas D y G se emplea ampliamente como medida del desorden en materiales que no se alejan excesivamente del grafito ideal. La banda D´ suele aparecer como un hombro de la banda G en la vertiente de mayor frecuencia. Por otra parte, en el espectro de segundo orden surge una banda a ~2950 cm^{-1}, que proviene de la combinación de las bandas de primer orden D y G.

4.3.5 Espectroscopía Raman amplificada por superficie
(Surface-enhanced Raman spectroscopy, SERS)

Una clase de espectroscopía Raman que suscita gran interés es la espectroscopía Raman amplificada por superficie (SERS). Esta técnica aprovecha los plasmones superficiales inducidos por el haz incidente en nanoestructuras de ciertos elementos metálicos (Cu, Au, Ag principalmente) para lograr un aumento de la intensidad en un factor 10^6-10^8 [16].

Los espectros SERS mostrados en esta memoria se obtuvieron utilizando los espectrómetros HORIBA Jobin Yvon LabRAM y Nanofinder 30 (Tokyo Instruments Inc.). En ambos casos se utilizó como fuente de excitación un láser de longitud de onda λ=532 nm.

4.3.6 Espectroscopía fotoelectrónica de rayos X
(X-ray photoelectron spectroscopy, XPS)

La espectroscopía fotoeléctrónica de rayos X es una técnica no destructiva de análisis que consiste en hacer incidir un haz de fotones de rayos X sobre una muestra y examinar la energía cinética de los electrones que se emiten de ella, como consecuencia del efecto fotoeléctrico. Parte de la energía de la radiación incidente se emplea en vencer la energía de ligadura del electrón en el átomo y una cierta función trabajo, w, debida al entorno electrostático del que se arranca el electrón; el resto se transforma en energía cinética del electrón emitido. Por lo tanto, conocida la función trabajo, podemos determinar la energía de ligadura de los electrones a partir de su energía cinética [10]. En un espectro de XPS se representa el número de electrones emitidos que corresponden a una cierta energía de ligadura. Es habitual representar la energía de ligadura en orden invertido de manera que menores energías de ligadura (mayor energía cinética) se encuentran más a la derecha en el espectro.

Un espectro general de XPS [Figura 11 (a)], que abarca todas las energías de ligadura accesibles con la energía de la radiación incidente, permite la identificación de los elementos químicos que componen una muestra (excepto hidrógeno y helio), ya que la energía de ligadura del electrón es específica del elemento y del orbital en el que se encuentra. Los electrones de capas más internas o de átomos más pesados presentan una mayor energía de ligadura. Además, es posible determinar el estado de oxidación de un elemento o llegar a discernir el tipo de estructura química que presenta a partir de espectros de alta resolución de las diferentes bandas atómicas. En general, cuanta mayor sea la carga parcial positiva sobre un átomo antes de la fotoemisión, más difícil resultará la extracción de electrones y mayor será su energía de ligadura. No obstante, esta es una aproximación, donde sólo se considera el estado del átomo previo a la foto-

emisión. En la Figura 11 (b) se muestran los espectros de alta resolución de la banda C1s para el óxido de grafeno y el óxido de grafeno reducido, en los que se distinguen tres componentes. La de energía de ligadura más baja, localizada a 284.6 eV, corresponde a electrones arrancados de átomos de carbono con estructura grafítica. La componente situada a 286.6 eV se asigna a electrones de átomos de carbono con estado de oxidación +1, por ejemplo, en grupos como epóxido e hidroxilo. Los electrones con mayor energía de ligadura provienen de átomos de carbono con mayores estados de oxidación, como +2 en carbonilos y +3 en carboxilos. En XPS se observan también efectos de estado final, como el satélite $\pi \rightarrow \pi^*$ que aparece asociado a cualquier sistema que posea una nube de electrones π, como es el caso del carbono grafítico. Con el mismo estado inicial (carbono en red grafítica) se obtiene dos tipos de señales: la que ya se ha comentado, a 284.6 eV y otra ~ 7 eV más arriba en energía de ligadura. La primera, más intensa, corresponde a un estado final con el electrón más externo en orbital enlazante π mientras que la segunda corresponde a un estado final con el electrón más externo en un orbital π^*, siendo la diferencia en energía entre uno y otro estado ~ 7 eV. El satélite $\pi \rightarrow \pi^*$ es responsable de la mayor intensidad de señal que muestra el óxido de grafeno reducido frente al óxido de grafeno a energías de ligadura por encima de 290 eV.

Debido a la facilidad con la que son dispersados los electrones, sólo alcanzan el exterior de la muestra aquellos que son emitidos desde las capas más superficiales del material, por lo que la fracción sondeada por XPS se limita a los primeros 10 nm. La mayoría de los electrones emitidos han sufrido colisiones inelásticas dentro del material y perdido parte de su energía cinética, lo que explica el escalón o aumento de la señal de fondo (background) que acompaña a cada pico en los espectros generales de XPS. Debido a que la fracción sondeada de material se limita a los primeros nanómetros de la superficie, no se puede utilizar esta técnica para analizar la composición total de una muestra, ya que la composición superficial y en volumen de un material pueden ser muy diferentes. Sin embargo, es posible utilizar esta técnica para determinar la composición de materiales bidimensionales como el óxido de grafeno o el óxido de grafeno reducido. Para ello se estudian normalmente muestras preparadas apilando gran cantidad de capas de este material, bien sea mediante la preparación de un filme mediante filtrado a vacío de una dispersión o depositando repetidamente la dispersión sobre un soporte precalentado y permitiendo que se evapore el disolvente. En este caso, la fracción sondeada comprenderá varias decenas de capas de material en la muestra, pero su composición es igual que la de una sola capa. De este modo, se puede determinar la proporción atómica O/C en óxido de grafeno y en óxido de grafeno reducido.

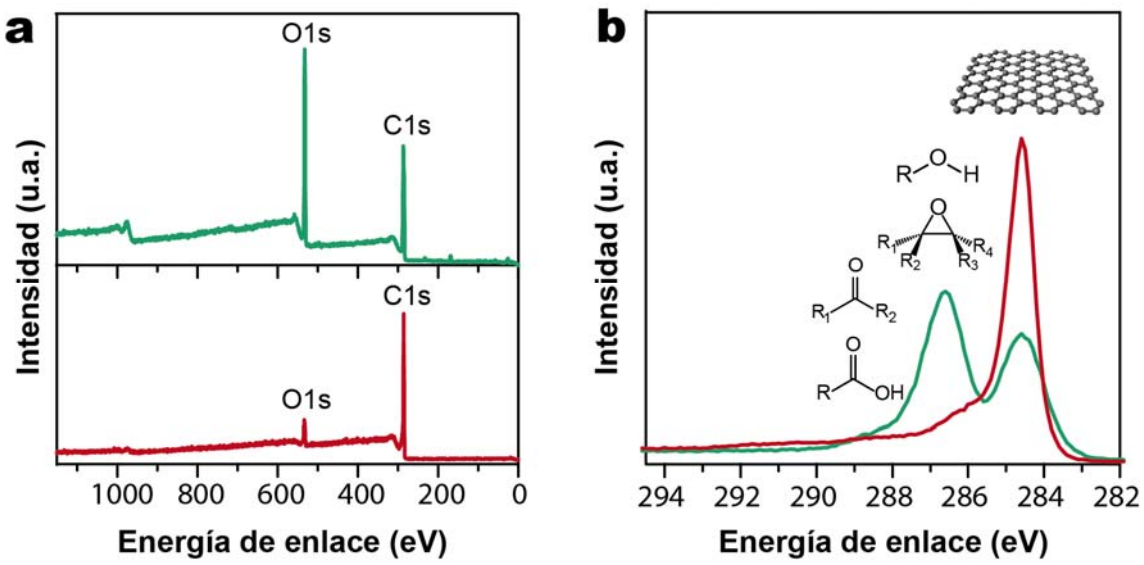

Figura 11. **Espectros XPS general (a) y de alta resolución para la banda C1s (b) para el óxido de grafeno (verde) y el óxido de grafeno reducido (rojo).**

Las medidas se realizaron en un espectrómetro SPECS a una presión inferior a 10^{-7} Pa. El ultra-alto vacío es necesario para evitar la dispersión de los electrones expulsados de la superficie por choques con moléculas de gas, así como para evitar que se adsorba una capa de contaminación sobre la muestra y sea ésta la que se analice, en lugar de la superficie de la muestra. Se empleó una fuente monocromática Al K_α (1486.6 eV) trabajando a un voltaje de 14.00 kV y una potencia de 100-250 W. La acumulación de carga superficial en las muestras poco conductoras fue corregida *in situ* mediante un cañón de electrones con energía de 0.4 eV e intensidad de 10 mA.

4.4 Difracción de rayos X

(X-ray Diffraction, XRD)

Cuando un haz de rayos X incide sobre una muestra, parte de la radiación es dispersada en todas direcciones como consecuencia de la interacción de la radiación con la nube electrónica de los átomos que forman el material. La dispersión puede ser elástica si la longitud de onda de la radiación dispersada no varía o inelástica (dispersión Compton), en cuyo caso la longitud de onda de la radiación aumenta.

Se puede considerar que una red cristalina está formada por conjuntos o familias de planos cristalográficos. Una familia de planos cristalográficos consiste en un conjunto de planos paralelos y equidistantes que, considerados globalmente, contienen todos los puntos de la red cristalina. La radiación dispersada elástica y coherentemente (con relación de fase constante) por planos de una misma familia de planos cristalográficos puede interferir de modo constructivo en caso de que la diferencia de camino sea un

múltiplo entero de la longitud de onda. Esta condición se conoce como ley de Bragg y se expresa matemáticamente como:

$$n\lambda = 2d_{hkl}sen\theta \quad (7)$$

donde θ es el ángulo de dispersión y d_{hkl} el espacio interplanar de la familia de planos cristalográficos definida por los índices de Miller (hkl). La obtención del difractograma se realiza permitiendo la variación del ángulo θ, obteniéndose un máximo de intensidad cuando se satisface la condición anterior. La ecuación (7) permite determinar la distancia interplanar de las diferentes familias de planos cristalográficos a partir de la posición de los distintos máximos del difractograma.

La anchura de los picos del difractograma, B, proporciona información adicional del grado de perfección cristalina de la muestra. Esta anchura resulta de una combinación de la anchura debida a factores instrumentales, b, y la anchura debida al tamaño finito de los microcristales, β, expresándose dicha combinación como $B^2=\beta^2+b^2$. En el grafito, el tamaño aparente de cristal a lo largo del eje c (L_C) está relacionado con la anchura debida al tamaño finito de los microcristales asociada al pico (002) mediante la ecuación de Scherrer:

$$Lc = \frac{0.9\,\lambda}{\beta\,cos\theta} = \frac{0.9\,\lambda}{\sqrt{B^2 - b^2}\,cos\theta} \quad (8)$$

Por lo tanto, conocida la anchura debida a factores instrumentales, b, podemos calcular el tamaño de cristal aparente mediante la evaluación de la ecuación (8). El parámetro b se obtiene experimentalmente a partir de un monocristal de una substancia pura, cuyos picos de difracción se encuentren próximos a los picos de la substancia objeto de estudio, ya que el valor de b varía con el ángulo de difracción [17]. A partir del difractograma del silicio se estima el valor de la anchura debida a factores instrumentales en b=0.161°.

La difracción de rayos X se empleó en este trabajo para estudiar la grafitización de filmes de óxido de grafeno reducido. Conforme se aumenta la temperatura de tratamiento, se observa una disminución gradual de la distancia interplanar d_{002} (aproximándose éste al valor del grafíto HOPG, d_{002}=3.355 Å) y un aumento progresivo del tamaño aparente de cristal, L_C (tendiendo hacia el valor del grafito HOPG, L_C=52.8 nm).

El equipo empleado en este trabajo fue un difractómetro Bruker D8 Advance con radiación K_α del Cu (0.15406 nm), con un paso de 0.02° (2θ) y un tiempo de adquisición por paso de 1 s.

4.5 Análisis térmico

4.5.1 Análisis termogravimétrico

(Thermogravimetric analysis, TGA)

El análisis termogravimétrico o termogravimetría consiste en registrar cambios en la masa de una muestra cuando ésta es sometida a un programa de temperatura controlado. El tratamiento puede tener lugar en aire o en atmósfera inerte o de otro tipo. De esta manera es posible obtener información de los procesos de tipo físico o químico que dan lugar a dicha variación. En los termogramas se representa la masa de la muestra en función de la temperatura o del tiempo (al existir una relación lineal entre ambos) [10].

La termogravimetría derivada (DTG) constituye una manera alternativa de mostrar los resultados de un experimento de termogravimetría, que consiste en representar la primera derivada de la curva termogravimétrica.

La TGA y la DTG son sensibles al grado de reducción del óxido de grafeno. Esto se debe a que el proceso de reducción elimina esencialmente los grupos funcionales más lábiles y por lo tanto, a diferencia de lo que ocurre con el óxido de grafeno, el termograma del óxido de grafeno reducido no muestra una brusca pérdida de masa en el rango 200-250 °C.

a

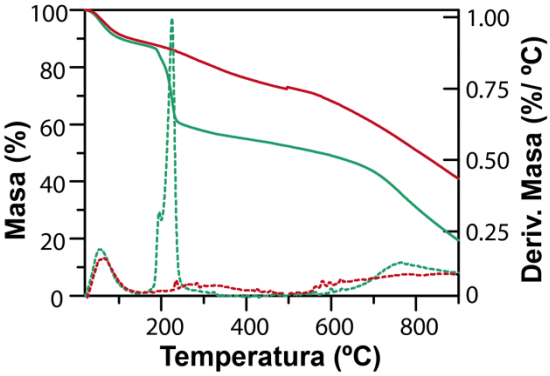

b

Temp. (ºC)	Pérdida de Masa (%)	Proceso Asociado
20-100	15	Eliminación de agua adsorbida
200-250	30	Descomposición de grupos funcionales lábiles
250-600	20	Descomposición de grupos funcionales estables

Figura 12. (a) Termograma (línea sólida) y termograma derivado (línea de puntos) de óxido de grafeno (verde) y óxido de grafeno reducido mediante radiación UV (rojo). (b) Principales procesos asociados a la pérdida de masa en el óxido de grafeno en cada rango de temperatura.

En este trabajo se empleó una termobalanza SDT Q600 (TA Instruments) usando crisoles de Pt, bajo un flujo de argón o de aire (100 mL min^{-1}) y una velocidad de calentamiento de 10 °C min^{-1}.

4.5.2 Desorción a temperatura programada

(Temperature-programmed desorption, TPD)

La desorción a temperatura programada es una técnica de análisis de superficies que consiste en realizar un calentamiento progresivo y controlado de una muestra bajo una determinada atmósfera y, simultáneamente, medir la concentración de determinadas especies gaseosas que se van desprendiendo de su superficie, bien porque estuviesen adsorbidas bien porque se generasen como consecuencia de determinadas reacciones [18]. Los perfiles de TPD [Figura 13 (a)] consisten en la representación de la cantidad liberada de una determinada especie en función de la temperatura. Mediante la integración de dichos perfiles, la técnica permite determinar la cantidad total de una determinada especie desprendida. Las especies que se desprenden habitualmente cuando se calientan materiales carbonosos en atmósfera inerte son H_2O, CO y CO_2. El agua proviene de humedad absorbida o de reacciones de deshidratación entre grupos funcionales de la superficie. Algunos grupos funcionales como carboxilo y lactona dan lugar a una molécula de CO_2 cuando se descomponen, mientras que otros, como fenol, éter, carbonilo y quinona dan lugar a una molécula de CO. Los anhídridos carboxílicos dan lugar a una molécula de CO y otra de CO_2. Como cada grupo funcional posee una temperatura o rango de temperaturas de descomposición característico relacionada con su estabilidad, es posible establecer la presencia de grupos funcionales específicos en la superficie de un material mediante la deconvolución de los perfiles TPD. Por ejemplo, es posible distinguir el CO liberado a partir de un grupo fenol del liberado a partir de un grupo carbonilo porque la temperatura necesaria para descomponerlos es diferente (600-700 °C para fenol frente a 700-980 °C, para carbonilo).

La mayor parte de los trabajos publicados en la literatura sobre TPD de materiales carbonosos corresponden a materiales que durante su preparación han sido sometidos a altas temperaturas, de modo que los grupos funcionales se encuentran situados en los bordes de planos grafíticos y poseen cierta estabilidad térmica [19]. No obstante, como hemos visto en la Introducción, la gran mayoría de los grupos funcionales presentes en el óxido de grafeno son grupos hidroxilo y epóxido situados en el plano basal en altas concentraciones (más inestables). Por ello, en los perfiles de TPD de óxido de grafeno se observa una fuerte liberación de CO y CO_2 a temperaturas mucho más bajas (entre 160 y 190 °C) que las observadas para los materiales de carbono habituales. La liberación de CO_2 es comparable a la de CO, mientras que cabría esperar mayor liberación de CO que de CO_2, dado que los grupos carboxilo de bordes del óxido de grafeno son minoritarios frente a los grupos hidroxilo y epóxido de plano basal. La gran densidad de grupos funcionales en el plano basal y su consiguiente proximidad espacial favorecerá que grupos que individualmente se eliminarían como CO se liberen conjuntamente como CO_2, cuyo desprendimiento es energéticamente favorable frente al de CO.

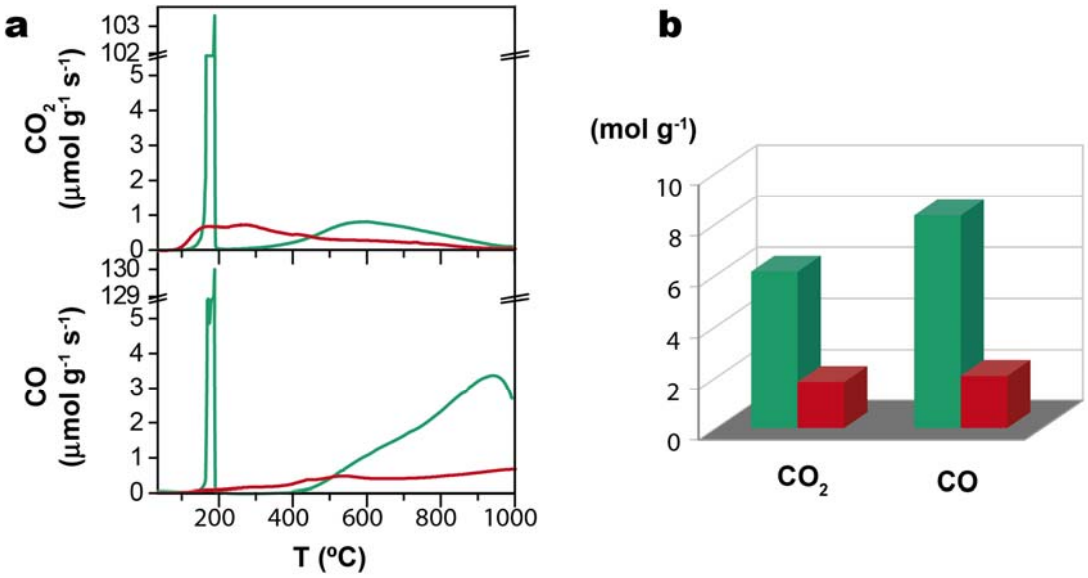

Figura 13. (a) Perfiles de TPD de CO_2 y CO para el óxido de grafeno (verde) y óxido de grafeno reducido (rojo) y (b) cantidad total liberada de dichas especies obtenida a través de la integración de los perfiles.

Se ha utilizado un equipo de Quimisorción Autochem II 2920 (Micromeritics), el cual está totalmente automatizado y es en esencia un sistema de reacción con tres zonas: alimentación de gases, reactor en horno de temperatura y analizadores de gases, que en este caso es un espectrómetro de masas OmniStar 3000 TM (PFEIFFER VACUUM). Para el ensayo TPD, se coloca la muestra sobre fibra de vidrio en un reactor de cuarzo. Antes de iniciar la rampa de calentamiento se hace una calibración haciendo pasar una mezcla de gases puros de concentración conocida (en este caso argón con 1% CO y 1% CO_2) por el espectrómetro de masas acoplado al equipo. A continuación, se calienta la muestra hasta 1000 °C, con una rampa de 10 °C min^{-1}, bajo flujo de argón (50 mL min^{-1}). Este gas arrastra los gases desprendidos por la muestra hasta llegar al espectrómetro, donde son analizados. Una vez alcanzada la temperatura se inicia automáticamente el enfriamiento de la muestra y se realiza una segunda calibración.

4.6 Medidas de propiedades eléctricas

4.6.1 Método de van der Pauw

La conductividad eléctrica, σ, constituye una propiedad específica de los materiales que cuantifica su capacidad para permitir el flujo de portadores de carga cuando se les somete a un campo eléctrico. La magnitud inversa de la conductividad se denomina resistividad, ρ, relacionándose con la resistencia R de una muestra por medio de la ecuación:

$$R = \rho \frac{l}{A} = \frac{l}{\sigma A} \qquad (9)$$

El método de van der Pauw [20] es una técnica que permite determinar la conductividad de una muestra de cualquier geometría. Para poder aplicar dicha técnica la muestra debe conducir la electricidad relativamente bien, ser plana y tener un grosor uniforme. Además, debe ser homogénea e isótropa y no contener agujeros. Por otra parte, los contactos deben situarse en los bordes de la muestra y el área de los contactos debe ser un orden de magnitud menor que el área de la muestra [21].

El método de van der Pauw se ilustra en la Figura 14 y consiste en hacer pasar una corriente I_{13} mientras se mide V_{24}. A continuación se hace pasar una corriente I_{12} mientras se mide V_{34}. El dispositivo experimental empleado incluye un conmutador, de modo que estas medidas pueden realizarse consecutivamente sin cambiar la posición de los contactos.

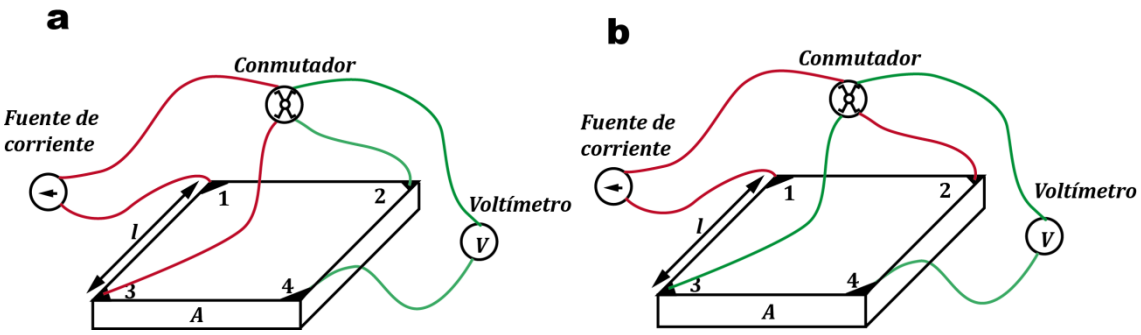

Figura 14. Esquema de funcionamiento del dispositivo experimental para la determinación de la conductividad de un filme basado en el método de van der Pauw.

Van der Pauw demostró que las resistencias $R_{13,24}=V_{24}/I_{13}$ y $R_{12,34}=V_{34}/I_{12}$ se relacionan con la resistencia real de la muestra R_s mediante la siguiente ecuación trascendente:

$$e^{-\pi R_{13,24}/R_s} + e^{-\pi R_{12,34}/R_s} = 1 \qquad (10)$$

El valor de R_s se calcula resolviendo la ecuación (10) numéricamente, tras lo cual se aplica la ecuación (9) para obtener σ.

En este trabajo se determinó la conductividad de filmes de óxido de grafeno reducido y óxido de grafeno reducido tratados térmicamente (grafitización).

El dispositivo experimental empleado incluye una fuente de alimentación Agilent 6614C de corriente continua y un multímetro digital Fluke 45. Los filmes se cortaron en cuadrados de 12x12 mm^2 y su grosor fue determinado por SEM.

4.6.2 Transistores de efecto de campo basados en grafeno

(Graphene field-effect transistor, gFET)

Las propiedades eléctricas del grafeno pueden ser directamente evaluadas mediante la fabricación de transistores de efecto de campo basados en grafeno (gFET). En este tipo de dispositivos, el grafeno desempeña la función de "canal" del transistor, uniendo los electrodos "fuente" y "sumidero" [Figura 15 (a)] mientras que el propio substrato desempeña la función de "puerta" [22]. Mediante la aplicación de un voltaje de puerta V_G es posible modular la corriente fuente-sumidero I_D [Figura 15 (b)]. El mínimo de la curva de transferencia se conoce como punto de neutralidad de carga (V_{CNP}). Para que el transistor pueda ser empleado en dispositivos lógicos de modo eficiente, el voltaje aplicado a la puerta debe ser capaz de modular la corriente fuente-sumidero en varios ordenes de magnitud, de modo que sea posible obtener estados de encendido y apagado del transistor bien definidos. Esta capacidad de mide mediante el ratio on/off del transistor que se obtiene a partir de las curvas de transferencia, como el cociente entre la corriente I_D en el V_{CNP} y la corriente a 30V del V_{CNP}. En el caso del grafeno prístino este ratio es actualmente ~7, aunque se estudia la posibilidad de incrementar este valor utilizando diversas estrategias (dopaje, cintas de anchura nanométrica, etc). La posición del V_{CNP} permite conocer el grado de dopaje de una muestra. Por otra parte, la pendiente de la curva de transferencia está relacionada con la movilidad de huecos ($V<V_{CNP}$) y electrones ($V>V_{CNP}$). La movilidad de los portadores de carga puede ser calculada mediante la fórmula:

$$\mu = \frac{\left[\left(\partial I_d / \partial V_g\right) L\right]}{\left[W C_G V_d\right]} \qquad (11)$$

Donde L y W son la longitud y la anchura del canal, respectivamente, V_D es la diferencia de potencial entre la fuente-sumidero y C_G es la capacitancia de la puerta, que para un substrato de SiO_2 de 300 nm de grosor toma el valor $C_G = 1.15 \times 10^{-4}$ F m^{-2} [23].

En este trabajo se emplean transistores gFET para evaluar las propiedades eléctricas de grafeno crecido por CVD sobre Cu(111) [24]. El primer paso consiste en la fabricación de cintas de grafeno de 10 μm de ancho mediante fotolitografía combinada con plasma de oxígeno. Una vez fabricadas las cintas, éstas son tranferidas a SiO_2(300 nm)/Si. Para ello se recubren las cintas con polimetilmetacrilato (PMMA), se elimina el Cu mediante una disolución de $FeCl_3$ y, tras completar la transferencia, se disuelve el polímero utilizando acetona caliente. Finalmente, se crecen los electrodos mediante litografía seguida de evaporación de Au. Las curvas de transferencia se obtuvieron mediante un analizador de dispositivos semiconductores Agilent B1500A en condiciones de vacío (~5x10^{-4} Pa) y a temperatura ambiente.

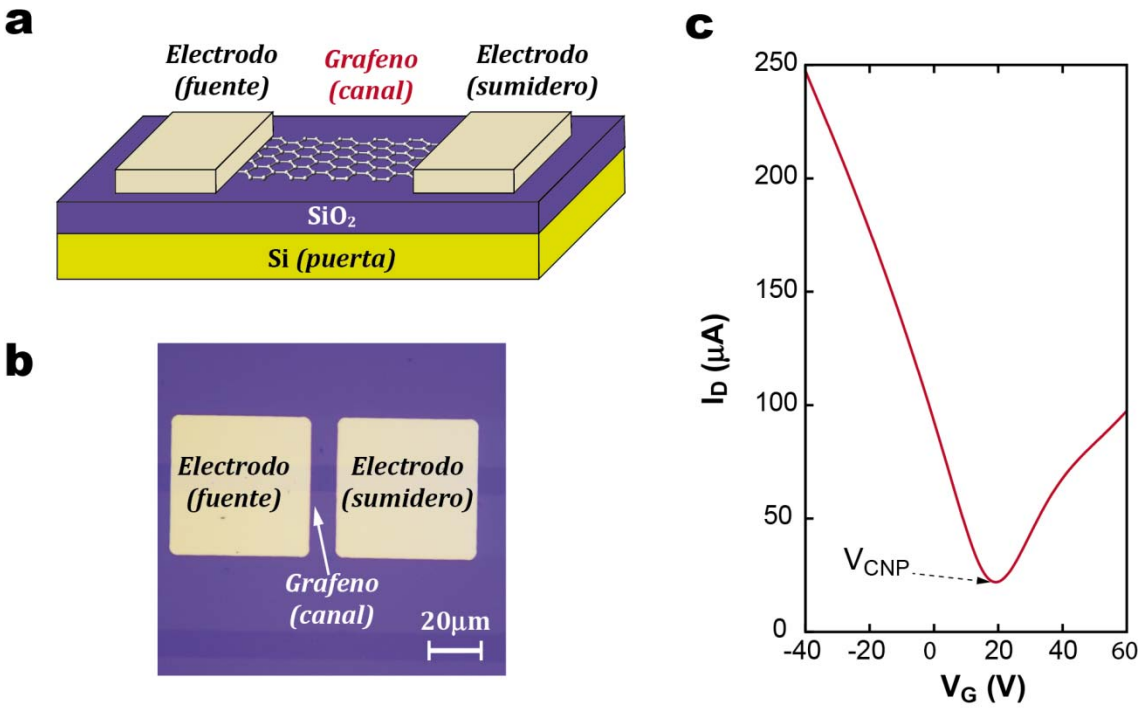

Figura 15. (a) Esquema de un gFET. (b) Imagen de microscopía óptica de un gFET. (c) Características de transferencia de un gFET fabricado con grafeno prístino.

4.6 Referencias

[1]Binning G, Rohrer H, Gerber C, Weibel E. Surface studies by scanning tunneling microscopy. Phys Rev Lett 1982;49(1):57-61.
[2]Binnig G, Quate CF, Gerber C. Atomic force microscope. Phys Rev Lett 1986;56(9):930-3.
[3]Sarid D. Exploring scanning probe microscopy with Mathematica. John Wiley & Sons; 2007.
[4]Magonov SN, Whangbo M-H. Surface analysis with STM and AFM: experimental and theoretical aspects of image analysis. John Wiley & Sons; 2008.
[5]Albrecht T, Grütter P, Horne D, Rugar D. Frequency modulation detection using high-Q cantilevers for enhanced force microscope sensitivity. Journal of Applied Physics 1991;69(2):668-73.
[6]James PJ, Antognozzi M, Tamayo J, McMaster TJ, Newton JM, Miles MJ. Interpretation of contrast in tapping mode AFM and shear force microscopy. A study of nafion. Langmuir 2001;17(2):349-60.
[7]Michler GH. Electron microscopy of polymers. Springer; 2008.
[8]Egerton RF. Physical principles of electron microscopy. Springer; 2005.
[9]Christian GD, O'Reilly JE. Instrumental analysis. 1988.
[10]Skoog DA, Holler FJ, Nieman TA, Gómez MdCM. Principios de análisis instrumental. McGraw-Hill Madrid; 2001.
[11]Harwood LM, Claridge TD. Introduction to organic spectroscopy. Oxford University Press New York; 1997.
[12]Solé J, Bausa L, Jaque D. An introduction to the optical spectroscopy of inorganic solids. John Wiley & Sons; 2005.
[13]Smith BC. Fundamentals of Fourier transform infrared spectroscopy. CRC press; 2011.
[14]Smith E, Dent G. Modern Raman spectroscopy: a practical approach. John Wiley & Sons; 2005.
[15]Amer MS. Raman spectroscopy, fullerenes and nanotechnology. Royal Society of Chemistry; 2010.
[16]Bordo VG, Rubahn H-G. Optics and spectroscopy at surfaces and interfaces. John Wiley & Sons; 2008.
[17]Seijo AIC. Factores determinantes de la reactividad de fibras de carbono y otros materiales carbonosos. 1994.
[18]Niemantsverdriet JW. Spectroscopy in catalysis. John Wiley & Sons; 2007.
[19]Figueiredo JL, Pereira MFR, Freitas MMA, Órfão JJM. Modification of the surface chemistry of activated carbons. Carbon 1999;37(9):1379-89.
[20]Van der Pauw L. A method of measuring the resistivity and Hall coefficient on lamellae of arbitrary shape. Philips Tech Rev 1958;20(8):220-4.
[21]Webster JG. Electrical measurement, signal processing, and displays. CRC Press; 2010.
[22]Schwierz F. Graphene transistors. Nat Nanotechnol 2010;5(7):487-96.
[23]Orofeo CM, Hibino H, Kawahara K, Ogawa Y, Tsuji M, Ikeda K-i, et al. Influence of Cu metal on the domain structure and carrier mobility in single-layer graphene. Carbon 2012;50(6):2189-96.

[24]Hu B, Ago H, Ito Y, Kawahara K, Tsuji M, Magome E, et al. Epitaxial growth of large-area single-layer graphene over Cu(111)/sapphire by atmospheric pressure CVD. Carbon 2012;50(1):57-65.

Resúmenes y artículos 5

5. Resúmenes y artículos

5.1 Reducción química del óxido de grafeno

Artículo I

Publicado en la revista Journal of Alloys and Compounds: "Chemical and microscopic analysis of graphene prepared by different reduction degrees of graphene oxide"

Articulo II

Publicado en la revista Carbon: "UV light exposure of aqueous graphene oxide suspensions to promote their direct reduction, formation of graphene–metal nanoparticle hybrids and dye degradation"

Entre los métodos disponibles en la actualidad para la producción de grafeno, la preparación de suspensiones coloidales, en especial a partir de óxido de grafito, constituye una vía muy atractiva debido a su bajo coste y a que es fácilmente escalable a nivel industrial. Además, mediante este enfoque el grafeno puede ser fácilmente ensamblado o transferido a un sustrato aislante, lo que representa una ventaja tecnológica añadida. La reducción del óxido de grafito exfoliado (óxido de grafeno) es un proceso que se realiza con el fin de eliminar los grupos funcionales oxigenados presentes en las láminas de óxido de grafeno y recuperar la conjugación de los enlaces carbono-carbono y, con ello, la conductividad eléctrica.

En el *artículo I* hemos investigado la composición química y estructural de láminas de óxido de grafeno reducidas con diferentes agentes reductores, lo que da lugar a distintos grados de reducción. Se consiguieron reducciones suaves usando sólo amoniaco, reducciones intermedias usando pirogalol y reducciones fuertes usando ácido ascórbico (vitamina C) o hidrazina. El creciente grado de reducción de estas muestras pudo ser confirmado por la disminución gradual de su contenido en oxígeno (determinado por XPS) y el aumento progresivo de la conductividad eléctrica (medida en filmes de dichas láminas), que indica una recuperación de la conjugación electrónica en la red grafítica.

De acuerdo con el modelo de Lerf-Klinowski, los grupos funcionales que decoran el óxido de grafeno son principalmente grupos hidroxilo y epoxi en posiciones de plano basal y grupos carboxilo y carbonilo situados en los bordes de las láminas. A partir del análisis de los espectros XPS de C1s y O1s de alta resolución se deduce que los grupos funcionales oxigenados que se sitúan típicamente en el plano basal (hidroxilo y epoxi)

son eliminados en el proceso de reducción más fácilmente que los grupos situados en los bordes de las láminas (grupos carboxilo y carbonilo).

El estudio de las distintas muestras mediante desorción a temperatura programada (TPD) permite respaldar esta visión. Para entender los resultados de TPD resulta necesario tener en cuenta que la alta densidad de grupos funcionales oxigenados en las láminas hace posible reducir el coste energético de generar una vacante en el plano basal, ya que otros grupos cercanos pueden migrar a estos defectos y estabilizar los enlaces no saturados del carbono, formando grupos oxigenados más estables. Por esta razón, la descomposición de los grupos funcionales más lábiles tiene lugar a temperaturas inusualmente bajas para un material carbonoso (intensa liberación de CO_2 y CO entre 160 °C y 190 °C). Debido a que en las muestras ya reducidas (que poseen menos grupos oxigenados) se generan menos grupos estables a las temperaturas relativamente bajas mencionadas, la descomposición de grupos funcionales estables a mayor temperatura es menor que en la muestra de GO no reducido (menor liberación de CO por encima de 500 °C).

El estudio de las distintas muestras mediante AFM y STM revela la influencia del grado de reducción en la morfología de las láminas. Mientras que las imágenes de AFM o de STM a escala nanométrica de las láminas poco reducidas muestran una superficie irregular sin rasgos distinguibles, las imágenes de AFM de las láminas con un mayor grado de reducción revelan la presencia de protuberancias de 10 nm de diámetro y 0.5 nm de altura que también están presentes en las imágenes de STM a escala nanométrica. Las imágenes de STM a escala atómica revelan que estas protuberancias tienen su origen en el hundimiento de las regiones ordenadas libres de grupos funcionales oxigenados respecto a las regiones aún oxidadas. El hecho de que estas protuberancias sólo se observen en las muestras más reducidas se debe a que en estas muestras los dominios ordenados son más extensos, lo que facilita su observación.

En el *artículo II* hemos estudiado la reducción de dispersiones de GO mediante radiación ultravioleta. Al igual que la reducción química, la reducción fotoinducida permite eliminar grupos oxigenados de láminas de óxido de grafeno mientras éstas se encuentran en dispersión coloidal. Este proceso se realizó a temperatura ambiente en ausencia de reactivos químicos o catalizadores.

Para comprobar la efectividad del método, se caracterizó la muestra irradiada con luz UV y se comparó con el GO de partida. La espectroscopía de absorción UV-vis mostró un desplazamiento del máximo de absorción asociado a transiciones $\pi \rightarrow \pi^*$ hacia el rojo hasta situarse a 264 nm, que está en el rango de valores obtenidos con reductores químicos, además de un aumento generalizado de la absorbancia por encima de 260 nm. En las curvas TGA se observa que la pérdida de masa (~30%) entre 180 y 250 °C habitual en el óxido de grafeno desaparece tras la irradiación, lo cual indica que las funcio-

nalidades oxigenadas lábiles han sido eliminadas. La espectroscopía ATR-FTIR muestra un descenso en la intensidad de los picos asociados a distintas vibraciones de los grupos funcionales oxigenados. Por XPS se determina que la proporción O/C en la muestra reducida es de 0.22 (frente a 0.43 para el GO) y el espectro de alta resolución del C1s muestra una reducción de la intensidad de las componentes asociadas a funcionalidades oxigenadas lábiles en el material irradiado. Las imágenes de AFM confirman que las láminas continúan siendo monocapa. Las imágenes de STM muestran una morfología rugosa similar a la que se obtiene con otros reductores, que se atribuye a la distorsión creada por defectos y funcionalidades aún presentes.

El mecanismo responsable de la reducción de las láminas es de tipo fototérmico. La luz utilizada en el tratamiento tiene una longitud de onda entre 280 y 450 nm, que es absorbida por las láminas de óxido de grafeno. La absorción de luz ultravioleta excita los electrones que posteriormente se relajan no radiativamente induciendo vibraciones de la red atómica y dando lugar a un calentamiento local de las láminas. Este calentamiento local es suficientemente intenso como para producir la descomposición de los grupos funcionales más lábiles presentes en las láminas. Además, puede existir otro mecanismo adicional de tipo químico, ya que el calentamiento del medio acuoso más próximo a las láminas podría dar lugar a un cambio en las propiedades fisicoquímicas del agua (aumento de la constante de disociación), que a su vez puede promover reacciones de deshidratación.

En este estudio se demuestra además que es posible aprovechar el ambiente reactivo que se genera en las láminas debido a la irradiación con luz ultravioleta para lograr la fotodegradación de un contaminante en medio acuoso como la rodamina B. El rendimiento de este proceso depende de la exposición de las moléculas de rodamina B a dicho ambiente reactivo, por lo que la gran área superficial del grafeno juega un papel decisivo. El proceso también depende del pH del medio, debido a que la adsorción de la rodamina B en el grafeno depende de la interacción entre el grupo amonio de la molécula (carga positiva) y los grupos carboxílicos desprotonados del óxido de grafeno (carga negativa).

El calentamiento local de las láminas y el aumento de la reactividad en estos puntos también se puede aprovechar para la nucleación y crecimiento de nanopartículas de oro en las láminas de GO. Este crecimiento de nanopartículas de oro se llevó a cabo en las mismas condiciones que la reducción del GO, pero añadiendo $HAuCl_4$ como precursor. Tras la irradiación, el espectro de absorción UV-vis de la dispersión que contenía el precursor mostraba un máximo a 524 nm característico de nanoestructuras de oro. El análisis mediante AFM muestra que el oro se encuentra en la muestra en la forma de nanopartículas redondeadas de unos 15 nm de diámetro adheridas a las láminas de grafeno, cuya densidad en las láminas es de 10-15 μm^{-2}. Los resultados de FE-SEM y

SEM son consistentes con los de AFM y muestran una distribución homogénea de nanopartículas sobre las láminas.

Por último, estudiamos el rendimiento de este material híbrido como sustrato para SERS y como catalizador, por ser dos de las potenciales aplicaciones de nanoestructuras de oro. Para realizar el SERS utilizamos rodamina B como material de referencia, siendo la intensidad de las bandas vibracionales mayor cuando se utilizó el material híbrido como sustrato. También se estudió su eficacia como catalizador de la reducción de *p*-nitroanilina (*p*-NA) con borohidruro de sodio ($NaBH_4$). La reacción se completó en tan solo 1.7 min mientras que en presencia de nanopartículas de oro de tamaño semejante encapsuladas en polielectrolito la reacción requiere 30 min.

Journal of Alloys and Compounds 536S (2012) S532–S537

Contents lists available at SciVerse ScienceDirect

Journal of Alloys and Compounds

journal homepage: www.elsevier.com/locate/jallcom

Chemical and microscopic analysis of graphene prepared by different reduction degrees of graphene oxide

P. Solís-Fernández, R. Rozada*, J.I. Paredes, S. Villar-Rodil, M.J. Fernández-Merino, L. Guardia, A. Martínez-Alonso, J.M.D. Tascón

Instituto Nacional del Carbón, INCAR-CSIC, Apartado 73, 33080 Oviedo, Spain

ARTICLE INFO

Article history:
Received 20 June 2011
Received in revised form 10 January 2012
Accepted 17 January 2012
Available online 28 January 2012

Keywords:
Graphene oxide
Reduction
Temperature-programmed desorption
Scanning tunneling microscopy
Atomic force microscopy

ABSTRACT

Chemical reduction of exfoliated graphite oxide (graphene oxide) has become one of the most promising routes for the mass production of graphene sheets. Nonetheless, the material obtained by this method exhibits considerable structural disorder and residual oxygen groups, and reports on their microscopic structure are quite scarce. We have investigated the structure and chemistry of graphene oxide samples reduced to different degrees using atomic force and scanning tunneling microscopy (AFM/STM) as well as X-ray photoelectron spectroscopy (XPS) and temperature-programmed desorption (TPD), respectively. TPD and XPS results indicate that reduction proceeds mainly by eliminating the most labile oxygen groups, which are ascribed to epoxides and hydroxyls on basal positions of the graphene plane. AFM/STM shows that the sheets are composed of buckled oxidized regions intermingled with flatter, non-oxidized ones, with the relative area of the latter increasing with the reduction degree.

1. Introduction

Since it was first isolated in 2004, graphene, a two dimensional hexagonal network of carbon atoms, has grown in popularity within the scientific community due to its outstanding properties, which make it a potential candidate in many technological applications [1,2]. Achieving the practical implementation of graphene on a large scale will rely on finding feasible approaches for the mass production and processing of this material. In this regard, chemical reduction of exfoliated graphite oxide (graphene oxide) appears to be one of the most convenient routes for graphene production available at present, providing great quantities of material in the liquid phase [3,4]. However, the material obtained by this method differs chemically and structurally from pristine graphene obtained, e.g., by micromechanical cleavage of graphite [5]. In particular, its characteristics strongly depend on the extent of reduction achieved [6–8]. Here we have investigated the chemical and morphological evolution of graphene oxide (GO) sheets with different reduction degrees using X-ray photoelectron spectroscopy (XPS) and temperature-programmed desorption (TPD), which are useful techniques to provide relevant chemical information of carbon materials [9–12], and atomic force and scanning tunneling microscopies (AFM/STM), which allow imaging this type of graphene on the nanometer and atomic scales.

2. Materials and methods

Graphene oxide sheets were obtained in the form of aqueous dispersions (0.1 mg mL^{-1}) from graphite oxide on the basis of previously reported procedures [5,13]. Reduced graphene oxide (RGO) with different degrees of deoxygenation was prepared as follows [8]: highly reduced samples were made by heating the suspension at 95 °C for 1 h in the presence of 2 mM vitamin C (sample RGO-V), or 21 mM hydrazine (sample RGO-H) as a reductant; intermediate deoxygenation was achieved by the same procedure except for the use of 1 mM pyrogallol as a reducing agent (RGO-P); finally, mild deoxygenation was accomplished just in basic medium in the absence of any reductant. In the latter case, the suspensions were heated at 95 °C for 4 h in the presence of 26 mM (sample RGO-N1) and 206 mM (sample RGO-N2) of ammonia. The choice of these reducing agents and conditions has been made on the basis of previous experimental observations [8], which afford covering a wide range of reduction degrees. In particular, the efficiency of reduction depends on the nature of the reducing reagent, although the reason behind such differences is not currently known.

XPS was performed on a SPECS system at 10^{-7} Pa with a monochromatic Al Kα X-ray source at 100 W. The surface charging effect in GO was counteracted by the use of an electron flood gun operated at 0.4 eV and 0.10 mA. TPD analysis of the samples was conducted in a Micromeritics Autochem II chemisorption analyzer with a heating rate of 10 °C min^{-1} under flowing argon (50 mL min^{-1}). The amounts of released H_2O, CO and CO_2 were determined from the intensities of m/z = 18, 28, and 44, respectively, monitored by an Omnistar mass spectrometer (Pfeiffer Vacuum). Raman spectra were recorded with a Horiba Jobin-Yvon LabRam instrument at a laser excitation wavelength of 532 nm. AFM and STM investigations were conducted on a Nanoscope IIIa Multimode apparatus (Veeco Instruments) working under ambient conditions. The samples were prepared by drop-casting a small volume of diluted dispersion (5 μL, 0.01 mg mL^{-1}) onto a preheated (~50–60 °C) highly oriented pyrolytic graphite (HOPG) substrate and allowing it to dry. STM imaging

* Corresponding author. Tel.: +34 985 11 90 90; fax: +34 985 29 76 62.
E-mail address: rozada@incar.csic.es (R. Rozada).

0925-8388/$ – see front matter © 2012 Elsevier B.V. All rights reserved.
doi:10.1016/j.jallcom.2012.01.102

Table 1
O/C and N/C atomic ratios obtained from XPS survey spectra and total amount of released species obtained by integration of the TPD profiles. For the H_2O column, the first value was obtained by integration over the whole temperature range, so that it includes humidity (adsorbed water); the second value is a guess of the amount of water not coming from humidity calculated by integration in a temperature range above 150 °C.

Sample	Atomic ratios by XPS		Species released by TPD (μmol g^{-1})		
	O/C	N/C	CO	CO_2	H_2O
GO	0.43	0.02	8331	6134	854/~630
RGO-N1	0.30	0.04	2014	4415	469/~293
RGO-P	0.17	0.05	2113	3445	283/~205
RGO-V	0.08	0.01	2071	1827	225/~166
RGO-H	0.08	0.02	1407	1890	66/~45

was accomplished in the constant current mode (variable height) with mechanically prepared Pt/Ir (80/20) tips. AFM was carried out in the tapping mode of operation, employing rectangular Si cantilevers with nominal spring constant and resonance frequency of ~40 N m^{-1} and ~250–300 kHz respectively. The electrical conductivity of thin RGO films prepared by vacuum filtration of the different reduced suspensions was evaluated by measuring the resistance of rectangular strips with a Fluke 45 digital multimeter. The film thickness was estimated by scanning electron microscopy.

3. Results and discussion

The oxygen functionalities present in GO sheets transform much of the originally sp^2-hybridized carbon atoms of the graphene lattice to a sp^3-hybridized state, thus decreasing dramatically the electronic conjugation of the sheets and therefore their electrical conductivity. As reduction of GO proceeds and its oxygen-containing groups are removed, sp^2 bonding and electronic conjugation are progressively restored, and therefore electrical conductivity increases. As a matter of fact, it has been shown that this property is highly sensitive to the reduction degree attained for GO [7]. In our case, the electrical conductivity measured for samples RGO-N1, RGO-N2, RGO-P, RGO-V and RGO-H was 0.05, 0.32, 488, 7700 and 9660 S m^{-1}, respectively, suggesting their reduction degree to be in the same order.

To follow the chemical evolution of GO upon reduction, XPS and TPD analyses were performed. Table 1 shows O/C and N/C atomic ratios for the investigated samples. The aforementioned order in the reduction degree of the samples is confirmed by the decreasing O/C ratio in the series. A minor amount of nitrogen is introduced in every sample, which must be related to the used base (NH_3) and/or the reducing agent. Fig. 1 shows high resolution C 1s (a) and O 1s (b–d) core level XPS spectra of some selected samples: GO (green), RGO-N1 (blue), and RGO-V (red). Samples RGO-N2, RGO-P and RGO-H (not shown) yielded results that are consistent with their reduction degree. The C 1s band of GO consists of three components, assigned to carbons in unoxidized, aromatic sp^2 structures (binding energy of 284.6 eV), carbons singly bonded to oxygen (e.g., in hydroxyl and epoxy groups) and also possibly C—C bonds in defect structures (286.6 eV) [11], and carbon doubly bonded to oxygen (287.9 eV) [12]. From the relative intensity of such components, it is clear that oxygen groups present in GO are mainly epoxies and hydroxyls, both located in basal plane sites [14,15]. Upon reduction, there is a notable drop in the intensity of the component associated to these basal plane groups (286.6 eV). For the more extensively reduced samples (RGO-V and RGO-H) the restoration of electronic conjugation is confirmed by the appearance of a $\pi \rightarrow \pi^*$ band at ~291.1 eV [11] (see inset of Fig. 1a, where the ordinate scale of the spectra has been magnified). In the case of thermal reduction of GO, the appearance of such band has been reported for annealing temperatures above 400 °C [16]. The increase in the order and homogeneity in the chemical environment of sp^2 carbon is reflected in the narrowing of the corresponding band, from a full

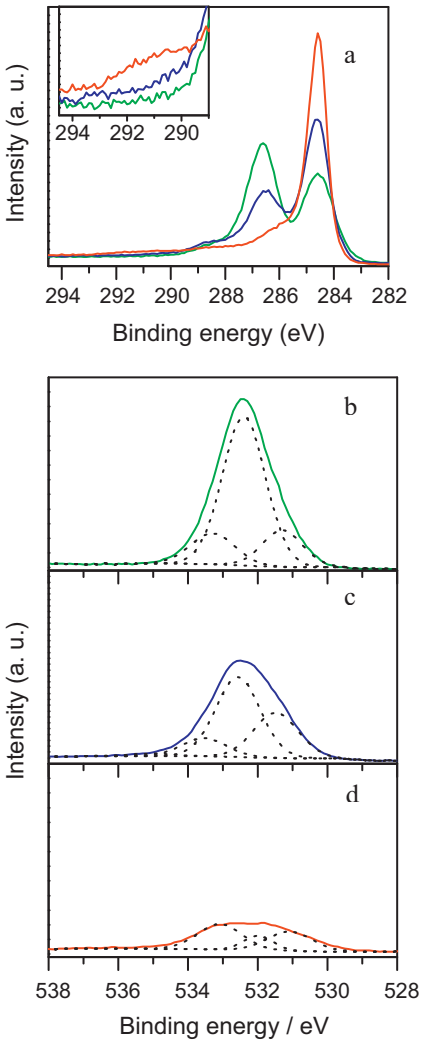

Fig. 1. High resolution C 1s (a) and O 1s (b–d) core level XPS spectra of GO (green), RGO-N1 (blue), and RGO-V (red). The spectra in (a) are normalized and a magnification of the higher binding energy range is shown in the inset. (For interpretation of the references to color in this figure legend, the reader is referred to the web version of the article.)

width at half maximum of ~1.4 eV in GO to ~1.1 eV and ~0.8 eV for RGO-N1 and RGO-V, respectively.

The O 1s band was peak-fitted into four components (Fig. 1b–d), which were assigned to the following species [17,18]: doubly bonded oxygen (~531.3 eV); singly bonded oxygen in alcohols, ethers, epoxides and peroxides (~532.4 eV); singly bonded oxygen in acids, esters, and hydroperoxides (~533.3 eV); and peroxyacid, peroxyester and/or charge effect (~534.8 eV). The intensity of the latter was almost zero in most cases. As already observed in the C 1s band, the intensity of the component at ~532.4 eV, which involves basal plane epoxides and hydroxyls, drops significantly with the reduction degree. On the other hand, the intensity of the bands related to groups at the edges of the graphene sheets remains basically unaltered by the reduction process. This is in agreement with recent theoretical calculations on the reduction mechanism of GO, which predicted a higher difficulty in the removal of oxygen-containing groups located at edges compared to those located at the interior of the basal planes [19].

Fig. 2 shows H_2O, CO and CO_2 TPD profiles for GO, RGO-N1 and RGO-V samples and Table 1 displays the total amounts released of such species also for samples RGO-P and RGO-H. The results for GO are similar to those found in the literature (reported only in

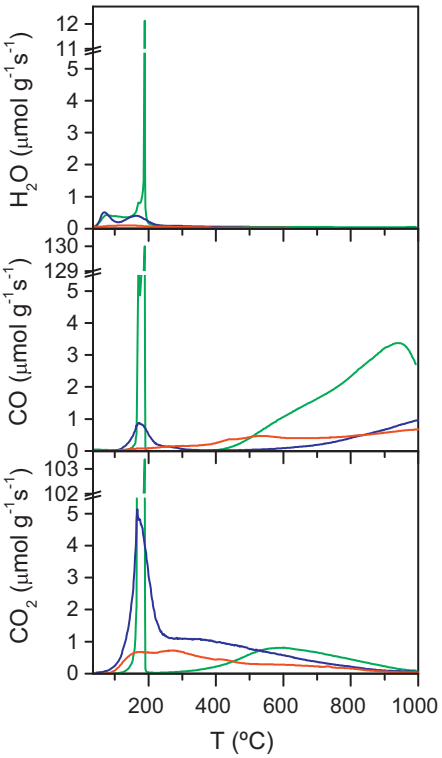

Fig. 2. From top to bottom, TPD profiles for the samples GO (green), RGO-N1 (blue), and RGO-V (red) for H_2O, CO, and CO_2. (For interpretation of the references to color in this figure legend, the reader is referred to the web version of the article.)

the temperature range below 300 °C) in that H_2O, CO and CO_2 are the primary desorption products of GO and the three of them are released at the same temperature [16,20]. Evolution of CO and CO_2 can be attributed to the presence of oxygenated functionalities in the sheets. Therefore, the observed diminution in the total amounts of CO and CO_2 evolved for reduced samples in comparison with those of GO (see Table 1) indicates a decrease in the overall amount of such species following reduction, which is also in agreement with the drop in the O/C ratio deduced by XPS (see Table 1). The TPD profiles for GO reveal that there is a strong evolution of CO in a very narrow range of low temperatures (~160–190 °C), which is quite unusual for carbon materials [9,21], but agrees with previous reports on GO [16,20]. As established from the XPS results, oxygen groups present in GO are mainly epoxies and hydroxyls (see Fig. 1a and b), both located in basal plane sites [14,15]. These are expected to be much more labile and therefore evolve at lower temperatures than the typically edge-located functionalities of carbon materials. Furthermore, although only CO evolution would be expected for isolated epoxy and hydroxyl functionalities, the very high density of these types of oxygen functionality present in the starting GO sample [1,4,5] should also facilitate the release of CO_2, which is energetically favorable in comparison with CO. Thus, we ascribe the low temperature release of CO and also CO_2 to desorption of basal plane epoxides and hydroxyls.

For the reduced samples, there is a pronounced decrease in the lower temperature evolution of CO and CO_2, indicating that chemical reduction involves mainly the most labile groups. These results are in agreement with previous theoretical and experimental studies of chemical reduction [8,19]. H_2O evolution for samples GO and RGO-N1 below ~150 °C may be ascribed to desorption of physisorbed water molecules, while the observed release in the 175–200 °C range could be due to either desorption of more strongly adsorbed water or, alternatively, to water molecules produced in dehydration processes (e.g., formed by reaction of two

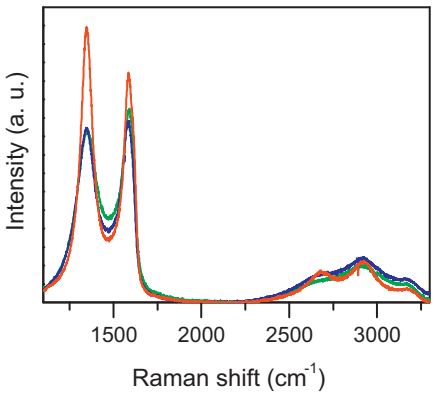

Fig. 3. Normalized Raman spectra of GO (green), RGO-N1 (blue), and RGO-V (red). (For interpretation of the references to color in this figure legend, the reader is referred to the web version of the article.)

hydroxyls). H_2O evolution for samples reduced to a higher extent is much smaller, which is consistent with their considerable degree of reduction (relatively little evolution of CO and CO_2, high electrical conductivity, lower O/C atomic ratio) and its subsequent expected hydrophobicity.

For temperatures above ~500 °C, the evolution of CO for GO is significantly larger than that of its reduced counterparts. This appears to contradict the fact that reduction mainly proceeds

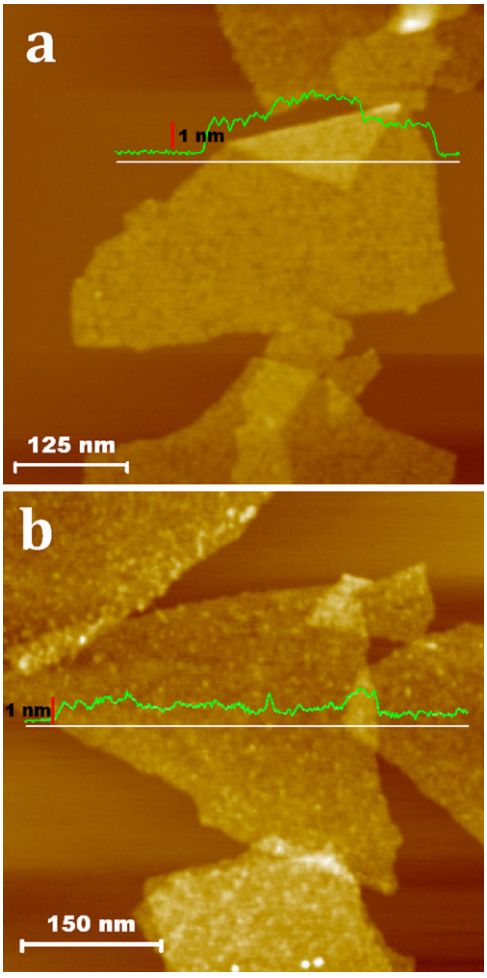

Fig. 4. Tapping mode AFM images of: (a) RGO-N1 and (b) RGO-V sheets, with included line profiles.

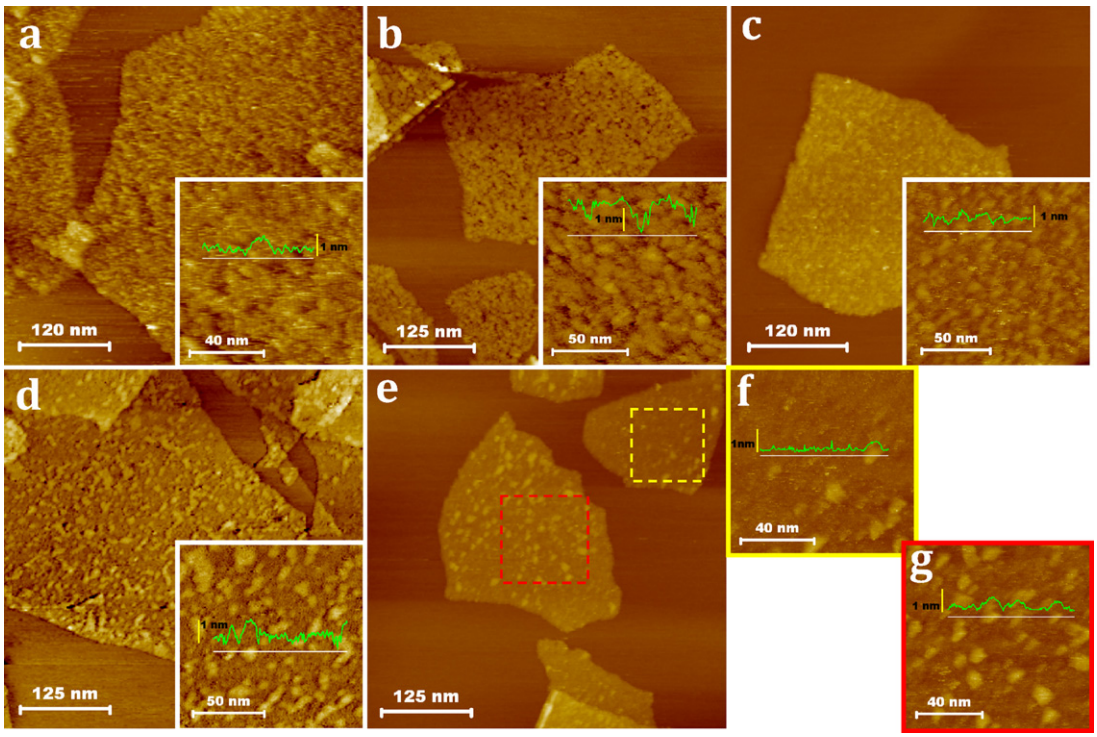

Fig. 5. STM images of: (a) RGO-N1 (75 pA, 2000 mV), (b) RGO-N2 (inset: 200 pA, 500 mV), (c) RGO-P, (d) RGO-V, and (e–g) RGO-H with insets showing more detailed areas. The tunneling parameters employed to collect these images were 250 pA and 1000 mV, except for the cases indicated in the parentheses.

through elimination of the most labile groups. Previous studies on carbon materials have attributed the evolution of CO at these temperatures to the presence of ethers, carbonyls and phenol-type hydroxyls [9]. Furthermore, recent theoretical calculations have suggested that chemical reduction cannot remove these types of oxygen-containing groups [19], so they should be still present in the reduced samples. We interpret that the stable oxygenated species responsible for the considerable release of CO above 500 °C in GO were not present in the original sample before the TPD experiment, but instead they were originated during such experiment at lower temperatures. It has been recently shown that thermal desorption of oxygen-containing functional groups from GO modifies the structure of the material, creating vacancies and small holes, and many of the remaining epoxide and hydroxyl groups can readily migrate to these defects and form more stable, edge-located functionalities [22]. Thus, epoxides could transform into carbonyls and ethers, and basal plane hydroxyls into phenol-type hydroxyls. For the reduced samples, the amount of labile oxygen groups is rather small (little evolution of CO and CO_2 at 160–190 °C), so only a small amount of stable groups will be generated as a result of thermal evolution for the former, thus explaining the comparatively small amounts of CO released for these samples above 500 °C.

Raman spectroscopy was employed in an attempt to gain some general structural information on the investigated materials. Fig. 3 shows normalized first and second order Raman spectra of GO, RGO-N1 and RGO-V. The first-order Raman spectrum of the materials under study is characterized by strong bands at ~1350 and ~1580 cm^{-1}, known as D and G bands, respectively. Defect-free graphite would only show the G band, as the D band corresponds to a phonon mode whose intensity is strictly connected to the presence of six-fold aromatic rings close to local lattice distortions (defects) of the graphitic network [23]. Such distortions can be due, for example, to the presence of edges of graphitic planes, atomic vacancies or oxygenated groups. Upon reduction of GO under the conditions used in this study, there is a rise in the relative intensity of the D band (see Fig. 3), which seems at odds with the idea that reduction should restore graphitic order and electronic conjugation as suggested by the aforementioned increase in conductivity and the appearance of a $\pi \rightarrow \pi^*$ shake-up peak in the high resolution C 1s XPS band. We note that an increase in the intensity ratio of the D and G bands (I_D/I_G) has been found in the early stages of graphene oxidation, caused by the gradual increase in the density of the aforementioned defects of the graphitic network [24]. However, such a trend is only observed up to a certain degree of oxidation and for further oxidation (i.e., upon additional introduction of lattice distortions), the I_D/I_G ratio exhibits a decreasing trend [24]. Such behavior can be attributed to the disappearance of the aromatic, electronically conjugated character from a large number of the six-fold rings as a result of extensive oxidation, which would therefore stop contributing to the D band [4,5]. Because the graphene sheets have been very extensively oxidized in GO, it would not be unexpected that the reduction led, at least at its first stages to an increase in I_D/I_G ratio, since more aromatic rings are becoming available to contribute to the D band. As chemical reduction with even the most effective reductants (e.g., hydrazine or ascorbic acid) is always limited and a significant number of oxygen-containing groups remain [O/C ratio of ~0.08 (Table 1), which should still amount to a large density of lattice distortions], it is not surprising that we only observe an increase in the D band with reduction (Fig. 3).

Inspection of individual sheets by AFM/STM revealed a clear influence of the reduction degree on their morphology. Fig. 4 shows representative tapping mode AFM images of RGO-N1 and RGO-V supported on HOPG. The measured sheet thickness tends to gradually decrease with reduction degree (see the included profiles), from 0.9–1.1 nm for GO (image not included) to 0.5–0.6 nm for the most extensively reduced samples (RGO-V and RGO-H). To obtain accurate and consistent results, thickness was determined by measuring heights from overlapped sheets, rather than measuring the sheet height relative to the HOPG substrate [25]. From Fig. 4 the sheets appear to be quite similar on the nanometer scale, except

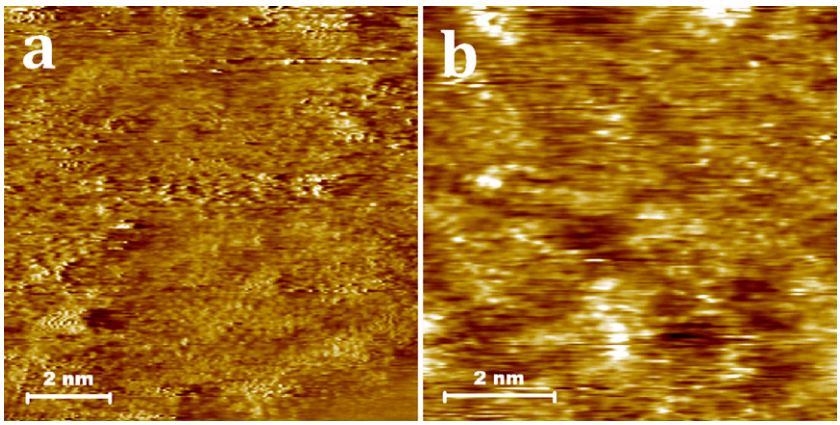

Fig. 6. Atomic scale STM images of: (a) RGO-N2 (2.5 nA, 10 mV) and (b) RGO-V (3.5 nA, 3 mV).

for some small protrusions ~0.5 nm high and ~10 nm in diameter seen in the RGO-V sheets.

More detailed images were obtained by STM as shown in Fig. 5, where the nanometer-scale morphological evolution of the samples with reduction can be better appreciated. The low conductivity of RGO-N1 and RGO-N2 sheets required the use of relatively low currents and high voltages for the tunneling parameters. To allow direct comparisons, STM images of all the reduced samples were taken employing similar tunneling parameters. The slightly reduced RGO-N1 sheets display a smooth irregular surface without distinguishable features, whereas the highly reduced samples RGO-V and RGO-H exhibit an almost flat surface decorated with isolated globular protrusions with lateral sizes of 8–15 nm. Atomic scale STM images of samples RGO-N2 and RGO-V are presented in Fig. 6 (the relatively low conductivity of RGO-N1 sheets did not allow attaining atomic resolution). For both samples, locally ordered or structured domains just a few nanometers large can be seen, which tend to be somewhat larger in the case of RGO-V, as well as for sample RGO-V (image not shown).

In the most widely accepted model, GO sheets are thought to be comprised of randomly distributed highly oxidized zones, in which the vast majority of the oxygen functional groups are present, intermingled with some very small (<3 nm), essentially pristine, isolated graphene regions [14,26]. Because functionalities should be the main source of local deformation of the sheets, oxidized areas are thought to be highly buckled, while pristine regions should be flatter. Presumably, reduction diminishes the area of the buckled, oxidized regions and increases that of pristine, flat ones, which is in accordance with the observations of Fig. 5: the STM images of the highly reduced RGO-V/RGO-H sheets (Fig. 5d–g) show a clear contrast between flat/pristine areas, which have become relatively abundant and buckled/oxidized ones (globular protrusions). Such a contrast is not observed for the mildly reduced samples RGO-N1 and RGO-N2 (Fig. 5a and b). In the STM images of the intermediately reduced RGO-P sample (Fig. 5c) the differentiation between both kinds of zones starts to become apparent, thus showing a transition between samples reduced to a lower and a higher extent. Furthermore, the expansion of the more pristine and flatter areas should contribute to the decrease in thickness observed with increasing reduction degree.

4. Conclusions

Chemical reduction of GO can be accomplished to different degrees by controlling several experimental parameters, such as the nature and relative amount of reagents or the reaction time. XPS and TPD analysis showed that reduction mainly proceeds by elimination of the most labile functional groups of GO, which are thought to be mostly located on basal plane positions rather than at edges of the graphene sheets. AFM and STM investigations suggested that reduced GO sheets are composed of a random patchwork of buckled oxidized areas and relatively flat, non-oxidized regions. The relative area of the latter increases with the extent of reduction, which leads to an appreciable decrease in the measured thickness of the sheets. Partial restoration of the graphitic lattice with reduction was also confirmed by the observed increases in electrical conductivity and the appearance of a $\pi \rightarrow \pi^*$ shake-up peak in the high resolution C 1s XPS band.

Acknowledgements

Financial support from the Spanish MICINN (projects MAT2008-05700 and MAT2011-26399) is gratefully acknowledged. R.R. and M.J.F.-M. are thankful for the receipt of a pre-doctoral contract (FPU and FPI, respectively) from MICINN. L.G. acknowledges CSIC for the receipt of postdoctoral JAE-Doc contract.

References

[1] Y. Zhu, S. Murali, W. Cai, X. Li, J.W. Suk, J.R. Potts, R.S. Ruoff, Adv. Mater. 22 (2010) 3906–3924.
[2] V. Singh, D. Joung, L. Zhai, S. Das, S.I. Khondaker, S. Seal, Prog. Mater. Sci. 56 (2011) 1178–1271.
[3] S. Stankovich, R.D. Piner, X. Chen, N. Wu, S.T. Nguyen, R.S. Ruoff, J. Mater. Chem. 16 (2006) 155–158.
[4] S. Stankovich, D.A. Dikin, R.D. Piner, K.A. Kohlhaas, A. Kleinhammes, Y. Jia, Y. Wu, S.T. Nguyen, R.S. Ruoff, Carbon 45 (2007) 1558–1565.
[5] J.I. Paredes, S. Villar-Rodil, P. Solís-Fernández, A. Martínez-Alonso, J.M.D. Tascón, Langmuir 25 (2009) 5957–5968.
[6] T. Szabo, O. Berkesi, P. Forgo, K. Josepovits, Y. Sanakis, D. Petridis, I. Dekany, Chem. Mater. 18 (2006) 2740–2749.
[7] I. Jung, D.A. Dikin, R.D. Piner, R.S. Ruoff, Nano Lett. 8 (2008) 4283–4287.
[8] M.J. Fernández-Merino, L. Guardia, J.I. Paredes, S. Villar-Rodil, P. Solís-Fernández, A. Martínez-Alonso, J.M.D. Tascón, J. Phys. Chem. C 114 (2010) 6426–6432.
[9] J.L. Figueiredo, M.F.R. Pereira, M.M.A. Freitas, J.J.M. Órfão, Carbon 37 (1999) 1379–1389.
[10] H. Nishihara, Q.-H. Yang, P.-X. Hou, M. Unno, S. Yamauchi, R. Saito, J.I. Paredes, A. Martínez-Alonso, J.M.D. Tascón, Y. Sato, M. Terauchi, T. Kyotani, Carbon 47 (2009) 1220–1230.
[11] D.-Q. Yang, E. Sacher, Langmuir 22 (2006) 860–862.
[12] S. Biniak, G. Szymanski, J. Siedlewski, A. Swiatkowski, Carbon 35 (1997) 1799–1810.
[13] W.S. Hummers, R.E. Offeman, J. Am. Chem. Soc. 80 (1958) 1339.
[14] A. Lerf, H. He, M. Forster, J. Klinowski, J. Phys. Chem. B 102 (1998) 4477–4482.
[15] W. Cai, R.D. Piner, F.J. Stadermann, S. Park, M.A. Shaibat, Y. Ishii, D. Yang, A. Velamakanni, S.J. An, M. Stoller, J. An, D. Chen, R.S. Ruoff, Science 321 (2008) 1815–1817.
[16] A. Ganguly, S. Sharma, P. Papakonstantinou, J. Hamilton, J. Phys. Chem. C 115 (2011) 17009–17019.
[17] D.T. Clark, B.J. Cromarty, A. Dilks, J. Polym. Sci. Polym. Chem. Ed. 16 (1978) 3173–3184.
[18] D. Rosenthal, M. Ruta, R. Schlögl, L. Kiwi-Minsker, Carbon 48 (2010) 1835–1843.
[19] X. Gao, J. Jang, S. Nagase, J. Phys. Chem. C 114 (2010) 832–842.

[20] I. Jung, D.A. Field, N.J. Clark, Y.W. Zhu, D.X. Yang, R.D. Piner, S. Stankovich, D.A. Dikin, H. Geisler, C.A. Ventrice, R.S. Ruoff, J. Phys. Chem. C 113 (2009) 18480–18486.
[21] U. Zielke, K.J. Huttinger, W.P. Hoffman, Carbon 34 (1996) 983–998.
[22] A. Bagri, C. Mattevi, M. Acik, Y.J. Chabal, M. Chhowalla, V.B. Shenoy, Nat. Chem. 2 (2010) 581–587.
[23] A.C. Ferrari, J. Robertson, Phys. Rev. B 61 (2000) 14095–14107.
[24] D.C. Kim, D.Y. Jeon, H.J. Chung, Y. Woo, J.K. Shin, S. Seo, Nanotechnology 20 (2009) 375703.
[25] P. Solís-Fernández, J.I. Paredes, S. Villar-Rodil, A. Martínez-Alonso, J.M.D. Tascón, Carbon 48 (2010) 2657–2660.
[26] K. Erickson, R. Erni, Z. Lee, N. Alem, W. Gannett, A. Zettl, Adv. Mater. 22 (2010) 4467–4472.

CARBON 50 (2012) 1014–1024

Available at www.sciencedirect.com

SciVerse ScienceDirect

journal homepage: www.elsevier.com/locate/carbon

UV light exposure of aqueous graphene oxide suspensions to promote their direct reduction, formation of graphene–metal nanoparticle hybrids and dye degradation

L. Guardia *, *S. Villar-Rodil, J.I. Paredes, R. Rozada, A. Martínez-Alonso, J.M.D. Tascón*

Instituto Nacional del Carbón, INCAR-CSIC, Apartado 73, 33080 Oviedo, Spain

ARTICLE INFO

Article history:
Received 25 May 2011
Accepted 4 October 2011
Available online 12 October 2011

ABSTRACT

The use of UV light to trigger different processes involving graphene oxide sheets suspended in aqueous medium at room temperature has been investigated. These processes include (1) deoxygenation of the sheets in the absence of photocatalysts, reducing agents and stabilizers, (2) selective nucleation and growth of metal nanoparticles on the sheets to yield graphene-based hybrids and (3) decomposition of the dye molecule rhodamine B in the presence of only graphene oxide. Photoinduced heating of the suspended graphene oxide sheets by intense UV irradiation (~1 W cm^{-2} delivered at the surface of the dispersion) was interpreted to generate at high temperature and reactive environment strictly localized at the sheets and their immediate aqueous medium, which in turn brings about the mentioned processes. In addition to providing a simple route toward reduction of graphene oxide dispersions, the present results suggest that intense UV light can be used to promote reactions at ambient conditions with this material that would otherwise require high temperatures, chemical reactants and/or catalysts.

1. Introduction

As a result of its first experimental isolation in 2004 and the subsequent discovery of its exceptional physical properties (electronic, mechanical, thermal and optical), graphene has rapidly become one of the most intensively investigated materials at present [1–4]. Research on graphene is currently focused both on fundamental science aspects and on the exploration of a large number of potential technological uses, for example in electronic devices [5], composite materials [6], sensors [7], energy generation and storage [8] or biomedicine [9]. Since the early days of the field, it has been recognized that one of the main obstacles to the realization of large-scale applications for graphene is the lack of simple and cost-effective methodologies toward the mass production of this material. For this reason, a significant amount of research effort has been, and still is, devoted to the development of different production methods, each of which possesses specific advantages and drawbacks, and is therefore best suited for certain uses [10]. Among these methods, the one based on reduction of exfoliated graphite oxide (graphene oxide) is particularly attractive and has received considerable attention as a result [11–13]. The main reason is that, even though the structural quality of this type of graphene is lower than that of graphenes produced by other methods (e.g. micromechanical exfoliation of pristine graphite or chemical vapor deposition) [4,10,14], the graphite oxide-based approach boasts several advantages that are important for many practical applications of this material: massive scalability, versatility for chemical functionalization, or easy processability of single-layer sheets in aqueous and organic media [10,12,14,15].

Reduction of graphene oxide in the liquid-phase is usually carried out with hydrazine as a reducing agent [12,15,16]. Nevertheless, environmental and safety concerns related to

* *Corresponding author:* Fax: +34 985 29 76 62.
E-mail address: lauraguardia@incar.csic.es (L. Guardia).
0008-6223/$ - see front matter
doi:10.1016/j.carbon.2011.10.005

the use of this chemical have driven a search for more sustainable reduction strategies. The proposed alternatives encompass solvothermal, electrochemical and biomolecular (e.g. vitamin C) deoxygenation of graphene oxide dispersions [17]. Other elegant methods suitable for liquid-phase production that have recently been explored include sonolytic reduction in aqueous solution of poly(ethylene glycol) [18], pulsed laser-assisted (photothermal) reduction [19,20] and photoreduction induced by UV light, which has been mostly accomplished using the mediating role of a photocatalyst (titania [21], zinc oxide [22,23] or polyoxometalates [24]) or with hydrogen as a reductant [25], usually resulting in a suspension of graphene–photocatalyst hybrid. However, the effect of UV illumination alone (i.e. in the absence of photocatalysts and reducing agents) is not well known and has just started to be explored [26]. UV light in the near and middle ranges is strongly absorbed by graphene oxide sheets [16,27]. Subsequent relaxation processes could trigger a local heating of the sheets and, by thermal energy transfer, of their surrounding liquid medium, thus favouring their deoxygenation and probably facilitating additional local reactions involving this type of graphene that could be exploited. To this end, further research along these lines would be required.

Here, we investigate the use of intense UV light as a simple means to trigger several processes involving graphene oxide sheets dispersed in aqueous medium at close to ambient temperature. These processes include, most notably, the photoreduction of the aqueous graphene oxide dispersions in the absence of photocatalysts, reducing agents and dispersants, but also the nucleation and growth of metal nanoparticles to yield graphene-based hybrids or the photodegradation of the dye molecule rhodamine B (RhB) in the presence of only graphene oxide. The present results indicate that a simple UV setup can be employed to promote room-temperature processes with graphene oxide that would normally require high temperatures, chemical reactants and/or photocatalysts.

2. Experimental

2.1. Preparation of aqueous graphene oxide dispersions

Graphite oxide was prepared by the Hummers method with $NaNO_3$, H_2SO_4 and $KMnO_4$ starting from natural graphite powder (Fluka 50870) [28]. The oxidized product was purified by first rinsing with 10% HCl solution and then copiously washing with deionized water. The resulting thick graphite oxide slurry was dispersed in water, sonicated in an ultrasound bath cleaner (J.P. Selecta Ultrasons apparatus) for 4 h, centrifuged (Eppendorf 5424 microcentrifuge) at 20,000*g* for 10 min, and the top ~75% of the supernatant volume, which was the as-prepared graphene oxide dispersion (pH ~ 5), collected for use in the subsequent experiments. The concentration of the suspension was determined by UV–vis absorption spectroscopy using a previously reported procedure [29].

2.2. UV-assisted photoreduction of graphene oxide dispersions

Photoreduction was carried out by exposing aqueous graphene oxide dispersions placed in a three-neck round-bottomed flask to a high intensity UV spot lamp (BlueWave 50 unit, from Dymax). The UV light was generated by a 50 W short arc mercury bulb, which irradiated in the 280–450 nm wavelength range with output intensities approximately distributed as follows: 15%, 40% and 45% for the 280–320, 320–390 and 390–450 nm wavelength ranges, respectively. The UV light was emitted from the tip of a lightguide 5 mm in diameter, which was positioned a given distance (typically 15 mm) from the surface of the graphene oxide dispersion while bubbling an argon flow (45 mL min^{-1}). The intensity delivered by the lamp at a given distance from the lightguide tip was measured with a hand-held sensor (model UVM-CP, from UV-Consulting Peschl). A thermometer was inserted through one of the necks of the flask to monitor the suspension temperature. The investigated irradiation times ranged from 5 min to 24 h.

2.3. Preparation of graphene–gold nanoparticle hybrids

Graphene–gold nanoparticle hybrids were prepared using the same setup as that employed for reduction of the graphene oxide dispersions. In a typical preparation, a given amount of $HAuCl_4$ (3 μmol) and 10 μL of 25% NH_3 solution were added to 10 mL of 0.1 mg mL^{-1} graphene oxide suspension and irradiated with the UV spot lamp for times usually ranging between 30 min and 6 h while bubbling the suspension with an argon flow (45 mL min^{-1}). The preparation could be carried out both without and with the addition of citric acid (30 μmol). Purification of the graphene–gold nanoparticle suspensions was carried out by repeated cycles (4–10) of sedimentation via centrifugation (20,000*g*, 30 min) and re-suspension of the sedimented material in deionized water.

2.4. Photodegradation of rhodamine B (RhB) in the presence of graphene oxide

UV-induced photodegradation of RhB in the presence of graphene oxide was investigated by irradiating aqueous solutions of the dye molecule (10 mL, 10^{-4} M) containing suspended graphene oxide sheets (0.4 mg mL^{-1}) with the spot lamp while stirring with a magnetic bar. For comparison purposes, irradiation of RhB solutions was also carried out in the presence of titania (anatase form, mean particle size ~21 nm, from Sigma–Aldrich) as a reference photocatalyst and surface-oxidized, water-dispersible non-porous carbon black particles (Spheron 6, from Cabot Corporation) as a model low surface area carbon material.

2.5. Surface enhanced Raman scattering (SERS) and catalytic activity of graphene–gold nanoparticle hybrids

The SERS performance of the graphene–gold nanoparticle hybrids was evaluated by recording Raman spectra for RhB, which is a well-known probe molecule for SERS [30]. The spectra were obtained with a Horiba Jobin-Yvon LabRam instrument at a laser excitation wavelength of 532 nm. An aqueous solution of the molecule (60 μL, 2×10^{-3} M) was cast either onto bare 5×5 mm^2 SiO_2/Si substrates or onto SiO_2/Si substrates covered with a film of graphene–gold nanoparticle hybrid pre-heated at 50–60 °C and allowed to dry.

The catalytic activity of the hybrids was probed by studying the reduction of *p*-nitroaniline (*p*-NA) to *p*-phenylenediamine (*p*-PDA) with $NaBH_4$ at room temperature by means of UV–vis absorption spectroscopy. In a typical reduction experiment, 0.3 mL of an as-prepared aqueous graphene–gold nanoparticle suspension was diluted with 2.4 mL of deionized water, and then 0.2 mL of 1.5×10^{-3} M *p*-NA and 0.1 mL of 0.3 M $NaBH_4$ were added. The progress of reaction was monitored by measuring the absorbance of the 380 nm peak characteristic of *p*-NA, which decreased steadily as reduction proceeded until it finally leveled off, marking the end of reaction.

2.6. *Characterization techniques*

UV–vis absorption spectra were recorded in a double-beam Helios α spectrophotometer (Thermo Spectronic). X-ray photoelectron spectroscopy (XPS) was accomplished with a SPECS apparatus working at a pressure of 10^{-7} Pa and using a monochromatic Al Kα X-ray source (100 W). Samples for XPS were prepared by casting the corresponding dispersion drop-wise onto a pre-heated (~50–60 °C) flat metallic disk (12 mm in diameter) until a uniform film was seen to cover the whole substrate. Attenuated total reflection Fourier transform infrared (ATR-FTIR) spectroscopy was carried out in a Nicolet 8700 spectrometer (Thermo Scientific) using a diamond crystal. Thermogravimetric analysis (TGA) was accomplished on Pt crucibles with an SDT Q600 thermobalance (TA Instruments) under argon gas flow (100 mL min^{-1}) at a heating rate of 10 °C min^{-1}. ATR-FTIR spectroscopy and TGA measurements of the unreduced and UV-reduced graphene oxide materials were carried out on free-standing paper-like films, which were prepared by filtering the corresponding aqueous suspensions through polycarbonate membranes (47 mm in diameter and 0.2 μm of pore size, from Whatman).

Atomic force and scanning tunneling microscopy (AFM/STM) imaging was carried out with a Nanoscope IIIa Multimode instrument (Veeco) under ambient conditions. AFM measurements were performed in the tapping mode of operation using rectangular silicon cantilevers. For STM, mechanically prepared Pt/Ir (80/20) tips were employed. To image individual sheets, a small volume of diluted dispersion (20 μL, 0.01–0.02 mg mL^{-1}) was dropped onto a preheated (~50–60 °C) highly oriented pyrolytic graphite (HOPG) substrate and allowed to dry. Field emission scanning electron microscopy (FE-SEM) images were recorded with a Quanta FEG 650 system (FEI Company) for samples deposited onto HOPG substrates following a similar procedure to that described in the case of AFM/STM. Transmission electron microscopy (TEM) imaging was performed on a JEOL 2000 EX-II instrument operated at 160 kV. A few microliters of aqueous sample suspension diluted with ethanol (50:50 vol/vol) were cast onto copper grids (200 mesh) covered with either a lacey or a continuous carbon film and allowed to dry.

3. Results and discussion

In a typical UV-assisted photoreduction experiment, an aqueous graphene oxide dispersion (10 mL, 0.1 mg mL^{-1}) was placed in a round-bottomed flask and irradiated with the high intensity UV spot lamp. An argon flow (45 mL min^{-1}) was bubbled through the suspension both for 10 min before and during the whole irradiation process with a twofold purpose: (1) to stir the suspension and ensure a uniform exposure of the graphene oxide sheets to the UV light spot, and (2) to deaerate the dispersion and avoid the possibility of sheet re-oxidation by dissolved oxygen molecules. The UV light was emitted through a lightguide 5 mm in diameter, which was positioned 15 mm above the surface of the dispersion, delivering a measured intensity of 1.0–1.2 W cm^{-2}. Upon irradiation with the spot lamp, the transparent yellow–brown color characteristic of the unreduced graphene oxide dispersion (inset to Fig 1a, left) changed progressively to dark brown and finally turned black and opaque, suggesting that sheet deoxygenation was effectively taking place. These changes came about in a timeframe of a few tens of minutes to a few hours and were monitored with UV–vis absorption spectroscopy, in particular by measuring the position of the absorption peak. The absorption peak for unreduced graphene oxide is located at ~231 nm and can be ascribed to $\pi \rightarrow \pi^*$ transitions in small electronically conjugated domains present on this material [16,27,31]. It is well-known that, as reduction proceeds and the size of the electronically conjugated domains increases, the absorption peak position gradually red-shifts, which can thus be considered, to a first approximation, as an indicator of the reduction degree attained [16,31,32].

Fig. 1a (green squares) shows the evolution of the absorption peak position with irradiation time for as-prepared (pH ~ 5) graphene oxide dispersions, which is seen to reach a plateau value of ~264 nm after about 15 h of UV light exposure. Even though these irradiated suspensions did not precipitate, they were not totally homogeneous and stable either, and some aggregates visible to the naked eye formed after about 3 h of UV treatment. This behavior can be put down to the fact that, in the absence of an added dispersant, the colloidal stability of reduced graphene oxide sheets in water relies on electrostatic repulsions afforded by deprotonated residual oxygen groups (e.g. carboxylates), and such

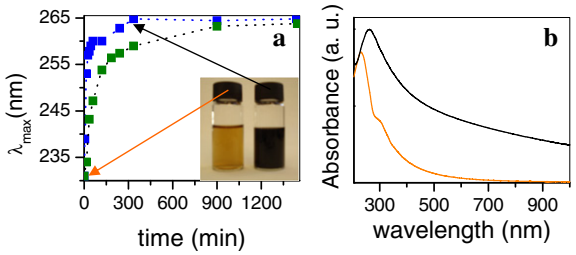

Fig. 1 – (a) UV–vis absorption peak position for as-prepared (pH 5, green squares) and basified (pH 11, blue squares) 0.1 mg mL^{-1} aqueous graphene oxide dispersions irradiated with UV light for different times. Inset: digital pictures of starting dispersion (left) and dispersion at pH 11 irradiated for 5.5 h (right). (b) UV–vis spectra of as-prepared (orange) and UV-irradiated (5.5 h, black) graphene oxide dispersions (pH 11). (For interpretation of the references to color in this figure legend, the reader is referred to the web version of this article.)

stability decreases under neutral and acidic conditions [16]. Therefore, in a second set of experiments (Fig. 1a, blue squares) the dispersions were irradiated after raising their pH to 10–11 with NH_3 or KOH. In this case, the plateau (also 264 nm) was reached after ~5 h of UV treatment. This absorption peak position lies within the range of values previously documented for graphene oxide suspensions deoxygenated with a number of reductants (e.g. hydrazine, $NaBH_4$, pyrogallol, vitamin C or glucose [16,32–34]), implying that a reasonably efficient reduction was attained. Such reduced suspensions (inset to Fig. 1a, right) were homogeneous and displayed long-term stability (several months). Hence, optimized parameters for reduction were chosen to be 5.5 h of irradiation time and pH 10–11, although irradiation for, e.g. 1 h already afforded a significant degree of reduction (absorption peak at ~260 nm, Fig. 1a). Fig. 1b shows the UV–vis absorption spectra for dispersions before (orange plot) and after (black plot) the optimized reduction. In addition to a red-shifted absorption peak, the latter exhibits increased absorbance in the wavelength range above 264 nm, indicative of well-reduced dispersions. Likewise, the spectrum of the unreduced dispersion exhibits a shoulder at ~300 nm that disappears after reduction. This shoulder has been attributed to $n \rightarrow \pi^*$ transitions in C=O bonds [27,31]. In principle, one could argue that the removal of oxygen functionalities that takes place during reduction can be responsible for the disappearance of the shoulder. However, this explanation is probably not correct, because spectroscopic data (e.g. XPS; see below) suggest that C=O groups are not significantly removed during reduction, and thus the absorption component at 300 nm should still be present after reduction. We believe the main reasons for the disappearance of the shoulder to be (1) the red-shift of the absorption peak from 231 to 265 nm and (2) the increase of absorbance in the whole wavelength range due to restoration of electronic conjugation, which contribute to make the shoulder less prominent up to a point where it is no longer visible. We also notice from Fig. 1a that reduction appears to be faster under basic conditions, particularly for short irradiation times. This observation is consistent with previous reports which indicated that alkaline media favor the deoxygenation of graphene oxide [35], although the underlying mechanism is currently not understood.

Reduction of the graphene oxide dispersions by UV light was corroborated using TGA, ATR-FTIR spectroscopy and XPS. TGA revealed that the mass loss step in the 180–250 °C range characteristic of unreduced graphene oxide (~30% weight loss, Fig. 2a, orange plot) disappeared following irradiation with the UV spot lamp (Fig. 2a, black plot), which suggests that the labile oxygen functionalities originally present in the former were eliminated [32,36]. The ATR-FTIR spectrum of the starting graphene oxide material (Fig. 2b, orange) revealed a number of bands ascribed to vibrations of oxygen-containing groups, located at 3000–3500 cm^{-1} (O–H stretching), 1720 cm^{-1} (C=O stretching), 1300–1350 cm^{-1} (C–OH stretching), 1220 cm^{-1} (breathing vibration from epoxy groups) and 990 cm^{-1} (attributed to epoxy, ether or peroxide groups) [32]. The intensity of these bands was seen to drop for UV-irradiated graphene oxide dispersions (Fig. 2b, black), implying a reduction in the amount of oxygen functionalities.

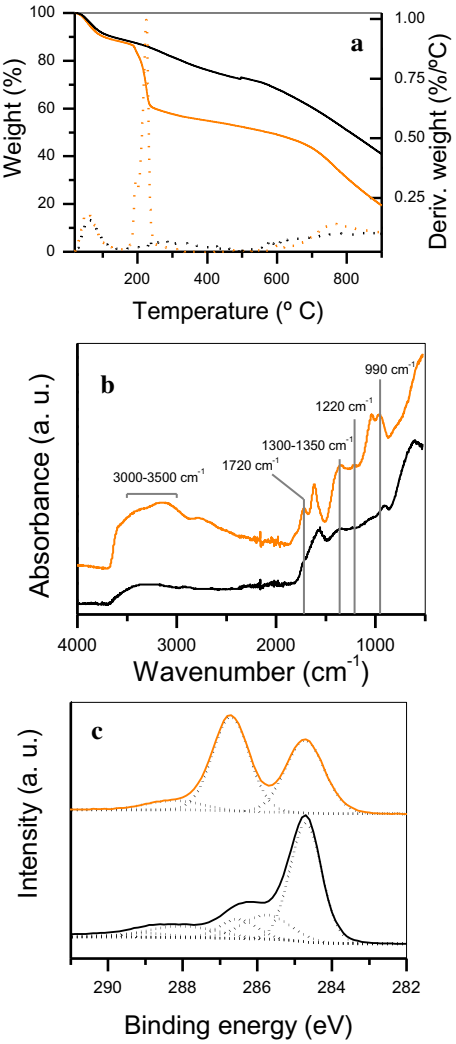

Fig. 2 – Characterization of the starting graphene oxide (orange) and the material irradiated with UV light for 5.5 h (black): thermogravimetric (solid lines)/differential thermogravimetric (dotted lines) plots in inert atmosphere (a), ATR-FTIR spectra (b) and peak-fitted high resolution C1s XPS spectra (c). (For interpretation of the references to color in this figure legend, the reader is referred to the web version of this article.)

XPS data shown in Fig. 2c indicate that the high resolution C 1s band of unreduced graphene oxide (orange plot) has two main components, located at ~284.6 and 286.5 eV and attributed to carbon atoms in graphitic, unoxidized structures and carbon atoms singly bonded to oxygen in hydroxyl/epoxy groups, respectively, together with a minor contribution of carbonyl groups at ~288.0 eV [32]. Upon UV irradiation (Fig. 2c, black plot), the C1s spectrum requires two additional components for appropriate fitting: a peak at ~285.7 eV corresponds to defective C–C (localized aromatic sp^2 structures) and a $\pi \rightarrow \pi$ shake-up band at ~291 eV, ascribed to partial restoration of the aromaticity of the graphene sheets [37]. The carbon component at 284.6 eV becomes narrower because of the more homogeneous chemical environment. Globally, the ratio of oxidized to unoxidized carbon

diminishes significantly, which is indicative of a successful reduction. Particularly, the most apparent diminution involves carbon atoms singly bonded to oxygen, the contribution of carbonyl groups remaining basically unchanged. The C/O atomic ratio derived from the XPS survey spectra was measured to be 2.3 for the unreduced graphene oxide sample and 4.5 for its UV-reduced counterpart, which is similar to the results previously obtained with such reducing agents as $NaBH_4$ and pyrogallol [32,38], and is therefore also consistent with the UV–vis spectroscopic data discussed above. Thus, taken together, the thermogravimetric and spectroscopic results provide clear evidence of a significant deoxygenation of the graphene oxide sheets in the aqueous dispersion by UV irradiation.

In addition, AFM confirmed that the single-layer nature of the dispersed (pH ~ 10–11) graphene oxide material was preserved after UV-induced reduction. Fig. 3a shows a representative AFM image of unreduced graphene oxide sheets deposited onto an HOPG substrate. Their lateral size typically ranges from a few to several hundred nanometers, while their apparent thickness (measured as their height relative to the supporting substrate) is about 1 nm, consistent with the sheets being single-layer objects [39]. The UV-reduced graphene oxide sheets also exhibit an apparent thickness of ~1 nm (Fig. 3b), which again indicates that they are single graphene layers [39] and that the suspensions do not agglomerate after UV-induced photoreduction. As seen in more detail by STM (Fig. 3b, inset), the reduced sheets display a rough morphology similar to that reported for hydrazine-reduced graphene oxide [29], which can be attributed to distortions in their carbon skeleton brought about by structural defects and residual oxygen groups.

Previous UV-based approaches for the reduction of graphene oxide suspensions have mostly relied on the use of a photocatalyst (titania, zinc oxide or polyoxometalates) to transfer electrons from a sacrificial agent (e.g. ethanol) to the graphene oxide sheets, thus triggering their reduction [21–24]. Since none of these components were present in our case and a reducing agent was neither employed, a substantially different process must be responsible for the observed deoxygenation of the sheets. Similar to the pulsed laser-induced reduction of graphene oxide reported very recently [19,20], such a process is thought to be of photothermal origin. UV light in the wavelength range emitted by the spot lamp (280–450 nm) is significantly absorbed by graphene oxide (Fig. 1b). The photoexcited electrons that are subsequently generated would relax by transferring energy to the graphene oxide lattice (e.g. via excitation of atomic vibrations), which would thus be locally heated. Local heating would in turn promote sheet deoxygenation through thermal desorption of oxygen groups. In this regard, thermal reduction of graphene oxide suspensions in some organic solvents has been previously reported [40,41]. However, in the present case purely thermal effects are probably not the only source of sheet deoxygenation. Thermal energy transfer from the heated sheets can be expected to locally raise the temperature of the aqueous medium immediately surrounding them. Under such high temperature conditions, the physicochemical properties of water change (e.g. higher dissociation constant), providing a more chemically reactive environment that favors deoxygenation reactions in graphene oxide (for instance, dehydration reactions) [42]. The fact that the reduction rate was dependent on the dispersion pH (Fig. 1a), which is expected to further modulate the chemical reactivity of the aqueous medium, supports the idea that chemical effects, and not just purely thermal ones, are also relevant in our case.

Indication that the graphene oxide sheets were actually heated in our UV setup was obtained from the observation of a temperature rise in the dispersions upon irradiation. Fig. 4 (black squares) shows the temperature of the aqueous graphene oxide dispersion (pH 11) as a function of exposure time to the UV spot lamp. The temperature reached 35 °C following 1 h of UV irradiation and remained constant thereafter. For comparison, a control experiment was carried out in which water (pH 11) without suspended graphene oxide sheets was also subjected to UV irradiation (Fig. 4, blue squares). In this case, the temperature stabilized at ~26 °C.

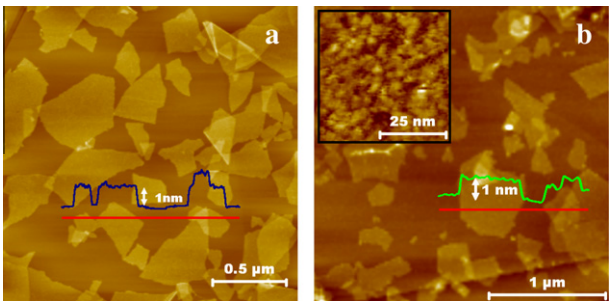

Fig. 3 – AFM images of unreduced (a) and photoreduced (b) graphene oxide sheets cast onto HOPG. In each case, a line profile taken along the red line is shown superimposed on the image. Inset to (b): STM image exhibiting the rough morphology of an individual sheet on the nanometer scale. (For interpretation of the references to color in this figure legend, the reader is referred to the web version of this article.)

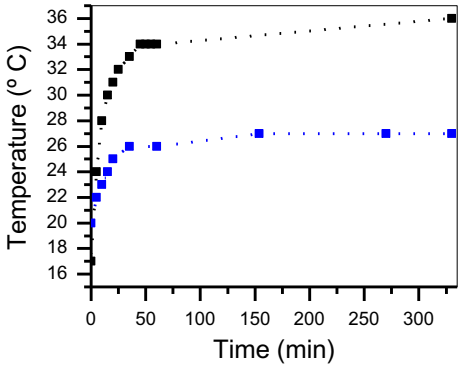

Fig. 4 – Evolution of the temperature of graphene oxide suspension in water (black squares) and of water in the absence of suspended graphene oxide sheets (control experiment, blue squares) as a function of irradiation time with the UV spot lamp. In both cases, the pH was adjusted to 11 with KOH at a concentration of 4 mM. (For interpretation of the references to color in this figure legend, the reader is referred to the web version of this article.)

Such results suggest that there is a transfer of thermal energy from the irradiated graphene oxide sheets to the aqueous medium, which in turn is consistent with the idea that the sheets are heated by the UV light. We also note that high intensity irradiation (in terms of power delivered per unit area at the surface of the dispersion) appears to be a key element in the successful deoxygenation of the suspended graphene oxide sheets. The experiments reported above were typically carried out with the UV lightguide tip positioned 15 mm above the surface of the dispersion, which received an intensity of 1.0–1.2 W cm^{-2}. Such intensity is at least one order of magnitude larger than that employed in the photocatalytic reduction experiments of graphene oxide documented in the literature [23]. In our case, when the intensity delivered to the surface of the dispersion was decreased one or two orders of magnitude by moving the lightguide tip farther away, deoxygenation of the graphene oxide sheets was seen to take place at a much slower rate, suggesting that the energy transferred to individual sheets is not enough for photothermal effects to activate their deoxygenation.

The generation of hot and reactive spots localized at the graphene oxide sheets and their close vicinity in the aqueous phase can be exploited to promote, using UV light, chemical reactions and processes with this material in addition to its reduction. One example is the preparation of graphene–metal nanoparticle hybrids. There is currently significant interest in such hybrids for their potential use in, e.g. catalysis or energy applications [43]. Although the aqueous synthesis of these hybrids was originally based on chemical reduction of both graphene oxide and a metal salt precursor with a suitable reductant (for example, $NaBH_4$), more recent work has harnessed the high temperature/reactive environment generated, e.g. by sonolysis in the presence of poly(ethylene glycol) [18] or by microwaves [44]. The use of UV illumination would be in line with the latter approaches. However, a specific feature of the UV method is that the reactive spots are not created at random locations in the aqueous medium, but selectively at and closely around the graphene oxide sheets. We produced graphene–gold nanoparticle hybrids under exactly the same conditions as those described above for reduction of graphene oxide dispersions, the only difference being that a gold precursor ($HAuCl_4$) was added to the suspension prior to irradiation. The use of, e.g. citrate anion, which is commonly employed as a reducing/stabilizing agent in the preparation of gold nanoparticles, was not required, and its introduction only led to small differences in the size of the resulting nanoparticles (see below). In both cases, deoxygenation of the graphene oxide sheets and generation of gold nanoparticles through reduction of the $AuCl_4^-$ anion were triggered through exposure to the UV light and took place simultaneously, yielding a suspension of gold nanoparticle-decorated graphene sheets. UV–vis absorption spectra of such irradiated suspensions displayed a peak at ~524 nm (Fig. 5a), which can be ascribed to the surface plasmon resonance band characteristic of gold nanostructures [45] [see also pictures of dispersions irradiated in the presence (absence) of $HAuCl_4$, inset to Fig. 5a, right (left)]. XPS measurements revealed two peaks at 84.1 and 87.8 eV (Fig. 5b) attributed to photoelectrons ejected from the $4f_{7/2}$ and $4f_{5/2}$ levels of Au(0), respectively, thus denoting the presence of metallic gold in the sample

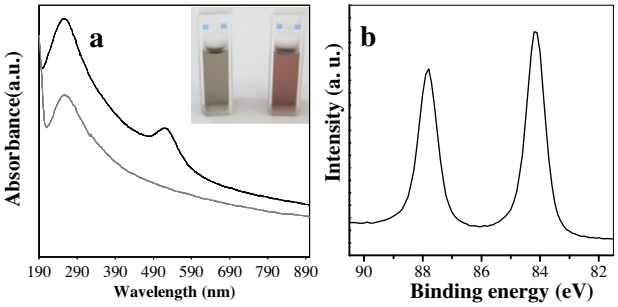

Fig. 5 – (a) UV–vis absorption spectra and digital pictures (inset) of aqueous graphene oxide dispersions (~0.01 mg mL^{-1}) irradiated with UV light in the absence (gray curve and inset left) and presence (black curve and inset right) of $HAuCl_4$. (b) Au 4f XPS spectrum of graphene–gold nanoparticle hybrid.

[46]. Peaks related to oxidized gold species (for instance, at ~91 eV) were not detected by this technique.

Microscopic characterization indicated that gold was present in the form of nanoparticles associated to the graphene sheets. Fig. 6a and b shows representative AFM images for graphene–gold nanoparticle hybrids prepared by UV irradiation of aqueous graphene oxide/$HAuCl_4$ dispersions in the absence (a) and presence (b) of citrate. The white dots seen in these images (i.e. the nanoparticles) were never observed for dispersions irradiated in the absence of $HAuCl_4$ (Fig. 3b). Particle size was estimated from the AFM images by measuring their height relative to the graphene sheet. The results (inset to Fig. 6a and b) indicate that slightly smaller and more uniform nanoparticles (14.6 ± 2.9 vs. 19.7 ± 5.2 nm in diameter) are obtained when the UV-induced growth is carried out in the absence of citrate. Images recorded by means of FE-SEM (Fig. 6c and d for samples without and with citrate, respectively) and TEM [Fig. 6e (without citrate) and f (with citrate)] support this finding and reveal a more or less even distribution of the gold nanoparticles on the graphene sheets. Energy-dispersive X-ray spectroscopy (inset to Fig. 6d) confirms the presence of gold in those samples bearing nanoparticles. Detailed TEM images (inset to Fig. 6e and f) indicate that the nanoparticles are approximately rounded in shape, though some of them exhibit a faceted structure. The nanoparticles were seen to be exclusively associated to the graphene sheets. For example, we never observed stand-alone nanoparticles, or collections of them, directly on the basal plane or at the step edges of HOPG by AFM or FE-SEM. The density of nanoparticles on the graphene sheets was estimated to be ~10–15 μm^{-2} in both cases by inspection of individual, single-layer sheets with AFM, which were identified through their well-documented apparent thickness of ~1 nm. The determination of layer number by FE-SEM and TEM is less straightforward, and thus such techniques are not so convenient for this purpose.

Control experiments indicated that gold nanostructures were formed neither by UV irradiation of aqueous $HAuCl_4$ solutions in the absence of graphene oxide nor by simply

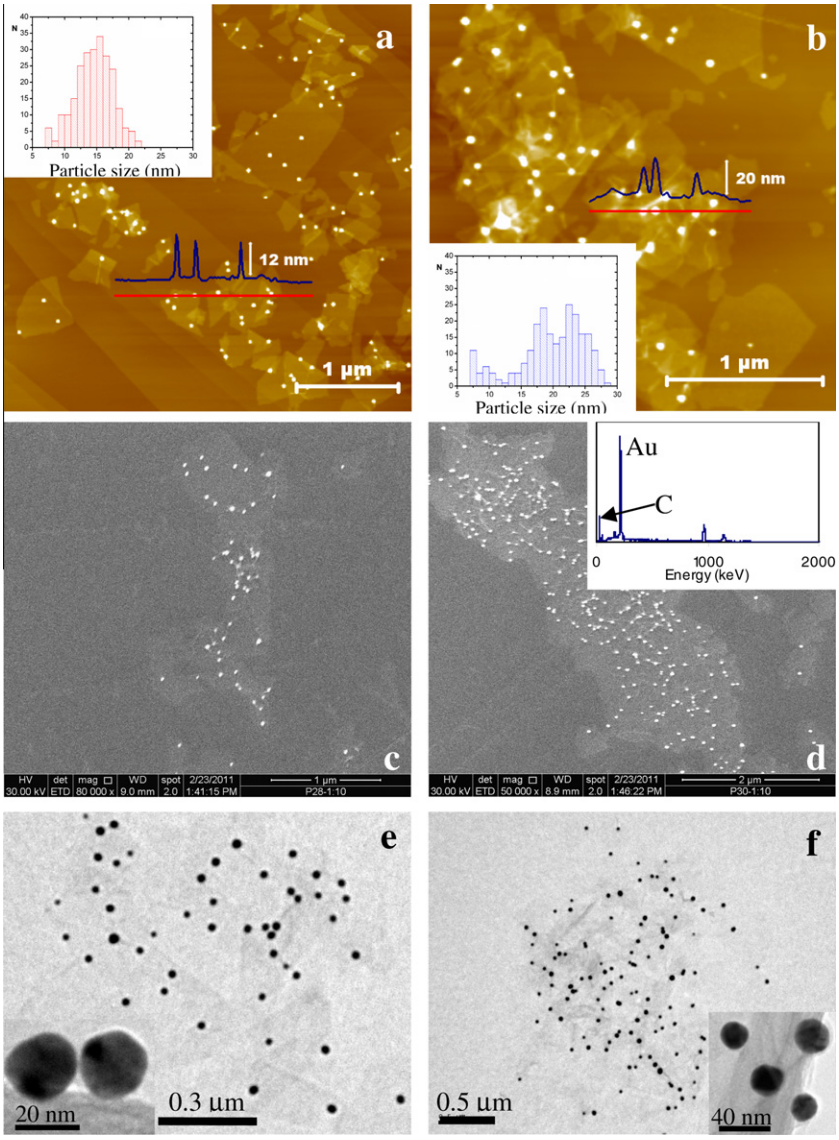

Fig. 6 – (a–d) AFM (a and b) and FE-SEM (c and d) images of graphene–gold nanoparticle hybrids prepared by UV irradiation of graphene oxide/$HAuCl_4$ dispersions in the absence (a and c) and presence (b and d) of citrate and deposited onto HOPG. Representative line profiles taken along the marked red lines are superimposed on the AFM images in a and b. Inset to a and b: particle size distributions determined from the height of the particles in the AFM images. Inset to d: energy-dispersive X-ray spectrum of the hybrid sample synthesised in the presence of citrate. (e and f) TEM images of hybrids prepared in the absence (e) and presence (f) of citrate. Inset to e and f: detailed images of individual gold nanoparticles. (For interpretation of the references to color in this figure legend, the reader is referred to the web version of this article.)

heating graphene oxide/$HAuCl_4$ dispersions (without citrate) at 80 °C under stirring. Such results support the idea that the growth of the nanoparticles is intimately related to the presence of an UV-induced, high temperature/high reactivity environment localized at the graphene oxide sheets, as previously discussed. Furthermore, on the basis of the known concentration of graphene oxide used to prepare the graphene–gold nanoparticle suspensions (0.1 mg mL^{-1}) and the estimated density of nanoparticles on the graphene sheets (~10–15 μm^{-2}), the concentration of nanoparticles in the as-prepared suspension was assessed to be ~10^{12} mL^{-1}. From such estimate and the average diameter of the gold nanoparticles (~15–20 nm), and assuming their mass density to be the same as that of bulk gold (19.3 g cm^{-3}), we conclude that the amount of gold in the nanoparticles is commensurate with that of the Au^{3+} ions added as $HAuCl_4$ in the preparation of the hybrid materials. This result suggests that at least the large majority of the gold precursor is converted to metallic gold nanoparticles in the UV-based synthesis approach. We also note that graphene–silver nanoparticle hybrids could be similarly prepared using $AgNO_3$ as a precursor.

An additional process made possible by the present UV approach is the degradation of dyes such as RhB. Photodegradation of dyes and other pollutants present in water is typically accomplished by means of UV-activated photocatalysts, most notably titania [47–49]. We show that RhB can be degraded

with a combination of intense UV light and graphene oxide sheets in the absence of a photocatalyst. Fig. 7 plots the relative changes in concentration of aqueous RhB solutions (10^{-4} M) as a function of irradiation time with the UV spot lamp in the absence and presence of an additional component (0.4 mg mL^{-1} of titania, graphene oxide or carbon black particles). The concentration was monitored by UV–vis absorption spectroscopy through changes in the absorption peak at 554 nm characteristic of this molecule. Irradiation of a solution containing only RhB (Fig. 7, green triangles) did not have a significant effect on its concentration over the course of a few hours. On the other hand, photodegradation of the dye was prompted by the addition of titania as anticipated (pink squares), but remarkably, it could also be achieved in the presence of graphene oxide sheets (as-prepared dispersion, pH ~5) without photocatalyst at a rate comparable to that attained with titania (blue diamonds). Similar to the processes discussed above, the degradation of the dye observed in the presence of graphene oxide is ascribed to the locally high temperature/reactivity conditions triggered at the graphene oxide sheets by UV illumination. RhB molecules are expected to readily adsorb onto the graphene oxide sheets by way of (1) electrostatic attraction between negatively charged groups present in the latter (e.g. carboxylates) [16] and the positively charged ammonium ion in the dye molecule, and (2) π–π interaction between the aromatic rings in the dye and small unoxidized, electronically conjugated domains that are known to remain on graphene oxide [50]. Such strong adsorption should facilitate an efficient exposure of the dye molecule to the locally hot and reactive medium at and around the graphene oxide sheets, thus promoting its decomposition. Significantly, RhB degradation was not observed in the presence of graphene oxide under basic conditions (pH ~ 10). In this case, the carboxylic acid group of RhB should be mostly deprotonated, so the resulting negatively charged carboxylate will probably hinder adsorption of the dye molecule to the (negatively charged) graphene oxide sheets [51], making its decomposition much more difficult. We note from

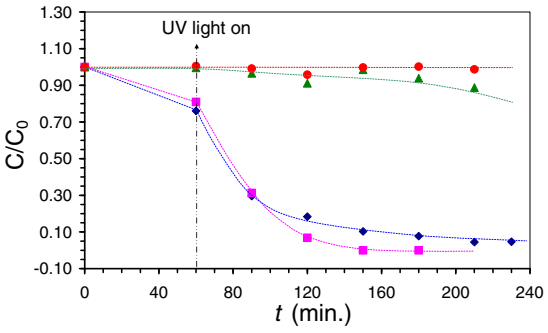

Fig. 7 – Evolution of the concentration (C) of RhB relative to its initial value (C_0) as a function of UV irradiation time in aqueous solution containing only the dye (green triangles), and in the presence of anatase titania (pink squares), grahene oxide (blue diamonds) and carbon black particles (red circles). The "UV light on" label indicates the time at which the UV lamp was switched on. (For interpretation of the references to color in this figure legend, the reader is referred to the web version of this article.)

Fig. 7 that after RhB is mixed with the aqueous graphene oxide dispersion and before the UV light is turned on (at t = 60 min), there is a small decrease in the RhB concentration, which is also observed for the case of titania. We believe that such a decrease is due to adsorption of RhB to the sheets. However, we have checked that if the UV light is not turned on at t = 60 min and the RhB/graphene oxide mixture is kept stirring for many hours, there is no further decrease in the concentration of the dye molecule, implying that there is no additional adsorption. It could still be argued that the amount of RhB adsorbed on the graphene oxide sheets could change (increase) upon their exposure to the UV light, because the sheets are being reduced and thus their surface characteristics are changing. Nevertheless, the adsorbed amount tends to decrease, not increase, for the reduced sheets due to weakened electrostatic attraction between the dye and the sheets with fewer ionizable oxygen groups (compared to the unreduced sheets). Consequently, the concentration decline observed when the UV light is turned on (from t = 60 min onwards) cannot be simply due to adsorption and should be attributed to the dye degradation. We should also stress that, contrary to the case of titania, the UV-induced photodegradation of RhB in the presence of graphene oxide is believed to be based on thermal (not photocatalytic) processes, even though the exact mechanism is not known at present. Elucidating this point will require more in-depth studies in the future.

As irradiation of the RhB/graphene oxide mixture proceeds and the sheets become progressively reduced, the adsorption of RhB molecules on the sheets should decrease, mainly due to the smaller number of negative charges present on the sheets and therefore to the weakened electrostatic attraction to the dye molecule. Therefore, the degradation rate of RhB should be expected to decrease with UV irradiation time, and this is what is actually seen in Fig. 7. Furthermore, once the graphene oxide sheets reach a certain level of reduction and the adsorption of RhB becomes sufficiently weakened, the degradation of the dye becomes arrested. In fact, we see from Fig. 7 that a small percentage of RhB remains indefinitely at long irradiation times (i.e. for t > 200 min). Thus, if the initial RhB/graphene oxide ratio is increased, then the amount of dye molecules that were not yet degraded by the time the sheets become sufficiently reduced and adsorption becomes arrested should increase, and this is what we have observed in additional experiments.

Photothermal degradation of RhB could in principle be also possible with other sp^2-based carbon materials, since the absorption of UV photons in the 280–450 nm wavelength range only requires the presence of C=C bonds in electronically conjugated structures [31]. However, the degradation rate is expected to be greatly modulated, among other possible factors, by the available surface area of the material, carbon materials with lower surface area affording slower degradation rates. This is exemplified in Fig. 7 (red circles) for the case of non-porous carbon black particles (<100 nm in diameter, surface area of ~100 $m^2\,g^{-1}$) that were made water-dispersible (pH ~ 5) through surface oxidation with oxygen plasma [52]. No significant degradation of RhB is observed in the presence of such a carbon material. In this regard, the large surface area of graphene oxide sheets individually suspended in solution, which should be comparable

to that of pristine graphene (~2600 $m^2 g^{-1}$), constitutes a significant advantage.

Finally, we tested the performance of the graphene–gold nanoparticle hybrids as substrates for SERS and as catalysts, which are two potential applications of gold nanostructures [53,54]. Fig. 8a shows Raman spectra of RhB, which is also a common probe molecule for SERS, deposited on a bare SiO_2/Si substrate (green) and on the same substrate covered with only gold nanoparticles (red) or with graphene–gold nanoparticle hybrid (blue). The two latter spectra exhibit a strong enhancement of vibrational bands at 1195, 1283, 1362, 1509, 1564 and 1649 cm^{-1} characteristic of this molecule [30], but the enhancement effect appears to be somewhat larger for the hybrid material. We attribute this observation to the recently reported fact that graphene itself displays also a SERS effect [55], so the combination of the two materials (graphene and gold nanoparticles) could be advantageous in this regard. The catalytic activity of the hybrids was studied for reduction of *p*-NA to *p*-PDA with $NaBH_4$ at room temperature. By monitoring the reaction progress with UV–vis absorption spectroscopy, in particular through changes in the peak at 380 nm characteristic of *p*-NA, we determined that reduction was completed in ~1.7 min for an initial reactant concentration of 10^{-4} (*p*-NA) and 10^{-2} ($NaBH_4$) M, and an estimated gold nanoparticle concentration of ~10^{11} mL^{-1} (Fig. 8b). Control experiments revealed that, under the investigated conditions, $NaBH_4$ did not react with the UV-reduced graphene oxide sheets and just very slowly with the unreduced ones (in fact, reduction of graphene oxide with $NaBH_4$ is usually carried out at 80–95 °C [32]). Similarly, we found no evidence of reaction between *p*-NA and the UV-reduced sheets, as judged from the absorption spectra. Such observations indicate that the graphene sheets in the hybrid material essentially play a role as a catalyst (or catalyst support) but not as a reactant. The reaction time obtained here (1.7 min) can be compared with a value of about 30 min previously reported for the same reaction with the same initial reactant concentration using stand-alone, polyelectrolyte-encapsulated gold nanoparticles of similar size (~14 nm) and concentration to those used here [56], suggesting that the hybrid system prepared by the UV method possesses a high catalytic activity.

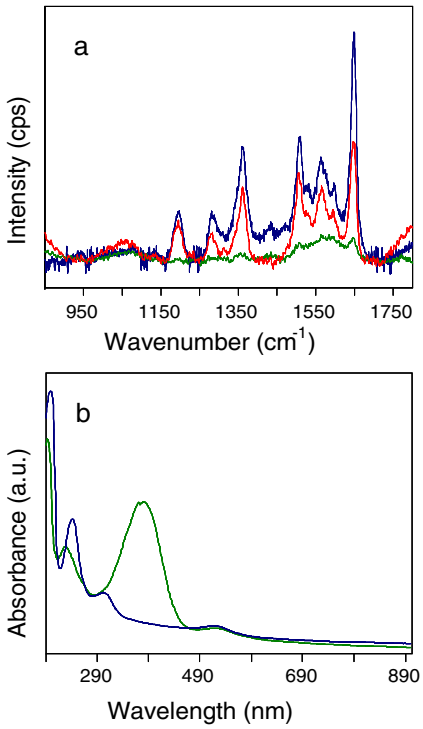

Fig. 8 – (a) Raman spectra of RhB deposited on SiO_2/Si (green) and SiO_2/Si covered with only gold nanoparticles (red) or with graphene–gold nanoparticle hybrid (blue). (b) UV–vis absorption spectra for the reduction of *p*-NA (10^{-4} M) with $NaBH_4$ (10^{-2} M) at room temperature in an aqueous graphene–gold nanoparticle dispersion (nanoparticle concentration ~10^{11} mL^{-1}) just before (green) and after (1.7 min, blue) reduction. After reduction, the 380 nm peak characteristic of *p*-NA is no longer present and bands at 240 and 305 nm, indicative of *p*-PDA, develop instead. (For interpretation of the references to color in this figure legend, the reader is referred to the web version of this article.)

4. Conclusions

Intense UV light has been used to prompt a number of different processes localized at or closely around graphene oxide sheets dispersed in aqueous medium at ambient temperature. These processes include deoxygenation of the graphene oxide sheets without the requirement of photocatalysts, reducing agents or stabilizers, selective nucleation and growth of metal nanoparticles on the sheets and degradation of a dye molecule (rhodamine B) in the presence of only graphene oxide. The use of intense UV light (~1 W cm^{-2} delivered at the surface of the dispersion) was essential for the successful realization of such processes, which are thought to be triggered by photoinduced heating of the graphene oxide sheets, creating a high temperature and reactive environment localized at the sheets and their immediate aqueous medium. The hybrid materials exhibited good SERS and catalytic performance.

Acknowledgements

Financial support from the Spanish MICINN (projects MAT2008-05700 and MAT2011-26399) is gratefully acknowledged. L.G. thanks the receipt of a post-doctoral contract (JAE-Doc) from CSIC. R.R. acknowledges MICINN for the receipt of a pre-doctoral contract (FPU).

REFERENCES

[1] Novoselov KS, Geim AK, Morozov SV, Jiang D, Zhang Y, Dubonos SV, et al. Electric field effect in atomically thin carbon films. Science 2004;306:666–9.
[2] Geim AK, Novoselov KS. The rise of graphene. Nat Mater 2007;6:183–91.
[3] Rao CNR, Sood AK, Subrahmanyam KS, Govindaraj A. Graphene: the new two-dimensional nanomaterial. Angew Chem Int Ed 2009;48:7752–77.
[4] Allen MJ, Tung VC, Kaner RB. Honeycomb carbon: a review of graphene. Chem Rev 2010;110:132–45.

[5] Schwierz F. Graphene transistors. Nat Nanotechnol 2010;5:487–96.
[6] Kim H, Abdala AA, Macosko CW. Graphene/polymer nanocomposites. Macromolecules 2010;43:6515–30.
[7] Yang W, Ratinac KR, Ringer SP, Thordarson P, Gooding JJ, Braet F. Carbon nanomaterials in biosensors: should you use nanotubes or graphene? Angew Chem Int Ed 2010;49:2114–38.
[8] Sun Y, Wu Q, Shi G. Graphene based new energy materials. Energy Environ Sci 2011;4:1113–32.
[9] Feng LZ, Liu ZA. Graphene in biomedicine: opportunities and challenges. Nanomedicine 2011;6:317–24.
[10] Dreyer DR, Ruoff RS, Bielawski CW. From conception to realization: a historical account of graphene and some perspectives for its future. Angew Chem Int Ed 2010;49:9336–44.
[11] Park S, Ruoff RS. Chemical methods for the production of graphenes. Nat Nanotechnol 2009;4:217–24.
[12] Compton OC, Nguyen ST. Graphene oxide, highly reduced graphene oxide, and graphene: versatile building blocks for carbon-based materials. Small 2010;6:711–23.
[13] Pei S, Zhao J, Du J, Ren W-C, Cheng H-M. Direct reduction of graphene oxide films into highly conductive and flexible graphene films by hydrohalic acids. Carbon 2010;48:4466–74.
[14] Eda G, Chowalla M. Chemically derived graphene oxide: towards large-area thin-film electronics and optoelectronics. Adv Mater 2010;22:2392–415.
[15] Dreyer DR, Park S, Bielawski CW, Ruoff RS. The chemistry of graphene oxide. Chem Soc Rev 2010;39:228–40.
[16] Li D, Müller MB, Gilje S, Kaner RB, Wallace GG. Processable aqueous dispersions of graphene nanosheets. Nat Nanotechnol 2008;3:101–5.
[17] Paredes JI, Villar-Rodil S, Fernández-Merino MJ, Guardia L, Martínez-Alonso A, Tascón JMD. Environmentally friendly approaches toward the mass production of processable graphene from graphite oxide. J Mater Chem 2011;21:298–306.
[18] Vinodgopal K, Neppolian B, Lightcap IV, Grieser F, Ashokkumar M, Kamat PV. Sonolytic design of graphene–au nanocomposites. Simultaneous and sequential reduction of graphene oxide and Au(III). J Phys Chem Lett 2010;1:1987–93.
[19] Abdelsayed V, Moussa S, Hassan HM, Aluri HS, Collinson MM, El-Shall MS. Photothermal deoxygenation of graphite oxide with laser excitation in solution and graphene-aided increase in water temperature. J Phys Chem Lett 2010;1:2804–9.
[20] Huang L, Liu Y, Ji L-C, Xie Y-Q, Wang T, Shi W-Z. Pulsed laser assisted reduction of graphene oxide. Carbon 2011;49:2431–6.
[21] Williams G, Seger B, Kamat PV. TiO_2–graphene nanocomposites. UV-assisted photocatalytic reduction of graphene oxide. ACS Nano 2008;2:1487–91.
[22] Williams G, Kamat PV. Graphene-semiconductor nanocomposites: excited-state interactions between ZnO nanoparticles and graphene oxide. Langmuir 2009;25:13869–73.
[23] Akhavan O. Photocatalytic reduction of graphene oxides hybridized by ZnO nanoparticles in ethanol. Carbon 2011;49:11–8.
[24] Li H, Pang S, Feng X, Müllen K, Bubeck C. Polyoxometalate assisted photoreduction of graphene oxide and its nanocomposite formation. Chem Commun 2010;46:6243–5.
[25] Matsumoto Y, Koinuma M, Kim SY, Watanabe Y, Taniguchi T, Hatakeyama K, et al. Simple photoreduction of graphene oxide nanosheet under mild conditions. ACS Appl Mater Interfaces 2010;2:3461–6.
[26] Ding YH, Zhang P, Zhuo Q, Ren HM, Yang ZM, Jiang Y. A green approach to the synthesis of reduced graphene oxide nanosheets under UV irradiation. Nanotechnology 2011;22:215601.
[27] Paredes JI, Villar-Rodil S, Martínez-Alonso A, Tascón JMD. Graphene oxide dispersions in organic solvents. Langmuir 2008;24:10560–4.
[28] Hummers WS, Offeman RE. Preparation of graphitic oxide. J Am Chem Soc 1958;80:1339.
[29] Paredes JI, Villar-Rodil S, Solís-Fernández P, Martínez-Alonso A, Tascón JMD. Atomic force and scanning tunneling microscopy imaging of graphene nanosheets derived from graphite oxide. Langmuir 2009;25:5957–68.
[30] Fang C, Agarwal A, Buddharaju KD, Khalid NM, Salim SM, Widjaja E, et al. DNA detection using nanostructured SERS substrates with rhodamine B as Raman label. Biosens Bioelectron 2008;24:216–21.
[31] Skoog DA, Holler FJ, Nieman TA. Principles of instrumental analysis. Philadelphia: Hartcourt Brace & Company; 1998 [chapter 13].
[32] Fernández-Merino MJ, Guardia L, Paredes JI, Villar-Rodil S, Solís-Fernández P, Martínez-Alonso A, et al. Vitamin C is an ideal substitute for hydrazine in the reduction of graphene oxide suspensions. J Phys Chem C 2010;114:6426–32.
[33] Zhang J, Yang H, Shen G, Cheng P, Zhang J, Guo S. Reduction of graphene oxide via L-ascorbic acid. Chem Commun 2010;46:1112–4.
[34] Zhu C, Guo S, Fang Y, Dong S. Reducing sugar: new functional molecules for the green synthesis of graphene nanosheets. ACS Nano 2010;4:2429–37.
[35] Fan X, Peng W, Li Y, Li X, Wang S, Zhang G, et al. Deoxygenation of exfoliated graphite oxide under alkaline conditions: a green route to graphene preparation. Adv Mater 2008;20:4490–3.
[36] Stankovich S, Dikin DA, Piner RD, Kohlhaas KA, Kleinhammes A, Jia Y, et al. Synthesis of graphene-based nanosheets via chemical reduction of exfoliated graphite oxide. Carbon 2007;45:1558–65.
[37] Zhang G, Sun S, Yang D, Dodelet J-P, Sacher E. The surface analytical characterization of carbon fibers functionalized by H_2SO_4/HNO_3 treatment. Carbon 2008;46:196–205.
[38] Shin H-J, Kim KK, Benayad A, Yoon S-M, Park HK, Jung I-S, et al. Efficient reduction of graphite oxide by sodium borohydride and its effect on electrical conductance. Adv Funct Mater 2009;19:1987–92.
[39] Solís-Fernández P, Paredes JI, Villar-Rodil S, Martínez-Alonso A, Tascón JMD. Determining the thickness of chemically modified graphenes by scanning probe microscopy. Carbon 2010;48:2657–60.
[40] Chen W, Yan L. Preparation of graphene by a low-temperature thermal reduction at atmospheric pressure. Nanoscale 2010;2:559–63.
[41] Zhu Y, Stoller MD, Cai W, Velamakanni A, Piner RD, Chen D, et al. Exfoliation of graphite oxide in propylene carbonate and thermal reduction of the resulting graphene oxide platelets. ACS Nano 2010;4:1227–33.
[42] Zhou Y, Bao Q, Tang LAL, Zhong Y, Loh KP. Hydrothermal dehydration for the "green" reduction of exfoliated graphene oxide to graphene and demonstration of tunable optical limiting properties. Chem Mater 2009;21:2950–6.
[43] Kamat PV. Graphene-based nanoarchitectures. Anchoring semiconductor and metal nanoparticles on a two-dimensional carbon support. J Phys Chem Lett 2010;1:520–7.
[44] Jasuja K, Linn J, Melton S, Berry V. Microwave-reduced uncapped metal nanoparticles on graphene: tuning catalytic, electrical, and Raman properties. J Phys Chem Lett 2010;1:1853–60.
[45] Hu M, Chen J, Li Z-Y, Au L, Hartland GV, Li X, et al. Gold nanostructures: engineering their plasmonic properties for biomedical applications. Chem Soc Rev 2006;35:1084–94.

[46] Boyen HG, Kastle G, Koslowski B, Dietrich C, Ziemann P, Spatz JP, et al. Oxidation-resistant gold-55 clusters. Science 2002;297:1533–6.
[47] Hoffmann MR, Martin ST, Choi W, Bahnemann DW. Environmental applications of semiconductor photocatalysis. Chem Rev 1995;95:69–96.
[48] Kabra K, Chaudhary R, Sawhney RL. Treatment of hazardous organic and inorganic compounds through aqueous-phase photocatalysis: a review. Ind Eng Chem Res 2004;43:7683–96.
[49] Ravelli D, Dondi D, Fagnoni M, Albini A. Photocatalysis. A multi-faceted concept for green chemistry. Chem Soc Rev 2009;38:1999–2011.
[50] Erickson K, Erni R, Lee Z, Alem N, Gannett W, Zettl A. Determination of the local chemical structure of graphene oxide and reduced graphene oxide. Adv Mater 2010;22:4467–72.
[51] Moreno-Villoslada I, Jofré M, Miranda V, González R, Sotelo T, Hess S, et al. PH dependence of the interaction between rhodamine B and the water-soluble poly(sodium 4-styrenesulfonate). J Phys Chem B 2006;110:11809–12.
[52] Paredes JI, Gracia M, Martínez-Alonso A, Tascón JMD. Nanoscale investigation of the structural and chemical changes induced by oxidation on carbon black surfaces: a scanning probe microscopy approach. J Colloid Interface Sci 2005;288:190–9.
[53] Daniel M-C, Astruc D. Gold nanoparticles: assembly, supramolecular chemistry, quantum-size-related properties, and applications toward biology, catalysis, and nanotechnology. Chem Rev 2004;104:293–346.
[54] Ko H, Singamaneni S, Tsukruk VV. Nanostructured surfaces and assemblies as SERS media. Small 2008;4:1576–99.
[55] Ling X, Xie L, Fang Y, Xu H, Zhang H, Kong J, et al. Can graphene be used as a substrate for Raman enhancement? Nano Lett 2010;10:553–61.
[56] Kundu S, Wang K, Liang H. Size-selective synthesis and catalytic application of polyelectrolyte encapsulated gold nanoparticles using microwave irradiation. J Phys Chem C 2009;113:5157–63.

5.2 Curado estructural de láminas de óxido de grafeno reducido

Artículo III

Publicado en la revista Nano Research: "Towards full repair of defects in reduced graphene oxide films by two-step graphitization"

Artículo IV

Enviado para publicación: "From graphene oxide to pristine graphene: revealing the inner workings of the full structural restoration"

Uno de los mayores inconvenientes de la denominada ruta del óxido de grafito reside en que las láminas de grafeno resultantes presentan un gran número de defectos y grupos funcionales oxigenados residuales, originados durante la preparación del óxido de grafito y que no se eliminan completamente en la etapa de reducción química. Estos defectos degradan las excelentes propiedades físicas del grafeno y limitan los posibles usos del material preparado por esta vía. Por ello, resulta interesante, tanto desde un punto de vista fundamental como aplicado, establecer la posibilidad del curado total de los defectos del grafeno proveniente del óxido de grafito y examinar en detalle los aspectos más relevantes de dicho proceso. Esto se ha hecho en los artículos III y IV.

En el *artículo III* se realiza un estudio exhaustivo de la reparación de la estructura con defectos de las láminas de óxido de grafeno reducido químicamente (rGO), efectuando tratamientos a alta temperatura (1500-2700 °C) de filmes macroscópicos de dichas láminas. El tratamiento a alta temperatura fue llevado a cabo en dos etapas: la primera a 1500 °C, en la que se produce la eliminación total de los grupos funcionales oxigenados de la muestra (lo que conlleva supone la generación de vacantes atómicas), y la segunda a 1800-2700 °C, en la que se produce la eliminación o curado de las vacantes generadas en la primera etapa y la coalescencia de láminas solapadas, dando lugar a capas policristalinas.

Varios resultados experimentales demuestran que la eliminación de los grupos funcionales y la aniquilación de las vacantes son procesos que requieren energías de activación diferentes y por lo tanto ocurren en distintos rangos de temperatura. En primer lugar, la eliminación completa de los grupos funcionales oxigenados en la primera etapa (1500 °C) pudo ser confirmada mediante XPS. Por otra parte, los espectros Raman obtenidos tras esta primera etapa muestran una relación I_D/I_G aún considerable (~0.72), mientras que ésta se reduce significativamente durante la segunda etapa (~0.11-0.02). Esto implica que, para superar la energía de activación de la migración de las vacantes

multiatómicas y provocar su aniquilación al llegar a los bordes de las láminas, es necesario utilizar temperaturas de tratamiento más altas, en el rango de las empleadas durante la segunda etapa (1800-2700 °C). Los resultados de termogravimetría respaldan la hipótesis planteada, ya que reflejan un drástico descenso de la reactividad frente a oxidación del filme tras la primera etapa, seguido de un descenso de la reactividad mucho más discreto durante la segunda etapa. Por último, las imágenes de STM a escala atómica confirman la descripción presentada anteriormente, ya que mientras antes del tratamiento la muestra presenta una estructura carente de dominios grafíticos ordenados (debido a la presencia de grupos funcionales y otro tipo de defectos), la muestra tratada a 1500 °C posee una estructura esencialmente ordenada en la que se aprecia un alto número de protuberancias atribuibles a vacantes multiatómicas. Las filmes tratados a mayor temperatura presentan una densidad decreciente de dichas protuberancias hasta su completa desaparición a 2700 °C.

Las altas temperaturas empleadas durante la segunda etapa de tratamiento tienen como resultado la aparición de un cierto grado de orden grafítico tridimensional en los filmes, tal y como sugieren diversos resultados experimentales. Los difractogramas de rayos X obtenidos revelan una reducción de la distancia interplanar, d_{002}, y un aumento del tamaño de cristal aparente en la dirección del eje c, L_C, que tiende paulatinamente hacia valores propios del grafito. Por otra parte, el tamaño de cristal aparente en el plano basal, L_a, determinado por espectroscopía Raman a partir de la relación I_D/I_G, es comparable al tamaño de las láminas que componen originalmente el filme (200-500 nm). Además, la banda 2D del espectro Raman de las muestras tratadas a 2400 y 2700 °C desarrolla un creciente grado de asimetría, que refleja la evolución desde un apilamiento turbostrático hacia un apilamiento ordenado tipo Bernal. Por último, las imágenes de STM a escala nanométrica muestran una evolución desde una topografía irregular de los filmes antes del tratamiento, debida al solapamiento aleatorio de las láminas durante el ensamblaje de los filmes, hacia una topografía plana con terrazas de un tamaño similar al de las láminas que integran el filme. Se interpreta que, para que dicha transformación tenga lugar, debe producirse la coalescencia de las láminas a alta temperatura. Esta hipótesis se ve además apoyada por la presencia de numerosas fronteras de grano en las imágenes de STM. Como consecuencia de todas las transformaciones descritas anteriormente, la conductividad eléctrica de los filmes tratados a la mayor temperatura (2700 °C) fue de 577.000 S m^{-1}, que es la mayor conductividad conseguida hasta el presente para un material derivado de óxido de grafito.

En relación con el trabajo anterior, en el *artículo IV* estudiamos el tratamiento térmico de láminas individuales de rGO depositadas sobre HOPG con el objetivo de comprender de forma detallada los mecanismos que gobiernan la eliminación de los grupos funcionales oxigenados y defectos estructurales presentes en dichas láminas.

Inicialmente se estudió la influencia de la densidad de grupos oxigenados presentes en las láminas sobre la evolución de su estructura durante el tratamiento térmico. Para ello se adquirieron imágenes de AFM a escala nanométrica de GO sin reducir, GO poco reducido y GO reducido en mayor extensión o rGO. La descomposición de los numerosos grupos funcionales en el GO sin reducir o poco reducido provoca una sustracción significativa de átomos de carbono, lo que implica la formación de vacantes de mayor tamaño y/o en mayores densidades. La coalescencia de estas vacantes a alta temperatura conduce a la formación de agujeros de gran tamaño en las láminas o a su desintegración. Por el contrario, el rGO presenta un menor número de funcionalidades oxigenadas y además, éstas han sido eliminadas en el proceso de reducción química sin que se produzca sustracción de átomos de carbono, por lo que se generan vacantes de menor tamaño y en menores densidades que en el caso anterior. De esta forma, las vacantes puedan migrar más fácilmente hacia los bordes y ser aniquiladas sin coalescer en el interior de la lámina, lo que conduce finalmente al curado de las láminas.

Para estudiar con mayor detalle el proceso de curado de las láminas de rGO, se analizó la evolución térmica de los defectos mediante imágenes de STM a escala atómica para muestras tratadas a temperaturas comprendidas entre 1500 y 1950 °C. A partir de dichas imágenes se pudo constatar que es posible restaurar la red grafítica de las láminas a 1800 °C. A esta temperatura, se observó la presencia de un tipo de defecto de simetría hexagonal que pudo ser finalmente eliminado a 1950 °C. Estos defectos se pueden atribuir a pequeños grupos de heteroátomos de nitrógeno procedentes de la reducción química con hidrazina.

Además de estudiar el curado de los defectos de láminas de rGO depositadas sobre un substrato inerte como las terrazas del HOPG prístino, en el que la interacción lámina-substrato es muy débil, se estudió el curado de láminas depositadas sobre distintos tipos de superficies reactivas, donde la interacción con el sustrato da lugar a la aparición de nuevos fenómenos que pudieron ser explicados en base a simulaciones de dinámica molecular. Uno de estos fenómenos es el de coalescencia, que en este caso pudo ser observado directamente mediante imágenes de STM de láminas de rGO depositadas sobre escalones de HOPG y tratadas a 1500 °C. Mediante simulaciones de dinámica molecular se pudo comprobar que el fenómeno de coalescencia resulta de la formación de enlaces covalentes entre los átomos de carbono insaturados en las vacantes de la láminas de rGO y los átomos de carbono insaturados del escalón del HOPG. Estos enlaces fijan las vacantes que se difunden a través de la lámina y debido a la alta densidad de vacantes en el rGO, una de las mitades acaba uniéndose con el escalón. Esta configuración es energéticamente favorable, ya que se elimina la curvatura local de la lámina de rGO depositada sobre el escalón. La coalescencia de láminas de rGO en un filme ocurre a una temperatura mayor que la de una lámina sobre un escalón de HOPG prístino (1800 °C frente a 1500 °C), ya que en el caso del filme la difusión de las vacan-

tes se ve entorpecida por la formación de enlaces covalentes interlaminares entre los átomos de carbono insaturados de las vacantes de dichas láminas.

También se observa una fuerte interacción interlaminar en imágenes de STM de regiones de solapamiento de láminas de rGO tratadas a 1650 °C, que en este caso conduce a la formación de agujeros en la lámina superior acompañada de la eliminación de las vacantes de la lámina inferior. Éste mismo comportamiento se observa en láminas de rGO depositadas sobre una superficie de HOPG en la que se han introducido previamente vacantes de manera artificial. Las simulaciones de dinámica molecular revelan que, fruto de la formación de enlaces covalentes interlaminares entre los átomos de carbono insaturados de las vacantes de dichas láminas y debido a la estabilidad adicional que proporciona la interacción de van der Waals, se produce una transferencia neta de átomos de carbono desde la lámina superior hacia la lámina inferior. La transferencia neta de átomos de carbono entre láminas es un fenómeno que se origina en este caso debido a la asimetría que introduce en el sistema la presencia de una superficie prístina totalmente conjugada. Por lo tanto, este fenómeno no se produce en un filme formado por láminas de rGO en el que no existe dicha asimetría y, por lo tanto, la probabilidad de transferencia de átomos de carbono de una capa a otra es esencialmente la misma que de esta a aquella.

Nano Research 2013, 6(3): 216–233
DOI 10.1007/s12274-013-0298-6
Research Article
ISSN 1998-0124
CN 11-5974/O4

Towards full repair of defects in reduced graphene oxide films by two-step graphitization

Rubén Rozada, Juan I. Paredes (✉), Silvia Villar-Rodil, Amelia Martínez-Alonso, and Juan M. D. Tascón

Instituto Nacional del Carbón, INCAR-CSIC, Apartado 73, 33080 Oviedo, Spain

Received: 18 December 2012
Revised: 29 January 2013
Accepted: 30 January 2013

KEYWORDS
graphene,
graphene oxide,
films,
annealing,
defect

ABSTRACT

The complete restoration of a perfect carbon lattice has been a central issue in the research on graphene derived from graphite oxide since this preparation route was first proposed several years ago, but such a goal has so far remained elusive. Here, we demonstrate that the highly defective structure of reduced graphene oxide sheets assembled into free-standing, paper-like films can be fully repaired by means of high temperature annealing (graphitization). Characterization of the films by X-ray photoelectron and Raman spectroscopy, X-ray diffraction and scanning tunneling microscopy indicated that the main stages in the transformation of the films were (i) complete removal of oxygen functional groups and generation of atomic vacancies (up to 1,500 ˚C), and (ii) vacancy annihilation and coalescence of adjacent overlapping sheets to yield continuous polycrystalline layers (1,800–2,700 ˚C) similar to those of highly oriented graphites. The prevailing type of defect in the polycrystalline layers were the grain boundaries separating neighboring domains, which were typically a few hundred nanometers in lateral size, exhibited long-range graphitic order and were virtually free of even atomic-sized defects. The electrical conductivity of the annealed films was as high as 577,000 $S \cdot m^{-1}$, which is by far the largest value reported to date for any material derived from graphene oxide, and strategies for further improvement without the need to resort to higher annealing temperatures are suggested. Overall, this work opens the prospect of truly achieving a complete restoration of the carbon lattice in graphene oxide materials.

1 Introduction

The last decade has witnessed the rapid emergence of graphene research on a remarkable variety of fronts. Research activities have covered basic science aspects of this two-dimensional carbon material, to provide fundamental insight into its electronic, mechanical, thermal and optical properties [1, 2], as well as the exploration of its potential for different technologically relevant applications, for instance in electronics [3],

Address correspondence to paredes@incar.csic.es

Nano Res. 2013, 6(3): 216–233 217

energy conversion and storage [4], chemical and biological sensing [5, 6], catalysis [7] or biomedicine [8]. The development of versatile and cost-effective methodologies for the mass production and processing of graphene has been, and continues to be, central to many of these efforts [9–11]. In this regard, one approach that has proved particularly fruitful is the so-called graphite oxide route, which is based on the exfoliation and reduction of this strongly oxygenated derivative of graphite to afford graphene sheets in large quantities [9, 12–17]. In addition to its scalable production, this type of graphene (usually referred to as reduced graphene oxide) exhibits several attractive features that are important from a practical viewpoint, including the fact that it is readily dispersible in aqueous and organic media and its versatility for chemical functionalization and combination with other materials [11, 12, 18].

On the other hand, the carbon lattice in reduced graphene oxide is well known to contain a large number of structural defects and distortions. Such distortions are mainly introduced as a result of the grafting of oxygen functional groups (e.g., hydroxyls and epoxides) during the conversion of graphite to graphite oxide [19]. Although the subsequent reduction step is intended to remove these functional groups and thus restore the original pristine graphene lattice, virtually all the strategies that have so far been put into practice to this end have yielded products with a significant amount of residual oxygen-containing groups and defects, which are apparently very difficult to eliminate [14, 15, 19]. This point has been verified both directly by high resolution microscopy imaging of reduced graphene oxide sheets [20, 21] and indirectly through the observation of a relatively poor recovery of highly defect-sensitive properties, such as the electrical conductivity [22, 23].

To improve the structural quality and properties of graphite oxide-derived graphene sheets, and ultimately the performance of devices and materials obtained therefrom, several groups have implemented defect repair techniques based on the supply of carbon atoms from a hydrocarbon gas source at ~600–900 ℃, i.e., by chemical vapour deposition (CVD) [24–26]. Even though the repaired sheets displayed significantly increased values of electrical conductivity, the actual degree of defect healing attained by this method was very far from complete. Furthermore, because the healing of subsurface defects does not appear to be possible [27], the CVD technique is only suited for the repair of monolayer, but not multilayer, graphene oxide/reduced graphene oxide films. Building upon the pioneering work on the heat treatment of graphite oxide reported some decades ago [28–33], the thermal annealing of graphene oxide up to moderately high temperatures (~1,100 ℃) has also been extensively investigated in recent years [14, 15, 23, 34–36], but the amount of residual oxygen and structural defects remaining on such thermally reduced graphene is generally comparable to that achieved with some of the most effective chemical reduction approaches carried out at much lower temperatures (< 100 ℃) [14, 15], i.e., it is still rather large. Thus, in the absence of other alternatives, it can be postulated that a full repair of defects in graphene oxide or reduced graphene oxide will be most realistically accomplished under graphitization conditions, which involve very high annealing temperatures (e.g., 2,000 ℃ or above) [37]. Some very recent work along this line suggests that this might indeed be the case [38, 39], but a thorough investigation of the topic (for example, encompassing a wide range of graphitization temperatures) has not yet been reported. Furthermore, complete removal of defects from the sheets has not been demonstrated and the details of their structural evolution down to the nanometer/atomic scales have remained unknown.

Here, we present a comprehensive study of the structural, chemical and electrical characteristics of free-standing, paper-like films of chemically reduced graphene oxide (reduced graphene oxide paper) that have been subjected to graphitization treatments at different temperatures, from 1,500 up to 2,700 ℃. Reduced graphene oxide paper is currently the focus of significant research efforts with a view to its practical use as components in, e.g., Li ion batteries, fuel cells, supercapacitors or electromechanical actuators [40–43]. In the present work, both global (e.g., Raman spectroscopy and X-ray photoelectron spectroscopy (XPS)) and local (scanning tunneling microscopy (STM)) characterization techniques have been employed to examine the graphitized films, revealing that atomic-sized (point) defects can be

218 Nano Res. 2013, 6(3): 216–233

eliminated altogether from the basal planes of the reduced graphene oxide sheets at sufficiently high annealing temperatures. Significantly, such extensive healing easily affords the highest values of electrical conductivity that have so far been documented for films obtained from graphene oxide, approaching those typical of pristine, highly oriented graphites.

2 Experimental

The graphitization experiments were carried out on free-standing, paper-like films of chemically reduced graphene oxide, which were prepared as follows. First, graphite oxide was synthesized from natural graphite powder (Fluka 50870) by the Hummers method, using H_2SO_4, $NaNO_3$, and $KMnO_4$, as described elsewhere [44]. After being rinsed with 10% HCl solution and thoroughly washed with deionized water, the oxidation product was suspended in deionized water, sonicated in an ultrasound bath cleaner (J.P. Selecta Ultrasons system, 40 kHz) for 4 h and centrifuged (Eppendorf 5424 microcentrifuge) at 10,000 g for 10 min. The resulting supernatant (top ~75% of the total volume), which is a dispersion of single-layer graphene oxide sheets, was collected for further use and its concentration determined by means of UV–vis absorption spectroscopy based on a previously reported procedure [45]. Aqueous graphene oxide dispersions (0.1 mg·mL^{-1}) were chemically reduced with hydrazine monohydrate (0.05 μL of reductant per mL of dispersion) by heating at 95 ˚C for 1 h under basic conditions (pH ~10, adjusted by adding 2 μL of 25% ammonia solution per mL of dispersion). This procedure has been formerly shown to afford stable dispersions of well-reduced graphene oxide sheets [46]. Finally, a given volume of the reduced dispersion (typically 250 mL) was vacuum-filtered through a silver membrane filter (47 mm in diameter and 0.2 μm of pore size, from Whatman). After drying under ambient conditions and peeling off the membrane filter, a free-standing paper-like film of reduced graphene oxide, denoted as HG, was obtained.

Reduced graphene oxide paper samples were subjected to high temperature annealing in a graphite furnace under argon flow (2 L·min^{-1}). For reasons that will be commented upon below, a two-step heat treatment procedure was implemented: The paper-like films were first annealed at 1,500 ˚C, and then, in a second independent run, annealed again at a higher temperature (1,800, 2,100, 2,400 or 2,700 ˚C). The following heating rates were applied: 50 ˚C·min^{-1} from room temperature to 700 ˚C, 100 ˚C·min^{-1} from 700 to 1,000 ˚C, 25 ˚C·min^{-1} between 1,000 and 2,000 ˚C, and 10 ˚C·min^{-1} between 2,000 and 2,700 ˚C. Once it was reached, the target temperature was kept constant for 1 h and finally the samples were cooled down to room temperature while maintaining the same argon flow. The graphitized samples were denoted as HG1500 (film heat treated only once, at 1,500 ˚C) and HG1500-T (film first heat treated at 1,500 ˚C and then at a temperature *T*; e.g., HG1500-1800, HG1500-2100, etc).

Characterization was carried out by means of UV–vis absorption spectroscopy (only for the starting aqueous dispersions), X-ray diffraction (XRD), Raman spectroscopy, thermogravimetric analysis (TGA), STM, atomic force microscopy (AFM), XPS and measurement of electrical conductivity of the films. UV–vis absorption spectra were recorded with a double-beam Heλios α spectrophotometer (Thermo Spectronic). XRD was performed on a Bruker D8 ADVANCE diffractometer using Cu Kα radiation (λ = 0.154 nm) at a step size and time of 0.02° (2θ) and 1 s, respectively. Raman spectra were obtained with a HORIBA Jobin Yvon LabRAM apparatus at a laser excitation wavelength of 532 nm. To avoid damage to the samples, a low incident laser power (~1 mW) was used. TGA was accomplished under air flow (100 mL·min^{-1}) on an SDT Q600 thermobalance (TA Instruments) at a heating rate of 10 ˚C·min^{-1}, using Pt crucibles. AFM and STM measurements were performed with a Nanoscope IIIa Multimode apparatus (Veeco) under ambient conditions. AFM was carried out in the tapping mode of operation with rectangular silicon cantilevers. STM images were recorded using mechanically prepared Pt/Ir (80/20) tips. A SPECS spectrometer, working with a monochromatic Al Kα X-ray source (100 W) at a pressure of 10^{-7} Pa, was used for the XPS measurements. The electrical conductivity of the different paper-like films, cut into 12 mm × 12 mm squares, was determined by the van der Pauw method with a home-made setup (Agilent 6614C DC power supply and Fluke 45 digital multimeter).

Nano Res. 2013, 6(3): 216–233 219

3 Results and discussion

Figure 1(a) shows a digital photograph of a vial containing a sample of the aqueous, hydrazine-reduced graphene oxide dispersion (0.1 mg·mL^{-1}) that was used for the preparation of the paper-like films. In contrast to the yellow-brown color of its unreduced counterpart (not shown), such dispersion exhibits a deep black tone, suggesting that the graphene oxide sheets have been effectively reduced. This point can be corroborated by UV–vis absorption spectroscopy, which has proved to be a useful technique to monitor the reduction degree of graphene oxide [46]. The UV–vis absorption spectrum of the reduced suspensions prepared here (Fig. 1(b)) displays a peak at about 268 nm and strong absorbance in the whole wavelength range above 268 nm, indicating that the hydrazine reduction step succeeded in deoxygenating the graphene oxide sheets to a significant extent [46, 47]. Further proof of the effective reduction of graphene oxide by XPS analysis is given in Fig. S1 in the Electronic Supplementary Material (ESM). A representative AFM image of the reduced sheets after being drop-cast from their aqueous suspension onto a highly oriented pyrolytic graphite (HOPG) substrate is shown in Fig. 1(c). The sheets display irregular shapes and are typically a few to several hundred nanometers in lateral size, with an apparent thickness, determined relative to the HOPG substrate, of ~1 nm (see the superimposed line profile in Fig. 1(c)). Such apparent thickness implies that the sheets are individual, single-layer objects (i.e., single-layer reduced graphene oxide) [45, 47]. Vacuum-filtering this reduced suspension afforded free-standing papers with a shiny metallic appearance (Fig. 1(d)), which were used in the subsequent heat treatments.

It should be stressed that paper-like films of chemically reduced graphene oxide were deliberately

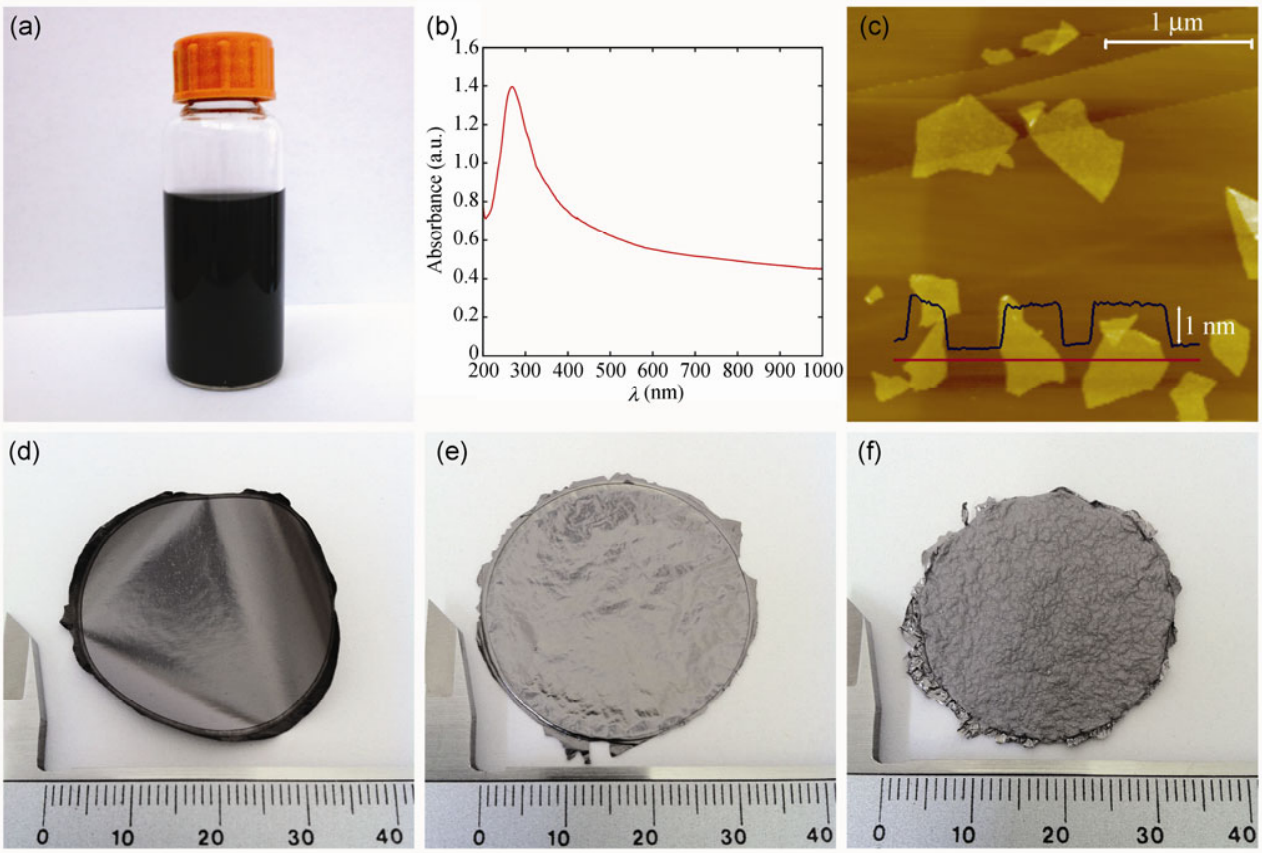

Figure 1 Digital photograph (a) and UV–vis absorption spectrum (b) of the starting aqueous dispersion of reduced graphene oxide. (c) Representative AFM image of the reduced graphene oxide sheets deposited onto HOPG. (d)–(f) Digital photographs of the starting HG film (d) as well as of annealed films HG1500 (e) and HG1500-2700 (f). The numbers in the scale in (d)–(f) correspond to millimeters.

220 Nano Res. 2013, 6(3): 216–233

chosen for the graphitization experiments as opposed to films of unreduced graphene oxide: During high temperature annealing, the oxygen functional groups present on both unreduced and chemically reduced graphene oxide are expected to be removed in the form of CO and CO_2 molecules [15, 19, 48–50]. This implies that carbon atoms should be abstracted from the graphene lattice, and as a result, structural defects such as atomic vacancies can be created [49], which would subsequently have to be healed if a pristine graphitic lattice is to be restored. Because chemical reduction with hydrazine removes a large fraction of the oxygen originally present in graphene oxide without significant evolution of carbon atoms [51–53] and thus without creating vacancies or other defects, the amount of structural defects brought about in chemically reduced graphene oxide upon stripping its residual oxygen functional groups by high temperature annealing should be much smaller than that generated on its unreduced, oxygen-crowded counterpart. By virtue of bearing a lower density of heat treatment-induced defects in its carbon lattice, the subsequent healing of the chemically reduced sheets should be easier to achieve compared to that of unreduced graphene oxide. Furthermore, very recent work has shown that paper-like films of unreduced graphene oxide tend to crack up at annealing temperatures as low as 800 ℃ [36], whereas the structural integrity of papers made of chemically reduced graphene oxide studied here was preserved for all the annealing temperatures up to 2,700 ℃ (Figs. 1(e) and 1(f)).

The previous reasoning also points to the idea that complete healing of reduced graphene oxide by means of heat treatment to yield a pristine graphitic lattice can be basically viewed as a two-step process, comprising first the removal of its oxygen functional groups and then the repair of the structural defects left behind in the carbon lattice by the evolving oxygen. Thus, we hypothesized that graphitization of the reduced graphene oxide paper could be similarly approached in two annealing steps: The first one would be carried out at a moderately high temperature to remove most of the residual oxygen that remains in reduced graphene oxide, while a second annealing at a higher temperature would allow the enduring lattice defects and structural imperfections to repair. In this way, the two steps could be studied independently. We chose the temperature of the first annealing step to be 1,500 ℃ based on previous work which suggested that a significant fraction of the original oxygen groups of graphene oxide (i.e., mostly hydroxyls and epoxies) are converted to carbonyls and ethers upon heat treatment [49]. The latter functional groups are thermodynamically very stable and probably require temperatures in excess of 1,000 ℃ to be removed [49, 54]. In fact, we observed by means of XPS that practically all the oxygen present in the as-prepared, chemically reduced graphene oxide films could be eliminated during the first annealing step at 1,500 ℃, up to the point where oxygen was below the usual detection level for this technique. This point can be appreciated from Fig. 2, where XPS survey spectra for the starting reduced graphene oxide film (sample HG) and the film subjected to a single annealing at 1,500 ℃ (sample HG1500) are presented. The O/C atomic ratios derived from the XPS data for these two and the remaining samples are given in Table 1. The ratio was 0.102 for the starting HG film (down from 0.430 for the unreduced graphene oxide film) but decreased to less than 0.001 for sample HG1500. As could be anticipated, the subsequent higher temperature treatments (second annealing step) also yielded negligible amounts of oxygen (spectra not shown). These results

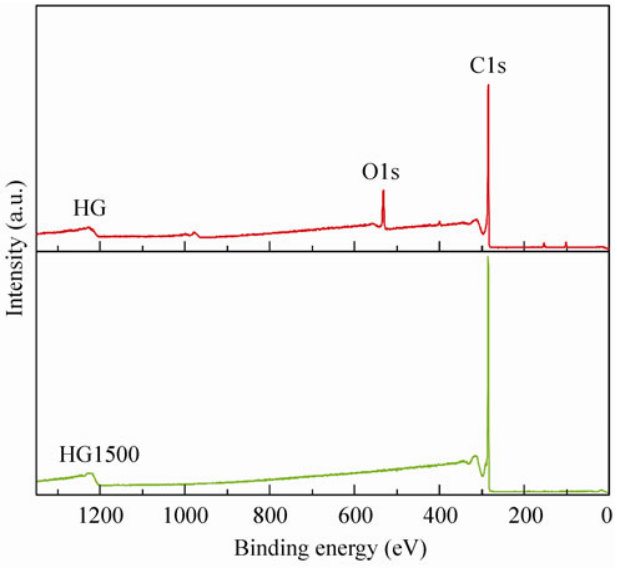

Figure 2 Survey X-ray photoelectron spectra for the starting HG film (red plot) and annealed film HG1500 (green).

Nano Res. 2013, 6(3): 216–233 221

Table 1 O/C atomic ratio derived from XPS; interlayer spacing (d_{002}) and apparent crystallite size in the *c* direction (L_c) obtained by XRD; integrated intensity ratio of the D and G bands (I_D/I_G) and apparent in-plane crystallite size (L_a) calculated through the Tuinstra–Koenig (T–K) and Cançado equations from Raman spectra; electrical conductivity of the starting reduced graphene oxide film, films annealed at different temperatures and HOPG

Sample	O/C at. ratio	d_{002} (Å)	L_C (nm)	I_D/I_G	L_a (nm) (T–K)	L_a (nm) (Cançado)	Conductivity ($S \cdot m^{-1}$)
HG	0.102	3.944	1.2	1.83	2.4	10.5	7,962
HG1500	< 0.001	3.416	7.2	0.72	6.1	26.7	2.18×10^5
HG1500-1800	< 0.001	3.431	10.2	0.11	40.6	177.2	1.71×10^5
HG1500-2100	< 0.001	3.423	13.6	0.09	50.6	221.2	2.31×10^5
HG1500-2400	< 0.001	3.378	27.4	0.07	62.5	273.1	3.34×10^5
HG1500-2700	< 0.001	3.366	35.6	0.02	236.6	1,033.6	5.77×10^5
HOPG	< 0.001	3.355	52.8	0	—	—	1.69×10^6

demonstrate that under the optimum conditions a virtually complete elimination of oxygen groups from reduced graphene oxide is possible. In contrast, residual oxygen was detected in all previous attempts to restore the original graphene lattice reported in the literature, even when temperatures above 1,500 ˚C were used [39]. Additional details of the XPS results of the films under study can be found in Fig. S2 in the ESM.

The global structural evolution of the heat-treated paper-like samples was investigated by means of XRD and Raman spectroscopy. The X-ray diffractograms of the different films and of HOPG as a reference sample are presented in Fig. 3(a). The non-annealed film (sample HG) displayed a relatively weak and broad diffraction peak at ~22.5° (2θ) [40, 55], which corresponds to an interlayer spacing, d_{002}, of 3.944 Å (see Table 1). After the first annealing step (sample HG1500) the diffraction peak became much sharper and the d_{002} spacing decreased to 3.416 Å. A further decrease was observed, down to 3.366 Å and thus approaching the HOPG value (3.355 Å), following the second annealing, but only for the highest heat treatment temperatures (2,400 and 2,700 ˚C; see Table 1). By contrast, the d_{002} spacing for the samples annealed at 1,800 and 2,100 ˚C (3.431 and 3.423 Å, respectively) was slightly larger than that measured for sample HG1500. A possible explanation to account for this *a priori* unexpected result will be given below. The decreasing width of the diffraction peak was reflected in the evolution of the apparent crystallite size in the *c* direction, i.e., the L_c parameter (Table 1), which was as low as 1.2 nm for the starting HG film, increased to 7.2 nm following the first heat treatment and finally reached 35.6 nm after the second annealing at 2,700 ˚C. Again, this value was relatively close, but not identical, to that of the HOPG reference sample (52.8 nm).

Figure 3(b) shows first- and second-order Raman spectra of the investigated samples. The first order spectrum (1,100–1,700 cm^{-1}) is dominated by three features: A strong peak at ~1,583 cm^{-1} (G band) and two additional peaks at 1,355 and 1,625 cm^{-1}, which correspond to the defect-related D and D′ bands, respectively [56, 57]. The Raman spectrum of the non-annealed HG film exhibited strong D and D′ peaks (relative to the G band), denoting a large amount of structural defects in its carbon lattice [45, 51]. Following the first heat treatment at 1,500 ˚C, the intensity of both defect-related bands decreased markedly, but in any case they were still relatively large, which suggests that a significant amount of disorder remained in the structure. At least in relative terms, the healing of defects appeared to be much more extensive during the second heat treatment step, as noticed by the evolution of the integrated intensity ratio of the D and G bands (I_D/I_G) for the different samples (Table 1), which provides a quantitative measure of the amount of defects present in graphitic materials [56, 57]. The I_D/I_G ratio was determined to be 1.83, 0.72, and 0.02 for samples HG, HG1500, and HG1500-2700, respectively. Such observation, together with the XPS results, lends

222 Nano Res. 2013, 6(3): 216–233

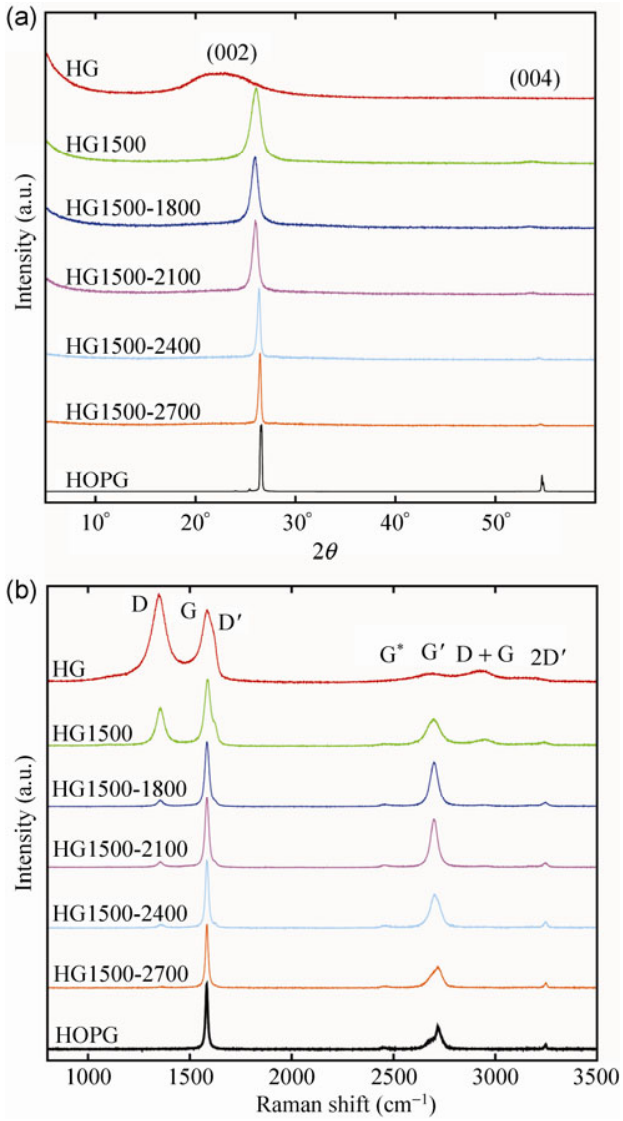

Figure 3 XRD patterns (a) and Raman spectra (b) for the starting HG film (red plots), heat-treated films HG1500 (green), HG1500-1800 (dark blue), HG1500-2100 (purple), HG1500-2400 (light blue), HG1500-2700 (orange), and HOPG (black).

support to the above assumption that a thorough healing of reduced graphene oxide by high temperature annealing proceeds mainly by first removing its residual oxygen groups and then repairing the structural defects left behind in the carbon lattice by the oxygen groups. The I_D/I_G ratio can be used to derive an apparent in-plane crystallite size (L_a parameter), either by means of the well-known Tuinstra–Koenig equation [58] or, alternatively, based on the formula proposed more recently by Cançado et al. [59]. L_a values obtained from both equations were somewhat different (Table 1), and were up to ~10 nm for the starting HG film, as is typical for chemically reduced graphene oxide [22], but reached values in the range of several hundred nanometers for sample HG1500-2700. The meaning of this parameter for the highly graphitized films will be discussed below in the light of the STM results.

The second-order Raman spectra (i.e., the 2,300–3,300 cm^{-1} region in Fig. 3(b)) display up to four different bands (G^*, G′, D + G, and 2D′), that are also characteristic of graphitic materials [57, 60]. The most relevant one is the G′ peak, located at about 2,695 cm^{-1}, which is the overtone of the D band (for this reason, it is usually referred to as the 2D band). Its intensity is sensitive to the presence of structural disorder (i.e., it tends to decrease in the presence of large amounts of disorder; e.g., sample HG), but most significantly, analysis of its lineshape reveals information about the three-dimensional stacking order of the sample [60]. As shown in detail in Fig. 4, the G′ band for a graphitic material with ordered stacking (AB Bernal stacking) such as HOPG exhibits a highly asymmetric lineshape that can be fitted with two Lorentzian components (G'_{3DA} and G'_{3DB}). By contrast, a material in which the graphene layers are randomly rotated with respect to each other around the *c* axis (turbostratic stacking) possesses a G′ band that is completely symmetric and can thus be fitted with a single Lorentzian component (G'_{2D}), located in-between the G'_{3DA} and G'_{3DB} lines. In the present case, because the reduced graphene oxide films were produced by vacuum-assisted assembly of the individual, single-layer sheets from their aqueous dispersion, the sheets are expected to be randomly piled over each other, leading to turbostratic stacking. In fact, the G′ band displayed an altogether symmetric lineshape for films heat-treated up to 2,100 °C in the second annealing step (see Figs. 3(b) and 4). However, asymmetry gradually arose at higher annealing temperatures, suggesting that AB Bernal stacking was developed to some degree. To evaluate the extent of three-dimensional ordering achieved, it was assumed that they consisted of a mixture of regions with turbostratic stacking and regions with AB Bernal stacking. Consequently, their G′ band was fitted using a combination of the G'_{2D}, G'_{3DA} and G'_{3DB} Lorentzian components (Fig. 4), so that

Nano Res. 2013, 6(3): 216–233 223

the fraction, *R*, of sample exhibiting Bernal stacking is given by [60]

$$R = \frac{I_{G'_{3DB}}}{I_{G'_{3DB}} + I_{G'_{2D}}} \quad (1)$$

Using Eq. (1), the fraction of Bernal-stacked regions was determined to be negligible for films heat-treated at 2,100 ℃ and below, ~40% for sample HG1500-2400 and ~70% for sample HG1500-2700, indicating that a significant degree of three-dimensional ordering can be attained at the highest annealing temperature. In other words, the films annealed at the highest temperatures are approaching highly oriented graphites.

The reactivity of graphitic materials, and in particular their reactivity towards oxidation, is known to be strongly dependent on the amount and type of defects present in their structure [61–64]. To assess the effect of annealing on the film reactivity, they were subjected to TGA under flowing air. The thermogravimetric (TG) plots were dominated by a sharp mass loss step that can be ascribed to gasification of the material by reaction with oxygen. Figure 5 shows the first derivative of the TG plots, i.e., the differential thermogravimetric (DTG) plots, for the paper-like films and HOPG. The peak in the DTG plots indicates the temperature at which gasification of the sample was fastest. For the non-annealed HG film, gasification took place at a relatively low temperature (~540 ℃), implying a high reactivity that can be attributed to the distorted carbon structure induced by the large amount of residual oxygen groups that this film contains. The first annealing (1,500 ℃) brought about a remarkable up-shift in the gasification temperature to ~731 ℃ and therefore a significantly less reactive material. The second annealing step gave rise to more modest changes (e.g., gasification at ~768 ℃ for HG1500-1800), and such changes were increasingly marginal with increasing heat treatment temperature. Considering that a relatively large amount of defects is eliminated in this second stage (see Raman results, Fig. 3(b)), such observation suggests that the defects remaining after annealing at 1,500 ℃ are associated

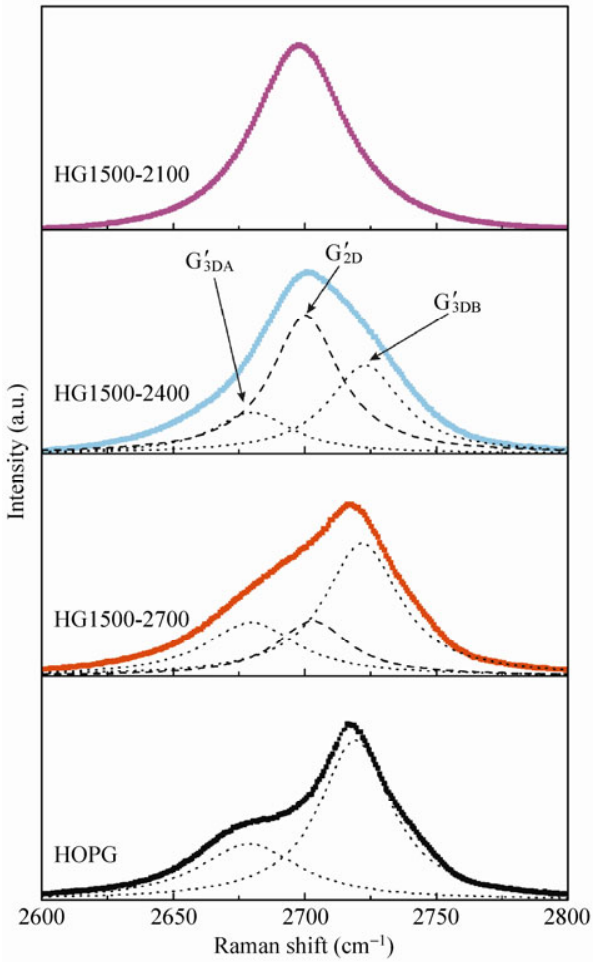

Figure 4 G′ Raman band spectra for the heat-treated films HG1500-2100 (purple plot), HG1500-2400 (light blue), HG1500-2700 (orange), as well as for HOPG (black).

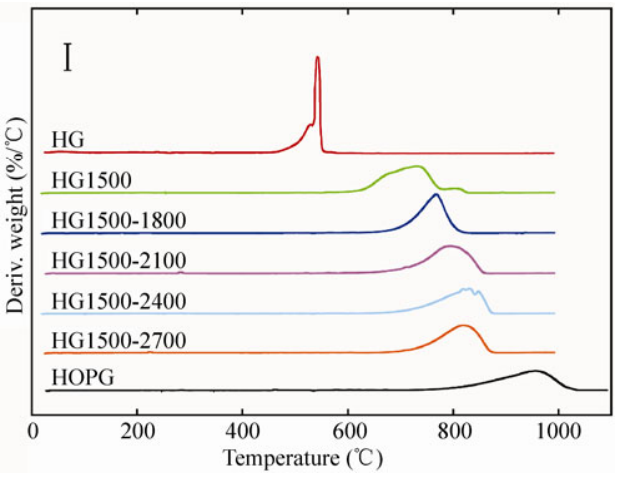

Figure 5 Differential thermogravimetric plots for the starting HG film (red plot), heat-treated films HG1500 (green), HG1500-1800 (dark blue), HG1500-2100 (purple), HG1500-2400 (light blue), HG1500-2700 (orange), as well as for HOPG (black). The vertical scale in the upper left part of the graph corresponds to a weight derivative value of 1%/℃.

224 Nano Res. 2013, 6(3): 216–233

to a lower reactivity compared to that of the original defects in the reduced graphene oxide film. The reactivity of films annealed at the highest temperature (HG1500-2700) still differed considerably from that of HOPG (gasification at ~956 °C), implying a somewhat less pristine structure for the former, in agreement with the XRD and Raman spectroscopy data.

The electrical conductivity is also a highly sensitive indicator of the presence of defects in graphitic carbon. Defects generally act as scattering sites for the charge carriers, thus hampering their mobility and in turn decreasing the overall conductivity of the material [64]. The values measured for the paper-like films and HOPG are given in Table 1. The non-annealed HG film exhibited an electrical conductivity (7,960 $S \cdot m^{-1}$) that is comparable to the values previously reported for chemically reduced graphene oxide paper produced by similar means [46, 47, 55]. A very large increase in conductivity (up to 218,000 $S \cdot m^{-1}$) was observed following the first annealing step, whereas further improvements could be attained with the second annealing, but only at the highest temperatures (2,400 and 2,700 °C), reaching a maximum value of 577,000 $S \cdot m^{-1}$ for sample HG1500-2700. To the best of our knowledge, this is by far the largest value of electrical conductivity that has been documented for a material derived from graphene oxide. The previous highest figure was very recently achieved for a chemically reduced graphene oxide paper that had been heat-treated at 1,900 °C (160,000 $S \cdot m^{-1}$) [39]. For comparison, a conductivity as high as 1,690,000 $S \cdot m^{-1}$ was estimated here for the HOPG sample, which is consistent with the values reported in the literature and close to those measured for single-crystal graphite (~2,500,000 $S \cdot m^{-1}$) [65–67].

As previously hypothesized, with a two-step approach to the restoration of the originally pristine carbon lattice, it has been possible to remove all the oxygen in the reduced graphene oxide films at a relatively low annealing temperature and then, on films with no residual oxygen, to independently investigate the healing of defects at higher annealing temperatures. The fact that these two processes (removal of oxygen and healing of defects) take place at so different temperatures suggests that their activation energies differ significantly. Although, in a practical case, a single annealing at the highest temperatures (e. g., 2,400 °C or 2,700 °C) could be used to completely restore the carbon lattice (see Fig. S3 in the ESM), even in such a case, the process with the lowest activation energy would be much more probable and therefore it would occur much faster. Summing up, in practice the treatment can be done in one stage but the physical process of annealing would always take place in two steps.

The previous results have revealed the general structural and chemical evolution of reduced graphene oxide films upon graphitization treatment. It has been determined that the structural characteristics and other features (reactivity and electrical conductivity) of the highly graphitized films approach very significantly, but do not match, those of a model graphitic material such as HOPG. It is reasonable to argue that the key to understanding this result lies in the evolution of the nanometer- and atomic-scale structure of the films during graphitization. Therefore, to shed light on this question the samples were examined by STM, a microscopy technique with sufficient resolution to image even atomic-sized (point) defects on graphitic materials [68–70]. Figure 6 shows representative STM images of the nanometer-scale morphology for the as-prepared and different heat-treated films, with the overlaid line profiles indicating the typical height variations that were observed in each case. For the starting HG film (Fig. 6(a)), a relatively rough topography can be noticed, which is made up of more or less smooth features ~10–30 nm in lateral size (with the exception of some elongated features; e.g., the lower right part of Fig. 6(a)). Such a characteristic feature size is at least one order of magnitude smaller than the size of the reduced graphene oxide sheets that served as building blocks for the film (Fig. 1(c)). The origin of this topography can be mainly attributed to the random overlapping of the sheets while they are being stacked over each other during film formation. Although an isolated sheet on a flat substrate displays an essentially flat profile (Fig. 1(c)), the successive build-up of further sheets inevitably leads to their overlapping, thus giving rise to an irregular topography with lateral feature sizes that necessarily have to be smaller than those of the sheets. Following the first annealing (sample HG1500, Fig. 6(b)), the distinctive

Nano Res. 2013, 6(3): 216–233 225

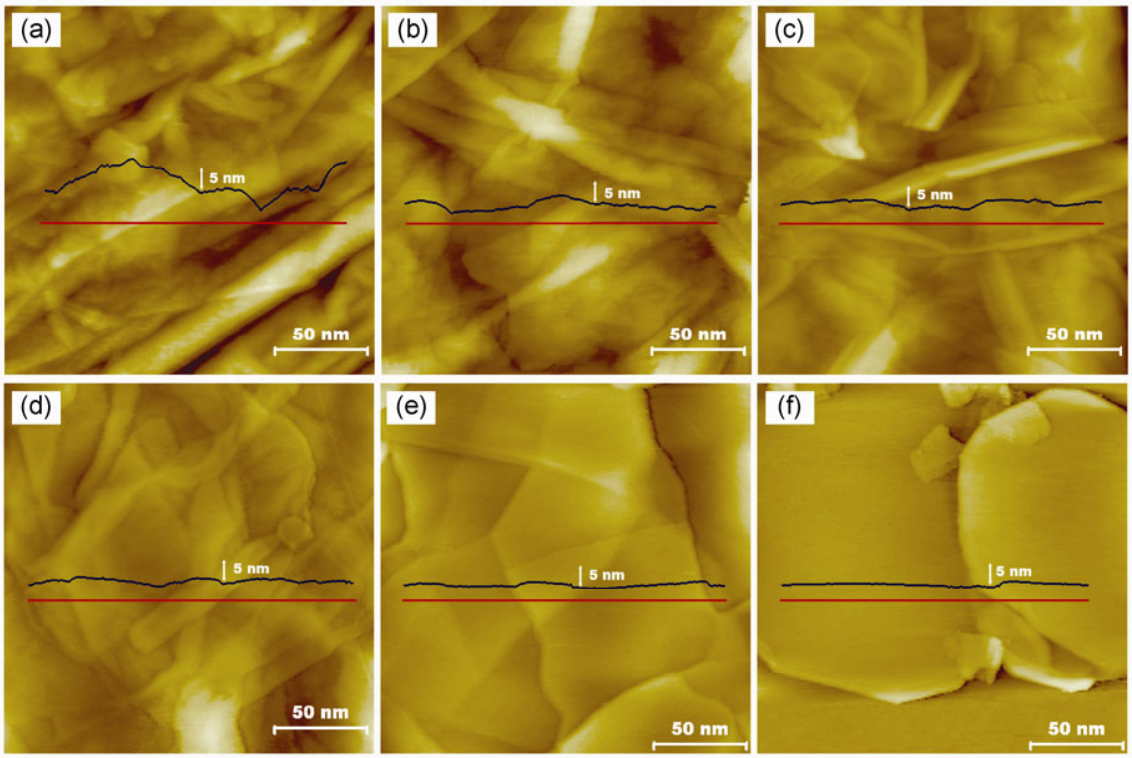

Figure 6 Nanometer-scale STM images for the starting HG film (a) and heat-treated films HG1500 (b), HG1500-1800 (c), HG1500-2100 (d), HG1500-2400 (e), and HG1500-2700 (f). Typical tunneling parameters were 100–300 pA (tunneling current) and 1,500 mV (bias voltage). In each case, a representative line profile (blue plot) taken along the marked red line is shown overlaid onto the image.

nanometer-scale morphology of the as-prepared film was essentially preserved. However, significant changes took place during the second heat-treatment step. Even at the lowest temperatures of 1,800 and 2,100 ℃ (Figs. 6(c) and 6(d), respectively), a clear trend towards a flat topography and features with larger lateral dimensions could be noticed, finally evolving into atomically flat and relatively large (a few hundred nm) terraces at the highest annealing temperatures (2,400 and 2,700 ℃, Figs. 6(e) and 6(f), respectively). Such a progression is basically consistent with the emergence of a high degree of graphitic order in the films (as already revealed by XRD and Raman spectroscopy), the large terraces being ascribed to well-developed basal planes.

The structural evolution of the films upon graphitization was also investigated by STM on the atomic scale. Some representative images are shown in Fig. 7. In agreement with previous STM studies of individual, chemically reduced graphene oxide sheets [45], the as-prepared HG film did not exhibit long-range order on the atomic scale (Fig. 7(a)). It is well-known that highly ordered graphitic surfaces display a perfect triangular pattern (or, in some cases, a honeycomb pattern) with a periodicity of ~0.25 nm in their STM images [71]. By contrast, although atomic-sized features were routinely observed for sample HG, such features were organized into very small (~3–4 nm) domains that usually lacked themselves an ordered triangular (or honeycomb) structure. This point can be better appreciated in the detailed images of a given domain (e.g., inset to Fig. 7(a)). The disordered arrangement of atomic-sized features can be associated to the presence of different types of defects in the carbon structure. Such defects should include the relatively abundant number of oxygen-containing groups that have been measured on the HG film (see XPS results above), but also probably non-hexagonal carbon rings (e.g., 5- or-7-membered rings), which have been suggested to form in reduced graphene oxide [20, 21]. The strain induced by these defects on the carbon lattice can be expected to alter

226 Nano Res. 2013, 6(3): 216–233

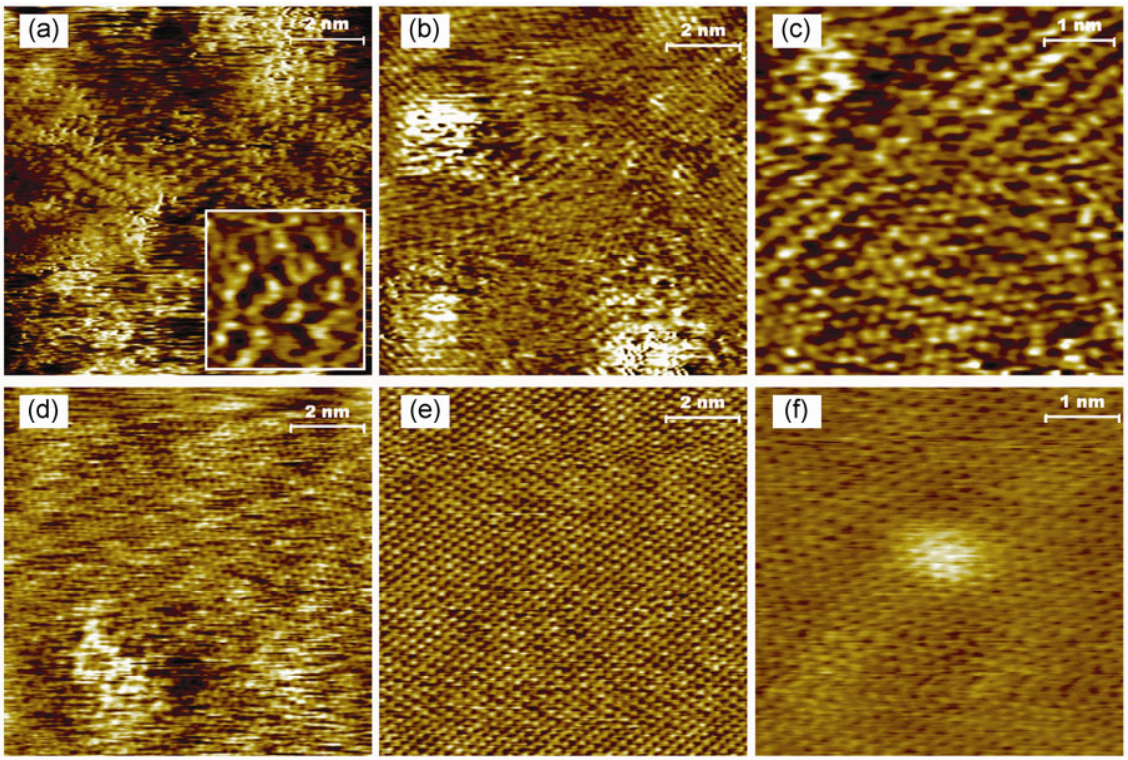

Figure 7 Atomic-scale STM images for the starting HG film (a) and heat-treated films HG1500 (b), (c), HG1500-1800 (d), and HG1500-2700 (e), (f). Typical tunneling parameters: 1–2 nA (tunneling current) and 5–100 mV (bias voltage). The inset to (a) is a detailed 2 nm × 2 nm image showing the highly distorted atomic-scale patterns of the HG film.

significantly its local electronic structure (compared to that of the perfect graphitic lattice), which is what the STM actually probes [72]. Furthermore, because the defects are most probably randomly arranged even on a local scale [20, 21], the resulting atomic-scale STM images should also display disorganized patterns, as actually observed (inset to Fig. 7(a)).

While the first annealing step did not bring about very significant changes to the nanometer-scale morphology of the films (compare Figs. 6(a) and 6(b)), their atomic-scale structure did in fact experience a remarkable transformation. As shown in Fig. 7(b), the atomic-scale STM images of sample HG1500 were characterized by the presence of a large number of apparent protrusions (bright features) ~2–3 nm wide scattered on an otherwise relatively ordered structure. The regions between the protrusions displayed in many cases the familiar triangular or honeycomb patterns archetypal of well-ordered graphitic systems, whereas in other instances these patterns were seen to be modulated by local superstructures (e.g., Fig. 7(c)). Such superstructures are known to reflect a modulation of electronic density arising in highly graphitic regions that lie in close proximity to defects [73]. The protrusions themselves generally exhibited locally distorted or unclear atomic patterns, and can be interpreted as isolated defects remaining in the film after its graphitic structure is largely restored as a result of the removal of its oxygen functionalities. On the atomic scale, the most obvious change taking place during the second annealing was the progressive disappearance of these isolated defects, as exemplified in Figs. 7(d) and 7(e) for samples HG1500-1800 and HG1500-2700, respectively. For the latter film, the large majority of the recorded 10 nm × 10 nm images were completely free from any defects and they always displayed long-range graphitic order (e.g., Fig. 7(e)). However, rather than protrusions with distorted atomic-scale pattern, the residual defects in this film were mostly smooth, dome-like bumps where the

Nano Res. 2013, 6(3): 216–233 227

pristine graphitic structure was not altered (Fig. 7(f)), suggesting that they were of a different nature to those prevalent at the lowest annealing temperatures (sample HG1500, Fig. 7(b)). The dome-like features were from ~one up to several nanometers in diameter and can in principle be attributed to interstitial species (e.g., clusters of carbon atoms) trapped in-between the topmost graphene layers [69].

As already noted above, the removal of the oxygen functionalities as CO and CO_2 molecules from the HG film with heat treatment at 1,500 ˚C should inevitably lead to the generation of a significant number of atomic vacancies/small holes on the carbon lattice [48–50]. It is also well established that atomic vacancies in graphitic structures induce an enhancement in the local density of electronic states near the Fermi level, so that the vacancy is imaged by STM as a protrusion (bright feature) with lateral dimensions (up to several nanometers) mainly determined by the number of missing carbon atoms [68, 70]. The protrusions observed for sample HG1500 (Fig. 7(b)) are consistent with their being atomic vacancies and are therefore ascribed to such a type of defect generated in the sheets by the first annealing step. Now, at sufficiently high temperatures the atomic vacancies can be expected to become mobile and annihilate at, e.g., the sheet edges, leading to their effective removal [70, 74]. Although a single-atom vacancy is thought to possess a significant mobility even at close to ambient temperature due to a relatively low migration barrier, the mobility of multi-atom vacancies should be extremely low, therefore requiring very high temperatures to annihilate. For instance, the migration barrier for a two-atom vacancy in graphene has been estimated to be 6–7 eV, compared to ~1.2–1.4 eV in the case of a single-atom vacancy [64]. The latter is indeed easily removed at temperatures of just a few hundred degrees Celsius [70]. Furthermore, the lateral size of the protrusions seen by STM for the HG1500 film (Fig. 7(b)) suggests that they mostly correspond to multi-atom vacancies and not to single-atom vacancies, which are associated to noticeably smaller protrusions (~0.6–0.9 nm) [70]. Consequently, these atomic vacancies should be expected to disappear only at very high temperatures, as was indeed the case during the second annealing.

Based on the previous results, it can be concluded that the central sequence of events in the graphitization process of the reduced graphene oxide films is the following: (i) removal of residual oxygen groups/vacancy generation (first annealing step), and (ii) vacancy annihilation (second annealing step). This mechanism can explain the development of essentially pristine, defect-free graphitic basal surfaces at the highest heat treatment temperature (i.e., sample HG1500-2700, Fig. 7(e)). Nevertheless, such a process alone cannot account for the nanometer-scale evolution of the film morphology that was described in Fig. 6. The generation and annihilation of atomic vacancies within the reduced graphene oxide sheets is not expected to significantly alter the random stacking/overlapping configuration of the sheets in the film. Consequently, if the rough morphology of the starting HG film (Fig. 6(a)) is due to the random arrangement of the sheets and only vacancy generation/annihilation processes come into play, then such a morphology should be essentially preserved throughout the whole annealing process, which was obviously not the case (Fig. 6(f)). Because topography of atomically flat terraces was seen to develop instead, we have to conclude that most of the overlaps between neighboring sheets in the starting HG film were eliminated, mainly during the second annealing step. We propose that adjacent sheets in the film coalesce at the points where a given sheet overlaps with the edge of another sheet, so that the film eventually transforms into a stack of non-overlapped, extended and flat graphitic layers. A schematic illustration of such structural transformation is given in Fig. 8. This interpretation is supported by very recent experiments carried out by Barreiro et al., who observed the coalescence of two overlapping graphene layers into one continuous sheet under Joule heating (temperatures up to 2,000 ˚C) inside a transmission electron microscope [75]. Even though the details of this transformation are currently not known and need to be elucidated, it can be argued that its main driving force is the elimination of the energy penalty associated to (i) the presence of a large amount of free graphene edges with dangling bonds and (ii) also probably the local strain of the carbon lattice due to curvature at the point where a sheet overlaps with the edge of another sheet in the starting film (Fig. 8).

228 Nano Res. 2013, 6(3): 216–233

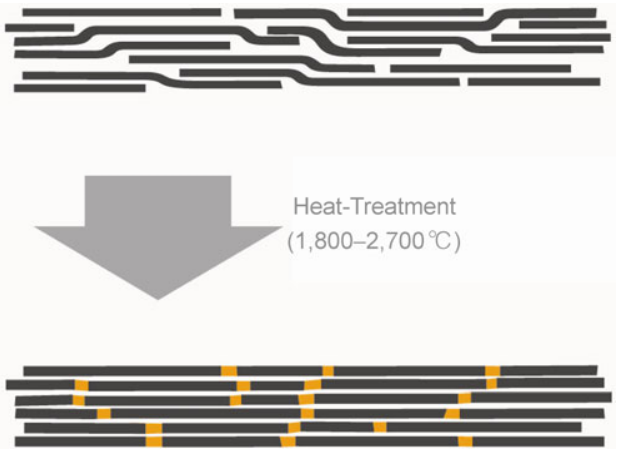

Figure 8 Schematic illustration of the sheet coalescence process in the reduced graphene oxide film during the second annealing step (1,800–2,700 ˚C). The yellow-brown squares shown in the annealed film represent grain boundaries between neighboring domains in the resulting extended polycrystalline layers.

If the hypothesis of sheet coalescence is correct, and because the coalescing sheets should in principle exhibit random in-plane crystallographic orientations, then we would expect the resulting layers to be highly polycrystalline and thus contain a significant amount of grain boundaries. As a matter of fact, grain boundaries were ubiquitously seen by STM for sample HG1500-2700. In its low energy configuration, this type of line defect is thought to be made up of a string of alternating pentagons and heptagons [76]. This lattice distortion induces localization of electronic states near the Fermi level at the grain boundary, which is therefore detected by STM as an apparently elevated line [71, 77]. Some examples of grain boundaries are shown in Fig. 9. Although this type of defect usually passed unnoticed among other features (e.g., surface and subsurface steps) in the low-resolution STM height images (Fig. 9(a)), it was readily detectable in their simultaneously recorded current images (Fig. 9(b); the grain boundaries are indicated by white arrows). The upper left part of Figs. 9(a) and 9(b) is presented in more detail in Figs. 9(c) and 9(d), respectively. The domain encircled inside the grain boundary as indicated by the white line in Fig. 9(d) exhibits a superperiodic structure (i.e., a Moiré pattern). Moiré patterns in graphitic systems result from the relative rotation of the two topmost graphene layers [71], and in the present work were frequently observed for the highly graphitized films. This is most probably a consequence of the random stacking of the reduced graphene oxide sheets in the starting HG film, which cannot be fully reverted to a perfect AB stacking even at the highest annealing temperature. High resolution images of a grain boundary and associated Moiré pattern are given in Figs. 9(e) and 9(f). The grain boundary is indicated by a red line in Fig. 9(e), which is seen in this case as a string of discrete bright features. The carbon lattice is resolved in Fig. 9(f), revealing a slightly different (~3°) crystallographic orientation on both sides of the boundary (see full and dotted white lines as a guide to the eye), which in turn confirms the nature of these line defects as grain boundaries and the development of continuous but polycrystalline layers upon graphitization. From Figs. 9(a) and 9(b) and additional STM images, the typical size of the grains was estimated to be a few hundred nanometers.

Hence, in the light of all the experimental evidence presented here, the graphitization process of the reduced graphene oxide films can be finally rationalized according to the following scheme: (i) First annealing step: Removal of oxygen functional groups and generation of atomic vacancies within the reduced graphene oxide sheets; (ii) Second annealing step: Annihilation of atomic vacancies and coalescence of overlapping sheets to yield continuous, polycrystalline layers that are essentially free of defects except for the presence of grain boundaries. Lastly, we note that such structural evolution can account for many of the results obtained by the different characterization techniques: (1) A highly graphitized film composed of polycrystalline layers having domains a few hundred nanometers large (i.e., sample HG1500-2700) can be expected to exhibit a non-negligible Raman D band arising from the grain boundaries, as was actually observed (see Fig. 3(b) and Table 1). (2) As the polycrystalline layers of sample HG1500-2700 were for the most part free of other defects, then its in-plane crystallite size (L_a) derived from Raman spectroscopy (Table 1) should be comparable to the size of the domains as observed by STM, which was the case as well. (3) In such a polycrystalline film, we cannot expect to have perfect AB Bernal stacking of the layers throughout the whole sample, as evidenced by the Moiré patterns of Fig. 9. This is

Nano Res. 2013, 6(3): 216–233 229

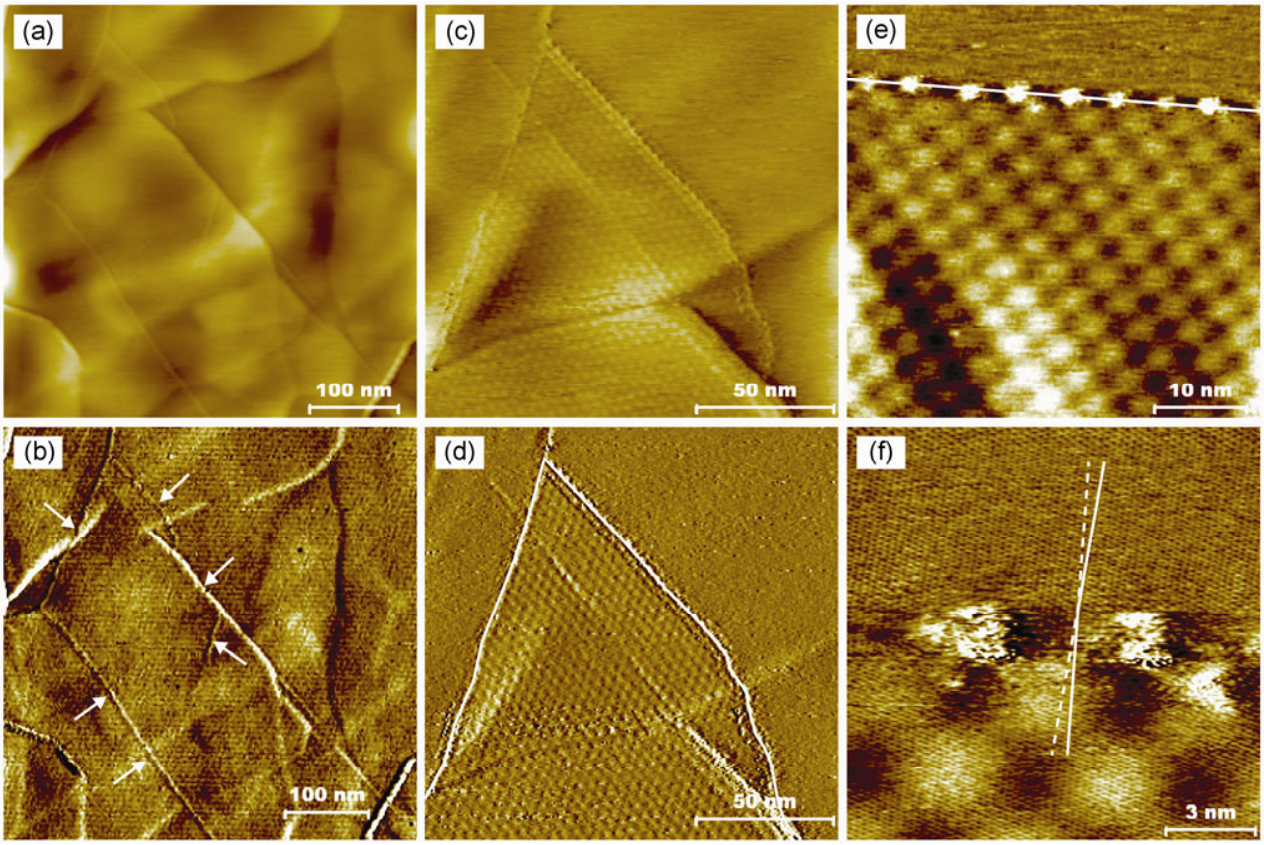

Figure 9 Height (a), (c) and corresponding current (b), (d) STM images of the HG1500-2700 film revealing the presence of grain boundaries (indicated by white arrows in (b) and by white lines in (d)). (e), (f) Height STM images of a grain boundary (indicated by a white line in (e)) and a Moiré pattern on one side of the boundary. The orientation of the carbon lattice on each side of the boundary is indicated by solid white lines in (f). Tunneling parameters: 0.2–0.8 nA (tunneling current) and 100–800 mV (bias voltage).

in agreement with the analysis of the Raman G′ band of sample HG1500-2700 (Fig. 4), which revealed a significant fraction of non-Bernal stacking. (4) Many properties of the highly graphitized films can be expected to be dominated by the presence of a high density of grain boundaries (i.e., relatively small domain sizes). Specifically, in comparing the electrical conductivity and reactivity towards gasification of the HG1500-2700 film with the results obtained for HOPG as a reference sample (Table 1 and Fig. 5), we have to take into account that HOPG, a mosaic crystal, possesses much larger domain sizes (typically from several to a few tens of micrometers) [78] and hence a much lower density of grain boundaries in its lattice. Because grain boundaries are highly reactive sites and generally act as scattering centers for the charge carriers [64], the reactivity of the HG1500-2700 film should be higher than that of HOPG (Fig. 5); similarly, its electrical conductivity should remain below that of HOPG and, a fortiori, below that of single-crystal graphite (Table 1). Consequently, further significant improvement in the electrical conductivity of the films should only be possible if we are able to decrease the density of grain boundaries. Since we cannot expect the annihilation of the grain boundaries even at graphitization temperatures higher than those employed here [76], a different approach must be adopted. Because the grain boundaries are assumed to originate from the edges of the individual reduced graphene oxide sheets, using much larger sheets in the preparation of the films could offer a way out. Aqueous dispersions of graphene oxide sheets with lateral sizes up to 50 μm have been reported and could be used to this end [79]. (5) The coalescence of the sheets to yield continuous polycrystalline layers should imply a very high mobility of the carbon atoms

230 Nano Res. 2013, 6(3): 216–233

involved in the process, particularly those at the sheet edges. It is thus conceivable that some of these atoms can go astray and end up trapped as interstitials in-between the graphene layers (Fig. 7(f)). The process of sheet coalescence could also be invoked to explain some *a priori* unexpected trends in the experimental results, for instance, the evolution of the d_{002} parameter (Table 1). The onset of coalescence, which appeared to take place at the lowest temperatures of the second annealing step (Fig. 6), could disturb the stacking of the sheets on a local scale before interlayer consolidation is eventually achieved at the highest graphitization temperatures. This mechanism would account for the transitional increase in the d_{002} parameter of the films graphitized at 1,800 and 2,100 ˚C observed during the second annealing step (Table 1).

4 Conclusions

A very high level of structural restoration has been achieved for reduced graphene oxide sheets assembled into free-standing, paper-like films by graphitization, yielding thin films that approach the characteristics of highly oriented graphites. As a result, the electrical conductivity of the graphitized films reached values as high as 577,000 $S \cdot m^{-1}$, which are by far the largest reported to date for any material derived from graphene oxide and about one quarter of the value measured for pristine single-crystal graphite, taken as the ultimate upper limit for graphitic systems. Extensive characterization of the films indicated that there are two main stages of transformation during their graphitization: (i) full removal of residual oxygen functional groups from the reduced graphene oxide sheets and concomitant generation of atomic vacancies (first annealing step, 1,500 ˚C), and (ii) annihilation of the vacancies and coalescence of adjacent overlapping sheets to yield continuous polycrystalline layers (second annealing step, 1,800–2,700 ˚C). The individual domains in the polycrystalline layers were seen to be essentially free of even point defects and their size (a few hundred nanometers) was mainly determined by the dimensions of the starting reduced graphene oxide sheets. As the domains themselves were defect-free, the prevailing type of defect within the layers was the grain boundaries separating neighboring domains, which were thought to govern many properties of the highly graphitized films. Finally, we envisage that the method proposed here can also be applied to fully restore the graphitic lattice of isolated, individual reduced graphene oxide sheets (as opposed to sheets assembled into films), provided that suitable substrates are used for the sheets. Because of its extreme heat resistance and the fact that it has already been shown to be an ideal substrate for pristine graphene, hexagonal boron nitride could be a good candidate to this end.

Acknowledgements

Financial support from the Spanish MINECO (project No. MAT2011-26399) is gratefully acknowledged. R. R. is grateful for the receipt of a pre-doctoral contract (FPU) from the Spanish MECD.

Electronic Supplementary Material: Further details of the XPS analyses of the samples and Raman spectra of samples prepared by one-step annealing are available in the online version for this article at http://dx.doi.org/10.1007/s12274-013-0298-6.

References

[1] Geim, A. K.; Novoselov, K. S. The rise of graphene. *Nature Mater.* **2007**, *6*, 183–191.

[2] Geim, A. K. Graphene: Status and prospects. *Science* **2009**, *324*, 1530–1534.

[3] Schwierz, F. Graphene transistors. *Nat. Nanotechnol.* **2010**, *5*, 487–496.

[4] Luo, B.; Liu, S. M.; Zhi, L. J. Chemical approaches toward graphene-based nanomaterials and their applications in energy-related areas. *Small* **2012**, *8*, 630–646.

[5] Liu, Y. X.; Dong, X. C.; Chen, P. Biological and chemical sensors based on graphene materials. *Chem. Soc. Rev.* **2012**, *41*, 2283–2307.

[6] Akhavan, O.; Ghaderi, E.; Rahighi, R. Toward single-DNA electrochemical biosensing by graphene nanowalls. *ACS Nano* **2012**, *6*, 2904–2916.

[7] Machado, B. F.; Serp, P. Graphene-based materials for catalysis. *Catal. Sci. Technol.* **2012**, *2*, 54–75.

[8] Feng, L. Z.; Liu, Z. Graphene in biomedicine: Opportunities and challenges. *Nanomedicine* **2011**, *6*, 317–324.

[9] Park, S.; Ruoff, R. S. Chemical methods for the production of graphenes. *Nat. Nanotechnol.* **2009**, *4*, 217–224.

[10] Wei, D. C.; Liu, Y. Q. Controllable synthesis of graphene and its applications. *Adv. Mater.* **2010**, *22*, 3225–3241.

[11] Guo, S. J.; Dong, S. J. Graphene nanosheet: Synthesis, molecular engineering, thin film, hybrids, and energy and analytical applications. *Chem. Soc. Rev.* **2011**, *40*, 2644–2672.

[12] Dreyer, D. R.; Park, S.; Bielawski, C. W.; Ruoff, R. S. The chemistry of graphene oxide. *Chem. Soc. Rev.* **2010**, *39*, 228–240.

[13] Esfandiar, A.; Akhavan, O.; Irajizad, A. Melatonin as a powerful bio-oxidant for reduction of graphene oxide. *J. Mater. Chem.* **2011**, *21*, 10907–10914.

[14] Mao, S.; Pu, H. H.; Chen, J. H. Graphene oxide and its reduction: Modeling and experimental progress. *RSC Adv.* **2012**, *2*, 2643–2662.

[15] Pei, S. F.; Cheng, H. M. The reduction of graphene oxide. *Carbon* **2012**, *50*, 3210–3228.

[16] Akhavan, O.; Ghaderi, E. Escherichia coli bacteria reduced graphene oxide to bactericidal graphene in a self-limiting manner. *Carbon* **2012**, *50*, 1853–1860.

[17] Akhavan, O.; Kalaee, M.; Alavi, Z. S.; Ghiasi, S. M. A.; Esfandiar, A. Increasing the antioxidant activity of green tea polyphenols in the presence of iron for the reduction of graphene oxide. *Carbon* **2012**, *50*, 3015–3025.

[18] Compton, O. C.; Nguyen, S. T. Graphene oxide, highly reduced graphene oxide, and graphene: Versatile building blocks for carbon-based materials. *Small* **2010**, *6*, 711–723.

[19] Eda, G.; Chhowalla, M. Chemically derived graphene oxide: Towards large-area thin-film electronics and optoelectronics. *Adv. Mater.* **2010**, *22*, 2392–2415.

[20] Gómez-Navarro, C.; Meyer, J. C.; Sundaram, R. S.; Chuvilin, A.; Kurasch, S.; Burghard, M.; Kern, K.; Kaiser, U. Atomic structure of reduced graphene oxide. *Nano Lett.* **2010**, *10*, 1144–1148.

[21] Erickson, K.; Erni, R.; Lee, Z.; Alem, N.; Gannett, W.; Zettl, A. Determination of the local chemical structure of graphene oxide and reduced graphene oxide. *Adv. Mater.* **2010**, *22*, 4467–4472.

[22] Gómez-Navarro, C.; Weitz, R. T.; Bittner, A. M.; Scolari, M.; Mews, A.; Burghard, M.; Kern, K. Electronic transport properties of individual chemically reduced graphene oxide sheets. *Nano Lett.* **2007**, *7*, 3499–3503.

[23] Mattevi, C.; Eda, G.; Agnoli, S.; Miller, S.; Mkhoyan, K. A.; Celik, O.; Mastrogiovanni, D.; Granozzi, G.; Garfunkel, E.; Chhowalla, M. Evolution of electrical, chemical, and structural properties of transparent and conducting chemically derived graphene thin films. *Adv. Funct. Mater.* **2009**, *19*, 2577–2583.

[24] López, V.; Sundaram, R. S.; Gómez-Navarro, C.; Olea, D.; Burghard, M.; Gómez-Herrero, J.; Zamora, F.; Kern, K. Chemical vapor deposition repair of graphene oxide: A route to highly-conductive graphene monolayers. *Adv. Mater.* **2009**, *21*, 4683–4686.

[25] Dai, B. Y.; Fu, L.; Liao, L.; Liu, N.; Yan, K.; Chen, Y. S.; Liu, Z. F. High-quality single-layer graphene via reparative reduction of graphene oxide. *Nano Res.* **2011**, *4*, 434–439.

[26] Cheng, M.; Yang, R.; Zhang, L. C.; Shi, Z. W.; Yang, W.; Wang, D. M.; Xie, G. B.; Shi, D. X.; Zhang, G. Y. Restoration of graphene from graphene oxide by defect repair. *Carbon* **2012**, *50*, 2581–2587.

[27] Kholmanov, I. N.; Edgeworth, J.; Cavaliere, E.; Gavioli, L.; Magnuson, C.; Ruoff, R. S. Healing of structural defects in the topmost layer of graphite by chemical vapor deposition. *Adv. Mater.* **2011**, *23*, 1675–1678.

[28] Matuyama, E. Pyrolysis of graphitic acid. *J. Phys. Chem.* **1954**, *58*, 215–219.

[29] Maire, J.; Colas, H.; Maillard, P. Membranes de carbone et de graphite et leurs propietes. *Carbon* **1968**, *6*, 555–560.

[30] Toyoda, S.; Yamakawa, T.; Kobayashi, K.; Yamada, Y. Anisotropy of g-value in a graphitized carbon film. *Carbon* **1972**, *10*, 646–647.

[31] Matsuo, Y.; Sugie, Y. Preparation, structure and electrochemical property of pyrolytic carbon from graphite oxide. *Carbon* **1998**, *36*, 301–303.

[32] Matsuo, Y.; Sugie, Y. Pyrolytic carbon from graphite oxide as an anode of lithium-ion cells in 1 M $LiClO_4$ propylene carbonate solution. *Electrochem. Solid-State Lett.* **1998**, *1*, 204–206.

[33] Matsuo, Y.; Sugie, Y. Electrochemical lithiation of carbon prepared from pyrolysis of graphite oxide. *J. Electrochem. Soc.* **1999**, *146*, 2011–2014.

[34] Yang, D. X.; Velamakanni, A.; Bozoklu, G.; Park, S.; Stoller, M.; Piner, R. D.; Stankovich, S.; Jung, I.; Field, D. A.; Ventrice Jr, C. A. et al. Chemical analysis of graphene oxide films after heat and chemical treatments by X-ray photoelectron and micro-Raman spectroscopy. *Carbon* **2009**, *47*, 145–152.

[35] Akhavan, O. The effect of heat treatment on formation of graphene thin films from graphene oxide nanosheets. *Carbon* **2010**, *48*, 509–519.

[36] Chen, C. M.; Huang, J. Q.; Zhang, Q.; Gong, W. Z.; Yang, Q. H.; Wang, M. Z.; Yang, Y. G. Annealing a graphene oxide film to produce a free standing high conductive graphene film. *Carbon* **2012**, *50*, 659–667.

[37] Oberlin, A. Carbonization and graphitization. *Carbon* **1984**, *22*, 521–541.

[38] Long, D. H.; Li, W.; Qiao, W. M.; Miyawaki, J.; Yoon, S. H.; Mochida, I.; Ling, L. C. Graphitization behaviour of chemically derived graphene sheets. *Nanoscale* **2011**, *3*, 3652–3656.

[39] Ghosh, T.; Biswas, C.; Oh, J.; Arabale, G.; Hwang, T.; Luong, N. D.; Jin, M. H.; Lee, Y. H.; Nam, J. D. Solution-processed graphite membrane from reassembled graphene oxide. *Chem. Mater.* **2011**, *24*, 594–599.

[40] Abouimrane, A.; Compton, O. C.; Amine, K.; Nguyen, S. T. Non-annealed graphene paper as a binder-free anode for lithium-ion batteries. *J. Phys. Chem. C* **2010**, *114*, 12800–12804.

[41] Liang, J. J.; Huang, Y.; Oh, J.; Kozlov, M.; Sui, D.; Fang, S. L.; Baughman, R. H.; Ma, Y. F.; Chen, Y. S. Electromechanical actuators based on graphene and graphene/Fe_3O_4 hybrid paper. *Adv. Funct. Mater.* **2011**, *21*, 3778–3784.

[42] Zhang, L. L.; Zhao, X.; Stoller, M. D.; Zhu, Y. W.; Ji, H. X.; Murali, S.; Wu, Y. P.; Perales, S.; Clevenger, B.; Ruoff, R. S. Highly conductive and porous activated reduced graphene oxide films for high-power supercapacitors. *Nano Lett.* **2012**, *12*, 1806–1812.

[43] Gao, H. C.; Wang, Y. X.; Xiao, F.; Ching, C. B.; Duan, H. W. Growth of copper nanocubes on graphene paper as free-standing electrodes for direct hydrazine fuel cells. *J. Phys. Chem. C* **2012**, *116*, 7719–7725.

[44] Hummers Jr., W. S.; Offeman, R. E. Preparation of graphitic oxide. *J. Am. Chem. Soc.* **1958**, *80*, 1339–1339.

[45] Paredes, J. I.; Villar-Rodil, S.; Solís-Fernández, P.; Martínez-Alonso, A.; Tascón, J. M. D. Atomic force and scanning tunneling microscopy imaging of graphene nanosheets derived from graphite oxide. *Langmuir* **2009**, *25*, 5957–5968.

[46] Fernández-Merino, M. J.; Guardia, L.; Paredes, J. I.; Villar-Rodil, S.; Solís-Fernández, P.; Martínez-Alonso, A.; Tascón, J. M. D. Vitamin C is an ideal substitute for hydrazine in the reduction of graphene oxide suspensions. *J. Phys. Chem. C* **2010**, *114*, 6426–6432.

[47] Li, D.; Müller, M. B.; Gilje, S.; Kaner, R. B.; Wallace, G. G. Processable aqueous dispersions of graphene nanosheets. *Nat. Nanotechnol.* **2008**, *3*, 101–105.

[48] Paci, J. T.; Belytschko, T.; Schatz, G. C. Computational studies of the structure, behavior upon heating, and mechanical properties of graphite oxide. *J. Phys. Chem. C* **2007**, *111*, 18099–18111.

[49] Bagri, A.; Mattevi, C.; Acik, M.; Chabal, Y. J.; Chhowalla, M.; Shenoy, V. B. Structural evolution during the reduction of chemically derived graphene oxide. *Nat. Chem.* **2010**, *2*, 581–587.

[50] Solís-Fernández, P.; Rozada, R.; Paredes, J. I.; Villar-Rodil, S.; Fernández-Merino, M. J.; Guardia, L.; Martínez-Alonso, A.; Tascón, J. M. D. Chemical and microscopic analysis of graphene prepared by different reduction degrees of graphene oxide. *J. Alloy. Compd.* **2012**, *536*, S532–S537.

[51] Stankovich, S.; Dikin, D. A.; Piner, R. D.; Kohlhaas, K. A.; Kleinhammes, A.; Jia, Y. Y.; Wu, Y.; Nguyen, S. T.; Ruoff, R. S. Synthesis of graphene-based nanosheets via chemical reduction of exfoliated graphite oxide. *Carbon* **2007**, *45*, 1558–1565.

[52] Kim, M. C.; Hwang, G. S.; Ruoff, R. S. Epoxide reduction with hydrazine on graphene: A first principles study. *J. Chem. Phys.* **2009**, *131*, 064704.

[53] Gao, X. F.; Jang, J.; Nagase, S. Hydrazine and thermal reduction of graphene oxide: Reaction mechanisms, product structures, and reaction design. *J. Phys. Chem. C* **2010**, *114*, 832–842.

[54] Figueiredo, J. L.; Pereira, M. F. R.; Freitas, M. M. A.; Órfão, J. J. M. Modification of the surface chemistry of activated carbons. *Carbon* **1999**, *37*, 1379–1389.

[55] Chen, H. Q.; Müller, M. B.; Gilmore, K. J.; Wallace, G. G.; Li, D. Mechanically strong, electrically conductive, and biocompatible graphene paper. *Adv. Mater.* **2008**, *20*, 3557–3561.

[56] Ferrari, A. C.; Robertson, J. Interpretation of Raman spectra of disordered and amorphous carbon. *Phys. Rev. B* **2000**, *61*, 14095–14107.

[57] Pimenta, M. A.; Dresselhaus, G.; Dresselhaus, M. S.; Cançado, L. G.; Jorio, A.; Saito, R. Studying disorder in graphite-based systems by Raman spectroscopy. *Phys. Chem. Chem. Phys.* **2007**, *9*, 1276–1290.

[58] Tuinstra, F.; Koenig, J. L. Raman spectrum of graphite. *J. Chem. Phys.* **1970**, *53*, 1126–1130.

[59] Cançado, L. G.; Takai, K.; Enoki, T.; Endo, M.; Kim, Y. A.; Mizusaki, H.; Jorio, A.; Coelho, L. N.; Magalhães-Paniago, R.; Pimenta, M. A. General equation for the determination of the crystallite size L_a of nanographite by Raman spectroscopy. *Appl. Phys. Lett.* **2006**, *88*, 163106.

[60] Malard, L. M.; Pimenta, M. A.; Dresselhaus, G.; Dresselhaus, M. S. Raman spectroscopy in graphene. *Phys. Rep.* **2009**, *473*, 51–87.

[61] Lahaye, J.; Ehrburger, P. *Fundamental Issues in Control of Carbon Gasification Reactivity*; Kluwer Academic Publishers: Dordrecht, 1991.

[62] Cuesta, A.; Martínez-Alonso, A.; Tascón, J. M. D. Carbon reactivity in an oxygen plasma: A comparison with reactivity in molecular oxygen. *Carbon* **2001**, *39*, 1135–1146.

[63] Solís-Fernández, P.; Paredes, J. I.; Villar-Rodil, S.; Guardia, L.; Fernández-Merino, M. J.; Dobrik, G.; Biró, L. P.; Martínez-Alonso, A.; Tascón, J. M. D. Global and local oxidation behavior of reduced graphene oxide. *J. Phys. Chem. C* **2011**, *115*, 7956–7966.

[64] Banhart, F.; Kotakoski, J.; Krasheninnikov, A. V. Structural defects in graphene. *ACS Nano* **2010**, *5*, 26–41.

[65] Spain, I. L. Electronic transport properties of graphite, carbons, and related materials. In *Chemistry and Physics of Carbon*. Vol. 16. Walker Jr., P. L.; Thrower, P. A., Eds.; New York: Marcel Dekker, 1981; pp 119–304.

[66] Morelli, D. T.; Uher, C. T^2 dependence of the in-plane resistivity of graphite at very low temperatures. *Phys. Rev. B* **1984**, *30*, 1080–1082.

[67] Nakajima, T.; Nakane, K.; Kawaguchi, M.; Watanabe, N. Preparation, structure and electrical conductivity of graphite intercalation compound with titanium fluoride. *Carbon* **1987**, *25*, 685–689.

[68] Hahn, J. R.; Kang, H. Vacancy and interstitial defects at graphite surfaces: Scanning tunneling microscopic study of the structure, electronic property, and yield for ion-induced defect creation. *Phys. Rev. B* **1999**, *60*, 6007–6017.

[69] Solís-Fernández, P.; Paredes, J. I.; Martínez-Alonso, A.; Tascón, J. M. D. New atomic-scale features in graphite surfaces treated in a dielectric barrier discharge plasma. *Carbon* **2008**, *46*, 1364–1367.

[70] Paredes, J. I.; Solís-Fernández, P.; Martinez-Alonso, A.; Tascón, J. M. D. Atomic vacancy engineering of graphitic surfaces: Controlling the generation and harnessing the migration of the single vacancy. *J. Phys. Chem. C* **2009**, *113*, 10249–10255.

[71] Wong, H. S.; Durkan, C.; Chandrasekhar, N. Tailoring the local interaction between graphene layers in graphite at the atomic scale and above using scanning tunneling microscopy. *ACS Nano* **2009**, *3*, 3455–3462.

[72] Magonov, S. N.; Whangbo, M. H. *Surface Analysis with STM and AFM: Experimental and Theoretical Aspects of Image Analysis*; VCH: Weinheim, 1996.

[73] Paredes, J. I.; Martínez-Alonso, A.; Tascón, J. M. D. Early stages of plasma oxidation of graphite: Nanoscale physicochemical changes as detected by scanning probe microscopies. *Langmuir* **2002**, *18*, 4314–4323.

[74] Banhart, F. Irradiation effects in carbon nanostructures. *Rep. Prog. Phys.* **1999**, *62*, 1181–1221.

[75] Barreiro, A.; Börrnert, F.; Rümmeli, M. H.; Büchner, B.; Vandersypen, L. M. K. Graphene at high bias: Cracking, layer by layer sublimation, and fusing. *Nano Lett.* **2012**, *12*, 1873–1878.

[76] Kurasch, S.; Kotakoski, J.; Lehtinen, O.; Skákalová, V.; Smet, J.; Krill, C. E.; Krasheninnikov, A. V.; Kaiser, U. Atom-by-atom observation of grain boundary migration in graphene. *Nano Lett.* **2012**, *12*, 3168–3173.

[77] Simonis, P.; Goffaux, C.; Thiry, P. A.; Biró, L. P.; Lambin, P.; Meunier, V. STM study of a grain boundary in graphite. *Surf. Sci.* **2002**, *511*, 319–322.

[78] Ohler, M.; Sanchez del Rio, M.; Tuffanelli, A.; Gambaccini, M.; Taibi, A.; Fantini, A.; Pareschi, G. X-ray topographic determination of the granular structure in a graphite mosaic crystal: A three-dimensional reconstruction. *J. Appl. Cryst.* **2000**, *33*, 1023–1030.

[79] Dong, X. C.; Su, C. Y.; Zhang, W. J.; Zhao, J. W.; Ling, Q. D.; Huang, W.; Chen, P.; Li, L. J. Ultra-large single-layer graphene obtained from solution chemical reduction and its electrical properties. *Phys. Chem. Chem. Phys.*, **2010**, *12*, 2164–2169.

From Graphene Oxide to Pristine Graphene: Revealing the Inner Workings of the Full Structural Restoration

Rubén Rozada[a], Juan I. Paredes[a], María J. López[b], Silvia Villar-Rodil[a], Iván Cabria[b], Julio A. Alonso[b], Amelia Martínez-Alonso[a], Juan M. D. Tascón[a]

[a]*Instituto Nacional del Carbón, INCAR-CSIC, Apartado 73, 33080 Oviedo, Spain*

[b]*Departamento de Física Teórica, Atómica y Óptica, Universidad de Valladolid, 47011 Valladolid, Spain*

High temperature annealing is the only method known to date that allows a complete repair of the defective lattice of graphenes derived from graphite oxide, but most relevant aspects of such restoration process are poorly understood. In this investigation, both experimental (scanning probe microscopy) and theoretical (molecular dynamics simulations), the thermal evolution of individual graphene oxide sheets is rationalized on the basis of the generation and dynamics of atomic vacancies in the carbon lattice. For unreduced and mildly reduced graphene oxide sheets, the amount of generated vacancies was so large that they disintegrated at 1773-2073 K. By contrast, highly reduced sheets survived annealing and their structure could be completely restored at 2073 K. For the latter, a minority atomic-sized defect with six-fold symmetry was observed and ascribed to a stable cluster of nitrogen dopants. The thermal behavior of the sheets was significantly altered when they were supported onto a vacancy-decorated graphite substrate, as well as for overlapped/stacked sheets. In these cases, a net transfer of carbon atoms between neighboring sheets via atomic vacancies takes place, affording additional healing process. Direct evidence of sheet coalescence with the step edge of the graphite substrate was also gathered from experiments and theory.

1 Introduction

Due to a combination of unsurpassed physical properties (e.g., electronic, mechanical, thermal and optical), it is generally agreed that graphene possesses a strong potential to become a key material in many relevant technological applications.[1,2] For example, this strictly two-dimensional, sp^2-hybridized carbon material and some of its derivatives are being extensively investigated towards their use in high frequency transistors,[3] transparent conducting electrodes,[4] energy conversion and storage devices,[5] mechanically reinforced polymer composites,[6] catalytic materials[7] and biomedical systems (drug delivery, imaging, etc.),[8] among other possibilities.

An obvious and necessary condition to the widespread implementation of graphene in such applications is the availability of cost-effective methods for the large-scale production of this material with characteristics that can be tailored to the specific intended use. To this end, significant research efforts have been directed over the last years to the development of both bottom-up and top-down synthesis approaches.[9,10] The former include most significantly chemical vapor

deposition of hydrocarbons onto suitable transition metal substrates (nickel, copper),[11] whereas the latter are mainly focused on the processing of either pristine graphite or graphite oxide by different means.[12,13] The so-called graphite oxide route to graphene has been particularly rewarding not only in terms of bulk production at an affordable cost, but also concerning other features that have a direct bearing on practical issues, such as the colloidal processability of the obtained material in aqueous and organic media or its ease of combination with other materials to form composites and hybrids.[10,14]

The main attraction of graphite oxide as a precursor to graphene lies in the fact that this derivative of graphite, as opposed to the case of its pristine counterpart, can be readily exfoliated to give single layer sheets (graphene oxide sheets), with a subsequent reduction step designed to remove the oxygen functional groups that heavily decorate the carbon skeleton of graphene oxide. Although the resulting product (referred to as reduced graphene oxide) as well as graphene oxide itself have become important materials on their own merit,[15] this approach has traditionally suffered from a significant limitation that hinders its wider utility in the graphene field: the apparent inability of the known reduction methods to fully convert graphene oxide back to pristine graphene. Indeed, virtually all the reduction methodologies that have been reported to this day, including those of chemical, electrochemical, thermal (up to moderately high temperatures) and catalytic nature, have yielded products that retain a significant amount of oxygen and structural defects, the presence of which degrades many of the exceptional properties of graphene.[16,17] To overcome this problem, alternative strategies aimed at the repair of defects in graphene oxide/reduced graphene oxide by the external supply of carbon atoms (chemical vapor deposition techniques) have been explored, but they have met with limited success.[18-20]

In this context, it has become increasingly apparent that high temperature (≥1773 K) heat treatment, i.e. graphitization, is probably the only effective way to achieve a thorough conversion of graphene oxide/reduced graphene oxide to graphene sheets of the highest structural quality. Indeed, recent work by several groups has demonstrated a dramatic decrease in the amount of structural defects and residual oxygen after subjecting reduced graphene oxide samples to graphitization treatments.[21-25] Nevertheless, such studies were conducted either on bulk powders[21-24] or on macroscopically assembled films,[23,25] which probably precluded the observation of many relevant processes taking place upon thermal annealing that can only be investigated and understood by the scrutiny of individual sheets under certain controlled conditions. More specifically, a number of fundamental questions concerning the high–temperature evolution of graphene oxide and reduced graphene oxide sheets have not yet been addressed, including the following: (1) Is it possible to convert a (reduced) graphene oxide sheet to pristine, completely defect-free graphene by heat treatment? If this is the case, what is the temperature required for it to happen? (2) How does the presence (amount) of oxygen functional groups grafted on the carbon skeleton of graphene oxide affect its thermal evolution? (3) What is the effect of other heteroatoms that may be present on graphene oxide (e.g., nitrogen) on its propensity to be healed? (4) Because the sheets need to be typically supported on a substrate, how do the characteristics of the substrate (e.g., inert vs. reactive) influence the thermal evolution of the sheets? (5) How do neighboring sheets interact with each other during the high temperature annealing?

To seek answers to these questions, in the work reported here we have carried out a combined experimental and theoretical study on the structural evolution of graphene oxide and reduced graphene oxide sheets upon graphitization treatments. Nanometer- and atomic-scale imaging of

individual sheets or assemblies of a few sheets by scanning tunneling and atomic force microscopy (STM/AFM), together with molecular dynamics simulations, revealed a wealth of new information on the basic processes underlying the healing of the carbon lattice in this graphene derivative. In addition to illuminating the thermal behavior of graphene oxide/reduced graphene oxide materials, the knowledge generated by the present results should be useful in assisting the design of improved thermal routes to their structural restoration.

2 Results and discussion

2.1 General thermal behavior of unreduced and chemically reduced graphene oxide sheets at high temperature

To provide the conceptual starting point and rationale for the investigations reported here, some general considerations about the known structure and thermal behavior of graphene oxide need to be taken into account. First, previous work has determined that the carbon skeleton in graphene oxide sheets is heavily decorated by epoxide and hydroxyl functional groups on their basal plane, whereas a minority of other functionalities (carboxyls, carbonyls, etc) can be found at the sheet edges.[26-28] The spatial distribution of these oxygen groups is locally inhomogeneous: isolated domains of essentially intact, defect-free graphene a few nanometers in lateral size are surrounded by strongly oxidized, predominantly sp^3-based areas where the epoxides and hydroxyls are concentrated.[29] Chemical reduction protocols (e.g., using hydrazine) typically remove most of these oxygen functionalities, so that the pristine graphene domains become larger, more numerous and interconnected in the reduced sheets.[29] Second, a large fraction of the oxygen functional groups in graphene oxide decompose by thermal annealing in a narrow range of low temperatures (~398-473 K) to yield mainly CO and CO_2 molecules, though a steady and slower CO/CO_2 evolution is observed up to at least 1273 K.[30,31] Following a heat treatment at such moderately high temperatures (~1273-1373 K), the carbon sheets still retain a non-negligible amount of residual, apparently quite stable oxygen groups.[32-34] This behavior has been qualitatively accounted for on the basis of recent theoretical simulations:[35,36] the very high local density of oxygen groups in graphene oxide promotes concerted reactions that favor, both kinetically (low activation barrier) and thermodynamically, the dissociation of many of these groups to yield CO/CO_2 molecules together with atomic vacancies in the carbon lattice. The formed carbon vacancies are rapidly saturated by some of the remaining oxygen to give, e.g., carbonyl or ether groups, which are very stable and can only be dissociated by overcoming a high energy barrier (high activation temperature).[35,36]

The previous considerations indicate that after annealing at moderately high temperatures (up to ~1373 K), the structure of the original graphene oxide/reduced graphene oxide sheets evolves into one dominated by (probably multiatomic) carbon vacancies decorated with stable oxygen groups.[37] Therefore, in the absence of an external supply of carbon atoms that could possibly close the vacancies,[38] further healing of the carbon structure towards a pristine, defect-free graphene sheet should be attained by annealing at higher temperatures to first dissociate the stable oxygen groups and then annihilate the unsaturated carbon vacancies. In this scenario, the amount of oxygen groups present on the sheets prior to their heat treatment should have a strong effect on the subsequent evolution of the carbon structure, because the number of carbon atoms that are removed from the

lattice as CO/CO_2, and therefore the number and/or size of the vacancies, must be directly related to the starting oxygen concentration. To investigate this point, graphene oxide sheets with different degrees of reduction (unreduced as well as mildly and highly reduced by chemical means) were deposited onto freshly cleaved highly oriented pyrolytic graphite (HOPG) substrates and first heat-treated at 1773 K. Such particular temperature was chosen because very recent work indicates that it suffices to remove virtually all the oxygen groups from graphene oxide-based films.[25]

Fig. 1a-c shows representative AFM images of the different starting, as-deposited sheets. They all display a similar appearance, i.e., irregular shapes with lateral sizes typically between a few and several hundred nanometers, and an apparent thickness (determined relative to the HOPG substrate) that in most cases was ~1 nm, indicating that the majority of the sheets are single-layer objects.[39] On the other hand, visible differences were observed in their thermal evolution depending on the reduction degree. The annealing step at 1773 K apparently caused a significant structural deterioration of the unreduced graphene oxide sheets (Fig. 1d), as large unfilled areas (up to a few hundreds of nanometers) of irregular shape and rough boundaries were developed within them (two examples are marked by red arrows in Fig. 1d). Their mildly reduced counterparts better endured the thermal process, although relatively large (tens of nanometers) pits were also seen to develop occasionally (Fig. 1e). By contrast, at this level of magnification in the AFM images, the highly reduced sheets were not seen to undergo any significant morphological changes (Fig. 1f) apart from a decrease in their apparent thickness, which was also observed for the unreduced and mildly reduced sheets. This thickness closely approached the value for single-layer, pristine graphene (~0.34 nm; see overlaid line profiles in Fig. 1d-f). Because the sheets were supported on the surface of a substrate (as-cleaved HOPG) that is chemically and structurally identical to perfect graphene, the AFM-derived thickness values are consistent with the idea that all these sheets have undergone extensive deoxygenation.[40]

Annealing at higher temperatures further accentuated the differences between sheets reduced to different extents. For example, heat treatment at 2073 K led to the disintegration of the unreduced graphene oxide sheets as only some disjoined fragments were left on the HOPG surface (Fig. 1g). The mildly reduced sheets experienced a lesser, but still considerable, level of disintegration as the sheets preserved in the sample were rather scarce and showed smaller sizes after the heat treatment (Fig. 1h). On the contrary, their highly reduced counterparts survived the annealing process without any apparent sign of deterioration (Fig. 1i). At such annealing temperature, the contour of the sheets become noticeable rounded, which is thought to be a result of the high mobility of the carbon atoms at the sheet edges.[41]

We interpret that in the case of unreduced graphene oxide (Fig. 1a,d and g), a very large fraction of carbon atoms are removed as CO and CO_2 from the lattice during the thermal annealing, in particular from the highly oxidized regions where the oxygen functional groups are clustered. Because the highly oxidized regions originally formed a continuous, percolated network in between intact graphene domains,[29] it is plausible that the number of carbon atoms left behind in such regions upon heat treatment is too low to be able to strongly hold the intact graphene domains together. As a result, the latter can easily detach from the sheets at the high annealing temperatures, thus giving rise to unfilled areas within the sheets at 1773 K (Fig. 1d) and to their disintegration at higher temperatures (Fig. 1g). This idea is supported by the presence of remains of the small fragments that agglomerate at the boundaries of these areas (e.g. see red arrows in Fig. 1d). Indeed, detachment of minute graphene domains (<10 nm) from this type of graphene derivative has been

previously observed in a somewhat different context (oxidation and etching processes at lower temperature).[42] For mildly reduced graphene oxide (Fig. 1b, e and h), the highly oxidized regions should be smaller and probably not so well interconnected, so a better endurance is envisaged in this case, but in any event the number of atomic vacancies that are thermally generated should still be relatively high. These vacancies can migrate and coalesce to form larger vacancies, so nanometer-sized pits would initially appear (Fig. 1e), and eventually a higher degree of damage would be generated upon further coalescence processes (Fig. 1h). Finally, in the case of highly reduced graphene oxide (Fig. 1c, f and i), relatively little oxygen is present and therefore a small number of vacancies will be thermally produced, which is not sufficient to create nanometer-sized pits in the sheets.

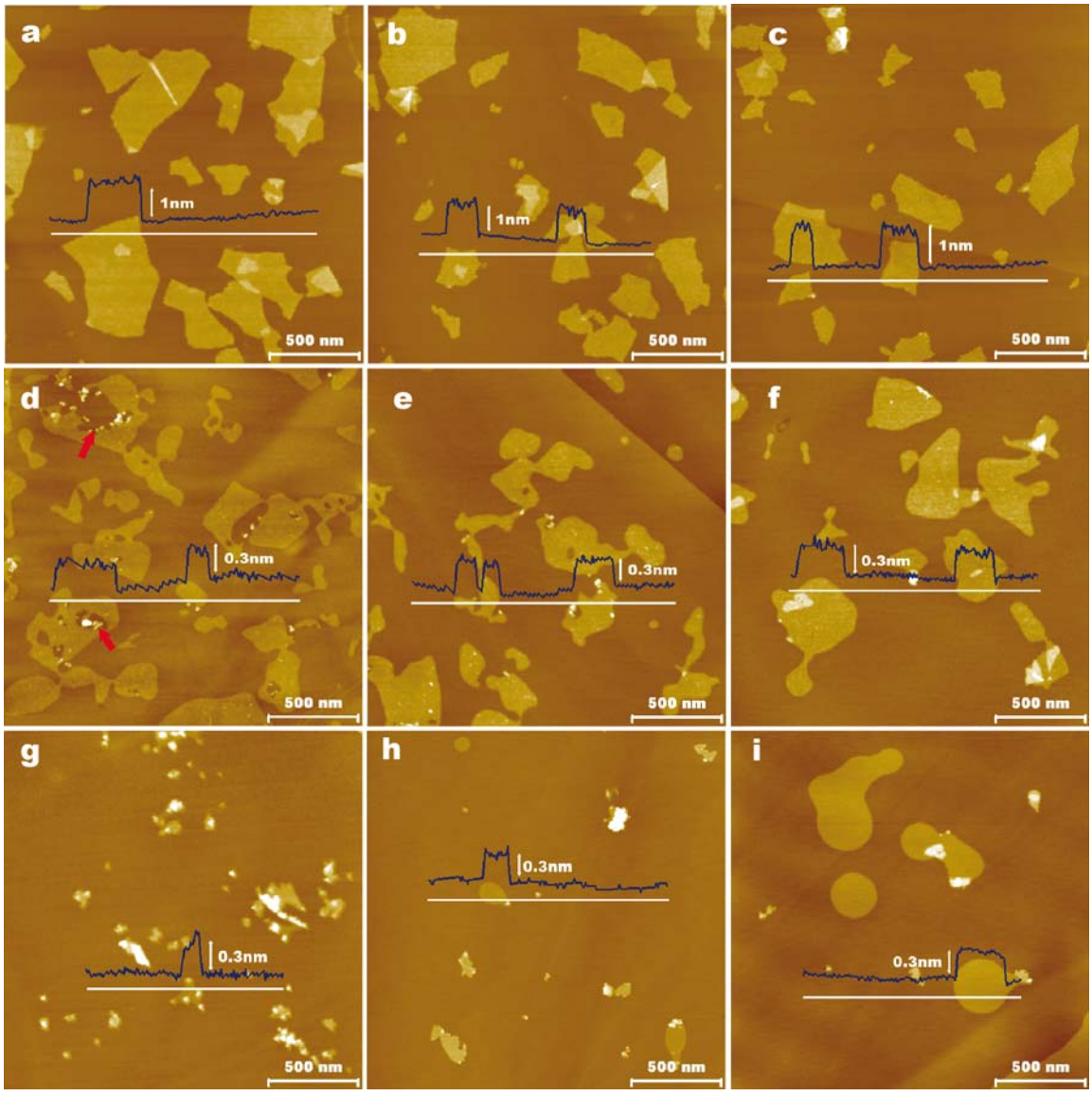

Figure 1 Nanometer-scale AFM images for the unreduced (a,d,g), mildly reduced (b,e,h) and highly reduced (c,f,i) graphene oxide sheets deposited on top of a HOPG substrate, prior to the thermal treatment (a-c) and annealed at 1773 K (d-f) and 2073 K (g-i).

To gain an approximate idea of the amount of vacancies that are involved in each of the three scenarios described in Fig. 1, we note that the fraction of carbon atoms thermally removed from the graphene oxide/reduced graphene oxide lattice can be quantitatively estimated on the basis of the

amount of CO and CO_2 evolved from the samples, as measured by temperature programmed desorption (TPD), together with the information on their elemental composition that can be obtained by X-ray photoelectron spectroscopy (XPS). The results are given in Table 1. It should be stressed that the calculated percentage of thermally removed carbon atoms most probably underestimates the actual values for the three samples. The reason is connected to the fact that the amount of evolved CO and CO_2 was measured only up to 1273 K due to limitations of the TPD apparatus. However, because the large majority (>80%) of the oxygen functional groups are removed in this temperature range,[32-34] the values provided in Table 1 should be fairly close to the real ones and therefore can be considered reasonable estimates. As could be expected, the (global) fraction of carbon atoms removed from unreduced graphene oxide is quite high (~ 28%), but locally it should be even higher in the heavily oxidized areas of the sheets. Such result lends support to the idea that only very loose connections between the intact graphene domains remain upon the heat treatment, thus facilitating the development of unfilled areas and the eventual disintegration of the sheets (Fig. 1d and g). On the other hand, it appears that the carbon lattice can withstand abstraction of about 4% of its atoms and still be healed without developing large and/or irreversible morphological changes (Fig. 1f).

Sample	Atomic composition by XPS (at. %)			Species released by TPD (mmol g^{-1})		Fraction of carbon atoms removed (%)
	C	O	N	CO	CO_2	
Unreduced graphene oxide	70.4	29.1	0.5	8.3	6.1	28
Mildly reduced graphene oxide	74.9	22.1	3.0	2.0	4.4	11
Highly reduced graphene oxide	90.1	8.1	1.8	1.4	1.9	4

Table 1 Atomic composition calculated from XPS spectra and amount of CO and CO_2 released during TPD up to 1273 K for graphene oxide and reduced graphene oxide paper-like films.

2.2 Achieving full structural restoration of individual, chemically reduced graphene oxide sheets: thermal evolution of atomic-scale defects

The previous results suggest that only graphene oxide sheets that have undergone considerable reduction by chemical means, a process not believed to be associated to significant carbon atom abstraction,[43-45] can be eventually healed through heat treatment, at least in the case of isolated sheets on the inert, atomically flat HOPG substrate. The unreduced sheets are damaged when their oxygen functionalities are completely stripped off, whereas mildly reduced graphene oxide develops pits that are too large to be eliminated at higher temperatures. For this reason, hereupon we will exclusively focus on aspects of the thermal behavior of the highly reduced sheets.

As noted above, when all the oxygen is eliminated from a sheet at a sufficiently high temperature (~1773 K),[25] the generated atomic vacancies will probably become mobile and start diffusing across the sheet. The diffusion of a given vacancy can be expected to proceed until either (1) it is annihilated at the edge of the sheet, thus effectively healing the defect, or (2) it bumps into

another vacancy, coalescing with it and forming a larger, more stable vacancy.[46] Obviously, to achieve full structural restoration of the sheet, event (1) must dominate over event (2) in the long run, but this should only be possible when the fraction of carbon atoms that were removed from the lattice is sufficiently small. Otherwise, the probability of vacancy coalescence would be very high, giving rise to large-sized vacancies. Taking into account that the mobility of a vacancy is expected to decrease with its size (for instance, the migration barrier for a monovacancy is 1.2-1.4 eV, but already 5-7 eV for a divacancy),[47,48] if the size of the coalesced vacancies becomes too large, their mobility will be severely reduced, which effectively inhibits their annihilation. On the other hand, when the vacancy size and density are kept below a certain level, efficient annihilation processes, and consequently an extensive restoration of the sheet, should be possible.

To investigate this question in the case of highly reduced graphene oxide, the sheets that had been heat treated at 1773 K were examined in more detail by STM, a technique that is well known to allow visualization of atomic vacancies and other point defects on graphitic surfaces.[49] Representative nanometer and atomic scale images for this sample are shown in Fig. 2c and d, respectively. For comparison, STM images of the starting, non-annealed sheets recorded at the same levels of magnification are also given (Fig. 2a and b). The latter display an atomically rough morphology on the nanometer scale (Fig. 2a) and a highly distorted, non-periodic structure on the atomic scale (Fig. 2b), which is consistent with the presence of residual oxygen groups and a locally strained carbon lattice, as expected for highly reduced graphene oxide.[39] Heat treatment at 1773 K brought about significant changes to the sheets, although it did not fully repair their structure: the morphology of the sheets was dominated by a large number of randomly scattered bright features (i.e. apparent protrusions) with somewhat ill-defined boundaries on the nanometer scale (Fig. 2c). The protrusions were approximately between 2 and 5 nm in lateral size and exhibited distorted patterns on the atomic scale, whereas the flat areas in-between displayed an essentially well-ordered, graphitic structure (Fig. 2d). Such characteristics are consistent with the basic hypothesis that heat treatment of the sheets generates a carbon structure decorated by atomic vacancies: it is well established that an atomic vacancy in graphite/graphene is imaged by STM as an apparent protrusion by virtue of an enhancement in the local density of electronic states near the Fermi level in the region surrounding the vacancy.[50-53] We therefore ascribe the protrusions seen in Fig. 2c and d to the atomic vacancies created in the sheets by the heat treatment. Furthermore, such features most probably correspond to multiatomic vacancies rather than monatomic ones, as the latter have been shown to be associated to smaller protrusions (~1 nm).[53] Due to the very high density of vacancies in the sample, individual protrusions were in many cases difficult to clearly make out in the nanometer-scale images (Fig. 2c), which thus tended to be visualized as slightly blurred features with ill-defined boundaries.

To probe the subsequent evolution of the vacancies, annealing experiments at increasingly higher temperatures were conducted and the resulting samples inspected again by STM: representative images are shown in Fig. 2e and f (1923 K), g and h (2073 K), and i and j (2223 K). Following heat treatment at 1923 K, a high density of protrusions was again observed, in this case ~3-5 nm wide (Fig. 2e). Although at first sight there were no drastic differences between this sample and the one annealed at 1773 K, a closer look revealed a subtle but unequivocal change, i.e., the protrusions in the former appeared to be more isolated and sharply defined features (compare Fig. 2e with c). We attribute this change to an overall decrease in the vacancy density due to the annihilation and/or coalescence of a fraction of those vacancies originally present in the sheets heat-

treated at 1773 K, which became sufficiently mobile when the temperature was increased to 1923 K. On the other hand, after annealing at 2073 K (Fig. 2g and h) the ~3-5 nm wide protrusions disappeared completely and the sheets developed an essentially pristine structure with long-range graphitic order that was only locally broken by the presence of small protrusions of uniform size (~1-1.5 nm), which were finally removed at 2223 K (Fig. 2i and j). Although such result demonstrates that a full recovery of the graphene lattice can be attained between 2073 and 2223 K,

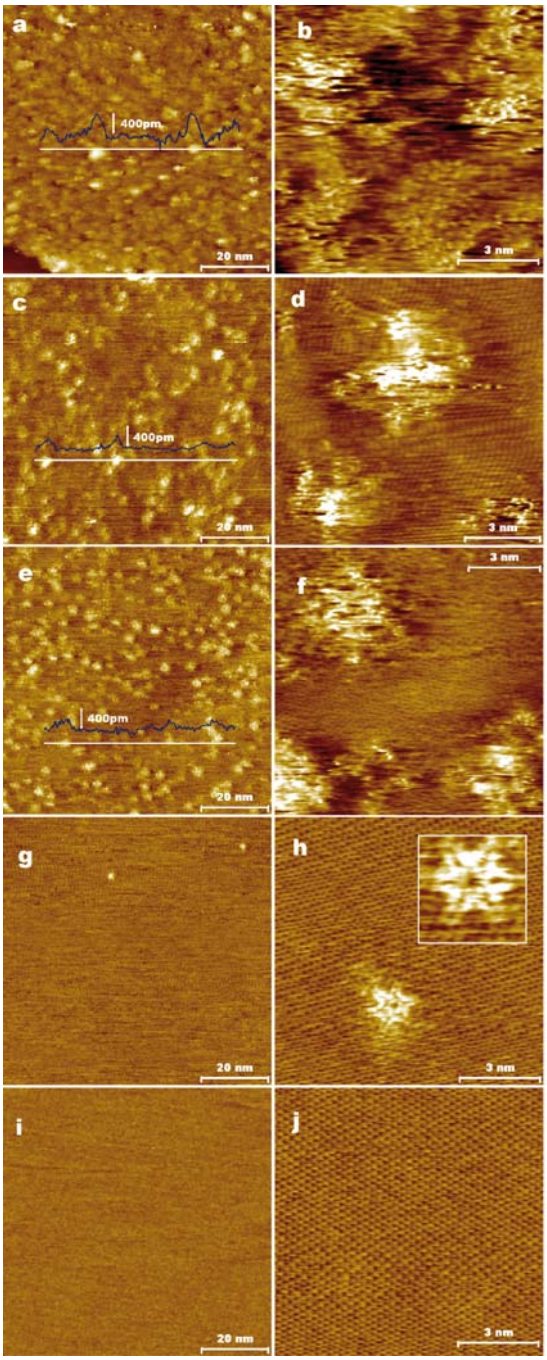

Figure 2 Nanometer- and atomic-scale STM images for the highly reduced graphene oxide sheets prior to the thermal treatment (a,b) and after annealing at 1773 K (c,d), 1923 K (e,f), 2073 K (g,h) and 2223 K (i,j). The inset to (h) is a detailed 2x2 nm^2 image showing a different image of the same type of defect. Imaging conditions: 0.3 nA (tunneling current) and 500mV (bias voltage) (a,c,e,g,i); 1-4 nA and 5-10mV (b,d,f,j); 0.5 nA and 80mV (h); 0.8nA and 50mV (inset).

it also challenges the implicit assumption that atomic vacancies are the only type of defect present in the highly reduced sheets upon thermal removal of their oxygen groups. If smaller vacancies can be associated to smaller STM protrusions and higher mobilities [47-53] and the ~1-1.5 nm wide protrusions were indeed atomic vacancies (probably monatomic ones, according to their size),[53] then the latter should not have survived the annealing process after all the larger vacancies (protrusions) were annihilated. On the contrary, they should have been the first to be annihilated. We therefore have to conclude that these small protrusions are not atomic vacancies but a different type of defect. Moreover, virtually all the protrusions remaining in the 2073 K sample exhibited a six-fold symmetry (Fig. 2h) that has never been reported for atomic vacancies (either monatomic or multiatomic) in graphitic materials. We stress that such characteristic is not the result of a tip artefact, as different STM tips consistently yielded the very same pattern. This also indicates that only one type of defect is present in the sheets following treatment at 2073 K. It is likewise worth noting that some ~1-1.5 nm wide protrusions could already be observed in the sheets annealed at 1923 K, but their proximity to larger protrusions did not allow their unambiguous identification as independent, stand-alone defects.

We believe that the small, symmetrical protrusions reflect the presence of some substitutional nitrogen species in the carbon lattice. First, the reduced graphene oxide used here was prepared with hydrazine as a reductant in the presence of ammonia, a process that is known to introduce nitrogen species on the sheets (see XPS data in Table 1).[54] Second, XPS provided evidence that some of this nitrogen survives heat treatment at high temperatures: survey spectra of reduced graphene oxide films annealed at 1773 K (not shown) revealed an amount of nitrogen close to the detection limit of the technique (~0.2 at%), but nonetheless still noticeable. In addition, the high resolution N1s spectrum of these films (Fig. 3) was dominated by a component at about 401.6 eV, which can be assigned to quaternary (substitutional) nitrogen in a graphitic lattice.[55,56] A smaller component observed at ~399.2 eV was attributed to pyridinic nitrogen, which is presumed to be located at the edge of the vacancies. It would thus not be unreasonable that a small fraction of such substitutional nitrogen still survives annealing at 2073 K. No nitrogen was detected by XPS for films heat treated at 2073 K, but this result could be anticipated due to the low density of protrusions (~4×10^3 μm^{-2}) seen by STM on the corresponding sheets (Fig. 2g). If we assume that every protrusion pinpoints the position of one or just a few nitrogen atoms, this element would be present in a proportion of the order of 0.01 at%, which is below the detection limit of XPS. Third, recent experimental and theoretical work has shown that substitutional nitrogen dopants in graphene/graphite transfer a fraction of their extra electron to their neighboring carbon atoms, so that this type of defect is visualized by STM as a small (< 2 nm) apparent protrusion.[57-59] More specifically, for a single substitutional nitrogen dopant the associated STM protrusion has been shown to display a trigonal symmetry that was not observed in the present case. Still, more complex symmetrical patterns have also been observed in nitrogen-doped graphene and attributed to small nitrogen dopant clusters of unidentified configuration.[57] It is therefore plausible that the six-fold symmetrical features reported here correspond to some specific type of dopant cluster, in particular one that seems to be especially stable.

A control experiment was carried out by which reduction of the graphene oxide was accomplished using vitamin C in place of hydrazine/ammonia. This treatment leads to the same extent of reduction as achieved with hydrazine, but is not expected to introduce nitrogen species.[60] We observed the same evolution of protrusions ~2-5 nm large in the 1773-2073 K temperature

range as described above for the hydrazine-reduced sheets. However, in this case no small-sized bright features were observed upon annealing at 2073 K, i.e. the sheets were completely defect free, suggesting that such features are indeed associated to nitrogen species. They also indicate that introduction of nitrogen, at least at concentrations of a few at%, does not significantly influence the ultimate thermal evolution of the sheets, as full repair of the carbon structure is achieved at 2073-2223 K both in the presence and absence of nitrogen. This result seems to be different to that observed when the sheets are just annealed at lower temperatures: a recent report has suggested that nitrogen introduced via hydrazine reduction favors the development of a somewhat less defected carbon structure at temperatures below 1373 K compared to sheets without nitrogen species.[61]

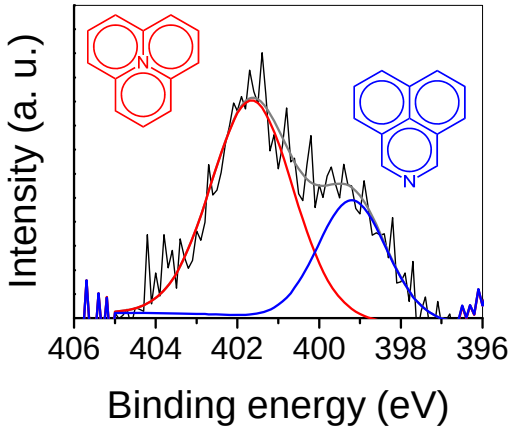

Figure 3 High resolution N1s core level XPS spectrum of the sample treated at 1773 K (black line), together with its deconvolution into two components at 401.6 eV (red line) and 399.2 eV (blue line), which are assigned to quaternary and pyridinic nitrogen, respectively. The corresponding envelope is included (grey line)

2.3 Influence of substrate defects and sheet-sheet interactions on the thermal evolution of chemically reduced graphene oxide sheets

The previous results on the thermal evolution of unreduced/chemically reduced graphene oxide were focused on isolated sheets supported onto the atomically flat and defect-free terraces of pristine HOPG. Under such conditions, it is reasonable to assume that there is a weak interaction between the sheets and the inert substrate, and therefore their thermal behavior will not be significantly affected by the latter. For example, it is not expected that atomic vacancies will migrate from the sheets to the pristine HOPG terrace: the activation energy for this process is estimated to be already as high as ~8 eV for a monatomic vacancy[62] and should be much higher for multiatomic ones, which would effectively prevent it from taking place. Nevertheless, in the presence of substrate defects or for stacked/overlapped/folded sheets this behavior might be altered as a result of interlayer interactions promoted by the defects. To investigate this point, three different situations were contemplated: (1) isolated sheets covering two neighboring pristine terraces across a step edge, (2) overlapped sheets supported onto a pristine terrace, and (3) isolated sheets supported onto a terrace densely decorated with atomic vacancies. The STM image of Fig. 4a shows an example of the first scenario, in which an individual sheet is seen to cross a monatomic step edge on the pristine HOPG surface. This type of feature was commonly found on account of the relatively small width of the terraces for the HOPG pieces used here (a few micrometers). After heat treatment at 1773 K, it was invariably observed that the lower-lying section of these sheets

merged with the upper terrace of the HOPG substrate, leaving their upper-lying section as an isolated entity (Fig. 4b). The unequivocal identification of the merged and isolated sections as arising from the thermal evolution of a given sheet was based on the following observations: (1) both the merged and isolated sections exhibited a large number of nanometer-sized protrusions (e.g., Fig. 4c and d), indicating the generation of atomic vacancies that is characteristic of the annealed sheets; (2) merged features were only seen after the heat treatment, but never before; (3) the isolated sections on the upper HOPG terrace were sitting next to the boundary between such terrace and the merged section.

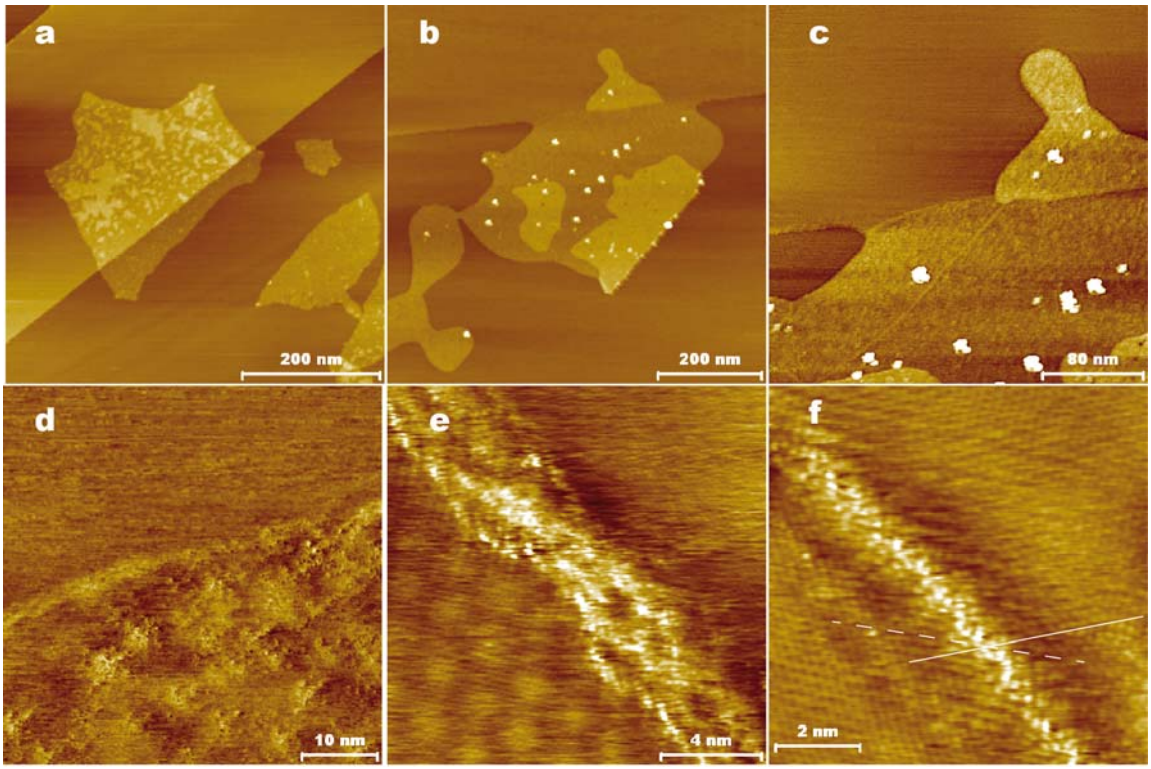

Figure 4 Nanometer-scale STM image of highly reduced graphene oxide sheets deposited on top of a HOPG substrate, showing an individual sheet covering two neighboring pristine terraces across a monatomic step edge, prior to the heat-treatment (a) and after annealing at 1773 K (b,c,d). Atomic-scale STM images of a Moiré Pattern (e) and a grain boundary (e,f) in highly reduced graphene oxide sheets annealded at 2223 K. Imaging conditions: 0.1-0.7 nA (tunneling current) and 300-1500 mV (bias voltaje) (a,b,c,d); 2nA and 5mV (e,f).

The merging process should be driven by strong interactions between the sheets and the step edges of the HOPG substrate. We interpret that many of the atomic vacancies thermally generated on the sheets will migrate and become pinned at a certain point of an imaginary line defined by the intersection of the sheet with the substrate step edge. Vacancy pinning would be due to formation of covalent bridges between unsaturated carbon atoms from the vacancy and the step edge. If the number of atomic vacancies on the sheets is sufficiently large, then it is plausible that a more or less continuous string of pinned vacancies could develop along this imaginary line. As a result, the linkages between the upper- and lower-lying sections of the sheet would be severely weakened and eventually broken, leading to the coalescence of the latter with the upper terrace of the HOPG substrate. Merging of the upper-lying section of the sheet with the HOPG terrace would be energetically unfavorable due to the high local curvature of the lattice along the seam line. We

recently proposed that overlapping sheets in macroscopic, paper-like films of chemically reduced graphene oxide undergo coalescence due to high temperature annealing.[25] However, such phenomenon could not be directly observed and was only inferred on the basis of general morphological changes of the films. The present results (Fig. 4b-d) provide direct evidence that coalescence processes do indeed take place on the sheets at high temperature. However, there is a discrepancy in the actual temperatures required for merging to occur between the isolated sheets on the HOPG step edges (1773 K) and the overlapped sheets in the macroscopic films (at least 2073-2373 K).[25] An explanation for this question will be provided below.

Because the sheets were randomly deposited onto the HOPG surface, they cannot be expected to be exhibit an ordered (AB) stacking registry with the latter, but rather a turbostratic one. This implies that the seam line where the sheet and terrace merge should constitute a grain boundary. In this type of line defect, the carbon lattice is locally distorted, e.g. by the presence of pentagons and heptagons, giving rise to localization of electronic states near the Fermi level.[63,64] Consequently, grain boundaries in graphitic structures are typically visualized by STM as apparently elevated features,[64,65] and this is indeed what we observed at the seam line where the sheet and the HOPG terrace met (e.g., Fig. 4d-f). The essentially electronic and non-topographic nature of the protruding lines seen here by STM was confirmed by the fact that such lines did not show up in AFM images, which are only sensitive to topography but not to partial electronic density.[66] The presence of a grain boundary-like defect at the seam line is also consistent with the observation that atomic vacancies (protrusions), which were still present on the sheets after coalescence took place at 1773 K, were never seen on the other side of the seam line (e.g, see Fig. 4c and d). Grain boundaries are known to act as vacancy sinks in graphitic systems,[46] and therefore diffusing vacancies can be expected to be annihilated once they reach this type of line defect. Another consequence of the random stacking of the sheets on the HOPG surface was the observation of Moiré patterns, which are superperiodic structures arising from the relative rotation of the two topmost graphene layers.[64] In the present case, such patterns were more easily seen for the highly graphitized sheets (e.g., those annealed at 2073 or 2223 K). An example of a Moiré pattern on a sheet annealed at 2223 K is given in Fig. 4e (bottom left part of the image).

Fig. 5a illustrates the thermal behavior at 1923 K of a sheet folding over itself supported onto the pristine HOPG surface. The most noticeable feature was the development of monolayer-deep pits of nanometric dimensions (~10 nm) in the overlapping region of the sheet, which is reminiscent of the evolution of pits in the mildly reduced sheets reported above. These pits, which start to be discernible at 1773 K (e.g., Fig. 4b), were also observed in overlapping regions involving different sheets but never in non-overlapping/non-folded areas or in isolated sheets (e.g., Fig. 1f). Thus, the generation of pits must be the result of interactions between the two sheets. In principle, the monolayer-deep pits might be located on either of the two sheets, but high resolution STM imaging of the pit edges should enable to determine their actual configuration: if a pit is located on the topmost sheet, then it should display an atomically sharp edge in the STM images (see upper schematic in Fig. 5b); on the other hand, if the pit was located in the underlying sheet, and therefore covered by the topmost sheet, we would expect to observe a continuous structure with a smoothly decreasing height when going from the edge to the bottom of the pit (Fig. 5b, lower schematic). Virtually all the examined pits exhibited atomically sharp edges (e.g., Fig. 5c and d), hence indicating that they formed only on the topmost sheet. If we assume that pits in this type of graphene sheets are generated when the fraction of carbon atoms missing from their lattice is large

enough, then we have to conclude that many more carbon atoms were abstracted from the topmost graphene sheet (in the overlapping/folded area) than expected a priori from their initial oxygen content. We hypothesize that these extra missing carbon atoms were not removed in the form of CO or CO_2, but were directly transferred to the underlying sheet instead.

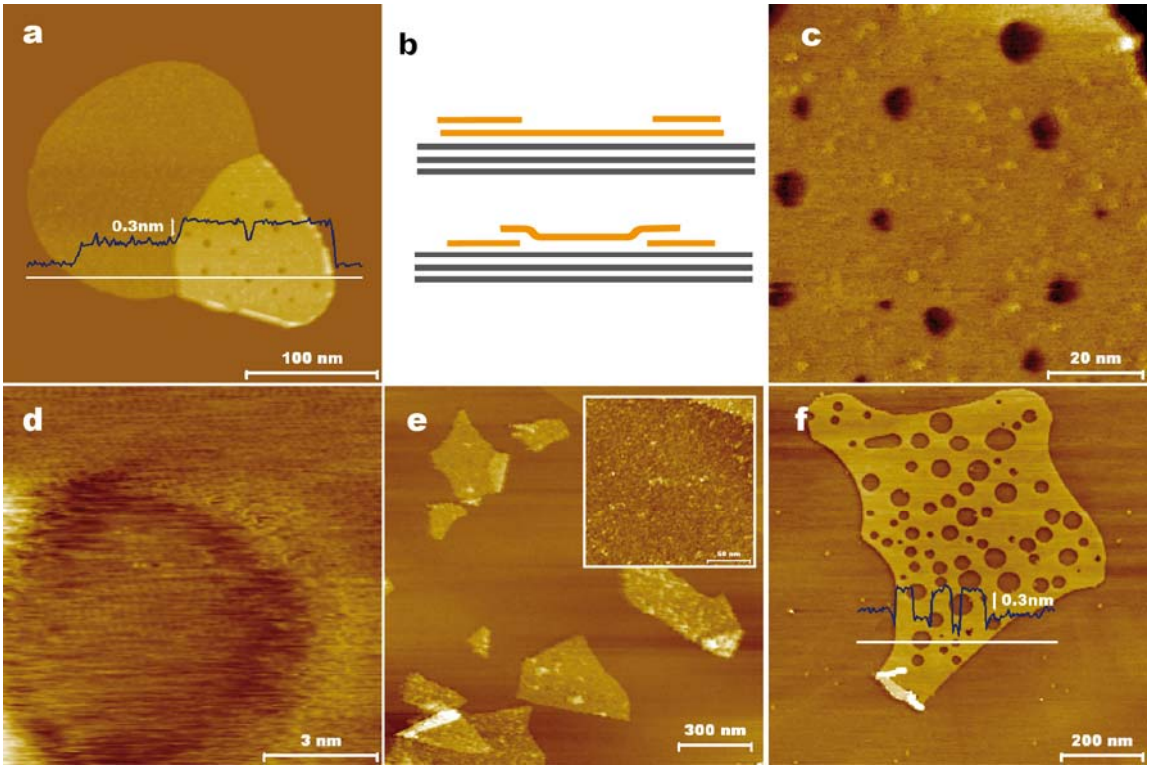

Figure 5 Nanometer-scale STM image of a highly reduced graphene oxide sheet folding over itself supported onto the pristine HOPG surface after annealing at 1923 K (a). Schematic illustration of the possible configurations of a pit in the region of overlapping of highly reduced graphene oxide sheets (b). Nanometer-scale (c) and atomic-scale (d) STM images of the region of overlaping shown in (a). Nanometer-scale image of highly reduced graphene oxide sheets deposited on top of a HOPG substrate previously exposed to dielectric barrier discharge (DBD)-generated plasma prior (e) and after annealing at 2073 K (f). The inset to (e) is a detailed image of the HOPG substrate after performing the BDB-generated plasma treatment. Imaging conditions: 0.2 nA (tunneling current) and 800 mV (bias voltage) (a), 0.3nA and 500 mV (c), 1.5nA and 5 mV (d), 1nA and 100mV (e,f).

According to theoretical calculations by different groups,[62,67-70] atomic vacancies from adjacent sheets in graphitic systems can form covalent interlayer bridges with a low energy barrier when they come sufficiently close to each other. Interlayer bonding (i.e., vacancy trapping) is made possible by a displacement of the carbon atoms surrounding the vacancies out of their respective planes of about 0.1 nm.[62,67] With a fraction of thermally removed carbon atoms in the highly reduced sheets of at least 4% (Table 1), vacancy trapping should be a highly probable event when these sheets are stacked over each other. It would then be conceivable that the carbon atoms that participate in the interlayer bonding could leap from one sheet to the other,[70] thereby increasing the vacancy size in the former and decreasing it in the latter. Very recent theoretical modeling has indeed demonstrated that such process is associated to moderate energy barriers (~3 eV),[71] so it would be readily accessible under the high temperature conditions used here. This carbon atom transfer process is also thermodynamically favorable because larger, coalesced vacancies tend to be

more stable than many smaller vacancies with equivalent total number of missing carbon atoms (due to minimization of the energy associated to dangling bonds).[46,71] However, why we only observe net transfers of carbon atoms from the topmost sheet to its underlying counterpart and not the reverse has to be explained.

The transfer of carbon atoms from the topmost reduced graphene oxide sheet to its underlying counterpart should entail, in addition to the creation of pits in the former, the shrinkage or even disappearance of the vacancies from the latter. Because smaller vacancies possess higher in-plane mobility,[47,48] the logical consequence would be that we observed an improved degree of structural restoration in the underlying sheet in an overlapping area at, e.g., 1923 K compared with the same sheet in their non-overlapping areas or for isolated sheets. Indeed, detailed STM inspection of underlying sheets, which became visible at the bottom of the pits, revealed a much more pristine, less defected structure at 1923 K (i.e., lower density of protrusions, Fig. 5d) than that of the same sheets in non-overlapping areas (images not shown) and isolated sheets annealed at the same temperature (e.g., Fig. 2e). To further demonstrate the involvement of vacancies from adjacent sheets in the observed processes, a further experiment was carried out. Isolated sheets were deposited onto HOPG, the surface of which had been previously decorated with atomic vacancies generated on purpose by plasma treatment (Fig. 5e).[49] A very high density of vacancies was produced exclusively on the topmost layer of the HOPG sample by the bombardment of energetic ions from the plasma, which induced an atomically rough surface morphology (see inset to Fig. 5e).[49] Following heat treatment at 2073 K, a large number of monolayer-deep pits with atomically sharp edges and relatively defect-free bottoms were seen to develop (Fig. 5f), indicating again that a transfer of carbon atoms, in this case from the sheet to the vacancy-decorated surface of HOPG, took place. This behavior was not observed for the same sheets supported onto pristine HOPG (Fig. 1i).

2.4 Further insight into the healing process by molecular dynamics simulations

To provide a deeper understanding of several relevant phenomena described in the previous sections, molecular dynamics simulations of the annealing process were undertaken. We first investigated the case of a reduced graphene oxide sheet covering two neighboring graphite terraces across a step edge. To simulate a step edge, the surface layer of graphite was replaced by a graphene ribbon of infinite length along the X direction and eight unit cells wide in the Y direction, with zig-zag terminations. This simulation cell thus contained two parallel step edges in the X direction. A reduced graphene oxide sheet was then deposited across the steps. Because our focus was neither on the generation of vacancies in the reduced sheets nor on their diffusion across the sheet, the latter of which has been extensively studied in the literature,[72] we began the simulations at the point where the vacancies had already been created in the sheet and had enough time to diffuse until they became pinned on top of the step edges. Vacancy pinning, i.e. the formation of covalent bridges between the vacancy and the step edge, was indeed observed in our simulations for isolated monatomic vacancies.

The structure of a slab consisting of three complete graphene layers, the ribbon that mimics the step edge and a pristine graphene sheet on top of it was first fully relaxed. We then generated 16 monatomic vacancies on the topmost sheet, i.e., a string of 8 vacancies on top of each step edge (the

edge has a length of 12 zig-zag unit cells). This arrangement can be seen in Fig. 6. The temperature of the system was subsequently ramped up, starting at 210 K and increased by 70 K every 10 ps until reconstruction of the structure was observed. We note that the simulation temperatures required to observe the reconstruction of the structure are in general higher than the experimental ones due to the very limited simulation time. In the simulation, once the vacancies are placed in the proximity of the step edge, some of their dangling bonds saturate very fast with some dangling bonds of the edge in less than 1 ps, forming covalent bonds that link the step with the deposited graphene sheet (see Fig. 7). With increasing temperature, more bonds form between the step edge and the lower lying section of the graphene sheet, and bond-forming and bond-breaking events become more frequent. Finally, at 2450 K (after 320 ps), the graphene sheet breaks along a line parallel to the step edge, so that its lower lying section merges with the step, reconstructing a perfect graphene leyer, and its upper section is left as an isolated fragment (Fig. 7), in agreement

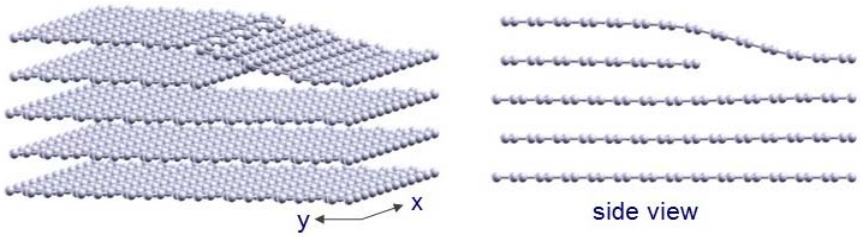

Figure 6 Relaxed structure of a graphene sheet covering two neighboring graphite terraces across a step edge. For clarity, only half of the simulation cell, containing one of the two step edges, is shown.

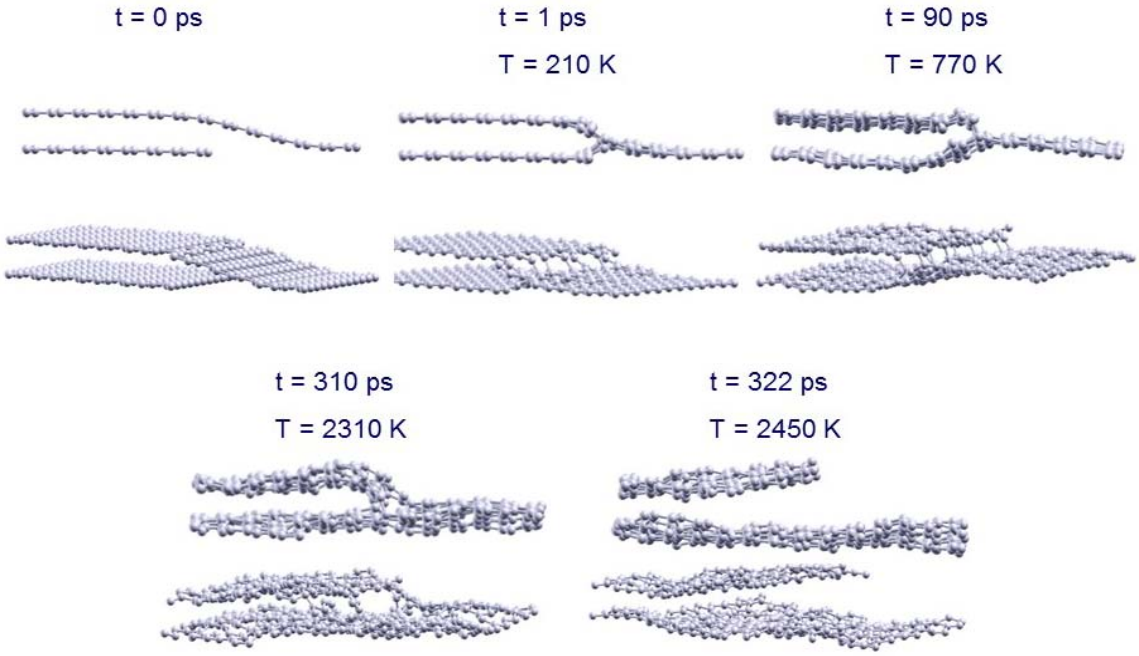

Figure 7 Side and perspective views of some snapshots taken along the dynamical simulations of the graphene sheet with a string of monatomic vacancies on top of the graphite step edge. For clarity, only half of the simulation cell and the two topmost layers, i.e. the graphene sheet with the string of vacancies and the upper terrace of the graphite surface, are shown.

with the experimental observations described above (Fig. 4). In the simulation, however, because the graphene sheet was deposited in registry with the step, its merged section did not develop any grain boundary at the seam line (Fig. 8).

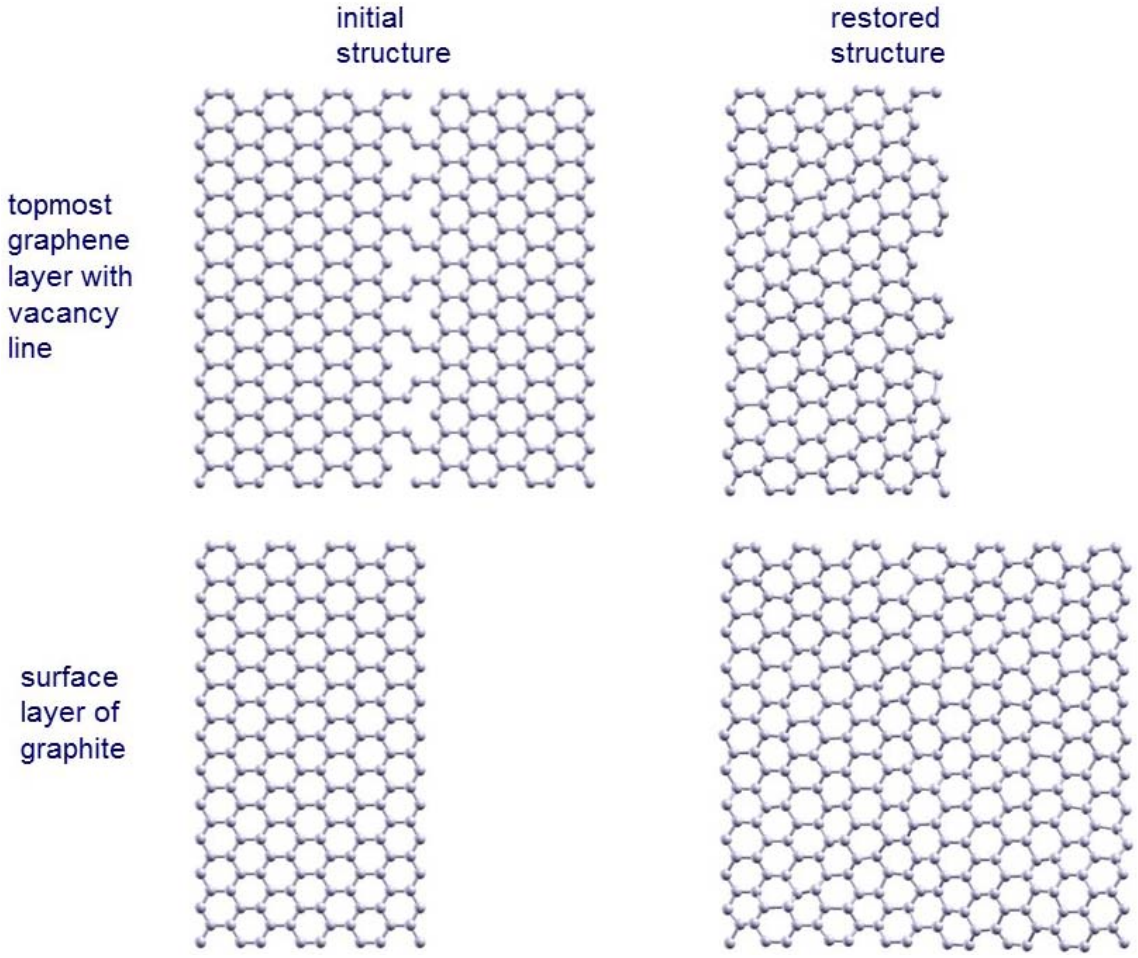

Figure 8 Top views of the initial and reconstructed structures of a graphene sheet decorated with a string of monatomic vacancies on top of the graphite step edge. For clarity, only the two topmost layers of the simulation, i.e. the graphene with the string of vacancies and the upper terrace of the graphite surface, are shown.

We also performed simulations of a graphene sheet deposited onto a vacancy-decorated graphite surface, to investigate the role played by interlayer interactions induced by this defect type in the thermal evolution of the sheet. In this case, we considered a graphite slab made up of 5 layers, where the two topmost ones have 60 randomly distributed monatomic vacancies each within the simulation cell. The selected number of vacancies (corresponding to the removal of 8 C at %) is related to the starting oxygen concentration in highly reduced graphene oxide sheets (see Table 1). The three remaining layers are kept defect free. The simulation began at 350 K and the temperature was increased stepwise by 70 K every 1 ps, reaching a final temperature of 3010 K after 39 ps. Snapshots of the simulation are shown in Fig. 9. The carbon atoms around the vacancies have dangling bonds and are very reactive, and exhibited, as expected, a strong tendency to bind to atoms from neighboring layers, preferentially atoms with dangling bonds from vacancies. Thus, a number of covalent bridges were seen to form between the two topmost layers of the system, although a few linkages also formed between the second (vacancy decorated) and third (pristine) layers. These

bridges are very efficient in saturating dangling bonds, but are quite costly in energy as compared to pristine graphene. As the simulation temperature is ramped up, bond-forming and bond-breaking events become more frequent, and some of these events give rise to the migration of carbon atoms between neighboring layers. Hence, such events provide a mechanism for the interlayer diffusion and coalescence of vacancies into larger, more energetically stable ones.

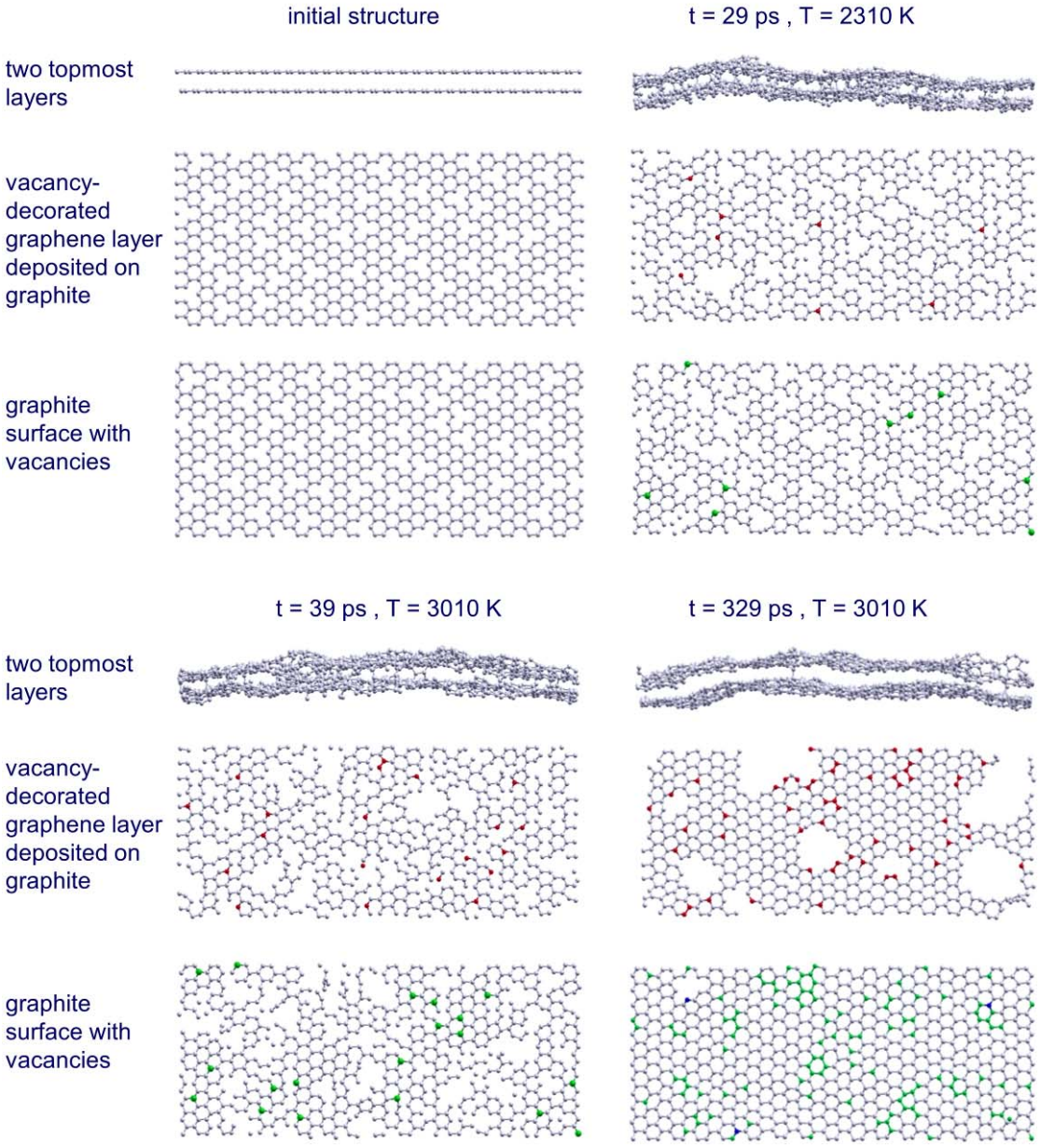

Figure 9 Side and top views of snapshots taken along the dynamical simulations of a vacancy-decorated graphene sheet deposited onto a vacancy-decorated graphite surface. Only the two topmost layers of the simulation, i.e. the two vacancy-decorated layers, are shown for clarity. Carbon atoms that originally belonged to the topmost graphene sheet but migrated to the underlying layer are represented in green, whereas carbon atoms that originally belonged to the surface layer of graphite and migrated to the graphene sheet are marked in red. A net migration of carbon atoms from the graphene sheet to the underlying graphite surface is observed, so that the latter is restored and large vacancies develop in the graphene sheet.

However, within the simulation time of 39 ps the number of carbon atoms exchanged between the two topmost layers remains small (about 19), and no net transfer, i.e. neither towards the graphene sheet on the top nor towards the graphite surface underneath, is observed. Moreover, these two layers exhibit a similar distribution of small multiatomic vacancies (see Fig. 9). Therefore, such results are not consistent with the experimental observations described above, where large vacancies (pits) only formed on the topmost graphene sheet while its underlying substrate was restored. To address this issue, the dynamical simulations were carried on for another 300 ps at a constant temperature of 3010 K. Bond-forming and bond-breaking events continued to provide the mechanism for the interlayer migration of carbon atoms and vacancy coalescence. Nevertheless, for these longer simulation times we observed a preferential migration (i.e., net transfer) of carbon atoms: about 52 atoms migrate from the graphite surface to the graphene sheet placed on top, whereas 108 atoms migrate in the opposite direction, yielding a net transfer of 56 atoms towards the graphite surface. As a consequence, the vacancy-decorated graphite surface is almost completely restored, whereas large multiatomic vacancies (pits) develop in the graphene sheet (Fig. 9). Such results are in agreement with the experiments reported in the previous section.

Concerning the mechanism that drives the net transfer of carbon atoms between the layers, we note that in the hypothetical case of free-standing, unsupported films comprising two or more stacked reduced graphene oxide sheets, the overall probability of carbon atom transfer from a given sheet to an adjacent one should be virtually the same as that of the reverse process. In such a case, no net transfer of carbon atoms between neighboring sheets, but only an enlargement of vacancies via interlayer coalescence processes, should be expected. On the other hand, when the film is supported onto a pristine, defect-free graphite substrate, the latter introduces an asymmetry in the system. Such asymmetry should involve an additional energetic stabilization for carbon atoms that are transferred to the reduced graphene oxide sheet immediately adjacent to the defect-free substrate. This additional stabilization is afforded by the weak, but non-negligible, van der Waals interaction associated to the fully conjugated, pristine graphite substrate, and would drive a net transfer of carbon atoms to this sheet. Indeed, recent calculations have revealed that the formation energy of an atomic vacancy in the bulk of graphite is somewhat larger than that on the graphite surface, suggesting that there is a thermodynamic drive for vacancies to migrate from the bulk to the surface.[62,69] In our case, the simulations indicate that interlayer vacancy (or carbon atom) migration is kinetically enabled by the covalent bridges formed between the vacancies.[70,71]

Regardless of the specific effects associated to the graphite substrate, the formation of covalent bridges (vacancy trapping) between the reduced graphene oxide sheets poses more general implications on their structural restoration. Because vacancy trapping is expected to increase the energy barrier to the in-plane migration of this defect[62,67-69] and the structural restoration of the sheets is thought to ultimately depend on its mobility, we have to conclude that full restoration of a multilayer film should be significantly harder to achieve compared to the restoration of an isolated sheet. The results from the present as well as a previous work[25] indicate that this is indeed the case. For example, atomic vacancies were still present in paper-like films annealed at 2073 K,[25] whereas they were completely removed from isolated sheets (Fig. 2g). Similarly, sheet coalescence, which appears to rely on the in-plane mobility of atomic vacancies (see above), was observed to occur at a lower temperature in isolated sheets compared with multilayer films. Taken together, all these results provide experimental support to the idea proposed by Heggie and co-workers that interlayer

bonding via defects should be determinant in the annealing behavior of highly defected graphitic materials.[67]

3 Conclusions

We have demonstrated that thermal annealing can convert individual, stand-alone graphene oxide sheets to completely defect-free graphene. Because healing of the sheets is a process dominated by the generation and migration (both intralayer and interlayer) of atomic vacancies in the carbon lattice, their successful restoration at temperatures as low as possible entails the fulfillment of two main requirements: (i) prior to annealing, the amount of oxygen groups on the graphene oxide sheets must be drastically decreased, e.g. by chemical reduction, to limit the thermal evolution of carbon atoms as CO/CO_2 and thus the creation of atomic vacancies, and (ii) the sheets must be supported onto an inert substrate to prevent interactions with the vacancies that could alter their migration dynamics. In those cases where the vacancies from a given sheet strongly interact with defects from the supporting substrate (e.g., step edges or atomic vacancies in graphite) or from neighboring sheets (stacked/overlapped configurations), the observed annealing behavior is significantly altered, giving rise to coalescence processes, slowed-down vacancy migration and/or carbon atom transfer between adjacent layers. With the graphene oxide sheets used here, which were prepared by standard oxidation protocols, full annihilation of defects could be achieved at 2073 K. However, we envisage that this temperature can be decreased to some extent using much less oxidized forms of graphene oxide, which have been previously reported in the literature. The latter should give rise to thermally induced vacancies of smaller size and/or in lower amounts, which would thus be easier to annihilate.

4 Experimental Section

4.1 Preparation of unreduced and chemically reduced graphene oxide sheets

Unreduced graphene oxide sheets as well as graphene oxide sheets chemically reduced to different degrees, obtained from the processing of graphite oxide, were used for the graphitization experiments. To this end, graphite oxide was prepared from natural graphite powder (Fluka 50870) by the Hummers method using H_2SO_4, $NaNO_3$ and $KMnO_4$.[73] Following a purification step that involved washing first with 10% HCl solution and then with copious amounts of Milli-Q water, the oxidized product was suspended in water, bath-sonicated (J.P. Selecta Ultrasons system, 40 kHz) for 2 h and finally centrifuged (Eppendorf 5424 microcentrifuge) at 10000 *g* for 10 min to sediment unexfoliated graphite oxide particles. The top ~75% of the resulting supernatant volume, which is a colloidal dispersion of unreduced graphene oxide sheets, was collected and kept for further use. The concentration of graphene oxide in this suspension was determined by UV-vis absorption spectroscopy as described elsewhere.[39] An aqueous dispersion of mildly reduced graphene oxide sheets was prepared by heating its unreduced counterpart (concentration ~0.1 mg mL^{-1}) at 368 K for 4 h in the presence of 26 mM ammonia. Similarly, an aqueous dispersion of highly reduced graphene oxide sheets was obtained by heating the unreduced suspension at 368 K for 1 h in the presence of both 26 mM ammonia and 1 mM hydrazine monohydrate. The role of ammonia is to provide a basic medium (pH ~10) that (i) confers colloidal stability to the sheets through electrostatic repulsion and (ii) induces a limited reduction of graphene oxide, probably by way of

nucleophilic attack from the hydroxide anions.[60,74] On the other hand, hydrazine is a powerful reducing agent and thus affords a more extensive reduction of the graphene oxide sheets.[54,60]

4.2 Thermal annealing experiments

For the graphitization experiments, the sheets need to be deposited onto suitable substrates that, among other requirements, are thermally stable up to very high temperatures. This prerequisite severely constrains the range of substrate materials that can be used, with HOPG being probably the most attractive option in the present case. In addition to its extreme heat resistance, HOPG provides a versatile supporting surface that is mostly atomically flat and inert in its pristine form but can be made atomically rough and reactive through appropriate surface treatment. Here, both pristine (inert) and surface-treated (reactive) HOPG substrates were used. The former were prepared just by cleaving HOPG pieces (grade ZYA, obtained from Tectra GmbH) with adhesive tape, whereas the latter were produced by means of dielectric barrier discharge (DBD)-generated air plasma treatment of the HOPG surface according to a procedure that has been described in detail elsewhere.[49] Briefly, freshly cleaved HOPG pieces were exposed to DBD-generated air plasma in a volume type apparatus (VB-A4, from Arcotec GmbH) at a power of 200 W for 0.35 s. This treatment leads to HOPG surfaces uniformly decorated with a high density of atomic vacancies, the carbon atoms alongside the vacancies constituting locally reactive sites on account of their dangling bonds.[49] The different unreduced and chemically reduced graphene oxide sheets were deposited on either pristine or plasma-treated HOPG substrates by drop-casting a small volume (~5 μL) of their corresponding diluted suspension (~0.01-0.02 mg mL^{-1}) onto the substrate pre-heated at ~323-333 K and allowing it to dry. These samples were subsequently introduced in a graphite furnace and heat treated at a given (target) temperature under continuous argon flow (2 L min^{-1}). For reasons that will be commented upon below, the range of target temperatures investigated here was between 1773 and 2273 K. The following heating rates were applied: 50 K min^{-1} from room temperature to 973 K, 100 K min^{-1} from 973 to 1273 K, 25 K min^{-1} from 1273 K up to the target temperature, then constant target temperature for 60 min and finally cooling down to room temperature.

4.3 Characterization techniques

Morphological and structural characterization of the heat-treated graphene oxide/reduced graphene oxide sheets on the nanometer and atomic scales was carried out by STM and AFM. To this end, a Nanoscope IIIa Multimode apparatus (Veeco Instruments) working under ambient conditions (relative humidity ~40%, temperature ~295-297 K) was used. STM imaging was accomplished in the constant current mode (variable height) using mechanically prepared Pt/Ir tips with typical tunneling parameters of 5-1500 mV (bias voltage) and 0.1-3 nA (tunneling current). AFM was performed in the tapping mode of operation using silicon cantilevers (spring constant ~40 N m^{-1}, resonance frequency ~250-300 kHz). Information on some aspects of the chemistry of the sheets (non-graphitized and graphitized) was obtained by means of XPS and TPD. Macroscopic, free-standing paper-like films of the sheets assembled via vacuum filtration of their corresponding aqueous dispersion were used as specimens for XPS and TPD rather than the HOPG substrates loosely decorated with the sheets that were employed for STM and AFM. Such films were subjected to the same annealing procedures as those applied to the HOPG-supported sheets. The

XPS measurements were carried out in a SPECS system working at a pressure below 10^{-7} Pa with a monochromatic Al Kα X-ray source (100 W). TPD profiles were recorded with a Micromeritics Autochem II chemisorption analyzer at a heating rate of 10 K min^{-1} under Ar flow (50 mL min^{-1}). CO and CO_2 evolution was quantitatively determined from the intensity of *m/z* = 28 and 44, respectively, as measured by an Ommistar mass spectrometer (Pfeiffer Vacuum).

4.4 Theoretical modeling

Molecular dynamics simulations were performed to attain further insight into several aspects of the annealing process. The simulations were focused on reduced graphene oxide sheets supported onto reactive graphite substrates, more specifically (i) a graphite surface decorated with atomic vacancies and (ii) a step edge on an otherwise pristine graphite surface, where interlayer interactions promoted by these defects are to be expected. Because heat treatment of reduced graphene oxide removes all residual oxygen groups and generates unsaturated atomic vacancies (see Results and discussion section), the simulations began at the point where the vacancies had been created and no oxygen groups were present in the sheets. The graphite substrate with the reduced graphene oxide sheet was mimicked by a slab of five graphitic layers. The simulations were performed using periodic boundary conditions in the graphitic planes (XY plane) and free conditions in their perpendicular direction (Z direction). The supercell in the XY plane contained 12×16 rectangular unit cells of graphene with size $\left(\sqrt{3}r_0, 3r_0\right)$, where r_0 is the carbon-carbon bond length in graphite and each unit cell contains four carbon atoms. Thus, a perfect layer of graphene contains 768 carbon atoms within the supercell. The bottom layer of the slab had a perfect, defect-free structure and was kept rigid during the simulations to represent the bulk of graphite for the remaining four layers. Four atoms at the edge of the supercell were also fixed in each of the 3 topmost layers to keep the layers bound to the graphitic surface even at the highest temperatures in the simulations. The slab was allowed to evolve dynamically at several temperatures. The interaction between carbon atoms was mimicked through a computationally efficient many-body empirical potential[75] that represents the carbon-carbon covalent bonds in graphite and diamond through a short-range Tersoff-like potential[76,77] and incorporates a long-range many-body potential[78] to represent weak van der Waals interactions between layers in graphite. This potential has proved to be reliable in the description of a wide variety of carbon systems, including fullerenes,[75] carbon nanotubes[79,80] or carbide-derived carbons.[81] The interatomic Tersoff potential gives a melting temperature for carbon of about 6000 K, whereas the experimental value is about 4300 K. Therefore, the temperatures given in this paper have been scaled by a factor of 0.7. The simulations were performed at constant number of particles and constant temperature, using the Nose-Hoover thermostat. The equations of motion were solved with a time step of 0.5 fs.

Acknowledgements

Financial support from the Spanish MINECO and the European Regional Development Fund (projects MAT2011-26399 and MAT2011-22781), as well as from Junta de Castilla y León (grant VA158A11-2) is gratefully acknowledged. R.R. thanks the receipt of a pre-doctoral contract (FPU) from the Spanish MECD.

References

[1] A.K. Geim, *Science* **2009**, *324*, 1530.

[2] K.S.Novoselov, V.I. Fal´ko, L.. Colombo, P.R. Gellert, M.G. Schwab, K. A Kim, *Nature* **2012**, *490*, 192.

[3] Y.Q. Wu, Y.M. Lin, A.A. Bol, K.A. Jenkins, F.N. Xia, D.B. Farmer, Y. Zhu, P. Avouris, *Nature* **2011**, *472*, 74.

[4] S. Bae, H. Kim, Y. Lee, X.F. Xu, J.S. Park, Y. Zheng, J. Balakrishnan, T. Lei, H.R. Kim, Y.I. Song, Y.J. Kim, K.S. Kim, B. Özyilmaz, J.-H. Ahn, B.H. Hong, S. Iijima, *Nature Nanotech.* **2010**, *5*, 574.

[5] B. Luo, S.M. Liu, L.J. Zhi,. *Small* **2012**, *8*, 630.

[6] J.R. Potts, D.R. Dreyer, C.W. Bielawski, R.S. Ruoff, *Polymer* **2011**, *52*, 5.

[7] B.F. Machado, P. Serp, *Catal. Sci. Technol.* **2012**, *2*, 54.

[8] H.Y. Mao, S. Laurent, W. Chen, O. Akhavan, M. Imani, A.A. Ashkarra, M. Mahmoudi, *Chem. Rev.* **2013**, *113*, 3407.

[9] D.R. Dreyer, R.S. Ruoff, C.W. Bielawski, *Angew. Chem. Int. Ed.* **2010**, *49*, 9336.

[10] S. Guo, S. Dong, *Chem. Soc. Rev.* **2011**, *40*, 2644.

[11] Y. Zhang, L. Zhang, C. Zhou, *Acc. Chem. Res.* **2013**, *46*, 2329.

[12] M. Cai, D. Thorpe, D.H. Adamson, H.C. Schniepp, *J. Mater. Chem.* **2012**, *22*, 24992.

[13] J.N. Coleman, *Acc. Chem. Res.* **2013**, *46*, 14.

[14] O.C. Compton, S.T. Nguyen, *Small* **2010**, *6*, 711.

[15] K.P. Loh, Q. Bao, G. Eda, M. Chhowalla, *Nature Chem.* **2010**, *2*, 1015.

[16] S. Pei, H.-M. Cheng, *Carbon* **2012**, *50*, 3210.

[17] S. Mao, H. Pu, J. Chen, *RSC Adv.* **2012**, *2*, 2643.

[18] V. López, R.S. Sundaram, C.;Gómez-Navarro, D. Olea, M.;Burghard, J. Gómez-Herrero, F. Zamora, K. Kern, *Adv. Mater.* **2009**, *21*, 4683.

[19] Dai, B.; Fu, L.; Liao, L.; Liu, N.; Yan, K.; Chen, Y.; Liu, Z. High-Quality Single-Layer Graphene via Reparative Reduction of Graphene Oxide. *Nano Res.* **2011**, *4*. 434.

[20] M. Cheng, R. Yang, L. Zhang, Z. Shi, W. Yang, D. Wang, G. Xie, D. Shi, G. Zhang, *Carbon* **2012**, *50*, 2581.

[21] D. Long, W. Li, W. Qiao, J. Miyawaki, S.-H. Yoon, I. Mochida, L. Ling, *Nanoscale* **2011**, *3*, 3652.

[22] M. Jin, T.H. Kim, S.C. Lim, D.L. Duong, H.J. Shin, Y.W. Jo, H.K. Jeong, J. Chang, S. Xie, Y.H. Lee, *Adv. Funct. Mater.* **2011**, *21*, 3496.

[23] T. Ghosh, C. Biswas, J. Oh, G. Arabale, T. Hwang, N.D. Luong, M. Jin, Y.H. Lee, J.-D. Nam, *Chem. Mater.* **2012**, *24*, 594.

[24] Y. Zhang, D. Li, X. Tan, B. Zhang, X. Ruan, H. Liu, C. Pan, L. Liao, T.;Zhai, Y. Bando, S. Chen, W. Cai, R.S. Ruoff, *Carbon* **2013**, *54*, 143.

[25] R. Rozada, J.I. Paredes, S. Villar-Rodil, A. Martínez-Alonso, J.M.D. Tascón, *Nano Res.* **2013**, *6*, 216.

[26] A. Lerf, H. He, M. Forster, J. Klinowski, *J. Phys. Chem. B* **1998**, *102*, 4477.

[27] T. Szabó, O. Berkesi, P. Forgó, K. Josepovits, Y. Sanakis, D. Petridis, I. Dékány, *Chem. Mater*. **2006**, *18*, 2740.

[28] W. Cai, R.D. Piner, F.J. Stadermann, S. Park, M.A. Shaibat, Y. Ishii, D. Yang, A. Velamakanni, S.J. An, M. Stoller, J. An, D. Chen, R.S. Ruoff, *Science* **2008**, *321*, 1815.

[29] K. Erickson, R. Erni, Z. Lee, N. Alem, W. Gannett, A. Zettl, *Adv. Mater.* **2010**, *22*, 4467.

[30] I. Jung, D.A. Field, N.J. Clark, Y. Zhu, D. Yang, R.D. Piner, S. Stankovich, D.A. Dikin, H. Geisler, C.A. Ventrice, R.S. Ruoff, *J. Phys. Chem*. C **2009**, *113*, 18480.

[31] P. Solís-Fernández, R. Rozada, J.I. Paredes, S. Villar-Rodil, M.J. Fernández-Merino, L. Guardia, A. Martínez-Alonso, J.M.D. Tascón, *J. Alloys Compd*. **2012** *536S*, S532.

[32] C. Mattevi, G. Eda, S. Agnoli, S. Miller, K.A. Mkhoyan, O. Celik, D. Mastrogiovanni, G. Granozzi, E. Garfunkel, M. Chhowalla, *Adv. Funct. Mater*. **2009**, *19*, 2577.

[33] O. Akhavan, *Carbon* **2010**, *48*, 509.

[34] C.-M. Chen, Q. Zhang, M.-G. Yang, C.-H. Huang, Y.-G. Yang, M.-Z. Wang, *Carbon* **2012**, *50*, 3572.

[35] A. Bagri, C. Mattevi, M. Acik, Y.J. Chabal, M. Chhowalla, V.B. Shenoy, *Nature Chem.* **2010**, *2*, 581.

[36] T. Sun, S. Fabris, S. Baroni, *J. Phys. Chem. C* **2011**, *115*, 4730.

[37]G. Lee, K.S. Kim, K. Cho, *J. Phys. Chem. C* **2011**, *115*, 9719.

[38] L. Liu, K.T. Rim, D. Eom, T.F. Heinz, G.W. Flynn, *Nano Lett.* **2008**, *8*, 1872.

[39] J.I. Paredes, S. Villar-Rodil, P. Solís-Fernández, A. Martínez-Alonso, J.M.D. Tascón, *Langmuir* **2009**, *25*, 5957.

[40] P. Solís-Fernández, J.I. Paredes, S. Villar-Rodil, A. Martínez-Alonso, J.M.D. Tascón, *Carbon* **2010**, *48*, 2657.

[41] C.Ö. Girit, J.C. Meyer, R. Erni, M.D. Rossell, C. Kisielowski, L. Yang, C.-H. Park, M.F. Crommie, M.L. Cohen, S.G. Louie, A. Zettl, *Science* **2009**, *323*, 1705.

[42] P. Solís-Fernández, J.I. Paredes, S. Villar-Rodil, L. Guardia, M.J. Fernández-Merino, G. Dobrik, L.P. Biró, A. Martínez-Alonso, J.M.D. Tascón, *J. Phys. Chem. C* **2011**, *115*, 7956.

[43] S. Stankovich, D.A. Dikin, R.D. Piner, K.A. Kohlhaas, A. Kleinhammes, Y.Y. Jia, Y. Wu, S.T. Nguyen, R.S. Ruoff, *Carbon* **2007**, *45*, 1558.

[44] M.C. Kim, G.S. Hwang, R.S. Ruoff, *J. Chem. Phys.* **2009**, *131*, 064704.

[45] X.F. Gao, J. Jang, S. Nagase,. *J. Phys. Chem. C* **2010**, *114*, 832.

[46] F. Banhart, *Rep. Prog. Phys.* **1999**, *62*, 1181.

[47] F. Banhart, J. Kotakoski, A.V. Krasheninnikov, *ACS Nano* **2011**, *5*, 26.

[48] J.Y. Huang, F. Ding, B.I. Yakobson, *Phys. Rev. B* **2008**, *78*, 155436.

[49] P. Solís-Fernández, J.I. Paredes, M.J. López, I. Cabria, J.A. Alonso, A. Martínez-Alonso, J.M.D. Tascón, *J. Phys. Chem. C* **2009**, *113*, 18719.

[50] J.R. Hahn, H. Kang, *Phys. Rev. B* **1999**, *60*, 6007.

[51] A.V. Krasheninnikov, K. Nordlund, M. Sirviö, E. Salonen, J. Keinonen, *J. Phys. Rev. B* **2001**, *63*, 245405.

[52]H. Amara, S. Latil, V. Meunier, Ph. Lambin, J.-C. Charlier, *Phys. Rev. B* **2007**, *76*, 115423.

[53] J.I. Paredes, P. Solís-Fernández, A. Martínez-Alonso, J.M.D. Tascón, *J. Phys. Chem. C* **2009**, *113*, 10249.

[54] D. Li, M.B. Müller, S. Gilje, R.B. Kaner, G.G. Wallace, *Nature Nanotech.* **2008**, *3*, 101.

[55] S. Kundu, W. Xia, W. Busser, M. Becker, D.A. Schmidt, M. Havenith, M. Muhler, Phys *Phys. Chem. Chem. Phys.* **2010**, *12*, 4351.

[56] H. Wang, T. Maiyalagan, X. Wang, *ACS Catal.* **2012**, *2*, 781.

[57] L. Zhao, R. He, K.T. Rim, T. Schiros, K.S. Kim, H. Zhou, C. Gutiérrez, S.P. Chockalingam, C.J. Arguello, L. Pálová, D. Nordlund, M.S. Hybertsen, D.R. Reichman, T.F. Heinz, P. Kim, A. Pinczuk, G.W. Flynn, A.N. Pasupathy, *Science* **2011**, *333*, 999.

[58] F. Joucken, Y. Tison, J. Lagoute, J. Dumont, D. Cabosart, B. Zheng, V. Repain, C. Chacon, Y. Girard, A.R. Botello-Méndez, S. Rousset, R. Sporken, J.-C. Charlier, L. Henrard, *Phys. Rev. B* **2012**, *85*, 161408.

[59] T. Kondo, S. Casolo, T. Suzuki, T. Shikano, M. Sakurai, Y. Harada, M. Saito, M. Oshima, M.I. Trioni, G.F. Tantardini, J. Nakamura, *Phys. Rev. B* **2012**, *86*, 035436.

[60] M.J. Fernández-Merino, L. Guardia, J.I. Paredes, S. Villar-Rodil, P. Solís-Fernández, A. Martínez-Alonso, J.M.D. Tascón, J. Phys. Chem. C 114 (2010), 6426.

[61] Y. Yoon, S. Seo, G. Kim, H. Lee, Chem. *Chem. Eur. J.* **2012**, *18*, 13466.

[62]G. Teobaldi, K. Tanimura, A.L. Shluger, *Phys. Rev. B* **2010**, *82*, 174104.

[63] S. Kurasch, J. Kotakoski, O. Lehtinen, V. Skákalová, J. Smet, C.E. Krill, A.V. Krasheninnikov, U. Kaiser, *Nano Lett.* **2012**, *12*, 3168.

[64] H.S. Wong, C. Durkan, N. Chandrasekhar, *ACS Nano* **2009**, *3*, 3455.

[65] P. Simonis, C. Goffaux, P.A. Thiry, L.P. Biró, P. Lambin, V. Meunier, *Surf. Sci.* **2002**, *511*, 319.

[66]S .N. Magonov, M.-H. Whangbo, Surface Analysis with STM and AFM, VCH: Weinheim, 1996.

[67] R.H. Telling, C.P.Ewels, A.A. El-Barbary, M.I. Heggie, *Nature Mater.* **2003**, *2*, 333.

[68] A.A. El-Barbary, R.H. Telling, C.P. Ewels, M.I. Heggie, P.R. Briddon, *Phys. Rev. B* **2003**, *68*, 144107.

[69] G. Teobaldi, H. Ohnishi, K. Tanimura, A.L. Shluger,*Carbon* **2010**, *48*, 4145.

[70] T. Trevethan, P. Dyulgerova, C.D. Latham, M.I. Heggie, C.R. Seabourne, A.J. Scott, P.R. Briddon, M.J. Rayson, *Phys. Rev. Lett.* **2013**, *111*, 095501.

[71] L. Liu, J. Gao, X. Zhang, T. Yan, F. Ding, *Nanoscale* **2014**, *6*, 5729.

[72] G.-D. Lee, C.Z. Wang, E. Yoon, N.-M. Hwang, D.-Y. Kim, K.M. Ho, *Phys. Rev. Lett.* **2005**, *95*, 205501.

[73] W.S. Hummers, R.E. Offeman, *J. Am. Chem. Soc.* **1958**, *80*, 1339.

[74] A.M. Dimiev, L.B. Alemany, J.M. Tour, *ACS Nano* **2013**, *7*, 576.

[75] P.A. Marcos, J.A. Alonso, A. Rubio, M.J. López, *Eur. Phys. J. D* **1999**, *6*, 221.

[76] J Tersoff, *Phys. Rev. B* **1999**, *37*, 6991.

[77] J. Tersoff,. *Phys. Rev. Lett.* **1988**, *61*, 2879.

[78]K. Nordlund, J. Keinonen, T. Mattila, *Phys. Rev. Lett.* **1996**, *77*, 699.

[79] M.J. López, A. Rubio, J.A. Alonso, L.-C. Qin, S. Iijima, *Phys. Rev. Lett.* **2001**, *86*, 3056.

[80] M.J. López, A. Rubio, J.A. Alonso, S. Lefrant, K. Méténier, S. Bonnamy, *Phys. Rev. Lett.* **2002**, *89*, 255501.

[81] M.J. López, I. Cabria, J.A. Alonso, *J. Chem. Phys.* **2011**, *135*, 104706.

5.3 Modificación de grafeno producido por depósito químico en fase vapor

Artículo V

Enviado para publicación: "Controlled generation of atomic vacancies in chemical vapor deposited graphene by microwave oxygen plasma"

La introducción de defectos en grafeno permite modificar sus propiedades intrínsecas y así obtener la funcionalidad deseada en diferentes tipos de aplicaciones basadas en este material. Es conocido que la oxidación mediante un plasma de oxígeno constituye un método muy efectivo para la modificación superficial del grafeno. En este tratamiento, la sustracción de átomos de carbono en forma de CO y CO_2 cuando las especies reactivas del plasma reaccionan con los átomos de carbono del material da lugar a la generación de vacantes y su decoración con grupos oxigenados, cuyo tamaño y densidad dependen de las condiciones de operación del plasma.

En el *artículo V* se introducen densidades controladas de vacantes multiatómicas en grafeno producido por depósito químico en fase vapor mediante plasma de oxígeno generado por microondas. La densidad de vacantes introducidas en los distintos tratamientos fue determinada a partir de imágenes de STM, en las que estos defectos se visualizan como protuberancias debido a que provocan un aumento de la densidad de estados cerca del nivel de Fermi. Variando la intensidad del plasma y el tiempo de exposición se consiguieron densidades en el rango de 10^3-10^5 μm^{-2}. La corta duración de los tratamientos permitió obtener vacantes distribuidas homogéneamente en las láminas con una estrecha distribución de tamaños (1-3 nm). Además, como consecuencia de la utilización de especies reactivas de oxígeno en la creación de las vacantes, se espera la introducción de grupos funcionales oxigenados en los bordes de dichas vacantes.

La introducción de densidades crecientes de vacantes atómicas introduce desorden estructural en las láminas de grafeno, como indican los espectros Raman, que muestran un aumento gradual de la relación I_D/I_G y una disminución progresiva de la intensidad de la banda 2D. Además, en las muestras con densidades de defectos más altas se observa la emergencia de la banda D´. Por otra parte, los resultados de espectroscopía Raman indican que la introducción de densidades crecientes de vacantes atómicas induce un exceso neto de portadores de carga positivos en las muestras (dopaje tipo p). Este dopaje se atribuye a la transferencia de carga electrónica a los átomos de oxígeno presentes en los bordes de las vacantes en virtud de su mayor electronegatividad.

Por último, se estudió la influencia de la introducción de vacantes sobre las propiedades eléctricas del grafeno. Para ello, se fabricaron transistores de efecto de campo con

cada una de las muestras y se midieron sus características de transferencia. Los resultados de dichas medidas muestran un desplazamiento del punto de neutralidad de carga hacia valores positivos del voltaje de puerta, lo que confirma la aparición de dopaje tipo p en las muestras tras la introducción de vacantes. También muestran un descenso de la movilidad de ambos tipos de portadores de carga (electrones y huecos), aunque la movilidad de los electrones experimenta un mayor descenso relativo debido al dopaje tipo p de las muestras. Esta reducción de la movilidad se atribuye a la dispersión de los portadores de carga en las vacantes.

Controlled generation of atomic vacancies in chemical vapor deposited graphene by microwave oxygen plasma

R. Rozada[a], P. Solís-Fernández[b], J.I. Paredes[a], A. Martínez-Alonso[a], H. Ago[b], J.M.D. Tascón[a]

[a]*Instituto Nacional del Carbón, INCAR-CSIC, Apartado 73, 33080 Oviedo, Spain*

[b]*Institute for Materials Chemistry and Engineering, Kyushu University, Fukuoka 816-8580, Japan*

The introduction of atomic-scale defects in a controllable manner and the understanding of their effect on the characteristics of graphene are essential to develop many applications based on this two-dimensional material. Here, we investigate the use of microwave-induced oxygen plasma towards the generation of small-sized atomic vacancies (holes) in graphene grown by chemical vapor deposition. Scanning tunneling microscopy revealed that tunable vacancy densities in the 10^3-10^5 μm^{-2} range could be attained with proper plasma parameters. Transport measurements and Raman spectroscopy revealed p-type doping and a decrease in charge carrier mobility for the vacancy-decorated samples. This plasma-modified graphene could find use in, e.g., gas or liquid separation, or molecular sensing.

Graphene is a two dimensional material consisting in a monolayer of carbon atoms arranged in a honeycomb lattice. The combination of unique electrical, mechanical, thermal and optical properties in this one-atom thick material has made graphene the object of intense research activity in recent years [1]. Unfortunately, bringing this material into real-life applications on a large scale is far from straightforward. For instance, large-area pristine graphene is a semimetal with zero bandgap, which constitutes an obstacle for the development of graphene-based logic devices as gate modulation is not enough to produce definite off states [2]. Nevertheless, the bandgap as well as many other characteristics of graphene can be engineered by the introduction of several types of defects. Thus, significant attention has been very recently focused on

the topic of defect generation in graphene, which has been accomplished by electron [3] or ion irradiation [4], or alternatively by methods involving reaction with oxygen, such as heat treatment in an oxygen gas flow [5], UV-generated ozone oxidation [6] or oxygen plasma treatment [7-9]. Oxygen plasma treatment is an attractive method from a practical point of view, as it can be easily integrated in current circuit mass-production schemes, usually requires very short exposure times and the density of defects could be potentially controlled through the plasma processing parameters. Furthermore, unlike methods involving electron or ion irradiation that lead to defect populations of polydisperse type [3], certain oxygen plasmas enable the introduction of just one type of defect (e.g., atomic vacancies) [10]. The generation of a defect population of monodisperse type would be considerably advantageous, as it could provide a better control of the material properties. Of particular interest is the generation of atomic vacancies in graphene and especially multiatomic vacancies, because this type of defect is stable up to very high temperatures [11] and would thus be able to endure the temperatures required both during the fabrication process and at the operating conditions of the devices. Furthermore, most of the work on defect generation in graphene has been limited to micromechanically exfoliated samples, whereas little attention has been paid to graphene grown by chemical vapour deposition (CVD), which is much more application-wise.

Here, we report the use of microwave (MW)-generated oxygen plasma to introduce atomic-sized defects in CVD graphene with tunable densities from ~10^3 to 10^5 μm^{-2}. These defects mostly comprise multiatomic vacancies of similar size and exhibit a regular distribution throughout the sample, as revealed by scanning tunneling microscopy (STM). In addition to the direct visualization of the defects and their density through STM, the introduction of structural disorder on the graphene samples has been confirmed independently by Raman spectroscopy. Finally, we investigate the effect of the atomic vacancies on the electronic transport properties of graphene by fabricating back-gated field-effect transistors and measuring their transfer characteristics (see experimental details in Supplementary information).

The generation of atomic-sized defects in graphene was accomplished by means of MW oxygen plasma, using appropriate plasma powers and exposure times to modulate the defect density. It has been previously established that attack of graphitic surfaces by this type of plasma proceeds via chemical reactions between the active species

generated in the plasma (mainly atomic oxygen and its ions) and carbon atoms from both the graphitic basal and edge planes. Such reactions lead to the removal of carbon atoms in the form of CO and CO_2 and hence to the production of atomic vacancies on the graphitic surface [10]. After abstraction of individual carbon atoms from the basal plane in the very first step of etching, the attack proceeds not only by removing additional carbon atoms from perfect sites of the basal plane, but also by enlarging the monoatomic vacancies previously generated. In our plasma setup, short exposure times (seconds) were used in order to accomplish a narrow distribution of vacancy sizes and avoid the generation of larger, nanometer-sized pits. On the other hand, higher MW plasma powers generally led to larger numbers of defects, most probably because higher densities of species are available to react with the surface carbon atoms. As shown in the following, this method allowed tuning the defect density in CVD graphene roughly between 10^3 and 10^5 μm^{-2}.

Nanometer- and atomic-scale STM images of the graphene samples prior to [Fig 1(a)] and after [Fig. 1(b-f)] different oxygen plasma treatments are presented in this figure. The starting, pristine graphene exhibited a smooth but not atomically flat topography on the nanometer scale [height variations <0.3 nm; see Fig. 1(a)] that is assumed to reflect the topographical conformation of the Cu(111) supporting substrate. On the atomic scale [inset to Fig. 1(a)], the sample displayed the well-known honeycomb pattern that is expected for single-layer graphene when it is electronically decoupled from the supporting substrate. This fact, together with the absence of any other modulations in the atomic-scale STM images suggests a weak graphene-Cu(111) interaction. Images (b-e) of Fig. 1 correspond to samples treated with the MW oxygen plasma at 10 W/9 s (b), 60 W/3 s (c), 300 W/1.5 s (d) and 390 W/1.5 s (e). In contrast to their pristine graphene counterparts, the STM images of the plasma-treated samples revealed a number of apparent protrusions (bright spots) of more or less uniform appearance and regularly distributed throughout the graphene basal plane. An atomic-scale STM image of one of these protrusions, corresponding to the 60 W/3 s sample, is shown in Fig. 1(f).

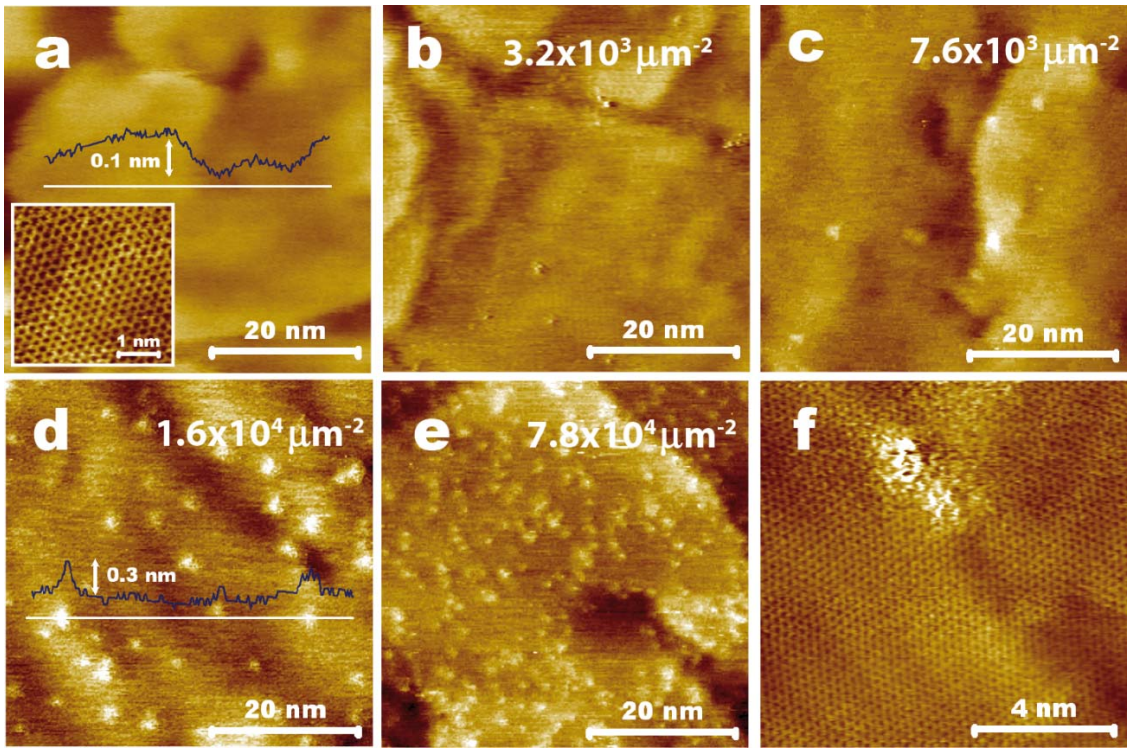

Figure 1: Nanometer-scale STM images for the pristine sample (a) and samples treated at 10 W/9 s (b), 60 W/3 s (c), 300 W/1.5 s (d) and 390 W/1.5 s (e). Atomic-scale STM images for the pristine sample (inset in a) and the sample treated at 60 W/3 s, showing one of the protrusions in more detail (f). Tunneling parameters: 200–500 pA (tunneling current) and 500–1000 mV (bias voltage) for nanometer-scale images and 600–700 pA (tunneling current) and 20 mV (bias voltage) for atomic-scale images.

According to previous work on graphite, the type of defect observed here by STM can be ascribed to atomic vacancies created through the removal of carbon atoms by atomic oxygen from the plasma [10]. The density of vacancies introduced by the plasma treatments could be readily determined from the STM images: ~3.2x10^3 μm^{-2} (b), ~7.6x10^3 μm^{-1} (c), ~1.6x10^4 μm^{-2} (d) and ~7.8x10^4 μm^{-2} (e). Due to the short exposure times used, in virtually all cases the observed protrusions exhibited similar heights (~0.2-0.4 nm) and a narrow diameter distribution (~1-3 nm) suggesting that all protrusions are associated with the same type of defect, i.e., small-sized multiatomic vacancies [10]. We note that larger vacancies, and even nanometer-sized holes, could be created for sufficiently long plasma exposure times. However, in that case small vacancies are also present because vacancy creation and enlargement take place

continuously during the treatment, giving rise to polydisperse vacancy populations. By contrast, under proper conditions (i.e., short exposure times), this MW plasma-based method essentially afforded monodisperse populations of small multiatomic vacancies with controllable density, which could be useful for different applications of graphene, such as gas separation or water desalination [5]. It is also worth mentioning that, because this method is based on the use of reactive oxygen species, the introduction of oxygen functional groups attached to the vacancy edges is very likely to occur [10].

Raman spectroscopy is a non-destructive technique widely used in the investigation of graphene materials, in particular to provide structural information (e.g., presence of defects, stacking order, etc) [12]. Fig. 2(a) shows representative Raman spectra for the MW plasma-treated samples under investigation. The high crystalline quality of the starting, untreated graphene sample was confirmed by the complete absence of the defect-related D band at ~1360 cm^{-1}. After plasma treatment a noticeable D band appeared, and its intensity (in particular, the integrated intensity ratio of the D and G bands, I_D/I_G) was generally seen to increase in parallel with the density of atomic vacancies observed by STM. Therefore, the emergence of the D band can be directly related to the presence of this type of defect defect in the graphene lattice. On the other hand, the intensity of the 2D band (located at ~2700 cm^{-1}) underwent an obvious reduction after plasma treatment, which was also consistent with the development of structural disorder in the graphene lattice [13]. The dependence of the I_D/I_G and I_{2D}/I_G ratios on the density of defects is quantitatively shown in Fig. 2(b) and (c), respectively. In addition to the evolution of the D and 2D bands, the D´ band emerged only for samples with defect densities larger than ~10^4 μm^{-2}. This band is seen as a shoulder of the G band at ~1620 cm^{-1} and is also known to be induced by defects. Overall, the Raman data were consistent with the STM results in that they indicated the possibility to finely tune the density of defects (atomic vacancies) generated on graphene by MW oxygen plasma.

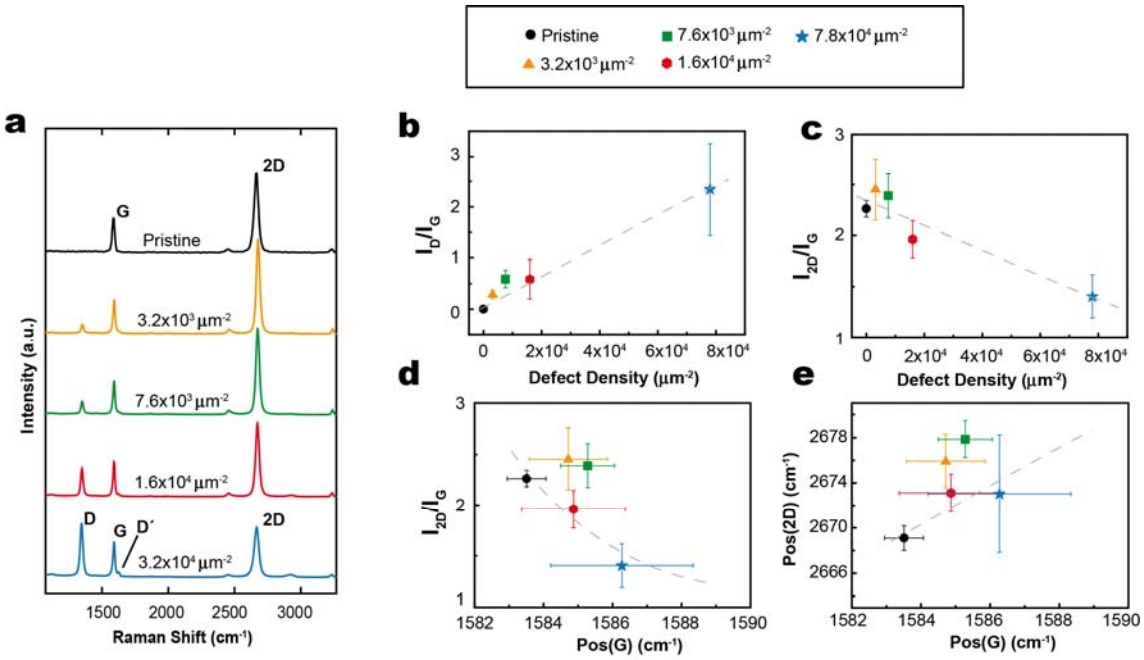

Figure 2: (a) Raman spectra for the pristine sample (black) and MW plasma-treated samples with defect densities ~3.2x10^3 µm^{-1} (orange), ~7.6x10^3 µm^{-1} (green), ~1.6x10^4 µm^{-1} (red) and ~7.8x10^4 µm^{-1} (blue). All the spectra were measured after transferring on SiO_2/Si substrates. I_D/I_G (b) and I_{2D}/I_G (c) intensity ratios as a function of the density of defects. I_{2D}/I_G intensity ratio (d) and position of the 2D band (e) versus the position of the G band. Figures (b-e) show the average value of measurements at ten different spots, the error bars represent the standard deviation and the dashed lines are a guide to the eye.

The introduction of vacancy defects decorated with oxygen functionalities by the oxygen plasma can be expected to introduce some level of doping in the graphene sheets. Raman spectroscopy also provided some information about the electronic properties of defected graphene, such as the presence of doping [12]. In Fig. 2(d), the I_{2D}/I_G ratio has been plotted against the position of the G band. For graphene samples that have been either p- or n-doped, it has been reported that the I_{2D}/I_G ratio decreases and the position of the G band shifts to higher wavenumbers [12]. In our MW plasma-treated samples, the value of I_{2D}/I_G decreased from values over 2 for both pristine graphene and graphene decorated with a relatively low density of vacancies, to ~1 for the sample with the highest vacancy density. Concurrently, a shift of the G band from about 1583 to 1586 cm^{-1} was observed, suggesting chemical doping in the plasma-treated graphenes, although the actual doping type cannot be determined from these

data. To reveal the doping type, the position of the G and 2D bands was plotted against each other in Fig. 2(e). It has been previously reported that hole (electron) doping in graphene results in a positive (negative) correlation of the 2D and G band positions [14]. In our case, a positive correlation is observed for the MW plasma-treated samples with respect to the pristine sample, suggesting hole doping. This excess of positive charge carriers could be explained by the transfer of electronic charge from the graphene lattice to the electronegative oxygen atoms present at the edges of the atomic vacancies.

Even though Raman spectroscopy is a powerful technique to identify doping in graphene, it also suffers from some degree of variability between samples that are produced under apparently identical conditions [14]. This effect is probably manifest in Fig. 2(d) and (e). More specifically, the pristine sample and the samples with defect densities of about $1.6x10^4$ and $7.8x10^4$ μm^{-2} are highly consistent with each other. Nevertheless, there is some noticeable mismatch between these three samples and the samples with defect densities of about $3.2x10^3$ and $7.6x10^3$ μm^{-2}, although they are still broadly consistent with the general trends described above. Interestingly, these two sets of samples belong to different batches of the CVD graphene growth and transfer process. Hence, we tentatively attribute such differences to slight deviations in the fabrication process that are very difficult to control.

The electronic performance of the MW plasma-treated graphene samples was directly evaluated in back-gated field-effect transistors. Fig. 3(a) shows the gate voltage (V_G) dependence of the drain current (I_D) for the starting, pristine graphene as well as for plasma-treated samples with defect densities of about $1.6x10^4$ and $7.8x10^4$ μm^{-2}. For pristine graphene, we note that the charge neutrality point (V_{CNP}) lies at ~19 V. Besides, instead of displaying perfect ambipolar behavior, the curve is slightly asymmetrical for holes and electrons. This phenomenon has been previously attributed to unintentional chemical doping that results from the microfabrication techniques and to the difference in work function between the graphene sample and its metal contacts [14, 15].

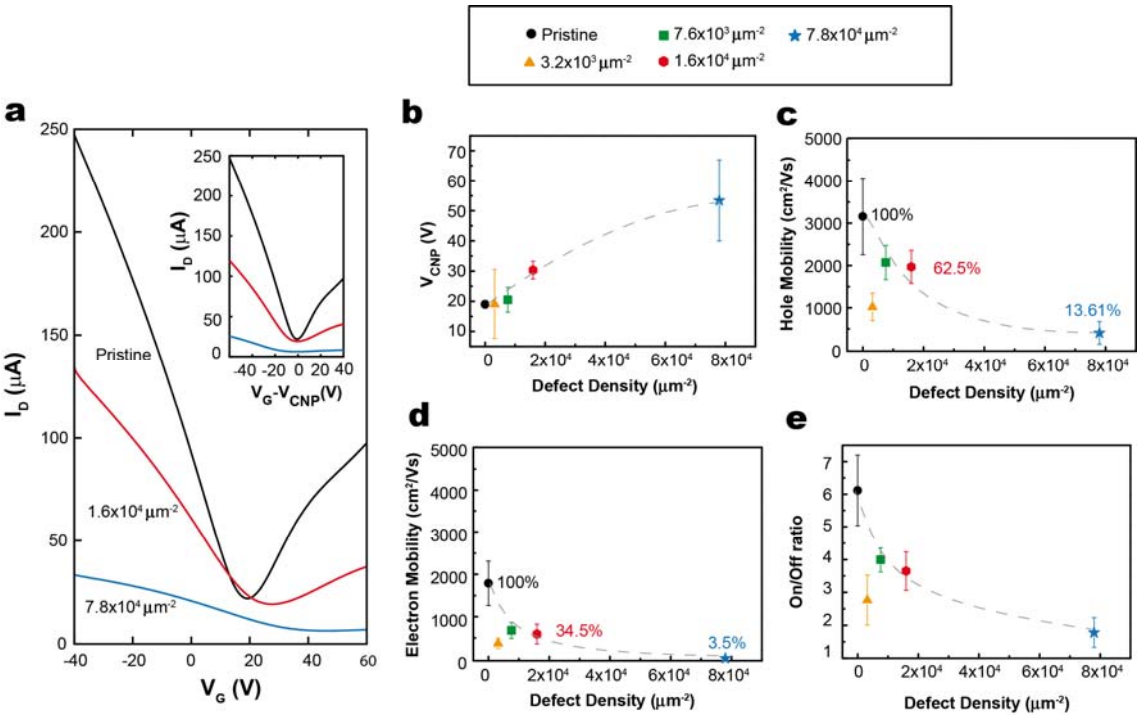

Figure 3: (a) V_G dependence of I_D for the pristine sample (black plot) and MW plasma-treated samples with defect densities ~1.6x10^4 µm^{-1} (red) and ~7.8x10^4 µm^{-1} (blue).The inset in (a) plots I_D against V_G-V_{CNP}, showing the dopant-induced asymmetry for holes (V_G-V_{CNP}<0) and electrons (V_G-V_{CNP}>0). The charge neutrality point position (b), the mobility of holes (c) and electrons (d), and the on/off ratio (e) are plotted as a function of the density of defects. Figures (b-e) show the average value of measurements at ten different spots, the error bars represent the standard deviation and the dashed lines are a guide to the eye.

One of the most important features observed in Fig. 3(a) is the upshift of the charge neutrality point for the defect-decorated samples compared to pristine graphene. Such upshift can be regarded as evidence of an enhancement in the p-type character of the plasma-treated samples [2]. In Fig. 3(b) it can be observed that the doping level correlates well with the density of atomic vacancies generated by the MW plasma. In addition to the upshift of the charge neutrality point, we see from Fig. 3(a) that the slope of the transfer curves on both sides of the charge neutrality point decreases in absolute value for plasma-treated graphene. The slope for gate voltages below (above) the charge neutrality point is directly related with the hole (electron) mobility. The mobility, μ, of the charge carriers was computed through the formula $\mu = \left[\left(\partial I_d/\partial V_g\right)L\right]/[WC_GV_d]$ where L and W are respectively the length and width of the transistor channel, V_d is the

drain voltage and C_G is the gate capacitance [2]. For a SiO_2 substrate with a thickness of 300 nm, C_G = 1.15 x 10^{-4} F m^{-2}. Fig. 3(c) and (d) summarize the mobility values for holes and electrons. It is clear from these plots, as well as from the inset to Fig. 3(a), that the electron mobility degrades to a higher extent than the hole mobility upon introduction of atomic vacancies with the MW oxygen plasma. Such evolution towards unipolar behavior is consistent with a progressive p-type doping of the plasma-treated graphene samples. In principle, the reduction in the charge carrier mobility can be ascribed either to scattering of the charge carriers at the defect sites that have been generated by the plasma treatment or to the opening of a bandgap [2]. The opening of a bandgap in graphene heavily decorated with oxygen groups has been theoretically predicted for the case where the graphene lattice retains its structural integrity [7]. However, this premise is not fulfilled in the present case, because structural defects in the lattice (atomic vacancies) have been created. More significantly, an increase in the on/off ratio of the FET would be expected if a bandgap was opened in graphene, whereas in our case the measured on/off ratio tended to decrease for all the plasma-treated samples [Fig. 3(e)]. Therefore, we conclude that in the present case the reduction in the charge carrier mobility was more likely produced by the scattering of the carriers at the defective sites created by the MW plasma rather than by the opening of a bandgap.

In summary, we have presented a MW oxygen plasma-based method for the introduction of small, similar-sized atomic vacancies in graphene with controlled density, in the range from about 10^3 to 10^5 μm^{-2}. The electronic properties of graphene undergo major changes as a result of its decoration with this type of defect. For example, we observed degradation in the mobility of both electrons and holes, although a net excess of positive charge carriers (p-type doping) was measured, the latter of which can be tentatively accounted for by the saturation of the vacancy edges with oxygen functional groups. We envisage that this method can be used for the tailored generation of tiny holes in graphene, which could then be used as membranes for, e.g., gas or liquid separation, DNA sequencing or molecular sensing. Furthermore, several schemes aimed at imparting specific chemical functionalities to graphene involve the introduction of atomic vacancies, so the present method can be used as a convenient starting point towards this end.

Acknowledgements

Financial support from the Spanish MINECO and the European Regional Development Fund (project MAT2011-26399) is gratefully acknowledged. Part of this work was supported by PRESTO, Japan Science and Technology. P.S.-F- acknowledges the receipt of a postdoctoral fellowship from JSPS. R. R. is grateful for the receipt of a pre-doctoral contract (FPU) from the Spanish MECD.

References

[1]Novoselov KS, Fal V, Colombo L, Gellert P, Schwab M, Kim K. A roadmap for graphene. Nature 2012;490(7419):192-200.
[2]Schwierz F. Graphene transistors. Nat Nanotechnol 2010;5(7):487-96.
[3]Robertson AW, Allen CS, Wu YA, He K, Olivier J, Neethling J, et al. Spatial control of defect creation in graphene at the nanoscale. Nat Commun 2012;3:1144.
[4]Kim J-H, Hwang JH, Suh J, Tongay S, Kwon S, Hwang CC, et al. Work function engineering of single layer graphene by irradiation-induced defects. Appl Phys Lett 2013;103(17):171604.
[5]Yamada Y, Murota K, Fujita R, Kim J, Watanabe A, Nakamura M, et al. Subnanometer vacancy defects introduced on graphene by oxygen gas. J Am Chem Soc 2014;136(6):2232-5.
[6]Yang D-P, Wang X, Guo X, Zhi X, Wang K, Li C, et al. UV/O_3 generated graphene nanomesh: formation mechanism, properties, and FET studies. J Phys Chem C 2014;118(1):725-31.
[7]Nourbakhsh A, Cantoro M, Vosch T, Pourtois G, Clemente F, van der Veen MH, et al. Bandgap opening in oxygen plasma-treated graphene. Nanotechnology 2010;21(43):435203.
[8]Xie G, Yang R, Chen P, Zhang J, Tian X, Wu S, et al. A general route towards defect and pore engineering in graphene. Small 2014;10(11):2280-4.
[9]Mao H, Wang R, Zhong J, Zhong S, Chen W. Mildly O_2 plasma treated CVD graphene as a promising platform for molecular sensing. Carbon 2014;76:212-9.
[10]Paredes JI, Solís-Fernández P, Martínez-Alonso A, Tascón JMD. Atomic vacancy engineering of graphitic surfaces: controlling the generation and harnessing the migration of the single vacancy. J Phys Chem C 2009;113(23):10249-55.
[11]Banhart F, Kotakoski J, Krasheninnikov AV. Structural defects in graphene. ACS Nano 2011;5(1):26-41.
[12]Ferrari AC, Basko DM. Raman spectroscopy as a versatile tool for studying the properties of graphene. Nat Nanotechnol 2013;8(4):235-46.
[13]Rozada R, Paredes JI, Villar-Rodil S, Martínez-Alonso A, Tascón JMD. Towards full repair of defects in reduced graphene oxide films by two-step graphitization. Nano Res 2013;6(3):216-33.
[14]Casiraghi C, Pisana S, Novoselov KS, Geim AK, Ferrari AC. Raman fingerprint of charged impurities in graphene. Appl Phys Lett 2007;91(23):233108.
[15]Orofeo CM, Hibino H, Kawahara K, Ogawa Y, Tsuji M, Ikeda K-i, et al. Influence of Cu metal on the domain structure and carrier mobility in single-layer graphene. Carbon 2012;50(6):2189-96.

Controlled generation of atomic vacancies in chemical vapor deposited graphene by microwave oxygen plasma

R. Rozada[a], P. Solís-Fernández[b], J.I. Paredes[a], A. Martínez-Alonso[a], H. Ago[b], J.M.D. Tascón[a]

[a]*Instituto Nacional del Carbón, INCAR-CSIC, Apartado 73, 33080 Oviedo, Spain*

[b]*Institute for Materials Chemistry and Engineering, Kyushu University, Fukuoka 816-8580, Japan*

Supplementary Information

Experimental

Single-layer CVD graphene was grown at ambient pressure over an heteroepitaxial thin Cu(111) film deposited on c-plane sapphire, following a method described elsewhere [1]. The CVD parameters were adjusted to obtain a complete coverage of high quality graphene. Briefly, a pre-annealing was conducted at 1000 °C for 40 minutes in an Ar/H_2 gas flow (H_2 concentration 2.5%), and then the temperature was raised to 1075 °C and CH_4 in a concentration of 10 ppm was added to the gas flow for 1 hour. The controlled generation of atomic vacancies on the as-grown graphene samples was performed in a MW-induced oxygen plasma apparatus (Technics Plasma 200-G system). O_2 (99.999% pure) was used for the treatment and the working pressure was set to 1.0 mbar. Proper combinations of plasma power and exposure time allowed tuning the density of defects created on graphene. Specifically, the selection of particular plasma power values and exposure times was the result of a feedback process that included visualizing by STM the appearance and density of defects generated in preliminary experiments. STM imaging was performed with a Nanoscope IIIa Multimode apparatus (Veeco Instruments) under ambient conditions using mechanically prepared Pt/Ir (80/20) tips. Images were recorded in the constant current mode with typical tunneling parameters of 200-500 pA and 500-1000 mV for nanometer-sized images and of 600-700 pA and 20 mV in the case of atomic-scale images. Following STM characterization, the graphene samples were transferred to a SiO_2(300 nm)/Si substrate by first coating them with poly(methyl methacrylate) (PMMA) and etching the Cu film in a $FeCl_3$ solution. After

transferring the PMMA/graphene film to the SiO_2/Si substrate, the polymer was dissolved using hot acetone. Raman characterization of the graphene samples on SiO_2/Si was carried out with a Nanofinder 30 confocal Raman microscope (Tokyo Instruments Inc.) using a laser excitation wavelength of 532 nm. For the electronic transport measurements, 10 μm-wide lines of graphene were patterned by photolithography, combined with oxygen plasma to remove the rest of the graphene film. Then, electrodes were made by photolithography followed by thermal evaporation of Au. The transport properties were measured under vacuum (~5×10^{-4} Pa) at room temperature using an Agilent B1500A (Agilent Technologies) semiconductor device analyzer.

References

[1]Hu B, Ago H, Ito Y, Kawahara K, Tsuji M, Magome E, et al. Epitaxial growth of large-area single-layer graphene over Cu(111)/sapphire by atmospheric pressure CVD. Carbon 2012;50(1):57-65.

Conclusiones 6

6. Conclusiones

Los resultados expuestos en la presente memoria permiten extraer las siguientes conclusiones generales.

- La reducción química del óxido de grafeno elimina mayoritariamente los grupos funcionales más lábiles situados en el plano basal, mientras que tiene un efecto muy limitado en la eliminación de los grupos más estables.
- Las imágenes de microscopía de proximidad a escala nanométrica de láminas de óxido de grafeno reducido químicamente muestran protuberancias cuyo origen se atribuye al desarrollo de regiones ordenadas libres de grupos funcionales oxigenados en coexistencia con algunas regiones aún oxidadas.
- Mediante irradiación con luz UV es posible lograr la reducción del óxido de grafeno en medio acuoso, a temperatura ambiente y en ausencia de reactivos reductores o fotocatalizadores.
- La radiación UV provoca el calentamiento local de las láminas y el aumento de la reactividad en su entorno. Este ambiente reactivo se puede aprovechar para la degradación de contaminantes como la rodamina B o para la nucleación y crecimiento de nanopartículas de oro y plata en las láminas. Estos híbridos "grafeno-nanopartículas" muestran un buen comportamiento como sustratos para SERS y como catalizadores.
- Es posible reparar la estructura aún defectuosa de las láminas de rGO, efectuando tratamientos a alta temperatura (1500-2700 °C) de filmes macroscópicos de dichas láminas. Esta reparación transcurre en dos etapas. En la primera (hasta 1500 °C) se produce la eliminación total de los grupos oxigenados aún presentes en la muestra. En la segunda etapa (1800-2700 °C) tiene lugar la aniquilación de las vacantes generadas en la primera etapa y la coalescencia de láminas solapadas, dando lugar a capas policristalinas.
- El principal mecanismo involucrado en la reparación a alta temperatura de láminas de rGO depositadas sobre una superficie no reactiva (terraza prístina de HOPG) es la migración de vacantes a través de dichas láminas y su aniquilación en los bordes. Para conseguir reparar completamente la estructura aromática de las láminas es esencial que estas últimas hayan sido sometidas a un proceso de eficiente de reducción química, lo cual limita la densidad y/o el tamaño de las vacantes generadas en el posterior tratamiento térmico.
- El tratamiento térmico de láminas de rGO depositadas sobre superficies reactivas (y de igual modo el solapamiento de láminas en un filme) provoca la formación de enlaces covalentes interlaminares que alteran la dinámica de migración de las vacantes, originan el fenómeno de coalescencia y pueden inducir la transferencia neta interlaminar de átomos de carbono bajo determinadas condiciones.

- Mediante plasma de oxígeno generado por microondas es posible introducir una distribución homogénea de vacantes multiatómicas con tamaño uniforme en grafeno producido por depósito químico en fase vapor. Variando la intensidad del plasma y el tiempo de exposición se consiguieron densidades de vacantes en el rango de 10^3-10^5 μm^{-2}.
- La introducción de vacantes multiatómicas en el grafeno genera un exceso neto de portadores de carga positiva (dopaje tipo p) y un descenso en la movilidad de los portadores de carga debido a su dispersión por dichas vacantes.

Anexo

Anexo

Durante el trabajo de tesis doctoral se generaron una serie de publicaciones, no incluidas en la presente memoria, de temática íntimamente relacionada.

[1]Ayán-Varela M, Paredes JI, Villar-Rodil S, Rozada R, Martínez-Alonso A, Tascón JMD. A quantitative analysis of the dispersion behavior of reduced graphene oxide in solvents. Carbon 2014;75(0):390-400.

[2]Guardia L, Paredes JI, Rozada R, Villar-Rodil S, Martínez-Alonso A, Tascón JMD. Production of aqueous dispersions of inorganic graphene analogues by exfoliation and stabilization with non-ionic surfactants. RSC Advances 2014;4(27):14115.

[3]Guardia L, Suárez-García F, Paredes JI, Solís-Fernández P, Rozada R, Fernández-Merino MJ, et al. Synthesis and characterization of graphene–mesoporous silica nanoparticle hybrids. Microporous and Mesoporous Materials 2012;160(0):18-24.

Aportaciones a congresos:

R. Rozada, J.I. Paredes, S. Villar-Rodil, A. Martínez-Alonso, J.M.D. Tascón. Two-step graphitization affords full repair of defects in reduced graphene oxide films. Imagine-Nano, Bilbao, España. 23-26 Abril 2013.

L. Guardia, F Suárez -Garda, J.I. Paredes, P. Solís-Fernández, R. Rozada, M.J. Fernández-Merino, A. Martínez-Alonso, J.M.D. Tascón. Reduced graphene oxide-mesoporous silica nanoparticle composites. Graphene Nanoscience: from Dirac Physics to Applications, Granada, España. 9-13 Septiembre 2012.

L. Guardia, S. Villar-Rodil, J.I. Paredes, R. Rozada, A. Martínez-Alonso, J.M.D. Tascón. Promoting processes in aqueous graphene oxide dispersions with UV light: graphene oxide reduction, formation of hybrids with metal nanoparticles and dye degradation. Graphene Nanoscience: from Dirac Physics to Applications, Granada, España. 9-13 Septiembre 2012.

P. Solís-Fernández, R. Rozada, J.I. Paredes, S. Villar-Rodil, M.J. Fernández-Merino, L. Guardia, A. MartínezAlonso, J.M.D. Tascón. Chemical and microscopic analysis of graphene prepared by different reduction degrees of graphene oxide. 18th International Symposium on Metastable, Amorphous and Nanostructured Materials, Gijón, España. 26 Junio-1 Julio, 2011.

L. Guardia, F Suárez -Garda, J.I. Paredes, P. Solís-Fernández, R. Rozada, A. Martínez-Alonso, J.M.D. Tascón. Synthesis of silica- and titania-graphene nanocomposite sheets.

18th International Symposium on Metastable, Amorphous and Nanostructured Materials, Gijón, España. 26 Junio-1 Julio, 2011.